# Nonlinear Optical Whispering Gallery Microresonators for Photonics

by

## John E. Heebner

Submitted in Partial Fulfillment
of the
Requirements for the Degree
Doctor of Philosophy

Supervised by
Professor Robert W. Boyd

The Institute of Optics
The College
School of Engineering and Applied Sciences

University of Rochester
Rochester, New York

2003

*for mom and dad*

# Curriculum Vitae

The author was born in Orange, New Jersey in 1974 and grew up in Livingston, New Jersey. He graduated first in his class with a B.E. degree in engineering physics from Stevens Institute of Technology in Hoboken, New Jersey in 1996. He then began graduate studies at the Institute of Optics and received a National Science Foundation Fellowship. He has carried out his doctoral research in nonlinear optics under the supervision of Professor Robert W. Boyd.

# Publications

J. E. Heebner and R. W. Boyd., "Strong Dispersive and Nonlinear Optical Properties of Microresonator-Modified Waveguides.", *SPIE Proc.*, 4969-41 (2003).

J. E. Heebner and R. W. Boyd., "'Slow and 'Fast Light in Resonator-Coupled Waveguides.", *J. Mod. Opt.* **49**, 2629-2636 (2002).

S. Pereira, J. E. Sipe, J. E. Heebner, and R. W. Boyd., "Gap Solitons in a Two-Channel SCISSOR Structure.", *Opt. Lett.* **27**, 536-538 (2002).

J. E. Heebner, R. W. Boyd., and Q. Park, "SCISSOR Solitons and Other Propagation Effects in Microresonator-Modified Waveguides.", *J. Opt. Soc. Am. B.* **19**, 722-731 (2002).

J. E. Heebner, R. W. Boyd., and Q. Park, "Slow Light, Induced Dispersion, Enhanced Nonlinearity, and Optical Solitons in a Resonator-Array Waveguide.", *Phys. Rev. E.* **65**, 036619 (2002).

S. Blair, J. E. Heebner, and R. W. Boyd., "Beyond the Absorption-Limited Nonlinear Phase Shift with Microring Resonators.", *Opt. Lett.* **27**, 357-359 (2002).

R. W. Boyd and J. E. Heebner., "Sensitive Disk Resonator Photonic Biosensor.", *Appl. Opt.* **40**, 5742-5747 (2001).

J. E. Heebner and R. W. Boyd., "Photorefractive Optical Recycling for Contrast Enhancement.", *Opt. Comm.* **182**, 243 (2000).

J. E. Heebner, R. S. Bennink, R. W. Boyd, and R. A. Fisher., "Conversion of Unpolarized Light to Polarized Light with Greater than 50% Efficiency by Photorefractive Two-Beam Coupling.", *Opt. Lett.* **25**, 257 (2000).

J. E. Heebner and R. W. Boyd., "Enhanced All-Optical Switching by Use of a Nonlinear Fiber Ring Resonator.", *Opt. Lett.* **24**, 847 (1999).

# Presentations

J. E. Heebner and R. W. Boyd., "Strong Dispersive and Nonlinear Optical Properties of Microresonator-Modified Waveguides.", SPIE Photonics West, San Jose, CA (2003).

J. E. Heebner and R. W. Boyd., "Exotic Linear and Nonlinear Optical Properties of Microresonator-Modified Waveguides.", Laboratory for Physical Sciences Seminar, U. Maryland, MD (2002)

J. E. Heebner, R. W. Boyd, and Q-Han Park., "SCISSOR Solitons.", OSA Nonlinear Guided Waves Meeting, Clearwater, FL (2001)

J. E. Heebner and R. W. Boyd., "Nonlinear Optical Whispering Gallery Disk Resonators for Photonic Switching.", OSA Annual Meeting, Providence, RI (2000)

J. E. Heebner and R. W. Boyd., "Contrast Enhanced Amplified Imaging by Photorefractive Recycling.", CLEO, San Francisco, CA (2000)

J. E. Heebner, R. W. Boyd, and R. A. Fisher., "Breaking the Law of Malus, and Building a Better Polarizer via a Photorefractive Demon.", OSA Annual Meeting, Santa Clara, CA (1999)

J. E. Heebner and R. W. Boyd., "Enhanced All-Optical Switching Using a Phase-Shift Enhancing Fiber Ring Resonator.", OSA Annual Meeting, Baltimore, MD (1998)

# Acknowledgments

"We have a habit in writing articles published in scientific journals to make the work as finished as possible, to cover up all the tracks, to not worry about the blind alleys or describe how you had the wrong idea first, and so on. So there isn't any place to publish in a dignified manner what you actually did to get to do the work."

I have taken this sentiment expressed by Richard Feynman as a guiding voice during the writing of this thesis. I have done my best to describe all the important things I did so that another may be able to repeat my findings. On the other hand, if the reader encounters any mistakes, I defer to my advisors words: "What's a factor of N amongst friends?"

Ever since I was a kid I was told not to run with scissors, but in my many trips to Cornell that is exactly what I did!

My research was partly supported by the National Science Foundation. Fabrication was accomplished partly at the Molecular Beam Epitaxy Laboratory (U of R) and at the Cornell Nanofabrication Facility.

I wish to acknowledge the support and guidance of my thesis advisor Professor

Robert W. Boyd. Professor Boyd not only taught me nonlinear optics and how to derive useful quantities from fundamental constants, he also taught me how to ski and windsurf. I am indebted to him for suggesting the topic of ring resonators which arose from a pet project he gave me when I first joined his group.

I would also like to thank Richart E. Slusher, John E. Sipe, Deborah J. Jackson, and Govind P. Agrawal for stimulating conversations and technical advice.

With regards to the fabrication effort, I want to thank Gary W. Wicks, Mike Koch, Ping-Tong Ho, Rohit Grover, Rebecca Welty, Alan Bleier, John Treichler, and Rob Ilic for assisting me in the fabrication of samples.

More thanks goes out to my fellow peers who have been there at one time or another: Mark Sanson, Brian Soller, Dawn Gifford, Ryan Bennink, Sean Bentley, Vincent Wong, Matt Bigelow, Giovanni Piredda, Aaron Schweinsberg, Collin O'Sullivan-Hale, Petros Zerom, Laura Allaire, Nick Lepeshkin, Young Kwon Yoon, and Alan Heaney.

Finally, I would like to thank my wife, Erika for all the support she has given me during the time I spent working on this thesis. Convincing her to come live with me in beautiful Rochester was not as easy as it might sound!

# Abstract

In this thesis, I have investigated the linear and nonlinear optical properties of whispering-gallery microdisk and microring resonators side coupled to an ordinary waveguide. A waveguide-coupled disk or ring resonator behaves much like a Gires-Tournois interferometer [1] which is simply a Fabry-Perot interferometer with a 100% reflecting back mirror. The configuration is simple and yet extremely interesting because, unlike a Fabry-Perot resonator which has two output ports, a Gires-Tournois interferometer restricts light to a single output port (reflection). For the waveguide-coupled microresonator, the equivalent reflection port is in the forward direction and no light is coupled into the backward direction. Thus, the device behaves as an "all-pass" or "phase-only" filter which only modifies the phase of light traversing it. The phase shift imparted is however, detuning-dependent and highly sensitive near resonance. In addition to this increased phase sensitivity, the light circulating inside the resonator is coherently built up to a higher intensity than that incident upon the resonator. The combined action of these two effects results in dramatically enhanced nonlinear phase-shifting properties. Additionally, the all-pass resonator exhibits strong group delay and

group delay dispersion effects. The elegant simplicity of such a configuration allows it to serve as a building block for constructing compact integrated optical switches, optical logic devices, and engineerable waveguides for exotic pulse modification. I have derived theoretical predictions for the construction of useful photonic devices and have outlined the physical limitations of their implementation. Finally, in order to test these predictions, I designed, fabricated, and tested several microresonator-based devices using nanofabrication technology.

# Table of Contents

# List of Figures

# Chapter 1

# Introduction

Optical resonators were employed as useful devices as early as 1899, when Fabry and Perot described the use of a parallel-plate resonator as an interferometric filter. [2] Through the use of recirculating feedback, a Fabry-Perot interferometer is able to increase the effective path length of light traversing it by a factor equivalent to its finesse. A configuration with strongly reflecting end mirrors will possess a high finesse and will proportionately possess a much narrower passband than that of a configuration with weakly reflecting mirrors. The narrowing of the passband is accompanied by a proportional coherent build-up of intensity circulating within the cavity. While this build-up is of little consequence to the linear transmission properties, it has a dramatic effect on the nonlinear transmission properties. In 1969, Szöke, et al. realized this fact and proposed inserting a nonlinear material (saturable absorber) between the mirrors and described optical multistability with possible applications for optical logic.

[3] Marburger and Felber later described the theory of a Fabry-Perot resonator containing a medium possessing a nonlinear (intensity-dependent) refractive index and showed that under certain operating conditions, the device could be implemented as an all-optical switch. [4] Miller [5] later experimentally demonstrated refractive bistability in a Fabry-Perot for use as an optical switch. Resonators constructed from guided-wave optical geometries (as opposed to previous bulk geometries or microwave-based guides) first surfaced in 1982, when Stokes, et al. of Stanford University analyzed and demonstrated the transmission characteristics of a 2-port single-mode fiber ring resonator (first schematic in 1.1). [6] Ohtsuka in Japan, [7] Yariv and Crosignani, of Caltech [8] analyzed in detail the effects of partial source coherence and multistability. [9] In the late eighties, ring resonators began seeing application in quantum optics. Shelby, et al. of IBM Almaden observed a finesse-squared enhancement dependence of squeezed light generation in a fiber ring resonator. [10,11] In 1988, the first quantum nondemolition (QND) experiments were performed by Bachor and Levenson et al. in a similar fiber ring resonator. [12] In 1989, Braginsky et al. in Russia studied the nonlinear properties of optical whispering-gallery modes; modes that skim along the inner curved surface of a cladded dielectric disk or sphere. [13] Braginsky proposed the application of such modes to the lofty goal of switching with a single quantum. [14] In the early nineties, ring resonators began seeing application as all-pass filters (purely phase-modifying elements) for dispersion compensation and

phase equalization in optical communications. In 1990, Cimini, Greenstein, and Saleh at Lucent, Holmdel proposed the use of the closely related Gires-Tournois interferometer (see schematic in 1.1) for just these means. [15] In 1992, Pandian and Seraji at the Indian Institute of Technology carried out an extensive study of the dynamic pulse response of a ring resonator with particular attention to chirping and dispersion compensation. [16,17] At around the same time, Richart Slusher et al. at Lucent, Murray Hill built the first whispering-gallery based disk lasers [18,19] ushering in a new class of semiconductor laser. Working with a fiber-based ring resonator, Capmany in Spain pointed out the dramatic increase in phase sensitivity near resonance, and observed differential phase amplification. [20] Along these lines, Inoue, et al. of NTT, Japan observed that a ring resonator side coupled to one arm of a Mach-Zehnder interferometer serves to flatten, or square-off the cosine-squared response curve, an effect related to decreased phase sensitivity and applications in the construction of flat filter response. [21] In 1995, Lefevre in France observed an extremely high Q of $10^9$ associated with the whispering gallery resonances of fused silica microspheres side coupled to an optical fiber. [22] Shortly after, in 1996, Vernooy and Kimble at Caltech performed cavity QED experiments which exploited the small mode volumes and high field strengths associated with the modes of micro-cavities. [23] In 1997 Chang et al. at Yale demonstrated Q-switching using enhanced saturable absorption associated with the WGM resonances of microdroplets. [24] In 1997, Blom et al. (Nether-

lands) proposed the development of an integrated all-optical switch based upon the high-Q whispering gallery modes of a nonlinear polymer disk. [25,26] More recently, Haus (MIT) and Little (Little Optics) have been the major proponents of a microring channel dropping architecture. [27] In 1998, Madsen and Lenz at Lucent, Murray Hill presented a framework for employing all-pass filters in the form of cascades of ring resonators for the design of any desired dispersion profile [28] and filter response. [29] Today, there continues to be much active work in the field of whispering gallery based microresonators, though mostly applied to dispersion compensation and overwhelmingly in the context of constructing add-drop wavelength division multiplexed (WDM) filters. [30] Some applications as lasers, most recently using the raman effect [31] and cavity QED [32,33] still continue to be explored. All-optical switching was recently demonstrated for the first time in a compact microring geometry based on principles similar to those derived in this thesis. [34–36] To the best of my knowledge however, the nonlinear *phase transfer* characteristics of microresonators have not been systematically studied, and few research groups appear to be interested in constructing devices exploiting the nonlinear phase shift enhancements offered by microresonators despite their great latent potential.

# Ring Configurations

Guided-Wave                    Free Space

All-Pass
Ring
Resonator

Gires-Tournois
Interferometer

r

OR

Fabry-Perot
Ring
Resonator

Fabry-Perot
Interferometer

OR

Loop Mirror
Fiber Gyro

Sagnac
Interferometer
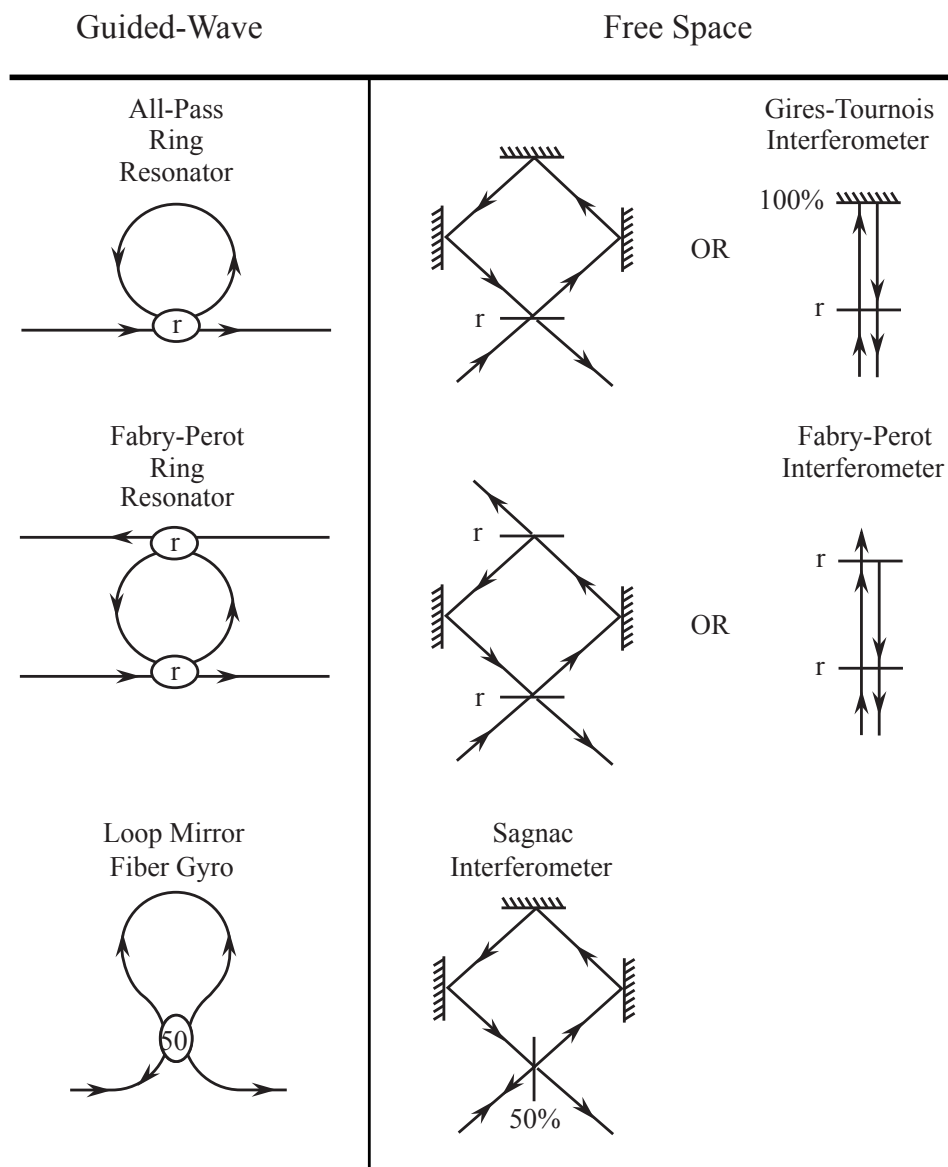
Figure 1.1: Various ring configurations and their free-space analogues.

# Chapter 2

# Linear Microresonator Theory

## 2.1  Introduction

A simple ring resonator is created by taking one output of a generic directional coupler and feeding it back into one input (see figure 2.1). Such a device exhibits a periodic cavity resonance when light traversing the ring acquires a phase shift corresponding to an integer multiple of $2\pi$ radians. The resonator is mathematically formulated from two components: a coupling strength and a feedback path.

## 2.2  Mathematical Formulation

The basic relations amongst the incident $E_1$, transmitted $E_2$, and circulating $E_3$, $E_4$ fields of a single resonator are derived by combining the relations for the coupler with that of the feedback path. In the spectral domain, the fields exiting
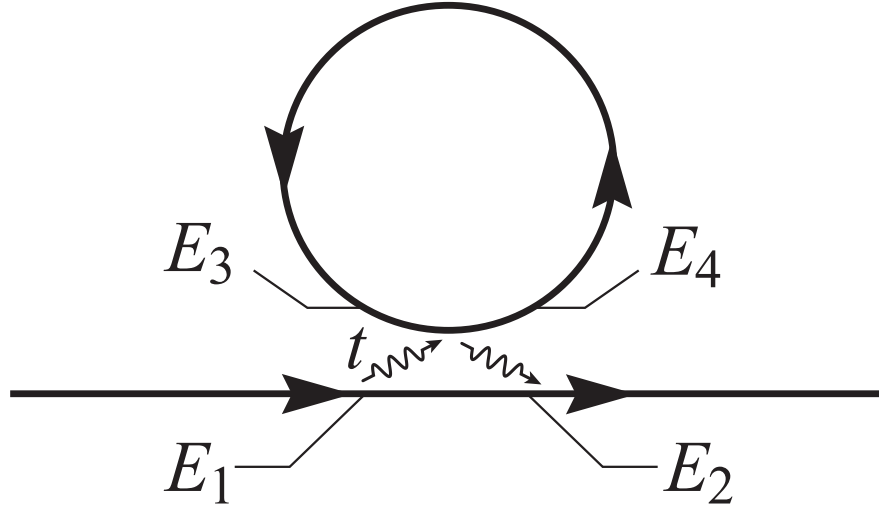
Figure 2.1: A prototypical all-pass ring resonator.

the coupling region[1] are related to the input fields via the following unitary matrix:

$$
\begin{pmatrix} E_4\left(\omega\right) \\ E_2\left(\omega\right) \end{pmatrix} = \begin{pmatrix} r & it \\ it & r \end{pmatrix} \begin{pmatrix} E_3\left(\omega\right) \\ E_1\left(\omega\right) \end{pmatrix}, \tag{2.1}
$$

where the self- and cross-coupling coefficients[2] $r$ and $t$ are assumed to be independent of frequency and satisfy the relation $r^2 + t^2 = 1$. The feedback path (of length $2\pi R$) connects the output from port 4 back into input port 3 where the field is expressed as:

$$
E_3 = e^{-\frac{\alpha}{2}L}e^{ikL}E_4 \equiv ae^{i\phi}E_4 \tag{2.2}
$$

---

[1]In the case of a microresonator, while the coupling is distributed over a significant angular portion of the disk, the coupling can be treated as being lumped and localized to a single point without loss of generality [37]

[2]The symbols, $r$ and $t$ were chosen to represent the amplitude coupling ratios because they are analogous to the reflectivity and transmissivity of an ordinary beam-splitter

Here, $a$ represents the single-pass amplitude transmission and $\phi$ represents the single-pass phase shift. Because adding or subtracting an integer number $m$ of $2\pi$ radians from the single-pass phase shift does not change the value of the function, the single-pass phase shift for all resonances is defined such that its value is zero for a local resonance of interest. Furthermore, because the single-pass phase shift is directly related to the radian frequency as $\phi = \omega T_\mathrm{R}$ where $T_\mathrm{R}$ is the transit time of the resonator, $\phi$ is interpreted as a *normalized detuning.*

## 2.3 Intensity Build-Up

Equations 2.1 and 2.2 are solved to obtain an expression for the ratio of the circulating field to the incident field:

$$\frac{E_3}{E_1} = \frac{itae^{+i\phi}}{1 - rae^{+i\phi}}. \tag{2.3}$$

The ratio of circulating intensity to incident intensity, or the build-up factor $\mathcal{B}$, is given by the squared modulus of this result,

$$\mathcal{B} = \frac{I_3}{I_1} = \left|\frac{E_3}{E_1}\right|^2 = \frac{(1 - r^2)\,a^2}{1 - 2ra\cos\phi + r^2a^2} \xrightarrow[\phi=0,a=1]{} \frac{1+r}{1-r}, \tag{2.4}$$

where the last form of this result refers to the situation in which the incident light is resonant with the ring ($\phi = m2\pi$) and attenuation is negligible ($a = 1$).

A passive ring resonator under these conditions attains the maximum ratio of circulating power to incident power that can be achieved (see figure 2.2).  As a result of this coherent build-up of intensity, the incident power required to achieve a desired single-pass nonlinear phase shift may be reduced accordingly.

It is crucial that this is a coherent build-up of intensity.  That is, were the resonator to be excited by partially coherent light, then the degree of build-up would be diminished.  If the resonator is excited with completely incoherent light, there would be no build-up of intensity circulating in the resonator.  In this case, the field intensity rather than the field amplitude combines in an additive manner. The situation is analogous to a fluid dynamic model where some fraction of current flowing in a pipe (waveguide) is diverted into an enclosed volume (resonator). In the absence of dissipation, the fluid pressure (intensity) is equal in the pipe and enclosed volume.  Mathematically this can be demonstrated in a number of ways.  Completely incoherent light possesses a uniform "white light" spectrum. Integrating over the periodic build-up function over a single period and dividing by the period width results in unity.  Thus, the average build-up over all frequencies is simply one.  This may be viewed as a basic conservation law for resonators. A resonance is typically characterized by a parameter termed the finesse which is defined as the periodicity of resonant peaks (or free-spectral range,

$$\Delta\nu_{\mathrm{FSR}} = \frac{c}{n2\pi R} = \frac{1}{T_{\mathrm{R}}}, \tag{2.5}$$
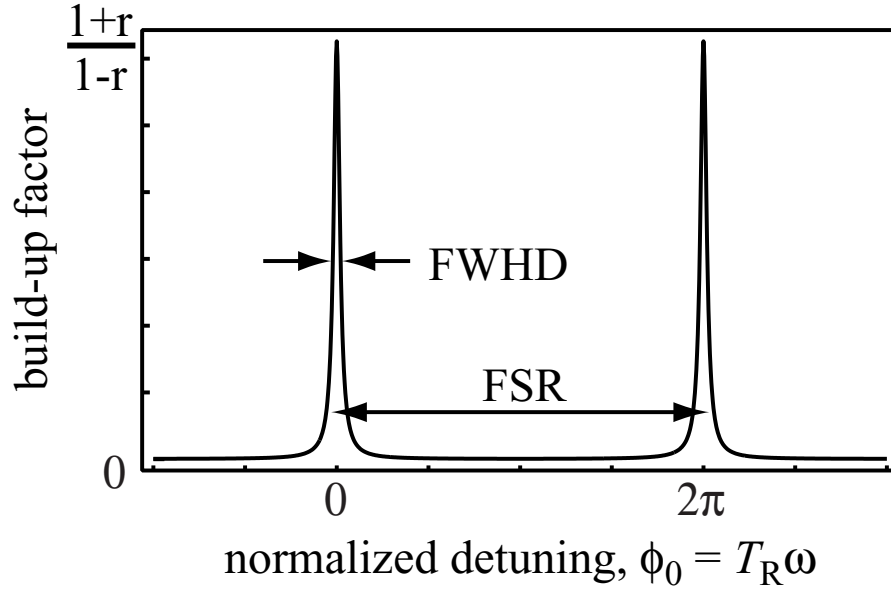
Figure 2.2: A plot of the build-up factor vs. single-pass phase shift for a ring resonator.

divided by the full-width at half depth, $\Delta\nu_{\text{FWHD}}$ of a resonant peak.

$$\mathcal{F} = \frac{\Delta\nu_{\text{FSR}}}{\Delta\nu_{\text{FWHD}}} = \frac{2\pi}{2\arccos\left(\frac{2ra}{1+r^2a^2}\right)} \xrightarrow[ra\approx1]{} \frac{\pi}{1-ra}. \tag{2.6}$$

A comparison of this expression with the build-up demonstrates the conservation law in another way. The peak of the build-up resonance is directly related to the compression of its width $\mathcal{B}_0 \approx \frac{2}{\pi}\mathcal{F}$ such that the area under the build-up (within a free-spectral range) is constant for any value of coupling $r$ provided that energy is conserved i.e. no internal attenuation. Finally, it is sometimes common to characterize the resonance in terms of a quality factor, $Q$. The quality factor is defined as the resonant frequency divided by the bandwidth,

$Q = \nu_0/\Delta\nu_{\text{FWHM}}$. The quality factor is simply related to the finesse by the number of optical wavelengths per ring circumference.

$$Q = \frac{n2\pi R}{\lambda}\mathcal{F} = m\mathcal{F} \tag{2.7}$$

where m is referred to as the azimuthal number. For some purposes, it is useful to approximate the build-up curve as a Lorentzian. See appendix A for a description of this approximation.

## 2.4 Effective Phase Shift

An examination of the transfer characteristics of the resonator reveals another periodically resonant feature. Equations 2.1 and 2.3 are solved to obtain the ratio of the transmitted field to the incident field:

$$\frac{E_2}{E_1} = e^{+i(\pi+\phi)}\frac{a - re^{-i\phi}}{1 - rae^{+i\phi}}. \tag{2.8}$$

The intensity transmission is given by the squared modulus of this quantity and has previously been studied extensively. [6,38] For negligible attenuation ($a = 1$), the equation predicts a unit intensity transmission for all values of detuning $\phi$. Such a device is directly useless as an amplitude filter, allowing 100% transmission for all frequencies and is aptly termed an "all-pass" filter. This result is satisfying

from an intuitive standpoint because light is offered only two choices: leave the device at port 2 or (re)enter the resonator at port 4. There is no mechanism for light to exit via port 1 and in steady state the optical powers entering and exiting the resonator are equal. Thus, to satisfy energy conservation, the device must transmit pass all frequencies completely. This requirement, however does not impose the same uniform requirement of constant phase across all frequencies. The phase of the transmitted light, as will be shown, can be dramatically different for differing frequencies especially near resonance. The effective phase shift is defined as the phase argument of the field transmission factor and is the phase shift acquired by light in crossing the coupler from port one to port two:

$$\Phi = \pi + \phi + \arctan\frac{r\sin(\phi)}{a - r\cos(\phi)} + \arctan\frac{ra\sin(\phi)}{1 - ra\cos(\phi)}$$
$$\xrightarrow[a=1]{} \pi + \phi + 2\arctan\frac{r\sin(\phi)}{1 - r\cos(\phi)}. \quad (2.9)$$

A plot of the effective phase shift vs. the single pass phase shift $\phi$ for different values of $r^2$ is shown in figure 2.3.

Near resonance ($\phi \approx 0$) the slope of the curve becomes very steep indicating that the phase that the device imparts is sensitively dependent upon the normalized detuning. [39] The phase sensitivity is obtained by differentiating the
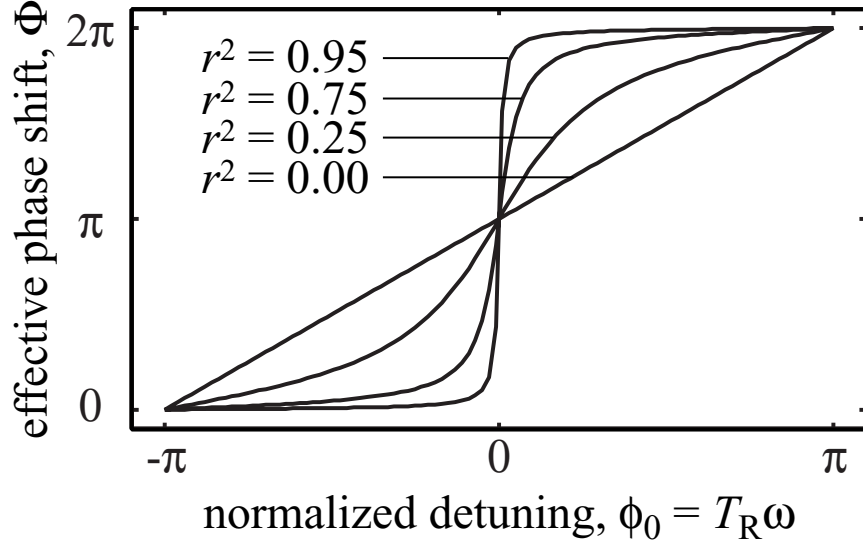
Figure 2.3: A plot of the effective phase shift vs. single-pass phase shift for a ring resonator. Note the increasing sensitivity near resonance for increasing values of R.

effective phase shift with respect to the detuning to obtain

$$\Phi' = \frac{d\Phi}{d\phi} = \frac{(1 - r^2)\, a^2}{1 - 2ra\cos(\phi)\frac{(1+a^2)}{2} + r^2 a^2 + \left(\sin^2(\phi)\left(1 - a^2\right)^2\right)r^2 - \left(1 - a^2\right)}$$

$$\xrightarrow[\phi=0, a=1]{} \frac{1+r}{1-r} \quad (2.10)$$

The last form of this result refers to the situation in which the incident light is resonant and attenuation is negligible ($a = 1$). A comparison with equation 2.4 reveals that under these conditions, the level of phase sensitivity is exactly equal to the level of intensity build-up. The main features associated with all-pass ring resonators are summarized in figure 2.4.
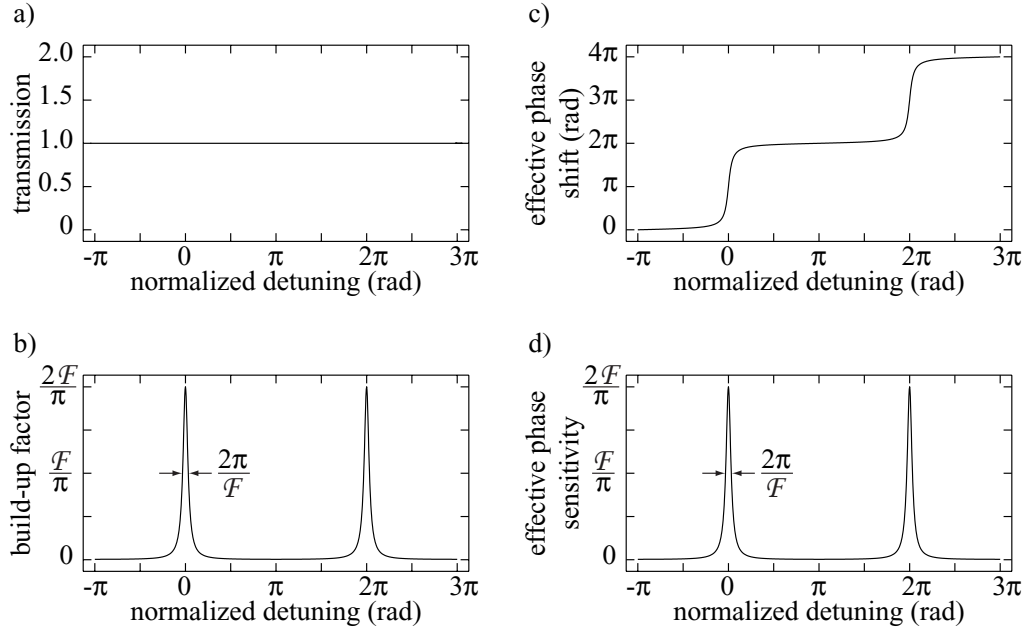
Figure 2.4: a) Transmission, b) build-up factor, c) effective phase shift acquired on transmission, and d) phase sensitivity (derivative of c) plotted vs. the internal phase shift for a waveguide-coupled ring resonator with a finesse of $10\pi$.

A finite difference time domain simulation at the level of Maxwell's equations for a ring resonator reveals that the approximations derived thus far in this chapter accurately describe the essential features associated with cavity resonances. Figure 2.5 displays the incident and circulating intensity for an all-pass ring resonator on resonance. Figure 2.6 displays spectral intensity and phase for the same resonator. The resonator contribution to the transmitted phase clearly dominates the waveguide contribution (which primarily introduces a linear offset).

If a device possess a unit frequency response but affects the phase of transmitted light in an nonuniform manner, it appears at first glance that such a device
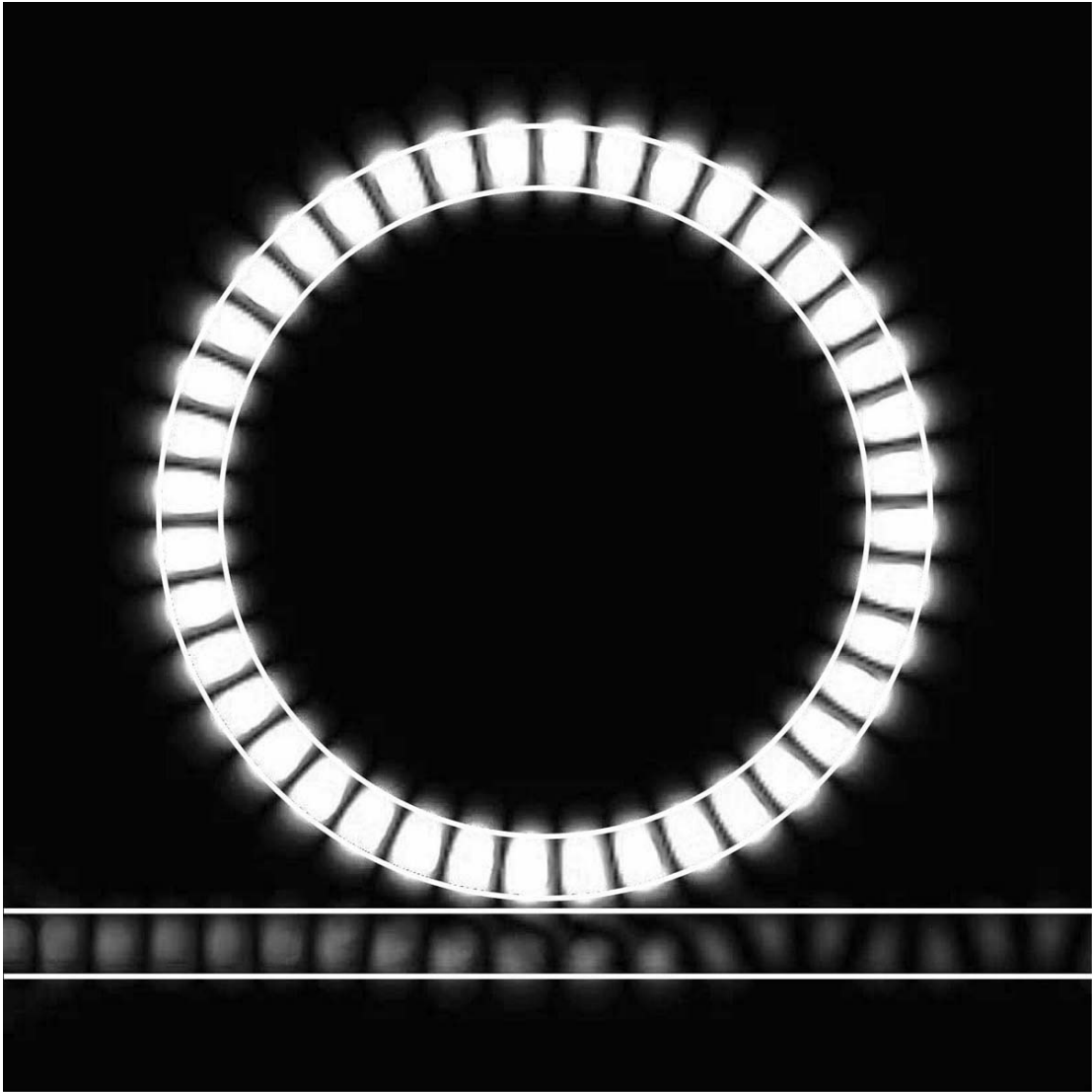
Figure 2.5: Finite difference time domain simulation demonstrating resonator build-up at 1.5749 $\mu$m. Guide and ring widths are 0.4 $\mu$m. Resonator radii are 2.5 $\mu$m (outer) and 2.1 $\mu$m (inner). All guiding structures have a refractive index of 2.5 that is cladded by air.
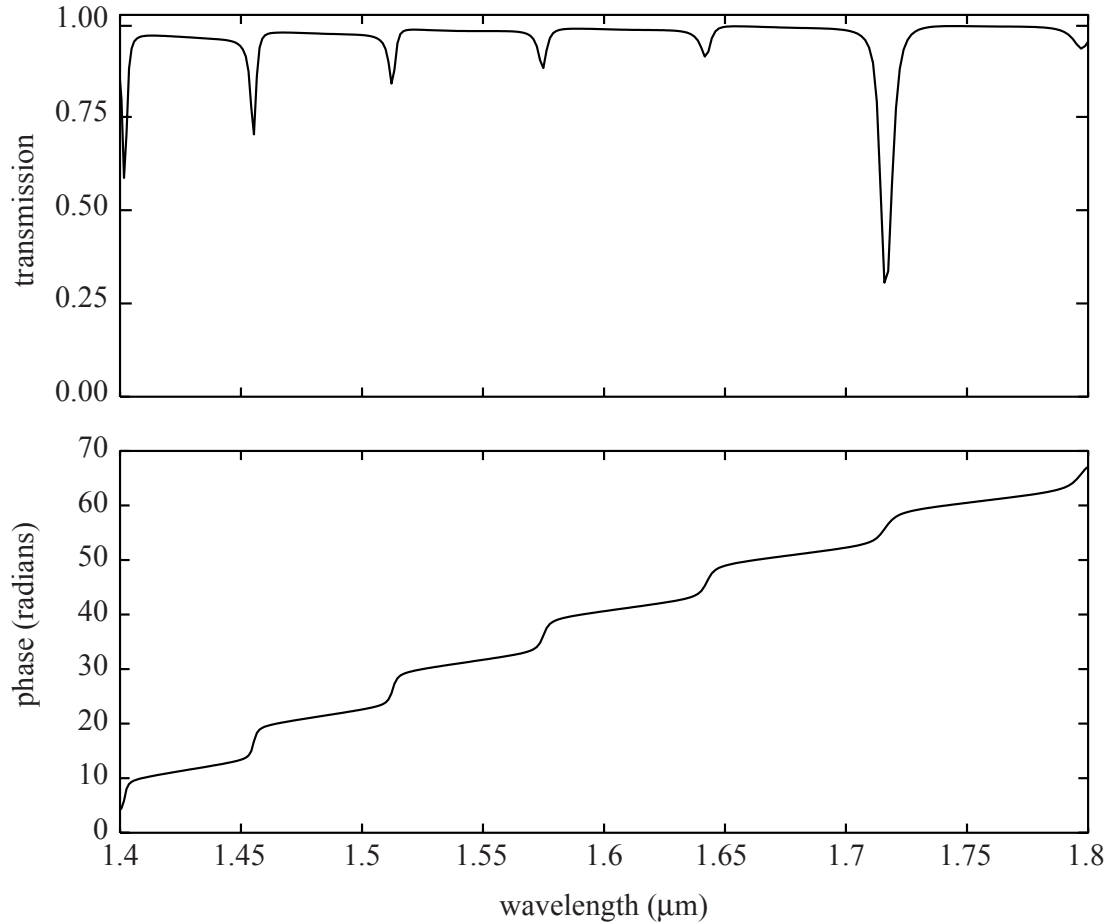
Figure 2.6: Transmitted spectral intensity and phase associated with the ring resonator in figure 2.5. Small transmission dips in the spectrum result from losses due to scattering from an imperfect computation grid. The spectral phase includes primarily linear contributions from the waveguide and the familiar "stair-step" contribution associated with the effective phase shift induced by the resonator. The resonator effective radius of 2.3 $\mu$m and index of 2.5 should result in a free-spectral range of 71 nm near 1600 nm which is in excellent agreement with the obtained spectrum.

has violated the Kramers-Kronig relations [40,41][3] which often hold for a causal device. This however is not the case as it can be shown that the real and imaginary parts of the transfer function do in fact satisfy the Kramers-Kronig relations. It is clear from examination of the impulse response (a comb of weighted delta functions appearing only for positive times) that causality is not violated. Thus, while the real and imaginary parts of the transfer function vary in a complicated manner, they do so in such a way that the amplitude is always unity. In certain cases it is possible to formulate Kramers-Kronig relations for the amplitude and phase of a transfer function. This is accomplished by taking the natural logarithm of the transfer function - a procedure which maps the amplitude and phase into real and imaginary components. Due to the presence of zeros in the upper half complex frequency plane of the transfer function, the logarithm of the transfer function is not everywhere analytic in the upper half plane. [42–45] As a result, Kramers-Kronig relations cannot be applied to the amplitude and phase. See appendix B for a more detailed description.

---

[3]In optics, it is the real and imaginary parts of the complex susceptibility and not the amplitude and phase which are related by a Hilbert transform in the frequency domain. The real part corresponds to the scattered field mixing in quadrature with the exciting field and imparting a phase delay which is parameterized macroscopically as a refractive index. The imaginary part corresponds to the scattered field mixing $\pi$ radians out of phase with the exciting field and imparting a decrease in amplitude which is parameterized macroscopically as an attenuation coefficient.

## 2.5 Group Delay and Group Delay Dispersion

The increased phase sensitivity is directly related to the increase in effective path length. This correspondence can be seen by examining the delay imposed by the resonator on a resonant pulse. The group delay for a linear device is given by the radian frequency derivative of the phase of the transfer function,

$$(T_{\mathrm{D}} = \frac{d\Phi}{d\omega}). \tag{2.11}$$

Because the detuning is related to the radian frequency as $\phi = \omega T_{\mathrm{R}}$, the group delay is simply related to the phase sensitivity as $T_{\mathrm{D}} = \Phi' T_{\mathrm{R}}$. The phase sensitivity can thus be interpreted as the effective number of round trips light traverses in the resonator.

Because the group delay associated with an all-pass filter is a frequency-dependent function, its transmission characteristics are inherently dispersive. The group delay dispersion (GDD) for a linear device is defined as the radian frequency derivative of the group delay,

$$\mathrm{GDD} = \frac{d^2\Phi}{d\omega^2} = \Phi'' T_{\mathrm{R}}^2. \tag{2.12}$$

The GDD can be strong enough to significantly disperse a pulse. On resonance, the GDD (and all even dispersive orders) is zero although higher-order dispersion exists. The GDD has extremum values at $\phi = \pm\pi/\mathcal{F}\sqrt{3}$ where it attains the value

## Resonator Pulse Response

a)



b)



c)



d)



| incident pulse | ——— |
| scaled circulating pulse | — — — |
| transmitted pulse | ·········· |
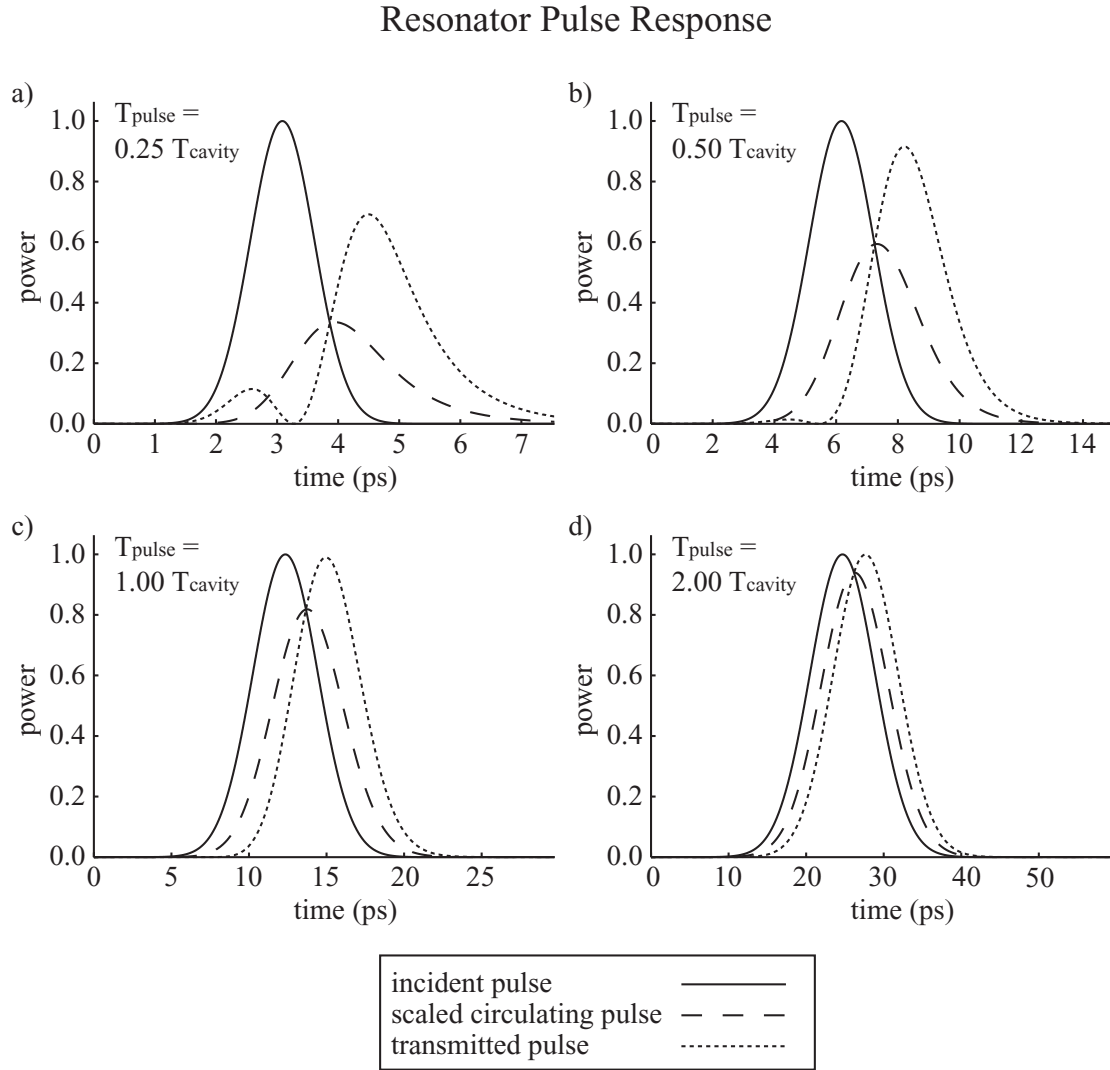
Figure 2.7: Four simulations of pulsed excitation of an all-pass ring resonator. The resonator parameters, kept constant in all cases, consisted of $r = 0.905$, $T_R = 0.157$ ps, $T_{cav} = \mathcal{F}T_R = 5$ ps. The pulse widths vary as a)1.25 ps, b)2.5 ps, c)5 ps, and d) 10 ps. Note that pulse fidelity is well preserved for widths larger than the cavity lifetime.
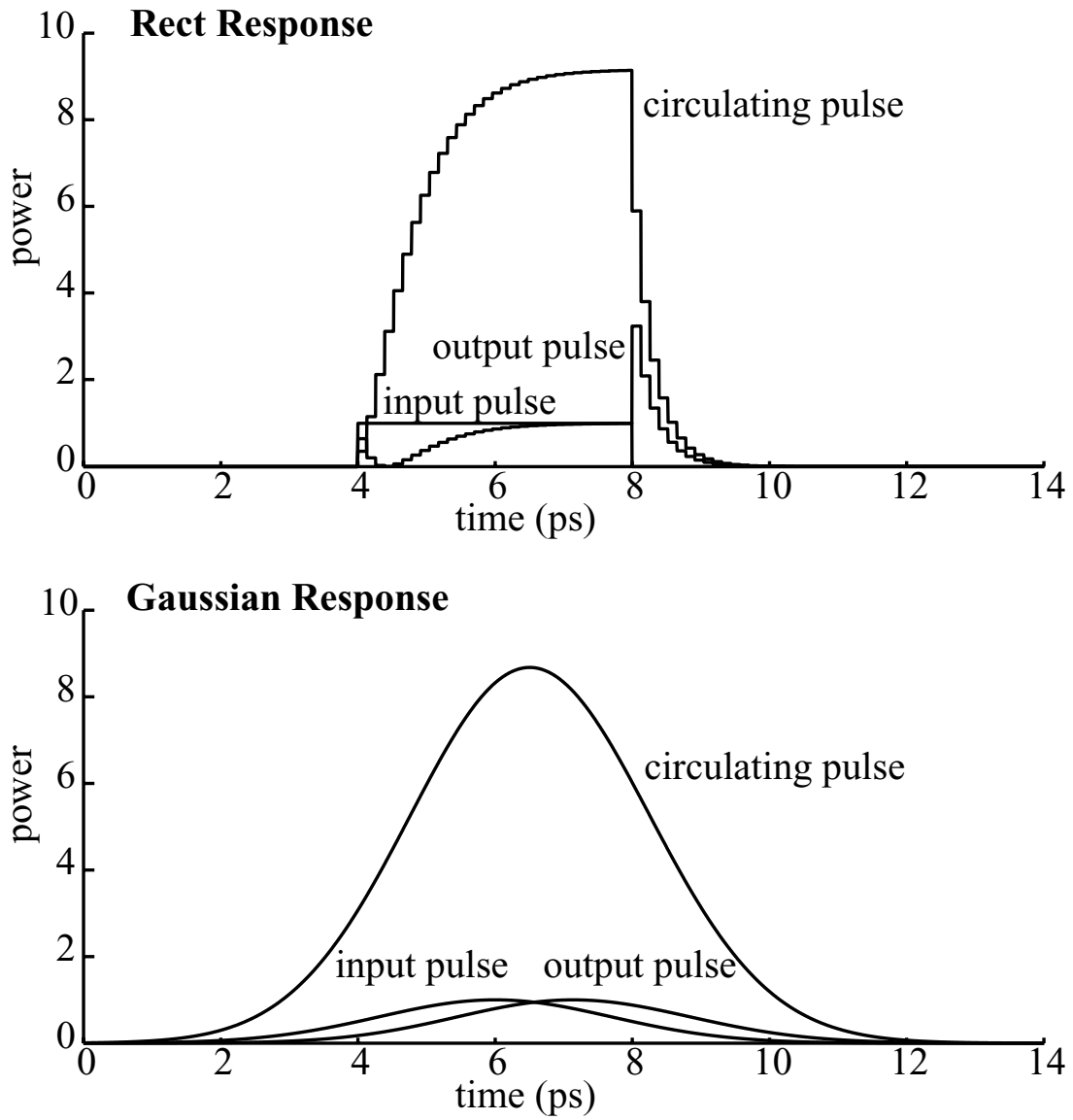
Figure 2.8: Rect response, and Gaussian response of a ring resonator with $r = 0.8$, $T_{\mathrm{R}} = 0.131$ ps, $T_{\mathrm{C}} = 1.9$ ps, and $T_{\mathrm{P}} = 4$ ps.
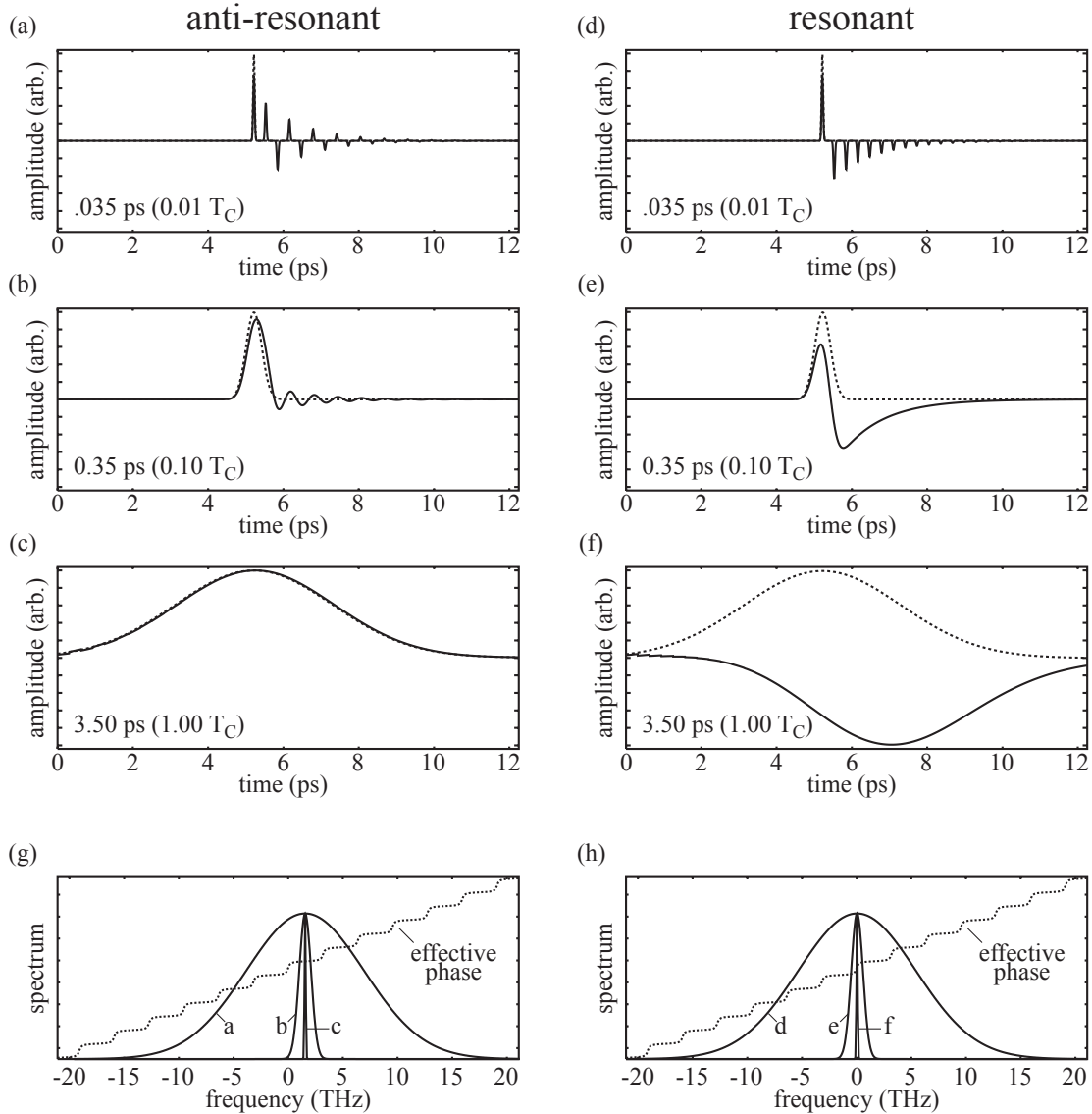
Figure 2.9: Simulations of interfering output field amplitudes for 6 input pulse cases. Pulse widths of 3.5, 0.35, and 0.035 ps are injected into a 10 $\mu$m diameter resonator ($n = 3$, $r = .75$). In a, b, and c, the carrier frequency is completely detuned from resonance. In d, e, and f, the carrier frequency is tuned directly on resonance. Note that for ultrashort pulse excitation, the output pulses are representative of the impulse response of an all-pass resonator. For pulsewidths of the order of the cavity lifetime ($T_C$) the pulse remains mostly undistorted. Plots g and h show the corresponding pulse spectra superimposed upon the effective phase of the transfer function.

$3\sqrt{3}\mathcal{F}^2 T_{\mathrm{R}}^2/4\pi^2$. Assuming a Gaussian pulse of FWHM equal to the cavity lifetime of a resonator, the quadratic depth of phase imparted across the FWHM of the spectrum is equal to $\frac{1}{2}\mathrm{GDD}_{\max}\left(\frac{2\ln 2}{\mathcal{F}T_{\mathrm{R}}}\right)^2$ which is approximately 0.1265 radians. A convenient parameter characterizing the depth of the spectral quadratic phase resulting from GDD across a pulse spectrum is the chirp parameter. The chirp parameter ($C$) is defined by the following expression for the spectral field of a Gaussian pulse:

$$E(\omega) = E_0 e^{-\frac{1+iC}{2}\left(\frac{\omega}{\omega_p}\right)^2} \tag{2.13}$$

At a spectral chirp of unity, the pulse spreads such that its peak intensity falls to $1/\sqrt{2}$ of its minimum value[4]. The maximum chirp per resonator then is of the order of $3\sqrt{3}\ln 2/\pi^2$ which is approximately 0.365. Thus approximately 3 resonators are required to impart a chirp of unity.

Because the properties of resonators are periodic in frequency, there exists a possibility for imparting equivalent phase profiles across multiple spectral bands. In this manner, ring resonators may be used to perform dispersion compensation across multiple wavelength division multiplexed channels simultaneously. [46] Similarly, a delay line may be built that operates for multiple wavelength multiplexed channels simultaneously. Furthermore, carrying this concept over for time division multiplexed signals it also appears that it is possible to operate a resonator with extremely short pulses (much sorter than the usual cavity lifetime

---

[4]This is analogous to the Raleigh range for a Gaussian beam

imposed restriction) as along as they are spaced by the round trip time. This method of operation is sometimes termed synchronous pumping. Such a pulse-train possesses a wideband spectrum but only in the discrete sense. That is the pulsetrain spectrum may completely lie within multiple resonance bandwidths and can thus advantage of the phase enhancing properties of the resonator. However, unless the pulse train changes take place at a time scale which is longer than a $\mathcal{F}$ number of pulses, spectral components will be present in the signal which will not lie within any resonance bandwidths and the synchronous operation will fail. Thus, it is fallacious to think that employing synchronous operation can circumvent the bandwidth limitation imposed by a resonator resonance on an information carrying signal.

## 2.6 Doubly-Coupled Resonators

The resonator analyzed thus far is coupled to a single waveguide and consequently behaves as an all-pass filter. The free-space analogy was previously shown to be a Gires-Tournois interferometer or Fabry-Perot interferometer with a 100% reflecting back mirror. The direct waveguide analogy of a free-space Fabry-Perot is obtained by adding a second guide which side couples to the resonator as in figure 2.10. This configuration now possess two output ports and is no longer an all-pass filter. Rather, because this configuration behaves as a narrow-band amplitude filter which can add or drop a frequency band from an incoming signal,
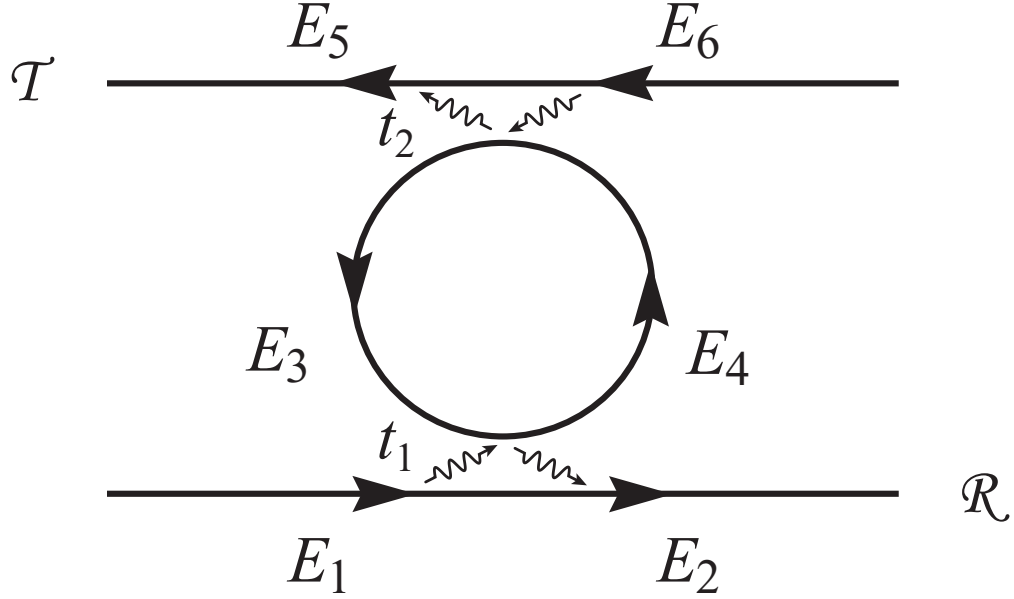
Figure 2.10: A prototypical doubly-coupled ring resonator.

it is commonly termed an add-drop filter. Because this configuration is mathematically equivalent to the extensively studied classic Fabry-Perot interferometer, the equations for build-up factor, finesse, and transmission coefficients are simply stated. The build-up factor is given by

$$\mathcal{B} = \frac{I_3}{I_1} = \left| \frac{E_3}{E_1} \right|^2 = \frac{\left(1 - r_1^2\right) r_2^2 a^2}{1 - 2 r_1 r_2 a \cos \phi + \left(r_1 r_2 a\right)^2}$$

$$\xrightarrow[a=1, r_1^2 = r_2^2 \equiv r^2]{} \frac{\left(1 - r^2\right) r^2}{1 - 2 r^2 \cos \phi + r^4} \xrightarrow[\phi=0]{} \frac{r^2}{1 - r^2}, \quad (2.14)$$

and the finesse:

$$\mathcal{F} = \frac{\Delta\nu_{\text{FSR}}}{\Delta\nu_{\text{FWHD}}} = \frac{2\pi}{2\arccos\left(\frac{2r_1r_2a}{1+r_1^2r_2^2a^2}\right)} \xrightarrow[r_1r_2a\approx 1]{} \frac{\pi}{1-r_1r_2a}. \tag{2.15}$$

Note that, for this configuration, the build-up factor is only 1/4 as strong and finesse is only 1/2 as large and the as that of the singly-coupled ring resonator. The intensity reflection coefficient corresponding to light exiting the same waveguide is:

$$\mathcal{T}_1 = \frac{I_2}{I_1} = \frac{r_2^2a^2 - 2r_1r_2a\cos\phi + r_1^2}{1 - 2r_1r_2a\cos\phi + (r_1r_2a)^2} \xrightarrow[a=1,r_1^2=r_2^2\equiv r^2]{} \frac{\frac{4r^2}{(1-r^2)^2}\sin^2\left(\frac{\phi}{2}\right)}{1 + \frac{4r^2}{(1-r^2)^2}\sin^2\left(\frac{\phi}{2}\right)}. \tag{2.16}$$

This corresponds to a transmitted signal of which a narrow frequency band[5] has been extracted, see figure 2.11. The extracted band exits at the transmission port with transmission coefficient:

$$\mathcal{T}_2 = \frac{I_5}{I_1} = \frac{\left(1-r_1^2\right)\left(1-r_2^2\right)a}{1 - 2r_1r_2a\cos\phi + (r_1r_2a)^2} \xrightarrow[a=1,r_1^2=r_2^2\equiv r^2]{} \frac{1}{1 + \frac{4r^2}{(1-r^2)^2}\sin^2\left(\frac{\phi}{2}\right)}. \tag{2.17}$$

While there are similar enhancements (as in the all-pass resonator) in the transmitted effective phase shifts at the two output ports, they are intermingled with amplitude effects. Thus, it is not expected that the phase transfer characteristics of this device would prove to be useful. Finally it is worth stating an

---

[5]The shape of the transmission curve as with the build-up, is effectively Lorentzian centered on a resonance
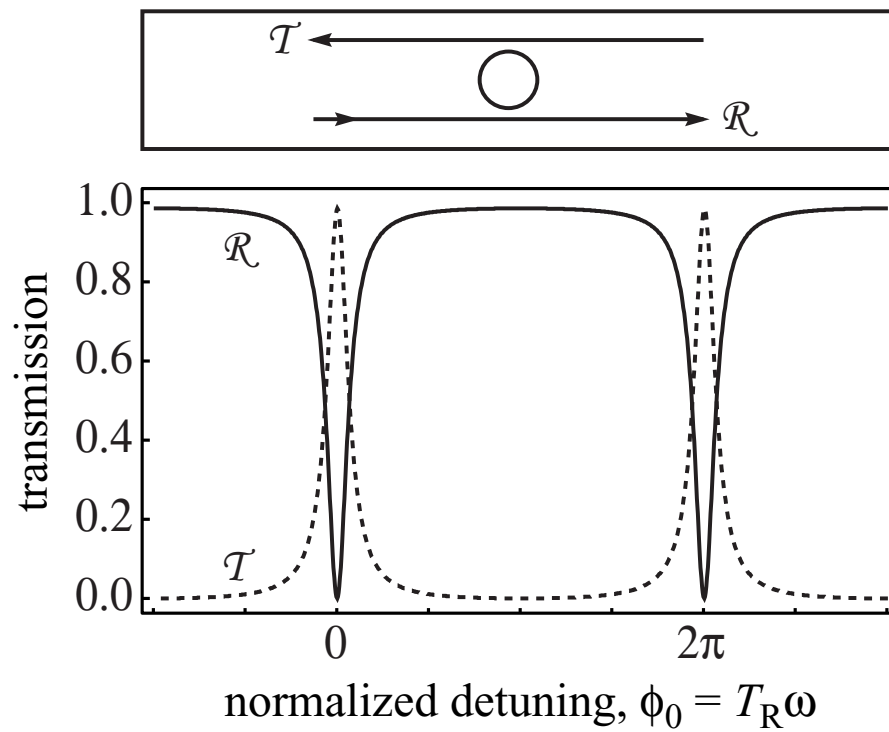
Figure 2.11: Transmission curves associated with the pass (or reflect, $\mathcal{R}$) and drop (or transmit, $\mathcal{T}$) ports of a doubly-coupled ring resonator. These curves are equivalent to those of a Fabry-Perot resonator.

interpretation of the doubly-coupled resonators.  Whereas in the lower coupler, interference exists between the input and circulating field, the upper coupler does not display any interference (provided that excitation is from the lower guide only).  The upper coupler may thus be viewed simply as a "tap" which leaks power out of the cavity.  This tap is formally equivalent to a lumped loss which is the subject of the following section.

Figure 2.12 displays the results of an FDTD simulation.  The steady-state intensities near resonance for a balanced doubly-coupled ring resonator are shown graphically.  Figure 2.13 displays spectral intensity and phase for the resonator in figure 2.5.  The phase variation near resonances here differs qualitatively from that found in the all-pass resonator simulation results in figure 2.6.  In the all-pass case, while some radiation loss is unavoidably present, the resonator is nevertheless over-coupled.  In this case, the couplers are designed to be balanced but the loss thrusts the resonator into the under-coupled regime.  A discussion of these coupling regimes is treated in the following section.  Figure 2.14 graphically depicts the sum of phasors contributing to the net complex output field for an all-pass resonator and a balanced doubly-coupled ring resonator[6].  Note that for small detunings near resonance ($\phi = 0$), the net phasor in each case sweeps through $\pi$ radians very rapidly.  In the balanced case the output amplitude is zero on resonance and grows as the net phasor sweeps away from the origin.

---

[6]or critically-coupled all-pass resonator
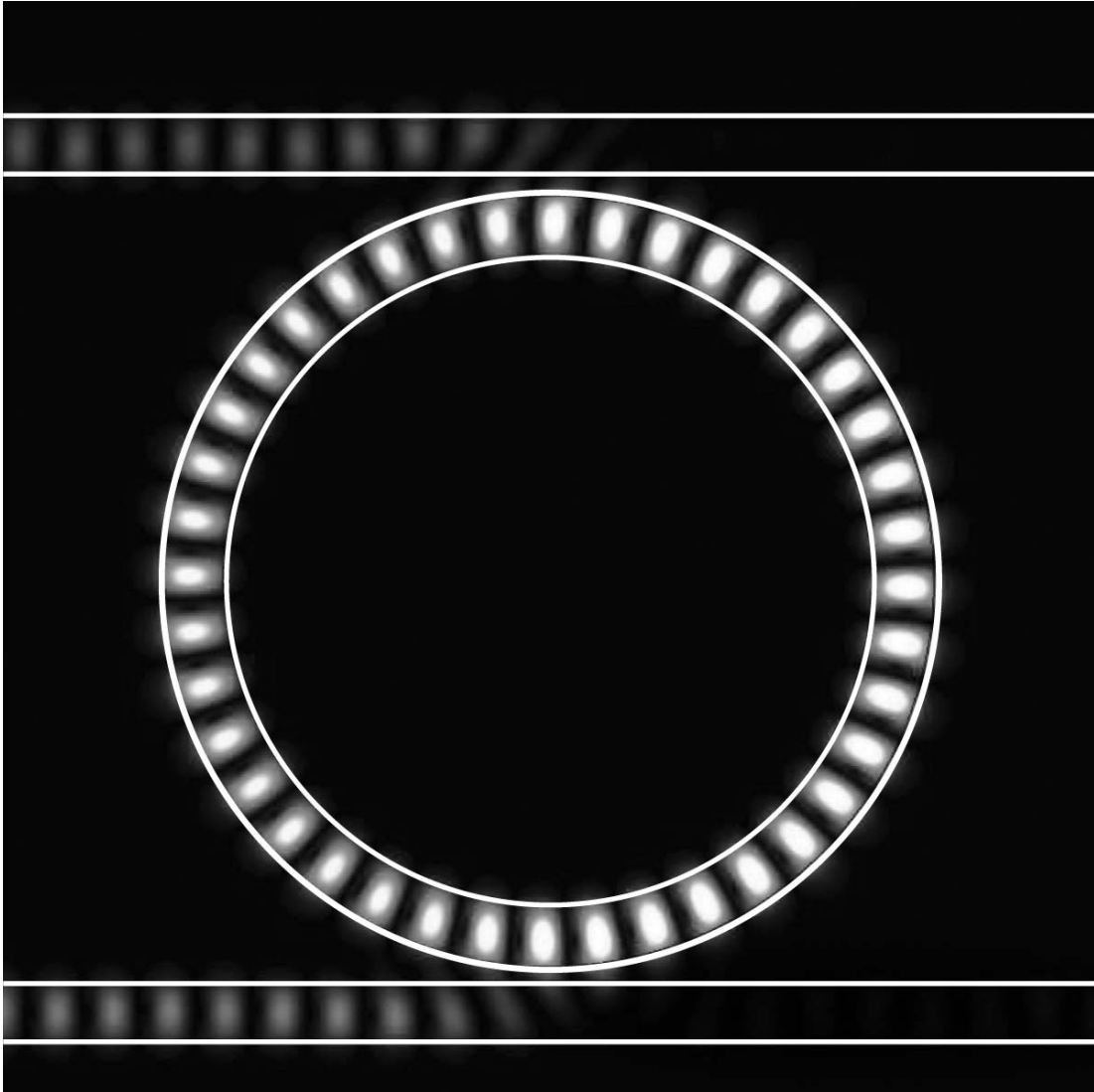
Figure 2.12: Finite difference time domain simulation demonstrating resonator build-up and rerouting (channel dropping) at 1.5736 $\mu$m. Guide and ring widths are 0.4 $\mu$m. Resonator radii are 2.5 $\mu$m (outer) and 2.1 $\mu$m (inner). All guiding structures have a refractive index of 2.5 that is cladded by air.
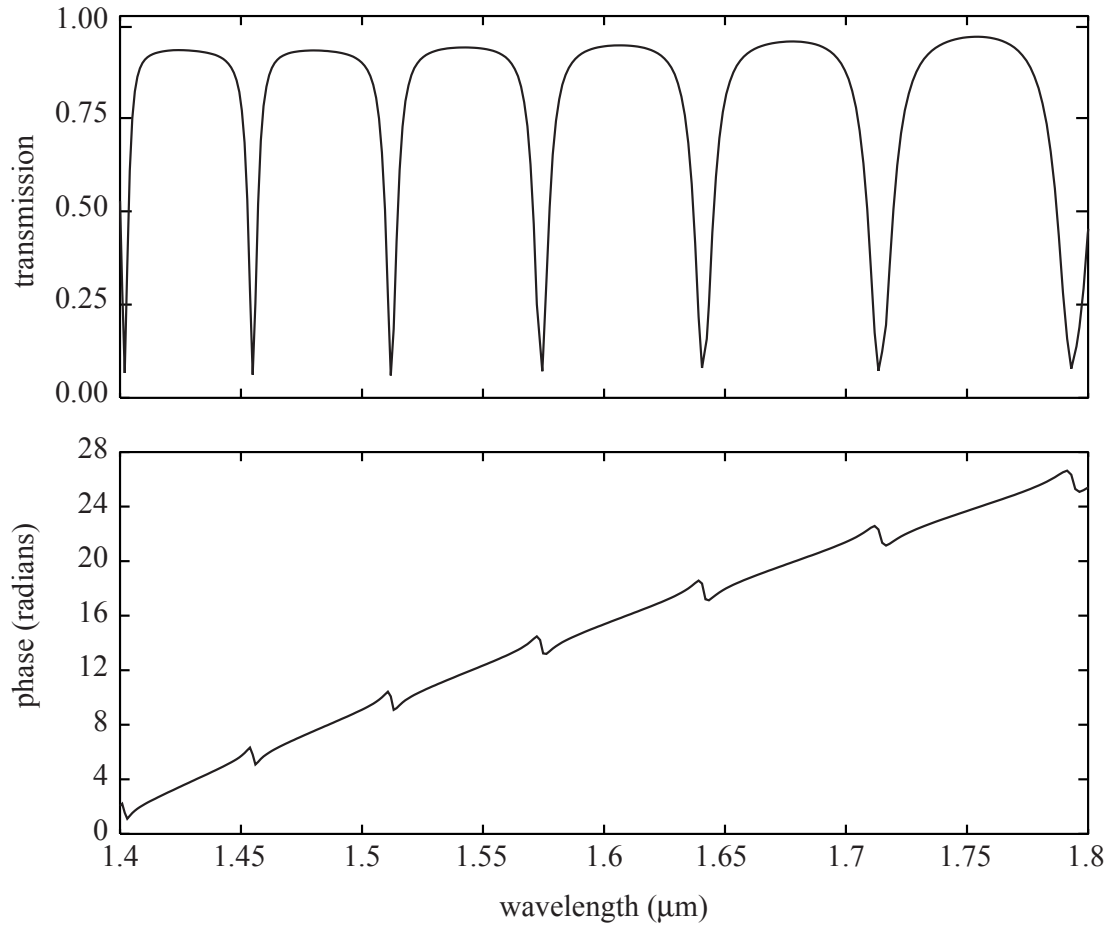
Figure 2.13: Transmitted spectral intensity and phase associated with the ring resonator in figure 2.12. Deep transmission dips in the spectrum result from wavelength bands extracted near resonances into the upper waveguide. The spectral phase includes primarily linear contributions from the waveguide and a reversed "stair-step" contribution associated with the effective phase shift induced by the resonator. The slope of the phase reverses here near resonances because loss in the resonator disrupts the balanced couplers forcing the resonator to be under-coupled. The resonator effective radius of 2.3 $\mu$m and index of 2.5 should result in a free-spectral range of 71 nm near 1600 nm which is in excellent agreement with the obtained spectrum.
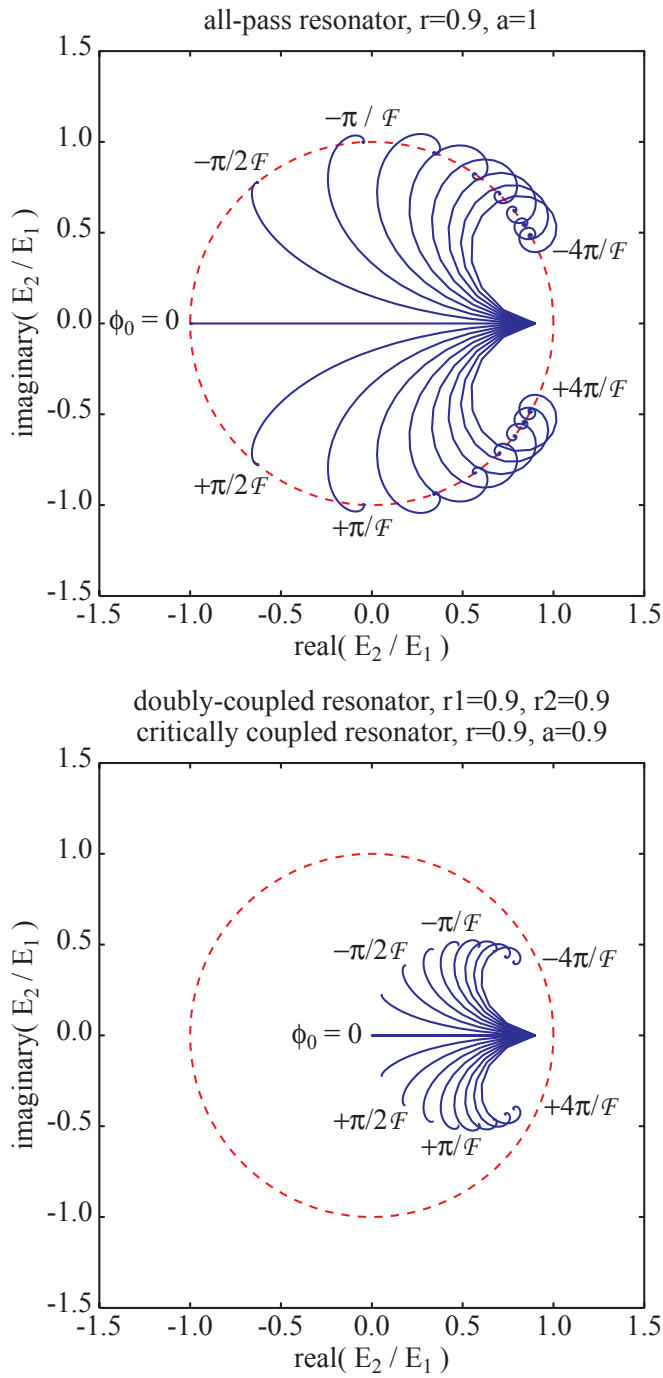
Figure 2.14: Graphical sum of phasors contributing to the overall out complex field for a single all-pass ($r = 0.9$) and balanced double-coupler ($r_1 = r_2 = 0.9$ or $r = a = 0.9$ ) resonator.

## 2.7 Attenuation

In reality, internal attenuation mechanisms are always present and thus render limitations as to when a ring resonator may closely approximate a true all-pass, phase-only filter. In particular, near resonance, the internal attenuation is increased such that dips appear in the transmission spectrum,

$$\mathcal{T} = \frac{a^2 - 2ra\cos\phi + r^2}{1 - 2ra\cos\phi + (ra)^2}.$$

(2.18)

Here, $a = e^{-\alpha\pi R}$ is the lumped amplitude transmission coefficient for a single pass through the resonator. The attenuation at the dips is equal to the single-pass attenuation magnified by the phase sensitivity. The width of the resonance also broadens, lowering the finesse:

$$\mathcal{F} = \frac{2\pi}{2\arccos\left(\frac{2ra}{1+(ra)^2}\right)} \xrightarrow{ra\approx1} \frac{\pi}{1-ra}.$$

(2.19)

If the attenuation is comparable to the cross-coupling, light is resonantly attenuated strongly. Under the condition known as *critical coupling*, $(r = a)$, the finesse drops by a factor of 2 and more importantly the transmission at resonances drops to zero. The circulating intensity peaks are diminished (eqn 2.4) and the phase sensitivity is paradoxically increased (eqn. 2.10). At resonances, the phase sensitivity increases without bound at the expense of a decreasing transmitted signal until the transmission is zero and the phase sensitivity is infinite. Of course

the phase only undergoes a finite and discrete phase jump at this point. If the resonator is dominated by bending or scattering loss, then the waveguide mode is perfectly coupled to the continuum of outward-going cylindrical waves outside the resonator. Under-coupling occurs when the loss dominates $(r > a)$. Many contra-intuitive effects may take place in this regime such as the inversion of the phase sensitivity demonstrated in figure 2.13. Over-coupling occurs when the round-trip loss does not exceed the coupling $(r < a)$ and is typically the favorable mode of operation for an all-pass resonator. For an add-drop filter, it is desirable to have critical coupling for complete extinguishment of a band in the through guide. Here the sum of all losses incurred in the resonator including at the outcoupled drop port must be taken into account.

Finally it is worth examining the introduction of gain. Gain may be implemented if possible to offset loss mechanisms and restore the all-pass nature of a normally lossy ring resonator. [47] If the round trip gain is equal to the round trip loss $(r^{-1} = a)$ the resonator achieves the self-lasing condition. If the gain is increased beyond this value, the resonator becomes extremely unstable.

## 2.8 Partial Coherence

Because ring resonators rely on interference between subsequent round trips, a coherent source is essential to achieving a build-up of intensity. In the following
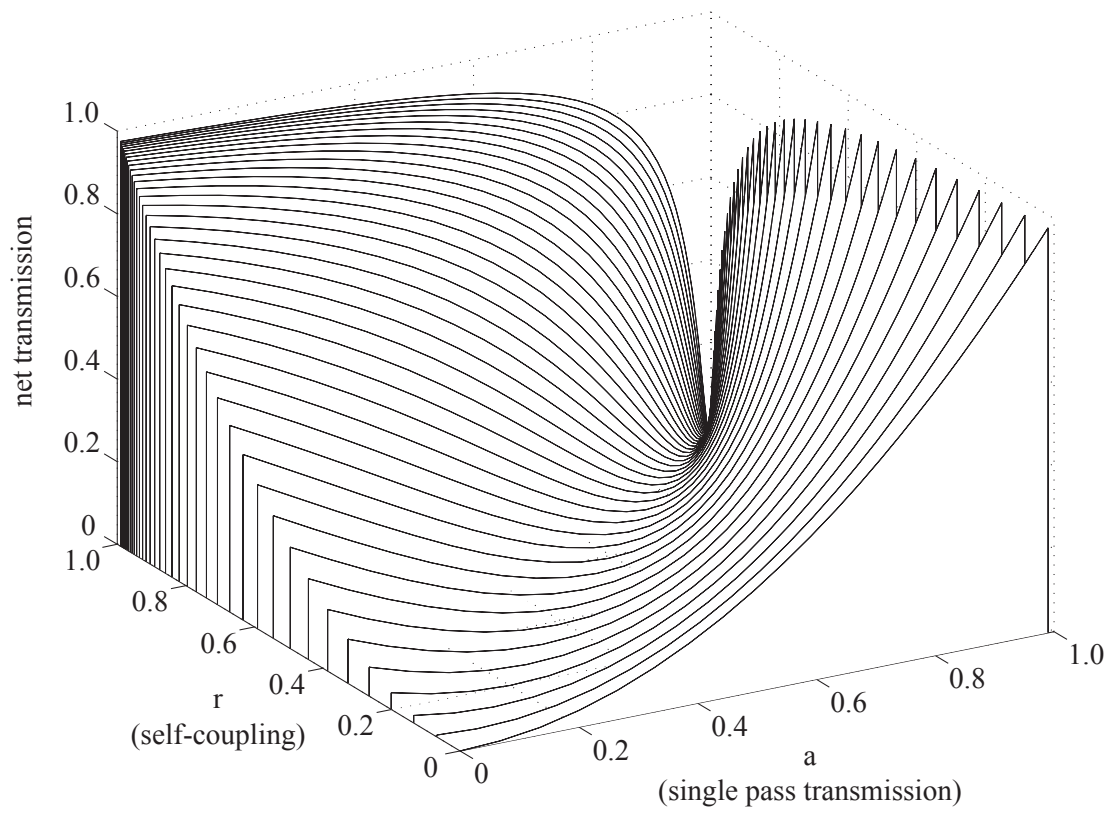
Figure 2.15: A plot of the net transmission of a ring resonator with varying loss for various values of the self-coupling coefficient, r.
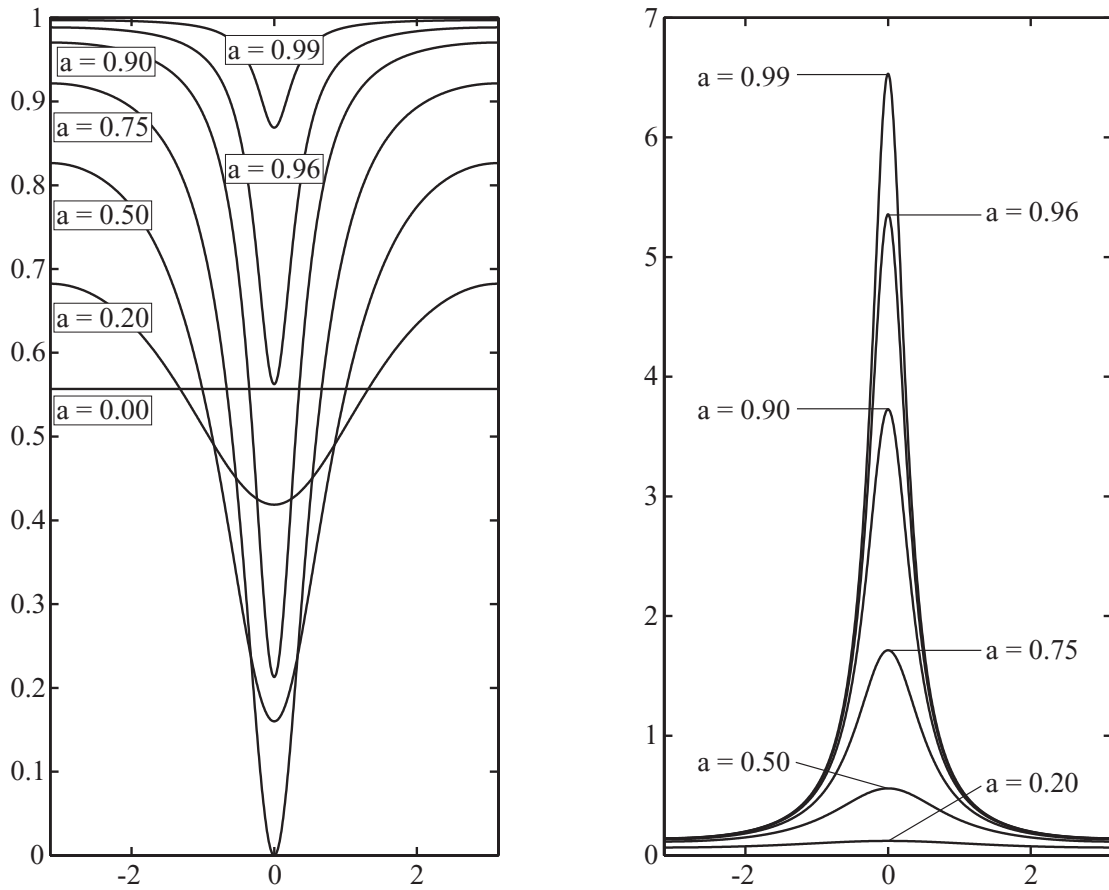
Figure 2.16: A plot of the a) net transmission and b) build-up vs normalized frequency for a resonator with r=0.75 and varying loss. The single-pass field transmission, $a$ is displayed for each curve in the figure.

analysis, it is assumed that subsequently delayed fields possess some degree of partial coherence which is related to random phase noise, $\delta\phi(t)$ in the source field.

Including the effects of random temporal phase noise, the circulating field is expanded as a sum of successively delayed field amplitudes in the time domain,

$$A_3(t) = itae^{+i\phi}\sum_{m=1}^{\infty}\left(rae^{+i\phi}\right)^{m-1}e^{-i\delta\phi(t-mT_{\mathrm{R}})}e^{+i\delta\phi(t)}A_1(t). \qquad (2.20)$$

If the statistics of the source are time-stationary, ensemble averages may be performed on the intensity autocorrelation. The partially coherent build-up of intensity can thus be expressed as,

$$\mathcal{B} = \left\langle\left(\frac{A_3}{A_1}\right)\left(\frac{A_3}{A_1}\right)^{\star}\right\rangle = t^2 a^2 \sum_{m=1}^{\infty}\sum_{n=1}^{\infty}\left(rae^{+i\phi}\right)^{m-1}\left(rae^{-i\phi}\right)^{n-1}\left\langle e^{-i\delta\phi(t-mT_{\mathrm{R}})+i\delta\phi(t-nT_{\mathrm{R}})}\right\rangle.$$
$$(2.21)$$

The autocorrelation of phase noise terms can be reduced to a single lumped parameter [48,7,8] denoted the degree of coherence,

$$\left\langle e^{-i\delta\phi(t-mT_{\mathrm{R}})+i\delta\phi(t-nT_{\mathrm{R}})}\right\rangle \equiv d. \qquad (2.22)$$

According to this definition, an infinitely narrow linewidth source with infinite coherence time possesses $d = 1$ for interference between two copies of the source with arbitrary time delay. On the other hand, a delta-correlated source with zero coherence time possesses $d = 0$ for all interferences except at zero time delay. Via

the Einstein-Wiener-Khintchine theorem, a Lorentzian source with bandwidth $\delta\omega$ is correlated in time via a decaying exponential, $d = e^{-\delta\omega|t|}$. Equation 2.21 may be simplified to the following expression,

$$\mathcal{B} = \left(\frac{1 - (rad)^2}{1 - (ra)^2}\right)\left[\frac{(1 - r^2)\,a^2}{1 - 2rad\cos(\phi) + (rad)^2}\right]. \tag{2.23}$$

Inserting $d = 1$ into the equation returns the perfectly-coherent build-up expression derived earlier in equation 2.4. Inserting $d = 0$ and $a = 1$ into the equation however, results in a build-up of unity for all detunings. This is an intuitive result which is easily derived by matching intensities rather than field amplitudes:

$$I_3 = t^2 I_1 + r^2 I_3 \longrightarrow I_3 = I_1 \tag{2.24}$$

Thus, for perfectly incoherent excitation, (and no attenuation) the intensity in the cavity equalizes with the incident intensity. This is analogous to the equalization of pressure between coupled cavities in hydrostatics. Implementation of a coherent source does not change the *average* build-up across a free-spectral range. Rather, with coherent excitation, the build-up greatly exceeds unity near resonances and is reduced below unity away from them such that the average never deviates from the incoherent case. The finesse is degraded slightly with partial

source coherence in the same manner as with attenuation,

$$\mathcal{F} = \frac{2\pi}{2\arccos\left(\frac{2rad}{1+r^2a^2d^2}\right)} \xrightarrow[rad\approx1]{} \frac{\pi}{1-rad}.$$
(2.25)

## 2.9  Summary

In this chapter, the linear properties of ring resonators were derived from 3 simple parameters: coupling, phase, and attenuation. The properties derived included the coherent build-up of intensity, the increase phase sensitivity or group delay, the induced group delay dispersion, and the concept of critical coupling.

# Chapter 3

# Whispering Gallery Modes

## 3.1 Introduction

In 1912, Lord Raleigh analyzed the curiosity of the "whispering gallery" which involved the propagation of sound waves skimming along the dome of St. Paul's Cathedral. [49] The term has since come to be applied to a family of modes of a cyclical curved interface such as a cylindrical or spherical surface, where wave propagation is confined primarily to the inside surface of an interface and guided by it by repeated reflection.

## 3.2 Modes

Light propagating in a straight waveguide is confined via total internal reflection (TIR) by two dielectric interfaces (along one dimension) to a region of high refractive index. The guiding region of high refractive index is formally equivalent to a potential well wherein the electric fields may be decomposed into eigenmodes

which are solutions of the Schrödinger equation. Light propagating in a curved

waveguide is still guided via TIR at the outer interface, but no longer demands an

inner interface to complete the confinement. Elimination of the inner boundary

leaves a dielectric disk which supports whispering gallery modes. These modes

consist of azimuthally propagating fields guided by TIR at the dielectric interface

and optical inertia which prevents the field from penetrating inward beyond a fixed

radius[1]. Mathematically, a whispering gallery mode is a solution of the Helmholtz

equation in a curved coordinate geometry. Attention is restricted to a cylindrical

geometry appropriate for the analysis of planar disk and ring resonators.

The Helmholtz equation $\left(\nabla^2 + k^2\right) E_z = 0$, written in cylindrical coordinates

for the axial field of a TM[2] whispering gallery mode is

$$\left(\frac{\partial^2}{\partial r^2} + \frac{1}{r}\frac{\partial}{\partial r} + \frac{1}{r^2}\frac{\partial^2}{\partial \varphi^2} + k^2\right) E_z\left(r, \varphi\right) = 0. \tag{3.1}$$

The equation can be simplified via the method of separation of variables by which

it is split into two equations for radial and azimuthal dependance. An integer[3]

parameter, $m$ is introduced which connects the two equations and physically cor-

responds to the number of optical cycles the field undergoes when completing one

---

[1]The inner bounding radius is termed the internal caustic

[2]The accepted nomenclature for assigning TE or TM designations for cylindrical whispering gallery modes, is to follow the conventions for that of planar waveguides. For example, the TM mode solution is the one in which in the limit of an infinitely long cylinder, only one electric field component exists and is directed axially. As a result, the TE and TM designations with respect to the sidewall seem to be reversed.

[3]the restriction that $m$ be an integer assumes a resonance.

revolution around the disk. The azimuthal equation takes the form,

$$\left(\frac{\partial^2}{\partial\varphi^2} + m^2\right) E_z(\varphi) = 0, \tag{3.2}$$

and has solutions which are simply complex exponentials, $E_z(\varphi) = e^{+im\varphi}, e^{-im\varphi}$.

The radial equation:

$$\left(\frac{\partial^2}{\partial r^2} + \frac{1}{r}\frac{\partial}{\partial r} + k^2 - \frac{m^2}{r^2}\right) E_z(r) = 0, \tag{3.3}$$

is Bessel's equation. Solutions of Bessel's equation are the Bessel functions of the

first, $J_m$ and second, $Y_m$ kind. Because the second kind function is singular at the

origin, only the first kind function is retained inside the disk. Outside the disk,

both functions are well behaved[4] and must be retained. The Hankel functions

are linear superpositions of the two Bessel function solutions corresponding to

outward, $H_m^{(1)} = J_m + iY_m$ and inward, $H_m^{(2)} = J_m - iY_m$ propagating cylindrical

waves. The analysis of waves arriving back at the resonator from the radial

horizon is not considered here and thus only the Hankel function of the first kind,

$H_m^{(1)}$ is retained. Thus, the appropriate solutions for the radial field dependence

---

[4]The fields outside the disk are not modified Bessel functions of the first kind, $K_m$ as in the case of bound modes of a circular dielectric waveguide or optical fiber. This is because the absence of an axial propagation constant eliminates the possibility of modified Bessel function solutions.

both interior $(r < R)$ and exterior $(r > R)$ to the dielectric disk [50] are

$$E_z(r < R) = A_m J_m(\widetilde{k}_1 r) \tag{3.4}$$

$$E_z(r > R) = B_m \, H_m^{(1)}(\widetilde{k}_2 r). \tag{3.5}$$

The complete axial electric field interior and exterior to the disk is constructed from the azimuthal and radial solutions including the boundary condition at the interface $(r = R)$ which forces the tangential electric field to be continuous:

$$E_z(r, \varphi) = A_m J_m\left(\widetilde{k}_1 r\right) e^{i(\pm m\varphi - \widetilde{\omega}t)} \tag{3.6}$$

$$E_z(r, \varphi) = A_m \frac{J_m\left(\widetilde{k}_1 R\right)}{H_m^{(1)}\left(\widetilde{k}_2 R\right)} H_m^{(1)}\left(\widetilde{k}_2 r\right) e^{i(\pm m\varphi - \widetilde{\omega}t)}. \tag{3.7}$$

Finally, the radial and azimuthal magnetic fields are easily derived from the axial electric field by use of Maxwell's equations,

$$H_r = \frac{-i}{Z_0 \widetilde{k}} \frac{1}{r} \frac{\partial}{\partial \varphi} E_z = \frac{m}{Z_0 \widetilde{k} r} E_z \tag{3.8}$$

$$H_\varphi = \frac{i}{Z_0 \widetilde{k}} \frac{\partial}{\partial r} E_z. \tag{3.9}$$

Intuitively, the WGM is characterized by some energy and confined within a radial potential well. Figure 3.2 depicts an optical whispering gallery mode with the associated radial potential well and illustrates the regions where the fields in
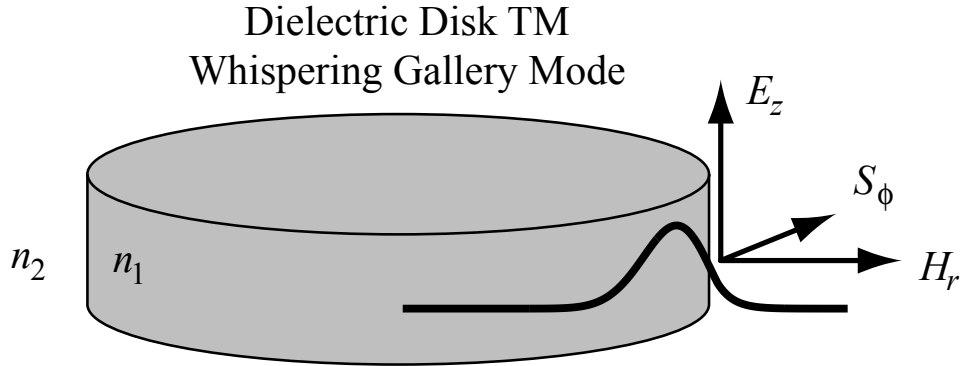
Figure 3.1: Geometry for a TM whispering gallery mode.

the mode are bounded, evanescent and radiative (outwardly propagating). The
nature of the radiative component of the field is examined in the following section.

## 3.3   Radiation Loss

For an open-boundary structure such as a dielectric disk,[5] whispering gallery
modes are in fact inherently "leaky." [51] The mechanism for loss is a tunnelling
or coupling of the azimuthally guided mode into radially outward-going radiation
modes. This phenomena is known as whispering gallery loss, bending loss, or
radiation loss and is a property of any curved open boundary waveguide config-
uration. A convenient measure parameterizing this loss is the *intrinsic* quality
factor which gives a measure of how many optical cycles a mode will last confined
within a resonator. Theoretical predictions show that the intrinsic quality fac-

---

[5]As opposed to a closed-boundary structure i.e. dielectric guiding region with perfectly
conducting walls.

tor ($Q = m\mathcal{F}$, where $m = 2\pi R/\lambda$) can be as high as $10^{11}$ and experiments have confirmed this fact. [52]

The radiation loss associated with whispering gallery resonators may be viewed physically as a tunnelling of the confined field through a potential barrier defined by the disk boundary and an external fixed radius out into a region of lower potential. This external radius is termed the external caustic and corresponds to the radius at which, following an evanescent decline, the field becomes propagating again. For a typical high-Q disk resonator, the field has decayed to such a low value that its leakage into cylindrical radiating waves is very small. The predominant propagation direction for a WGM is of course primarily in the azimuthal direction such that the phase contours behave like revolving spokes of a wheel. The pattern revolves about the disk center with a angular frequency of $\omega/m$. Because the azimuthal phase contours increase in separation with radius, the azimuthal phase velocity likewise increases without bound. At the external caustic, the azimuthal phase velocity is equal to the phase velocity in the surrounding medium. Beyond this radius, the fields cannot keep up and thus spiral away. Figure 3.3 graphically illustrates this fact for a very low Q WGM.

In order to calculate the mode propagation constants and quality factors for particular WGMs one must solve the complex WGM dispersion relation.[6] For

---

[6]The dispersion relation for whispering gallery modes can also be derived from the dispersion relation for fibers by setting the axial propagation constant to zero. See appendix D for more a more detailed description.

# Optical Whispering Gallery Modes
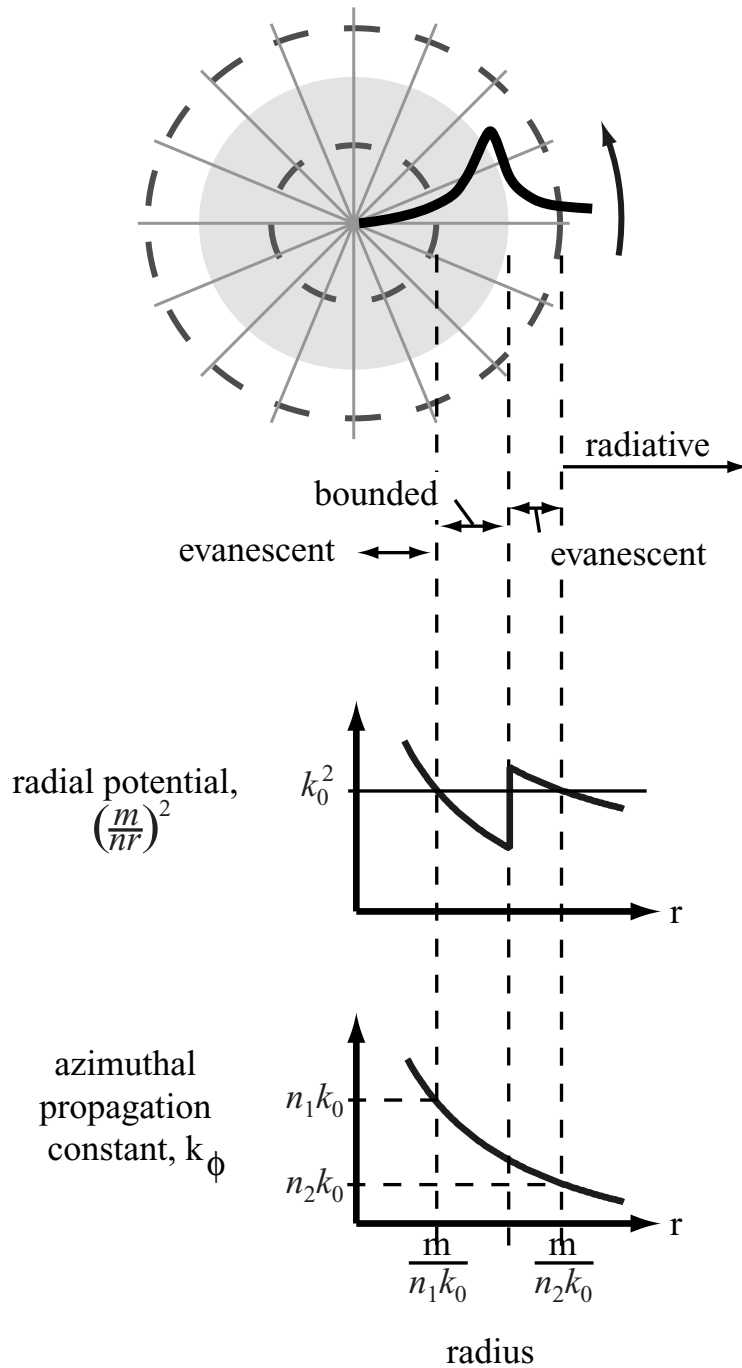


Figure 3.2: Propagation constant $k_\phi$ as a function of radial distance from disk axis for a whispering gallery mode. The circulating power is confined between an inner caustic and the disk edge. Beyond the outer caustic the radially evanescent field becomes propagating and acts as a loss mechanism.
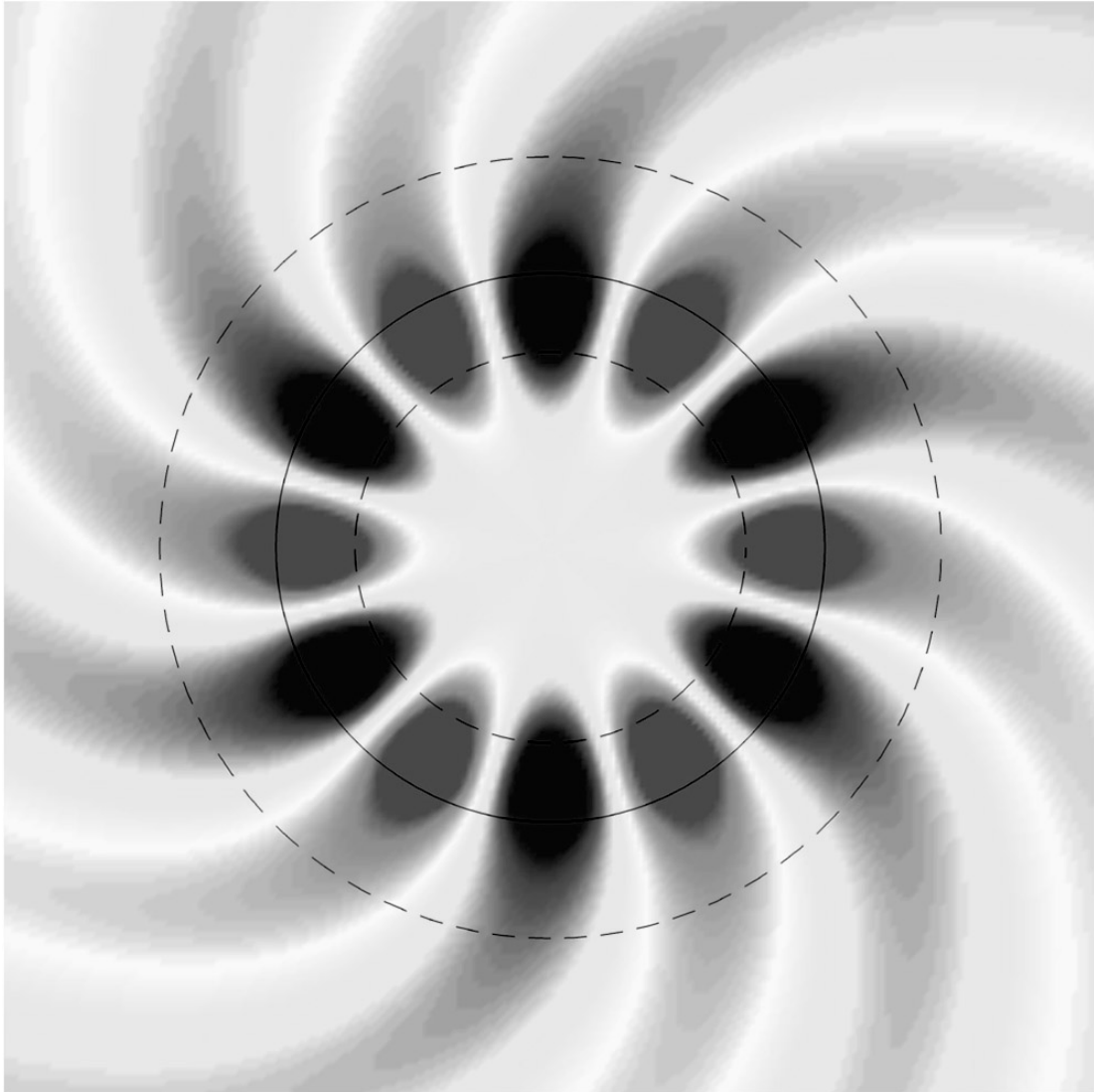
Figure 3.3: Plot of the electric field associated with the 6th order TM (axial E-field) whispering gallery mode.   Here $n1 = 2$, $n2 = 1$, and the resonant radius (solid line) is 1.04 $\mu$m at $\lambda =$1.55 $\mu$m.  This configuration was chosen because it is poorly confined with a low Q of 64 and thus allows easy visualization of the super-evanescent component of the field below the caustic radius (inner dotted line) and the radiating component of the field past the radiative caustic radius (outer dotted line).

an infinite cylinder of dielectric material with negligible absorption and no axial component of the propagation vector, the TM dispersion relation can be written analytically as:

$$\frac{n_1 J'_m \left[ n_1 \frac{2\pi R}{\lambda} \left( 1 - i\frac{1}{2Q} \right) \right]}{J_m \left[ n_1 \frac{2\pi R}{\lambda} \left( 1 - i\frac{1}{2Q} \right) \right]} = \frac{n_2 H'^{(1)}_m \left[ n_2 \frac{2\pi R}{\lambda} \left( 1 - i\frac{1}{2Q} \right) \right]}{H^{(1)}_m \left[ n_2 \frac{2\pi R}{\lambda} \left( 1 - i\frac{1}{2Q} \right) \right]} \tag{3.10}$$

For a given size parameter $\left( \frac{2\pi R}{\lambda} \right)$, dielectric contrast $(n_1, n_2)$, and azimuthal mode number $(m)$, a Q-value may be obtained for a particular radial mode. The lowest order whispering gallery mode possesses the highest Q and corresponds to the highest order azimuthal mode that is supported by the structure.

## 3.4 Disks and Rings

A mode may be considered a "whispering galley mode" if the confinement along some dimension is provided by only a single reflective interface. For a given core-to-cladding refractive-index difference, the loss at a given bend radius decreases with increasing waveguide width until a limit is reached at which only the outer core interface is important for guiding. [53] A mode of a curved waveguide (forming a ring) defined by two interfaces would be considered a whispering gallery mode if the inner caustic radius (defined by the azimuthal index m and the wavelength) lies between the inner and outer interfaces. In this regime, light cannot penetrate (towards the origin) beyond the inner caustic and thus the in-
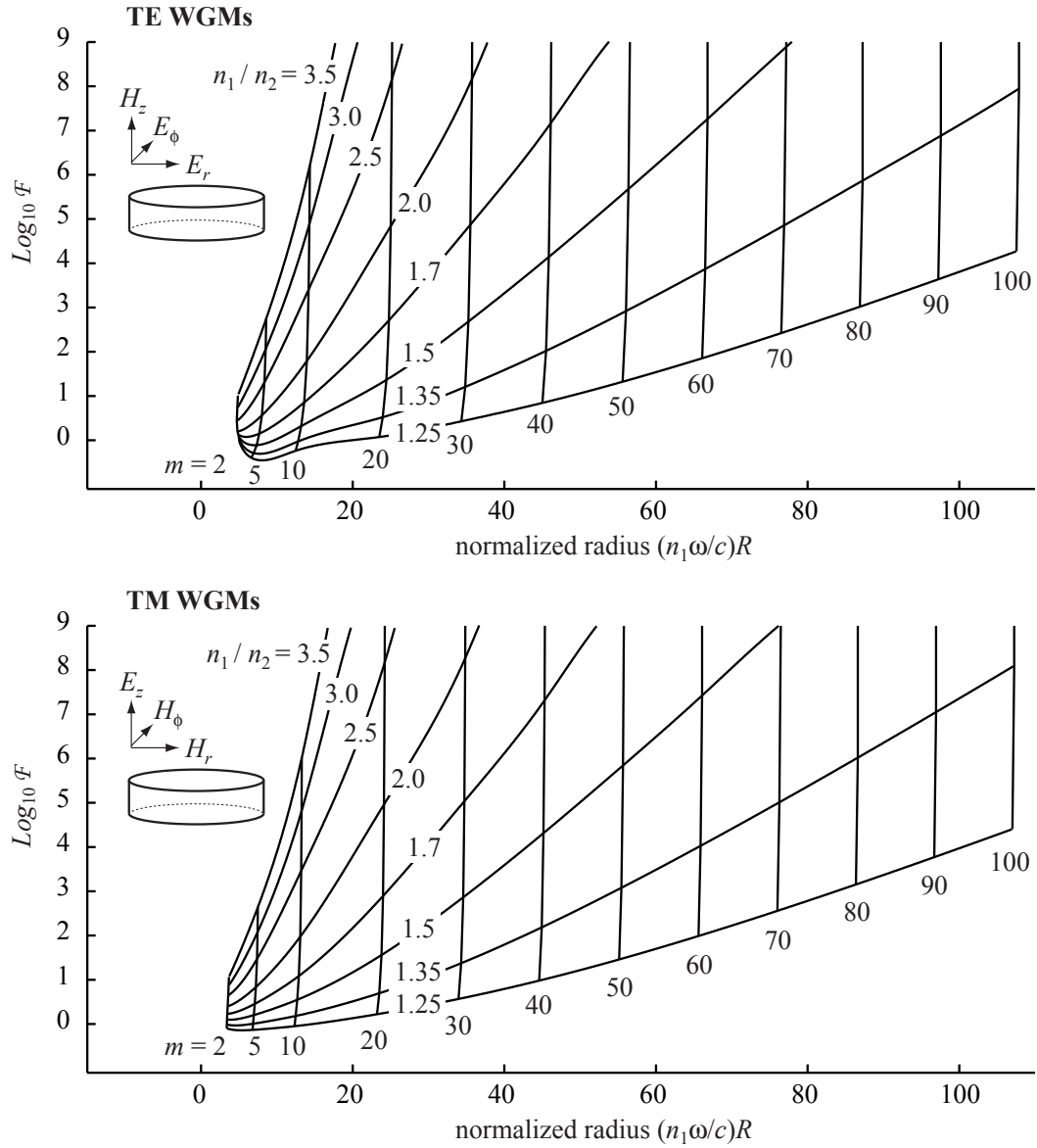
Figure 3.4: Radiation-loss-limited finesse of the lowest order radial TE and TM whispering-gallery modes of a dielectric cylinder of index $n_1$ in a medium of index $n_2$ plotted vs. normalized radius $(n_1\omega/c)\,R$. The family of diagonal lines represents varying refractive index contrast $(n_1/n_2)$. The family of nearly vertical lines corresponds to whispering gallery mode resonances, each characterized by an azimuthal mode number $m$. The plots were obtained by numerically solving the dispersion relation for whispering-gallery modes.

terior interface plays a negligible role in the guidance. Thus, a curved waveguide will have similar bending loss per unit radian as a disk with the same exterior radius. It is worthwhile pointing out the advantages and disadvantages of disks vs. rings. A microdisk may possess higher order radial modes primarily depending on the location of the inner caustic. These radial modes possesses differing resonant wavelengths and thus might be discriminated against by properly choosing the excitation wavelength. Depending on the quality factors associated with the modes, the resonant wavelength of a particular mode of a microdisk (defined by a radial and azimuthal number) might still overlap another. This may be a problem if only a single mode is desired[7]. A properly designed ring can be used instead to force single-radial-mode operation. However, as will be investigated in more detail in a later chapter, the presence of an extra sidewall contributes to nearly double the scattering losses. Figure 3.5 shows the radial field distribution associated with the TM modes of 1 micron radius disk resonator supporting 3 radial modes. Each of the modes possesses an energy $(k_0^2)$ that lies within the potential energy, $(m/nr)^2$, dictated by the azimuthal number and structure[8]. A ring resonator formed by removing the material within a 0.65 micron radius would cut off the second and third order radial modes. Its potential energy distribution,

---

[7]While the modes may overlap, the higher-order modes will typically posses a low coupling coefficient and high loss.

[8]Strictly speaking, these "energies" do not have the correct units of energy. However, they are formally mathematically equivalent to the energies involved in the solution of the radial Helmholtz equation.
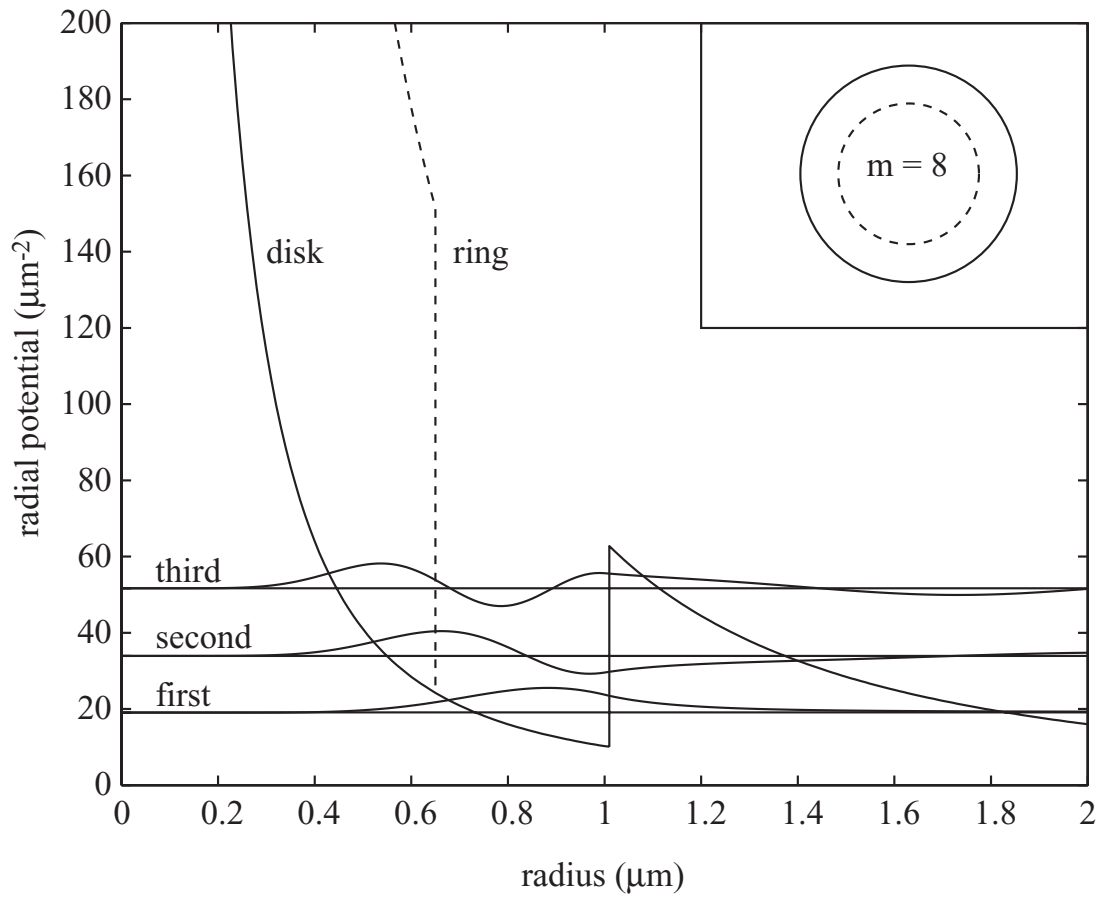
Figure 3.5: A plot of the 3 supported TM radial modes of an m=8, 1 micron radius microdisk resonator with index contrast n=2.5:1. The resonance wavelengths for the first, second, and third modes are 1438, 1079, and 874nm respectively. Mode quality factors are 3247, 224 and 72 respectively. By eliminating the interior of the disk to form a ring, here illustrated by a dashed line, elimination of higher order modes is possible.
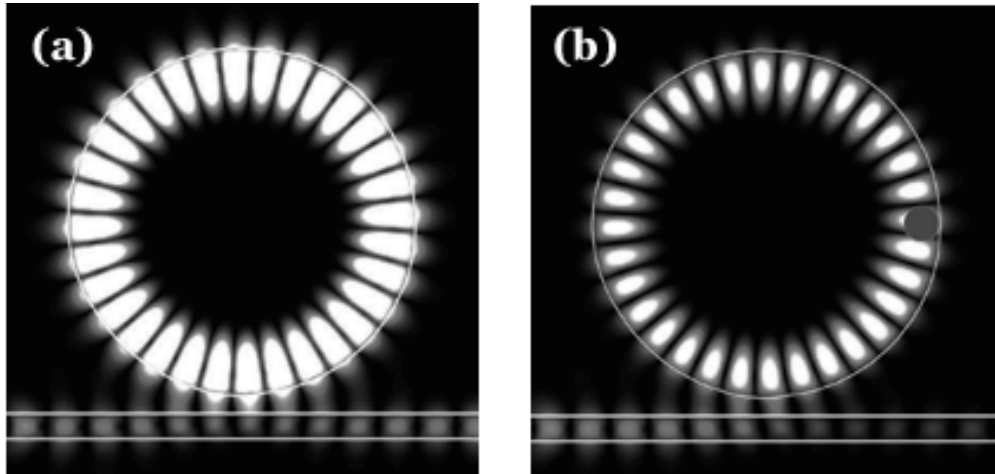
Figure 3.6: FDTD simulation of an integrated disk sensor operating in the 16th whispering gallery mode. Parameters include a disk radius of 2.54 $\mu$m, guide width of 0.4 $\mu$m, gap width of 0.25 $\mu$m, index contrast of 2:1 and TM polarization. The particle was modelled as an absorbing species with conductivity 3000 $\Omega^{-1}m^{-1}$ and particle radius of 0.25 $\mu$m. a) A build-up of 16 in the absence of the particle b) the build up is reduced to 3 in the presence of the particle.

shown as a dashed line, forms a potential well that will only support the lowest order mode.

## 3.5  Summary

Whispering gallery modes have found applications in spectroscopy, [54] linewidth narrowing of diode lasers, [55] explicitly as lasers, [18,31] cavity QED media, [23] add-drop filters, [56] and biosensing. [57] As an example of the capability of a whispering gallery disk resonator to act as an integrated biosensor [58,59] see figure 3.6.

Propagating whispering gallery modes have been imaged by scanning a near-

field probe across the surface of fused-silica microspheres, [60,61] and silicon nitride cylindrical disks [62] whereby light is collected (as it is injected [63]) via frustrated total internal reflection.   In the past decade WGMs have attracted increasing attention for their ability to sustain very high Q-factors and low mode volumes. This thesis aims to implement the enhancing properties of resonators at a very compact scale in which guidance is primarily governed by whispering gallery total internal reflections from the outer interface.

# Chapter 4

# Nonlinear Microresonator Theory

## 4.1    Introduction

The previous two chapters were concerned with the fundamental linear optical properties of microresonators. This chapter examines how the contributions of coherent build-up and increased phase sensitivity combine to enhance the nonlinear optical properties of microresonators.

## 4.2    Material Nonlinear Susceptibility

The material polarization, $P$ may be expanded in a Taylor expansion of electric field strength, $E$ as follows: [64]

$$P = \chi^{(0)} + \chi^{(1)}E + \chi^{(2)}E^2 + \chi^{(3)}E^3 ...$$
(4.1)

where $\chi^{(N)}$ refers to the $N^{\text{th}}$ order susceptibility. The first order susceptibility gives rise to the linear refractive index,

$$n = Re\left[\sqrt{1 + \chi^{(1)}}\right] \tag{4.2}$$

and linear attenuation coefficient,

$$\alpha = Im\left[\sqrt{1 + \chi^{(1)}}\right] 4\pi/\lambda. \tag{4.3}$$

The second-order polarization term cannot have a frequency component which is composed of field components at that same frequency. This term is responsible for describing second-harmonic generation, the more generalized sum-frequency mixing, degenerate one-half subharmonic generation, the more general difference frequency mixing and optical rectification. Furthermore, in the case of a centrosymmetric material, the second-order polarization and all subsequent even orders vanish. The third-order polarization term describes third harmonic generation, four-wave mixing, intensity dependent refractive index, saturable absorption, and two-photon absorption

$$P^{(3)}(\omega = \omega_1 + \omega_2 + \omega_3) = \chi^{(3)}(\omega_1, \omega_2, \omega_3)E(\omega_1)E(\omega_2)E(\omega_3). \tag{4.4}$$

The last of these phenomena can occur for all three fields at the same frequency and has a degeneracy factor of 3

$$P^{(3)}(\omega) = 3\chi^{(3)}(\omega, -\omega, \omega)E(\omega)E^*(-\omega)E(\omega). \tag{4.5}$$

This gives rise to an intensity-dependent refractive index also known as the optical Kerr effect,

$$n(I) = n + n_2 I, \tag{4.6}$$

where the nonlinear coefficient is related to the third-order susceptibility as

$$n_2 = 3Re[\chi^{(3)}]/n^2\varepsilon_0 c. \tag{4.7}$$

Two-photon absorption is a nonlinear effect by which two photons arrive within a coherence time of each other and can be simultaneously absorbed exciting an electron in a material at twice the photon energy. This gives rise to either induced or saturable absorption depending on the sign of the imaginary part of the third order susceptibility:

$$\alpha(I) = \alpha + \alpha_2 I, \tag{4.8}$$

where the two-photon attenuation coefficient is related to the third-order suscep-tibility as

$$\alpha_2 = 12\pi Im[\chi^{(3)}]/n^2\varepsilon_0 c\lambda. \tag{4.9}$$

## 4.3 Nonlinear Enhancement

If a microresonator is constructed with a material that possesses a third-order nonlinearity manifested as an intensity dependent refractive index, then the single-pass phase shift acquires a power-dependent term, $\phi = \phi_0 + 2\pi L n_2 P_2 / \lambda A_{\text{eff}}$ where $\phi_0$ is a linear phase offset. The derivative of the effective phase shift with respect to input power gives a measure of the power-dependent accumulated phase. This derivative can be expressed as

$$\frac{d\Phi}{dP_1} = \frac{d\Phi}{d\phi}\frac{d\phi}{dP_3}\frac{dP_3}{dP_1} \xrightarrow[\phi=0,a=1]{} \frac{2\pi L n_2}{\lambda A_{\text{eff}}}\left(\frac{1+r}{1-r}\right)^2 = \frac{2\pi L n_2}{\lambda A_{\text{eff}}}\left(\frac{2}{\pi}\mathcal{F}\right)^2 = \frac{\pi}{P_\pi}\left(\frac{2}{\pi}\mathcal{F}\right)^2.$$

$$(4.10)$$

where $P_\pi = \lambda A_{\text{eff}}/2n_2 L$ is the threshold power required to achieve a nonlinear phase shift of $\pi$ radians. The effect of the resonator is to introduce two separate enhancements for which the combined action on resonance yields an overall nonlinear response *quadratically* enhanced by the finesse. [65]

The dual effect can be understood intuitively noting that an increased interaction length arises from the light recirculation, and an increased field intensity arises from the coherent build-up of the optical field. The increased interaction length implies a reduction in bandwidth which will be examined in the next section.

## 4.4 Nonlinear Pulsed Excitation

In the previous sections, resonator enhancement of nonlinearity was derived in a steady state basis. The steady state analysis presented earlier breaks down when the bandwidth of the optical field incident on a ring resonator is of the order or greater than the cavity bandwidth. In order to simulate the time dependent nature of the resonator response, a recirculating sum of successively delayed and interfered versions of the incident pulse must be performed numerically. The circulating field after $M$ passes is built up from successive and increasingly delayed coupler splittings:

$$A_{3,M}\left(t\right) = it \sum_{m=0}^{M} \left(ra\right)^{m} e^{i\phi_m(t)} A_1\left(t - mT_{\mathrm{R}}\right) \tag{4.11}$$

where the phase cannot be treated as a constant due to the time-dependence of the nonlinear phase shift. The phase shift at each pass is computed as

$$\phi_{m=0}\left(t\right) = 0 \tag{4.12}$$

$$\phi_m\left(t\right) - \phi_{m-1}\left(t\right) = \phi_0 + \gamma \int_0^{2\pi R} dz \; \left|A_{3,M}\left(t\right)\right|^2 e^{-\alpha z} = \phi_0 + \left(\frac{a^2 - 1}{\ln a^2}\right) \gamma 2\pi R \left|A_{3,M}\left(t\right)\right|^2,$$

$$\tag{4.13}$$

where $\gamma$ is the self-phase modulation coefficient. Finally, the transmitted intensity is computed as

$$A_{2,M}(t) = rA_1(t) - t^2 a \sum_{m=1}^{M} (ra)^{m-1} e^{i\phi_m(t)} A_1(t - mT_R). \qquad (4.14)$$

In order to preserve pulse fidelity and achieve finesse-squared enhancement, it is necessary to operate the device with pulses of widths that are greater than or equal to the cavity lifetime.

## 4.5  Nonlinear Saturation

Another implicit assumption in derivations thus far is the fact that the resonator does not get power-detuned or pulled away from its initial detuning. One might call this the non-pulling pump approximation (NPPA). The pulling away from resonance decreases the nonlinear enhancement such that the process may be described mathematically as a saturation of the effective nonlinearity. Figure 4.1 displays the results of a simulation involving the interaction of a resonant pulse with a nonlinear resonator. The phase accumulation (c) across the pulse tracks the pulse intensity but falls short of reaching $\pi$ radians even though its peak power corresponds to twice the value predicted by the NPPA. Figures 4.1b and d illustrate why this is the case. As the incident intensity rises, the resonator is

indeed pulled off resonance and the circulating intensity and effective phase shift are pulled away from their respective NPPA predicted slopes (dashed lines).

A greater nonlinear phase shift may be extracted from the resonator by employing a small amount of initial detuning. In figure 4.3, an initially detuned pulse pulls itself through resonance and in the process acquires a nonlinear phase shift of $\pi$ radians.

The value of the detuning chosen ($\phi_0 = -\pi/\mathcal{F}$) corresponds to the point at which a symmetric pull through resonance results in a $\pi$ radian phase shift.

If the detuning is increased some more, the circulating intensity vs. incident intensity relation exhibits a very sharp upward sloping curve. The curve can in fact become steeper than that predicted by the NPPA. At a detuning of ($\phi_0 = -\sqrt{3}\pi/\mathcal{F}$), the curve becomes infinitely steep over a narrow range. This corresponds to an operating point just below the threshold of optical bistability. Operation in this regime will be examined more closely in a later section. For certain applications, this might be more or less useful than the previous case. Figure 4.4c demonstrates the phase accumulation across such a pulse. The phase shift actually can exceed $\pi$ radians but is confined to a narrower range near the peak of the pulse.
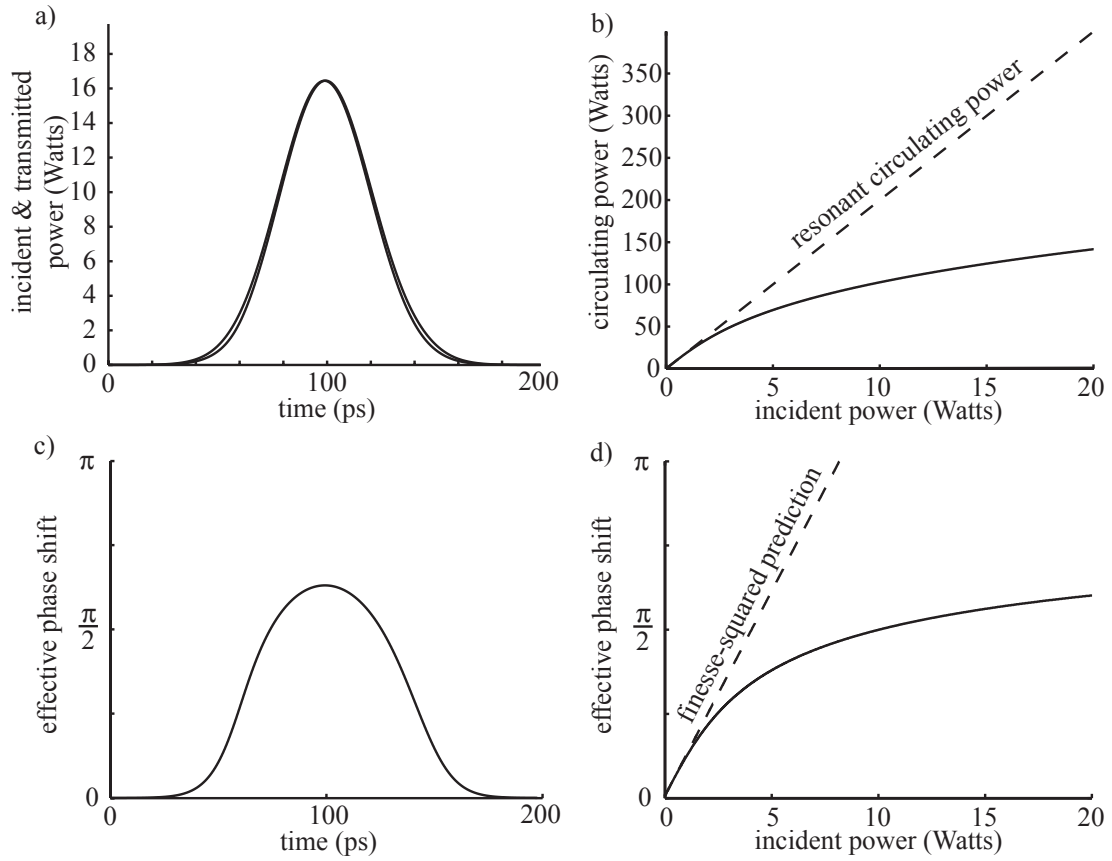
Figure 4.1: Simulations demonstrating the dynamic accumulation of nonlinear phase shift across a resonant pulse interacting with a nonlinear resonator. A 50 ps ($10t_{\mathrm{cav}}$), 16 W peak power pulse (corresponding to twice the reduced threshold power) interacts with a 5 $\mu$m diameter nonlinear resonator with $r = .905$ (build-up=20). a) incident & transmitted pulses, b) circulating power vs. incident power in steady state showing the nonlinear pulling (dashed line corresponds to resonant slope), c) accumulated effective phase shift, d) effective phase shift vs. incident power (dashed line corresponds to resonant slope). Notice that the effective phase shift accumulation at the center of the pulse falls short of reaching $\pi$ radians.
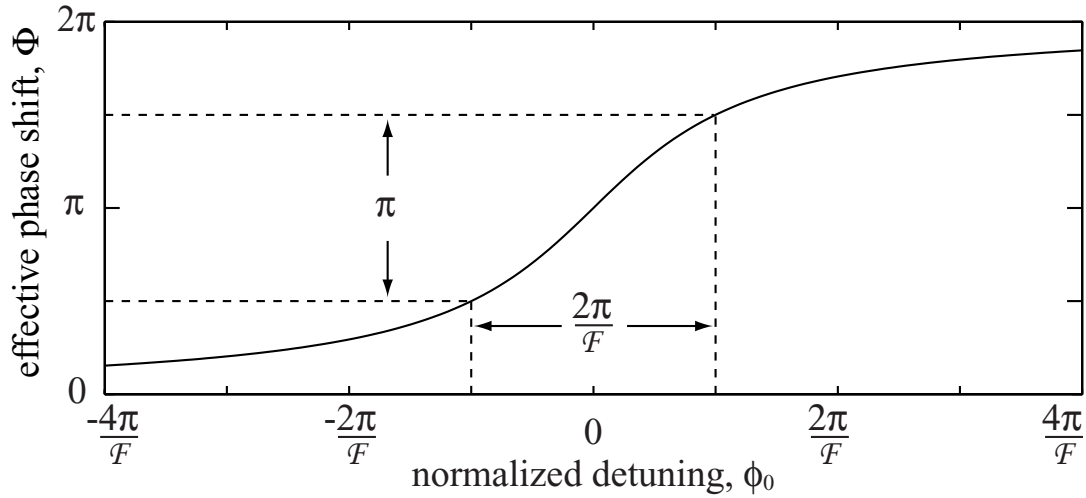
Figure 4.2: Linear effective phase shift showing the optimum amount of detuning such that the dynamic range of the effective phase shift is efficiently implemented near resonance.

## 4.6 Optical Power Limitation

The previous subsection, described how injected light initially tuned near the resonance of an all-pass resonator can pull itself off resonance via nonlinear refractive index changes. This was shown to lead to a saturation of the nonlinear phase shift at high circulating powers. By incorporating a resonator inside a Mach-Zehnder interferometer, the saturating nonlinear phase shift at high powers can be converted into a clamping of *transmission*. A more carefully designed device can provide a clamping of optical *power*. Figure 4.5 displays the results of a REMZ-based power limiter which provides near unit transmission until it is lowered systematically such that the power is clamped at 1 watt. Here the normal $\pi$ radian power for an equivalent length of waveguide is 1 kW. The other port of
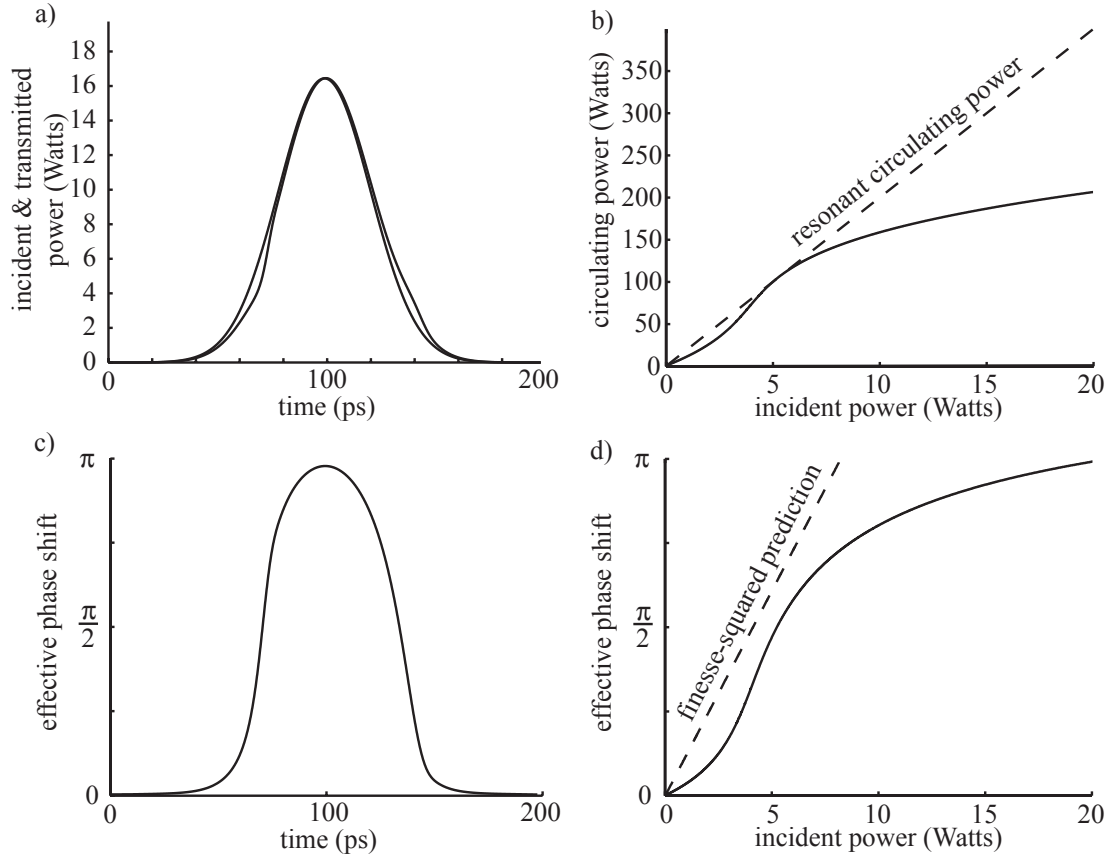
Figure 4.3: Simulations demonstrating the dynamic accumulation of nonlinear phase shift across an optimally detuned pulse interacting with a nonlinear resonator. All parameters with the exception of the detuning ($\phi_0 = -\pi/\mathcal{F}$) are the same as in figure 4.1. Notice that the effective phase shift accumulation at the center of the pulse reaches $\pi$ radians.

a)

incident & transmitted power (Watts)

b)

circulating power (Watts)

resonant circulating power

c)

effective phase shift

d)

effective phase shift

finesse-squared prediction
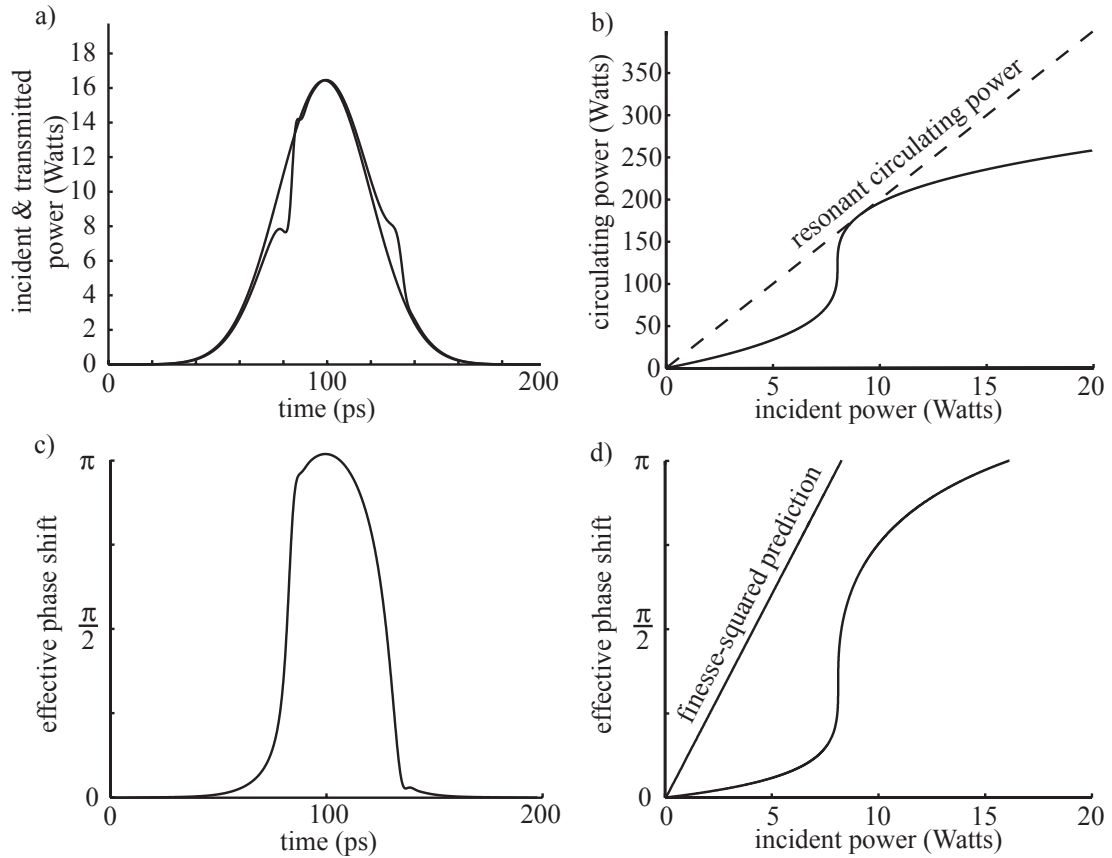
Figure 4.4: Simulations demonstrating the dynamic accumulation of non-linear phase shift across a pulse detuned just below the limit of bistability interacting with a nonlinear resonator. All parameters with the exception of the detuning ($\phi_0 = -\sqrt{3}\pi/\mathcal{F}$) are the same as in figure 4.1. Notice the very sharp jump in phase.
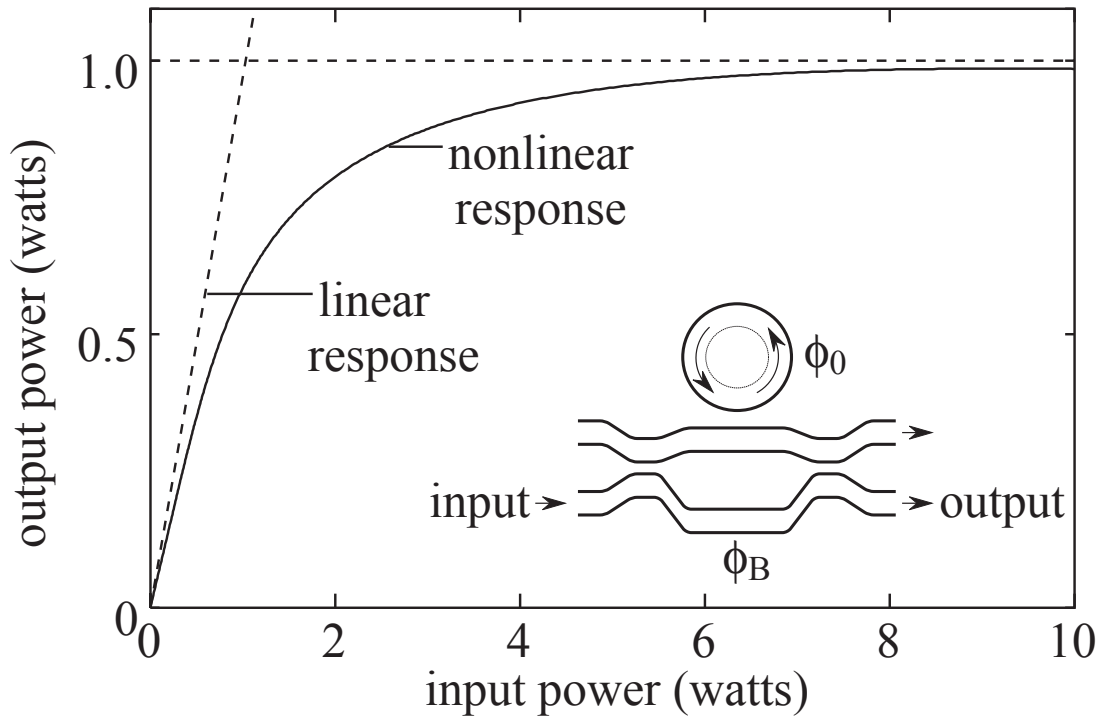
Figure 4.5: A resonator enhanced Mach-Zehnder (REMZ) interferometer can be implemented as a power limiter.  Here, the output power closely follows the input power for power levels much less than 1 W.  For higher input power levels, the output power is clamped below 1 W while excess power is diverted to the other output port.  The threshold power to achieve a nonlinear phase shift of $\pi$ radians in a single pass through the resonator is 1 kW, the coupling coefficient is $r = .95$, single pass transmission is 98%, resonator detuning is $\phi_0 = -0.0065\pi$, and the Mach-Zehnder bias is $\phi_b = -0.854\pi$.

the REMZ in fact mimics the properties of a saturable absorber where high power

levels are transmitted with low loss while low power levels are attenuated.

## 4.7   Multistability

The inclusion of nonlinearity changes the input-output relations in a qualitatively

different manner.   Multistable branches in the input-output relationships of a

resonator become possible. [66]  The circulating intensity is a function of detuning,

which in turn is a function of the circulating intensity and so on ad infinitum.
Mathematically, the circulating intensity can be expressed either as an infinitely
nested expression or more compactly as an implicit relation between the incident
and circulating intensities.

$$I_3 = I_1 \frac{(1 - r^2)}{1 - 2r \cos\left(\phi_0 + \frac{2\pi(2\pi R)}{\lambda} n_2 I_3\right) + r^2} \tag{4.15}$$

This implicit relation is easily converted into a single-valued function if the circu-
lating intensity is considered the independent variable and the incident intensity
the dependent variable. Multistability is always present in such a lossless nonlin-
ear resonator above some threshold intensity. One way to reduce this threshold
intensity is to red-detune the resonator slightly so that the resonator is initially
off resonance but forms two stable circulating intensity levels for a low intensity.
The onset of multistability takes place at $\phi_0 = -\sqrt{3}\pi/\mathcal{F}$. Optical bistability in
a resonator allows for the construction of all-optical flip-flops and other devices
exhibiting dynamic optical memory. [67]

# 4.8 Reduction of Nonlinear Enhancement via Attenuation

As was showing in chapter 2, the presence of attenuation mechanisms in the
resonator lead to a reduction in peak build-up, a paradoxical increase in phase
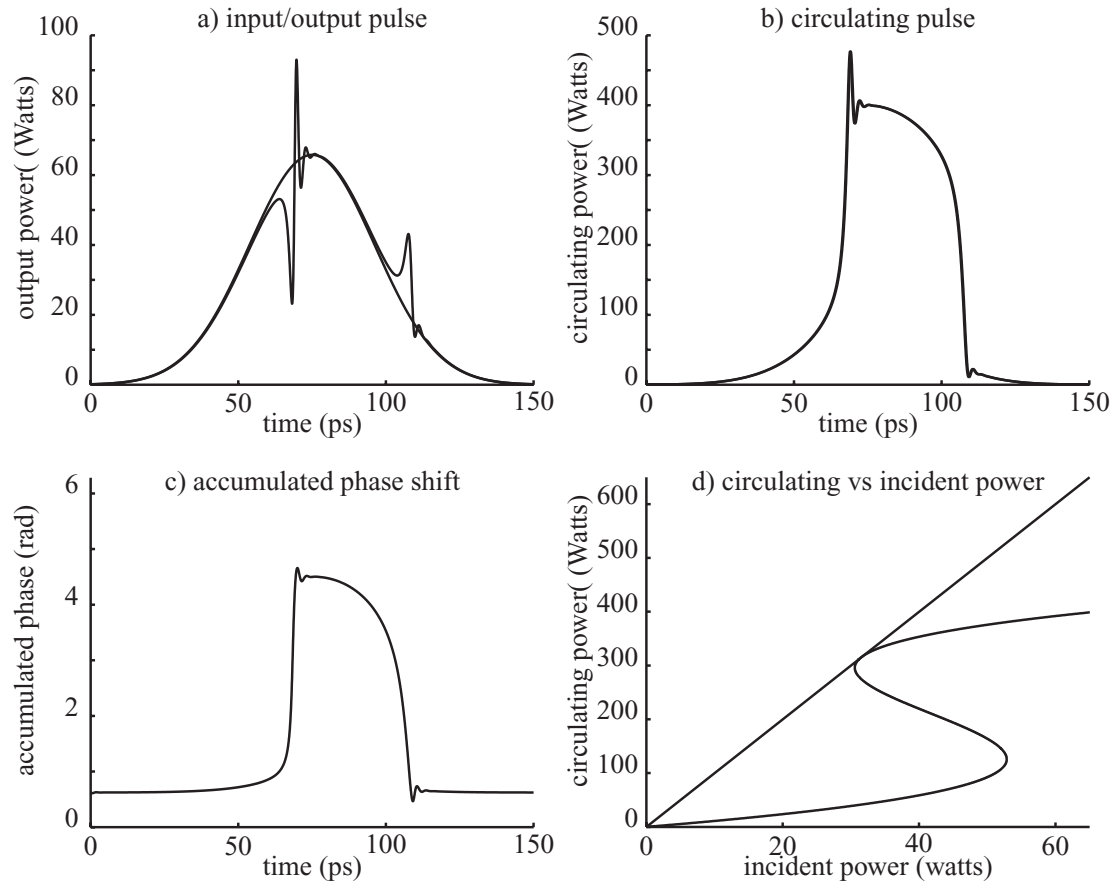
Figure 4.6: Demonstration of bistability in a 5 $\mu$m radius nonlinear resonator
with $r = .818$, $\phi_0 = -3\pi/\mathcal{F}$, $P_\pi = 1644.6$ W, and a 50 ps, 66 W peak power
pulse.  a) input/output pulse, b) circulating pulse, c) accumulated phase,
d) incident vs. circulating bistable power relation.  Notice the fast switch
between stable states, when the input pulse power reaches the hysteresis
"jump up" and "jump down" points at 53 and 30 Watts.

sensitivity, and a reduction in transmission. The dependence of the nonlinear enhancement on the round trip attenuation is thus non-trivial.

The peak build-up (and phase sensitivity) with no loss is termed $\mathcal{B}_0$ for simplicity in the following comparisons all taken on resonance. The build-up varies with the round-trip amplitude transmission, $a$ as,

$$\mathcal{B}(a) = \frac{1 - r^2}{(1 - ra)^2} \xrightarrow[r=a]{} \tfrac{1}{4}\mathcal{B}_0, \tag{4.16}$$

$$\mathcal{B}(\alpha 2\pi R) \approx \mathcal{B}_0 - \tfrac{1}{2}\mathcal{B}_0^2(\alpha 2\pi R) + \tfrac{3}{16}\mathcal{B}_0^3(\alpha 2\pi R)^2 + O(3). \tag{4.17}$$

where the second expression is Taylor expanded in loss about zero. The build-up drops with decreasing $a$ until reaching critical coupling $(r = a)$ where it drops to $1/4$ its lossless value. In contrast, the phase sensitivity increases from the lossless value without bound at critical coupling,

$$\mathcal{S}(a) = \frac{a(1 - r^2)}{(a - r)(1 - ra)} \xrightarrow[r=a]{} \infty, \tag{4.18}$$

$$\mathcal{S}(\alpha 2\pi R) \approx \mathcal{B}_0 + \tfrac{1}{16}\mathcal{B}_0^3(\alpha 2\pi R)^2 + O(3). \tag{4.19}$$

The nonlinear enhancement is equal to the product of the build-up and phase sensitivity. Additionally, since the intensity drops continuously when traversing the resonator, a correction factor is introduced, $\mathcal{C}(a) = \frac{1 - a^2}{\ln a^{-2}}$, such that the effective nonlinear phase shift induced by a much weaker single-pass nonlinear phase shift

is

$$\Delta\Phi_{\mathrm{NL}}(a) = \mathcal{B}(a)\mathcal{S}(a)\mathcal{C}(a)\Delta\phi_{\mathrm{NL}}. \tag{4.20}$$

Dividing this quantity by the the shift obtained for the lossless case results in a normalized nonlinear enhancement,

$$\mathcal{N}(a) = \frac{\Delta\Phi_{\mathrm{NL}}(a)}{\Delta\Phi_{\mathrm{NL}}(a=1)}. \tag{4.21}$$

$$\mathcal{N}(\alpha 2\pi R) \approx 1 - \tfrac{1}{2}\mathcal{B}_0(\alpha 2\pi R) + \tfrac{1}{4}\mathcal{B}_0^2(\alpha 2\pi R)^2 + O(3). \tag{4.22}$$

The lowest order variation in phase sensitivity with loss is quadratic. Thus, for small losses, the nonlinear enhancement is reduced primarily because of the reduction in peak build-up. Near critical coupling, the phase sensitivity increase without bound results in a growing enhancement as well, but at the expense of rapidly decreasing attenuation to zero at critical coupling. For comparison, the transmission varies as,

$$\mathcal{T}(a) = \frac{(a-r)^2}{(1-ra)^2} \xrightarrow[r=a]{} 0, \tag{4.23}$$

$$\mathcal{T}(\alpha 2\pi R) \approx 1 - \mathcal{B}_0(\alpha 2\pi R) + \tfrac{1}{2}\mathcal{B}_0^2(\alpha 2\pi R)^2 + O(3). \tag{4.24}$$

Figure 4.7 shows the variation of normalized nonlinear enhancement and transmission vs. loss. Notice that while the transmission steadily drops with increasing attenuation, the normalized enhancement is somewhat more stable and never dips
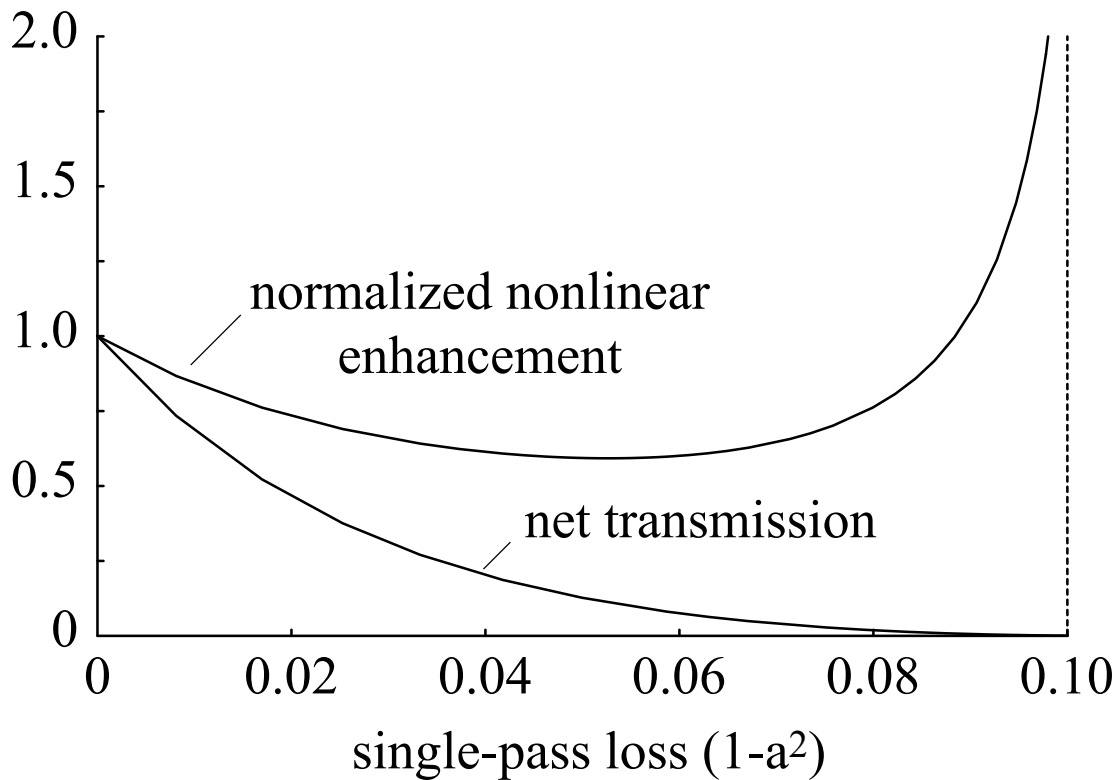
Figure 4.7: Variation in net transmission and normalized enhancement vs. loss for a resonator with $r^2 = 0.9$. For zero loss, both are equal to unity. The transmission steadily drops to zero at critical coupling ($r = a$), here at 10% loss. By contrast, the normalized enhancement is somewhat impervious to loss and never dips below a certain value due to an increasing phase sensitivity. While the enhancement diverges at critical coupling, it is of little use to operate there since the transmission drops to zero.

below a certain value.[1] For a nonlinear device, both enhancement and transmission are generally important and how their importance is weighted will affect how much loss can be tolerated.

---

[1].592 in the high-finesse limit

## 4.9 Figures of Merit

As will be examined in the next chapter, nonlinear photonic devices hold great promise for the implementation of densely integrated all-optical signal processing. Fundamental restrictions imposed by material properties have not allowed the promise to be fulfilled. The majority of refractive optical processing device require a $\pi$ radian nonlinear phase shift for successful operation which may in turn demand impractically high optical powers. In many material systems, strong nonlinear refractive indices are often accompanied by strong linear and nonlinear absorption which limit the achievable phase shift in many cases far below the target of $\pi$ radians. The limitations to the achievable nonlinear phase shift imposed by linear and nonlinear absorption thus merit examination.

Linear absorption limits the interaction length to an effective length given by:

$$L_\alpha = \frac{\left(1 - e^{-\alpha L}\right)}{\alpha} \qquad (4.25)$$

Because the effective length is independent of intensity, in theory, any desired nonlinear phase shift may still be obtained by making the intensity high enough. In practice of course, this may not be practical because all materials possess some threshold for optical damage. [64] There are several nonlinear figures of merit which are useful for comparing the relative strength of a nonlinear coefficient to absorption. A common definition is the nonlinear coefficient divided by the lin-

ear attenuation ($M_1 = 4\pi n_2/\lambda\alpha$). In general, this parameter is material property with some fixed value at a given wavelength. Most highly nonlinear materials are inherently absorptive because they operate via enhancement near some atomic or molecular resonance. For this reason, $M_1$ is useful for comparing the non-linearities of different material systems provided that interaction length is not a limitation. Silica single-mode fiber, for example has a very high $M_1$ despite a low intrinsic nonlinearity because its attenuation is extremely low ($5.3 \cdot 10^{-8}\mathrm{m}^2/\mathrm{W}$). There exist clever arrangements in which $M_1$ can be modified from its tradition-ally fixed value granted by nature. The techniques of electromagnetically induced transparency (EIT) for instance hold the promise of maintaining a strong nonlin-earity and cancelling the linear absorption via quantum interference. In the case of a nonlinear resonator, while the attenuation is increased in proportion to the effective number of round trips or finesse, the third order nonlinearity is increased in quadratic proportion.

Two-photon absorption imposes a more stricter limitation on the achievable nonlinear phase shift. In the presence of linear and nonlinear absorption, the reduced wave equation for nonlinear phase evolution (self-phase modulation) takes the form:

$$\frac{\partial}{\partial z}A = i\gamma\left(1 + iM_2^{-1}\right)|A|^2 A - \frac{1}{2}\alpha A. \tag{4.26}$$

Where a second FOM [68] is introduced proportional to the ratio of the nonlinear refractive index to the two-photon absorption coefficient, $M_2 = 4\pi n_2/\lambda\alpha_2$. Equa-

tion 4.26 has exact solutions for the transmitted intensity and nonlinear phase shift after propagating for a distance $L$. The fractional intensity remaining after propagating is:

$$T = \frac{e^{-\alpha L}}{1 + \alpha_2 I L_\alpha}. \tag{4.27}$$

Because two-photon absorption increases in proportion to the nonlinear refractive index, the achievable nonlinear phase shift saturates logarithmically with increasing intensity:

$$\phi_{\mathrm{NL}} = \frac{\mathrm{M}_2}{2} \ln\left(1 + 2\gamma I L_\alpha / \mathrm{M}_2\right) = \frac{\mathrm{M}_2}{2} \ln\left(1 + \frac{\mathrm{M}_1}{\mathrm{M}_2}\left(1 - e^{-2\gamma L/\mathrm{M}_1}\right) I\right), \tag{4.28}$$

$$\xrightarrow[\mathrm{M}_2 \to \infty]{} \gamma I L_\alpha = \frac{\mathrm{M}_1}{2}\left(1 - e^{-2\gamma L/\mathrm{M}_1}\right) I, \tag{4.29}$$

$$\xrightarrow[\mathrm{M}_1 \to \infty]{} \gamma I L. \tag{4.30}$$

Within a resonator, two-photon absorption[2] is likewise enhanced in proportion to the the nonlinear refractive index, i.e. quadratically with finesse. As a result, $\mathrm{M}_2$ would not be modified by the use of a resonator.

In general however, both linear and nonlinear absorptive processes are detrimental to switching devices based on the intensity-dependent refractive index. When considering both linear and nonlinear absorption, constructing a device that delivers a $\pi$ radian nonlinear phase shift using a resonator can exceed in

---

[2]it is expected that higher photon number absorptive processes of order N would be enhanced by a value of $\mathcal{F}^{\mathrm{N}}$
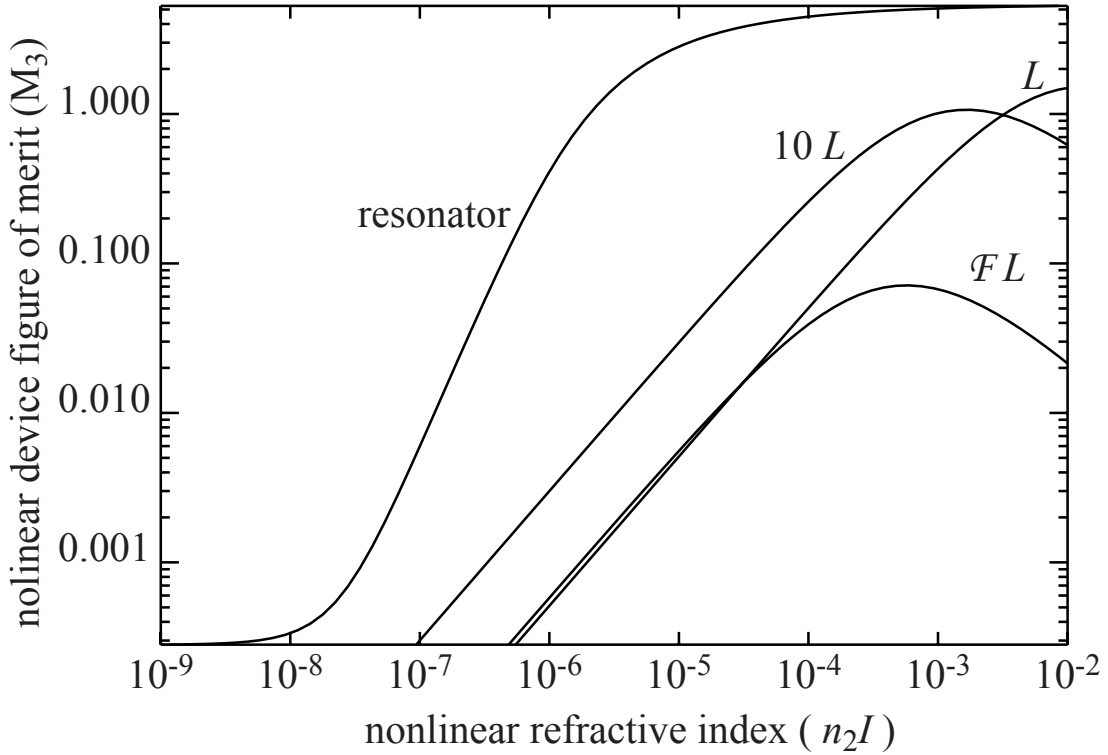
Figure 4.8: Comparison of the nonlinear device figure of merit ($M_3$) for a waveguide of length $L$, $10L$, $\mathcal{F}L$, with that of a resonator.

performance, an equivalent device formed from a simple waveguide. A third FOM, proportional to the nonlinear phase shift multiplied by the transmission, [69] $M_3 = \left(\frac{\Delta\phi_{\mathrm{NL}}}{\pi}\right)\left(e^{\frac{|E_2|^2}{|E_1|^2}}\right)$ is deemed more useful in such a comparison. This FOM is defined in such a way that a $\pi$ phase change over a $1/e$ intensity falloff results in $M_3 = 1$. This FOM can be favorably modified by use of a resonator. Figure 4.8 compares $M_3$ for a waveguide of length $L$, $10L$, $\mathcal{F}L$, with that of a resonator.

There are of course many other ways of characterizing the tradeoffs between attenuation and nonlinearity. Perhaps the most useful definition is the interfero-

metric contrast between a pulse that has acquired a given phase with some some unavoidable attenuation and a reference copy of the same pulse.

## 4.10 Inverted Effective Nonlinearity

The majority of refractive nonlinear materials behave in such a way that increasing intensity brings about a positive change in index. Negative nonlinear refractive indices are rare but nevertheless can be found in thermal (effectively) nonlinear phenomena and in semiconductors well above the half-gap. Neither case is useful for high speed all-optical switching. There are many proposed applications such as the nonlinear management, [70] which would greatly benefit from a negative nonlinear material. A negative effective nonlinearity may be achieved by use of a nonlinear ring resonator. In the undercoupled regime, the sign of the input-output phase relationship is inverted and thus allows for the possibility of inverting the sign of the intrinsic nonlinearity of the resonator medium. Figure 4.9 demonstrates a pulse propagating through a single resonator and acquiring a phase shift of *negative* $\pi/2$ radians.

## 4.11 Summary

This chapter examined the previous unstudied nonlinear optical phase transfer characteristics of microresonators. Typically, the nonlinear properties of most
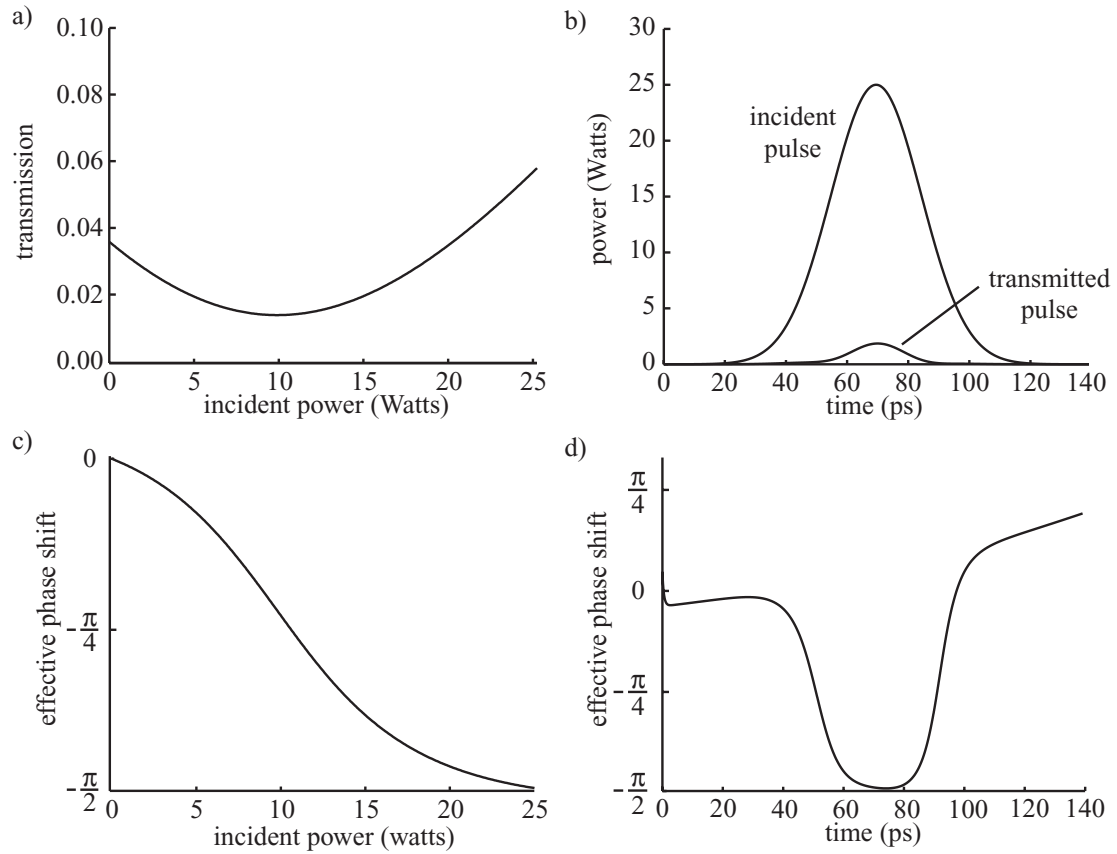
Figure 4.9: A resonator can display negative effective nonlinearity even if the intrinsic material nonlinearity is positive. This is possible only in the undercoupled regime and thus requires a lossy resonator or imbalanced add-drop filter. a) Transmission vs. incident power. b) Power vs. time. c) Effective phase shift vs. incident power. d) Effective phase shift vs. time. The parameters used in these simulations are $r = 0.9$, $a = 0.875$, $\phi_0 = -0.0115\pi$, $P = 20$ W, $P_\pi = 3183$ W, and $T_P = 20T_C = 35$ ps.

materials are ultraweak and require high optical intensities and or lengths to be observed. Through the use of microresonators, it is concluded that weak intrinsic nonlinearities may be enhanced in quadratic proportion to their finesse.

# Chapter 5

# Resonator Enhanced Microphotonic Switching

## 5.1   Introduction

The current state of optical communication systems involves the multiplexing of 10 and 40 gigabit/s channels generated electronically and transmitted optically via an optical fiber, each on different wavelengths.  This clever scheme, termed wavelength division multiplexing (WDM) [71] takes advantage of existing inexpensive but bandwidth limited electronic infrastructure and the currently limitless bandwidth offered by lightwave communications.  Passive optical filters are used to combine and split the channels, each of which consist of bit-encoded pulse trains with bit slots that are spaced far enough apart such that electronic detectors can discriminate among them.  One problem is that as the number of channels grows large, the complexity of the system, requiring thousands of lasers and detectors tuned to slightly different wavelengths becomes difficult to manage.   Another

scheme for combining several channels on a single light-carrying fiber is optical time division multiplexing (OTDM). In this optical analogue of electronic time-division multiplexed systems currently in widespread use, information carrying bits from different channels are interleaved in the time domain rather than in the spectral domain. [72] The individual pulses representing the bits would have to be ultra-short (10 picoseconds or less) to fill the fiber bandwidth. Conventional electronic switching device bandwidths are not expected to be able to meet the task of multiplexing and demultiplexing the pulses. All-optical means of accomplishing such tasks are thus necessary. All-optical switching devices offer great promise for reducing the complexity of optical communication systems and meeting the requirements of OTDM based networks. These networks may be built with such devices so as to fully exploit the terahertz bandwidths offered by lightwave carrier signals and eliminate the need for costly and unnecessary electronic-optical conversions.

## 5.2 Nonlinear Optical Switching

All-optical switching by definition refers to the manipulation of light by light. Because photons do not interact with themselves or other photons directly or even in linear media, only certain materials displaying nonlinear optical effects can be considered as candidates out of which an all-optical switch may be constructed . Furthermore, most material candidates for nonlinear all-optical switching, possess

**Optical Time Division Multiplexing (OTDM)**
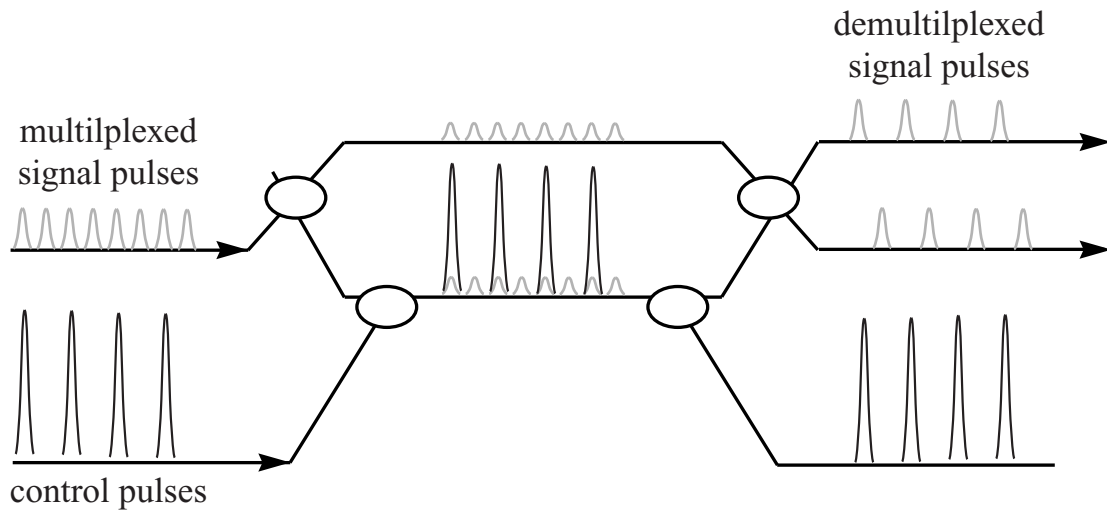


Figure 5.1: A scheme for optical time division multiplexing (OTDM) implementing cross-phase modulation in a nonlinear Mach-Zehnder interferometer.

extremely weak nonlinearities and thus require long interaction lengths. The industrially well-established silica fiber has an extremely weak nonlinearity, but is still useful as a nonlinear element because of its ability to confine light with low-loss over a long interaction length. Of course, devices built from silica fiber are practically kilometers long and have undesirably long latency times. More compact devices with shorter latency thus require stronger nonlinearities. Near resonance features, alkali metal vapors such as sodium have a long history of displaying strong nonlinear optical effects. The limited bandwidths and need for expensive containment chambers preclude their practical use. Active semiconductor-based devices relying on inter-band transitions offer strong nonlinearities in a compact geometry. however, their bandwidths are typically limited by recombination times

and require an undesirable active electrical source of power. Virtual transitions in low band-gap semiconductors typically offer the best compromise. AlGaAs below the half-gap has been known for some time to be a promising candidate for all-optical switching applications and has even been termed the "silicon of nonlinear optics." [73] More recently, chalcogenide glasses have attracted much attention because of the semiconductor-like optical properties and potential ease of incorporation with existing glass fabrication technologies.

In a prototypical configuration for optical switching, an unbalanced nonlinear Mach-Zehnder interferometer switches when the nonlinear phase shift difference between the two paths equals $\pi$ radians. Such a system possesses a threshold switching power given by $\lambda A_{\text{eff}}/2n_2\Delta L$. [74] Optical waveguides are ideal candidates for use as nonlinear switching devices because of their ability to confine light to wavelength-sized dimensions over interaction lengths that greatly exceed the Raleigh range governed by diffraction. [75,76] For typical single-mode silica fiber parameters at 1.55 $\mu$m and a peak power of 1 Watt, a path length difference $\Delta L$ of 1 kilometer is required. Air-clad AlGaAs or chalcogenide glass [68,77,78] waveguides, possessing 500 times greater nonlinearities and 500 times smaller effective area, offer the potential of lowering this length scale down to 4 mm. This is still not enough for large scale integration of photonic switches. It will be shown that the introduction of a ring resonator can greatly reduce the length scale fur-

ther down to the level of microns offering the possibility for passive, integrated
photonic architectures based upon nonlinear all-optical switching devices.

## 5.3 Resonator Enhanced Nonlinear Optical Switching

In the previous chapter, it was shown that microresonators can display enhanced
nonlinear phase shifts resulting from both an increase in effective path length and
build-up of intensity. The enhanced nonlinear phase shift can lead to important
consequences for microphotonic switching. For instance, by introducing the ring
resonator into one arm of a Mach-Zehnder interferometer, [79] as shown in figure
5.2, the phase switching characteristics are made manifest as power switching
characteristics allowing for the construction of an all-optical switching device with
a greatly reduced threshold power and/or size.

A comparison of the transmission vs. power characteristics for a standard
Mach-Zehnder interferometer and a resonator enhanced Mach-Zehnder interfer-
ometer (REMZ) for $\lambda = 1.55$ $\mu$m in single mode silica fiber plainly reveals the
advantage of using microresonators. The transmission for a standard nonlinear
Mach-Zehnder with unbalanced path lengths ($\Delta L = 10m$) is plotted versus inci-
dent power in figure 5.3. This standard geometry possesses a switching threshold
of 240 watts. Figure shows the transmission of a REMZ with a ring length of
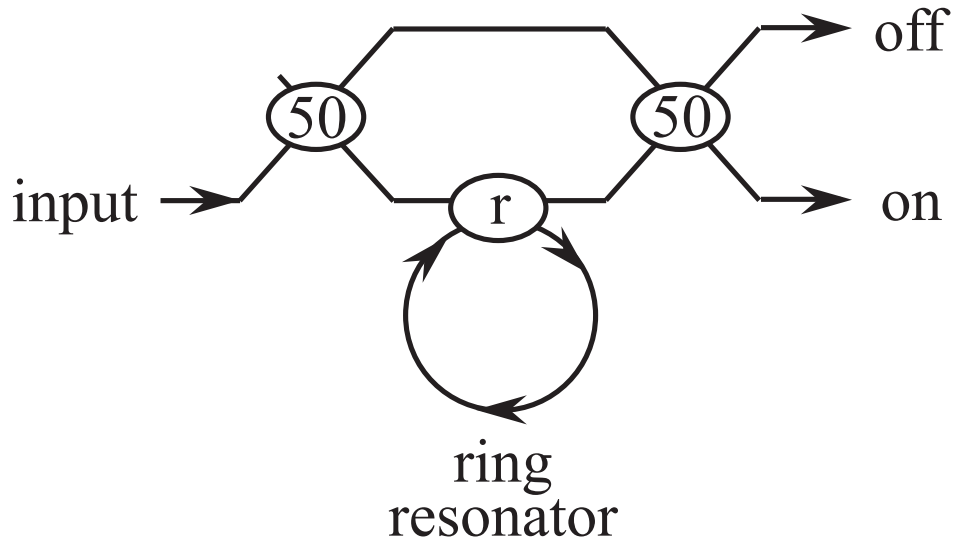
Figure 5.2: A resonator-enhanced Mach-Zehnder interferometer.

10 m and a reflectivity of ($r = 0.99$). The enhanced device exhibits a switching threshold of approximately 12 milliwatts. Both devices possess the same physical interaction length of 10 m, but the REMZ device possesses a switching threshold that is greatly reduced by a factor of $(2/\pi)^2 \mathcal{F}^2 = 20,000$. [65]

## 5.4  Switching Energy Vs. Bandwidth

It has been shown that a microresonator may be used to enhance nonlinear phase shifts thereby reducing the required power threshold for all-optical switching devices. These wonders do not come for free however. The use of a geometrical resonance, such as that of a Fabry-Perot cavity, to enhance some optical property
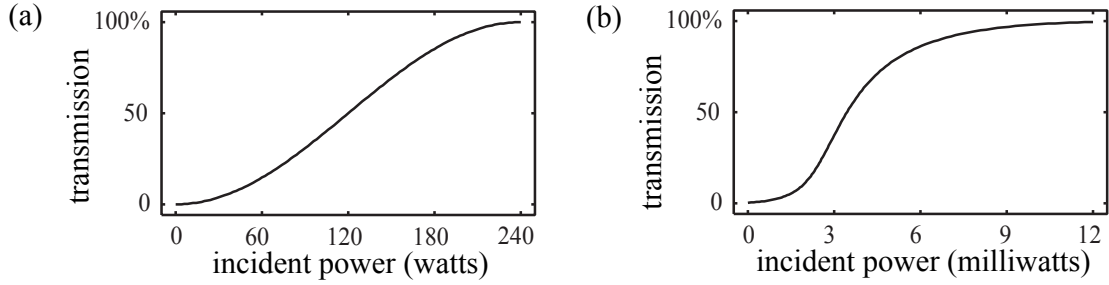
Figure 5.3: Transmission characteristics of (a) a standard nonlinear Mach-Zehnder interferometer and (b) a resonator enhanced Mach-Zehnder interferometer (REMZ). Note that the switching threshold of the REMZ device is lowered by four orders of magnitude.

usually comes at a price. A traditional Fabry-Perot cavity for example enhances the intensity circulating within it at the cost of imposing a limitation on the bandwidth over which this enhancement takes place. The limiting bandwidth is in direct proportion to the enhancement. While this conservation law holds for the linear optical properties, it may be circumvented for some nonlinear optical properties, for example self-phase modulation.

The bandwidth of a resonator is primarily governed by its size and finesse: $\Delta\nu = c/(n\pi D\mathcal{F})$. The finesse is directly related to the coupling strength $(t^2)$ according to $\mathcal{F} = 2\pi/t^2$. For an all-pass resonator, this bandwidth corresponds to the frequency interval over which the phase varies sensitively and in a nearly linear manner over $\pi$ radians. Outside this interval the sensitivity falls and the phase significantly departs from linear behavior such that a pulse with a larger bandwidth can become severely distorted.

To good approximation, the threshold power required to achieve a $\pi$ nonlinear

phase shift in a tightly confined waveguide mode is given by:

$$P_\pi = \frac{\pi \lambda A_{\text{eff}}}{8 \mathcal{F}^2 n_2 D}. \tag{5.1}$$

The threshold power multiplied by the cavity lifetime is a form of figure of merit for the operating characteristics of a resonator enhanced nonlinear optical switch. Of course this product is proportional to the lowest attainable switching energy required for switching the resonator. The lowest attainable switching energy is obtained when the pulse width is of the order of the inverse of the resonator bandwidth. This is easily understood because a longer pulse with the same peak power will carry more energy but not be any more effective at switching. A shorter pulse will not allow the resonator sufficient time to build-up in intensity and thus will experience a weakened nonlinear response in addition to being severely distorted. For a high contrast dielectric waveguide, the effective area to which the power is confined may be as small as $\lambda^2/8n^2$ where n is the refractive index of the guiding layer. The threshold energy required to achieve a $\pi$ nonlinear phase shift is accordingly:

$$U_\pi = \frac{\lambda^3 \sqrt{\pi^3 ln(2)}}{64 \mathcal{F} n n_2 c}. \tag{5.2}$$

In order to reduce the parameter space, some parameter choices are made ($n = 3, n_2 = 1.5 \cdot 10^{-17} \text{m}^2/\text{W}$) corresponding to AlGaAs or chalcogenide glass waveguides operating near 1.55 $\mu$m. Figure 5.4 plots a systems diagram display-
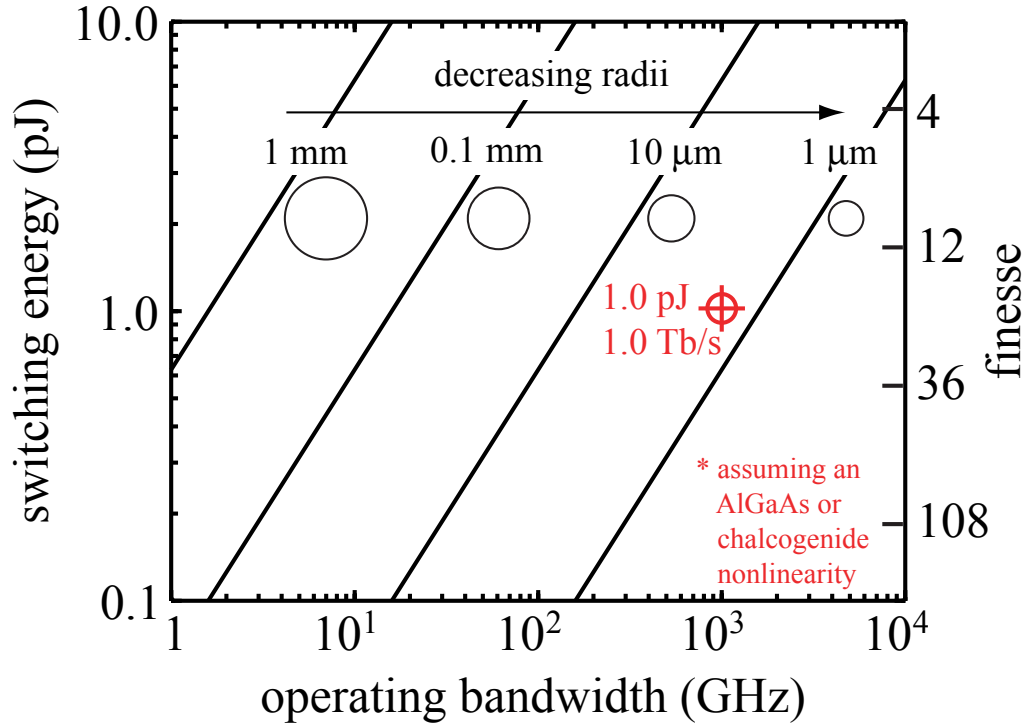
Figure 5.4: Operating diagram displaying the inherent tradeoff between pulse energy and bandwidth derived in eq. 5.2 for an AlGaAs or chalcogenide-based microresonator near 1.55 $\mu$m.

ing the tradeoff between switching energy and bandwidth for resonators of varying diameter. It is of technological interest to note that switching is possible with a 1 picosecond, 1 picojoule pulse.

Due to a physically large ring circumference and high finesse, our earlier, fiber-based proposal would be limited to operate at around 100 kHz. All-optical switching devices are not expected to play a role at these low frequencies. Values of the finesse larger than $10^6$ have been observed in the resonance features associated with the whispering gallery modes (WGMs) of microresonators. [52] Due to their

small dimensions and high finesse, coupling these resonators to an interferome-
ter would be able to provide large nonlinear phase shift enhancements, while at
the same time maintain high-speed switching characteristics. Despite the attrac-
tive promise of WGM-based all-optical switching devices, the field is relatively
untapped.

## 5.5   REMZ Vs. Fabry-Perot Switching

The placement of a nonlinear all-pass resonator within one arm of an interferom-
eter, for example a Mach-Zehnder, allows for the conversion of phase modulation
into amplitude modulation which can serve as a basis for an all-optical nonlin-
ear switch. One might ask why one would want to use this indirect method of
implementing a microresonator as an amplitude switching device when a nonlin-
ear add-drop filter accomplishes the same task in a more direct manner. The
properties of an add-drop filter are analogous to that of a traditional Fabry-
Perot interferometer which offers light the choice of two output ports and can
display nonlinear amplitude switching between them. A careful examination of
a nonlinear add-drop filter as a switching device; however, reveals a fundamental
limitation. The switching curve cannot be made to perform a complete switch
within the phase sensitive region near resonance. This is because the center of
the phase sensitive region (at a resonance frequency) directly coincides with a
minimum or maximum of the transmission spectrum. Only half of the sensitive

region is usable as a switch, the other half being wasted. It would be advantageous to shift the peak in phase sensitivity away from the transmission minimum such that it coincides with the linear portion of the transmission curve. However, there is simply no way to accomplish this in an add-drop filter or Fabry-Perot. The missing degree of freedom which can provide this capability can be found in a device formed from a nonlinear all-pass resonator coupled to one arm of an interferometer such as in a resonator-enhanced Mach-Zehnder (REMZ) interferometer. A REMZ can be used to independently set the peaks of nonlinear phase sensitivity and transmission. Figure 5.6 displays the linear transmission characteristics vs. detuning for a REMZ with offset bias phase between arms of $\phi_B = 0$, $\pi/2$, $\pi$, and $3\pi/2$. Optimized switching characteristics are obtained when the peak of the phase sensitivity coincides with the linear portion of the switching curve $\phi_B = \pi/2, 3\pi/2$. The characteristic switching curve of a Mach-Zehnder is cosine-squared. To build a effective switch it is important to switch in a region of this curve where the maximum change in transmission is brought about by the minimum change in accumulated phase. This is at the point of maximum switching sensitivity, which is related to the phase sensitivity as:

$$\frac{d\mathcal{T}}{d\phi} = -\tfrac{1}{2}sin(\Phi - \phi_B)\frac{d\Phi}{d\phi} \tag{5.3}$$

Figure 5.7 compares the switching characteristics for an add-drop filter, an unbiased REMZ and a properly-biased REMZ. For the add-drop filter, the build-up
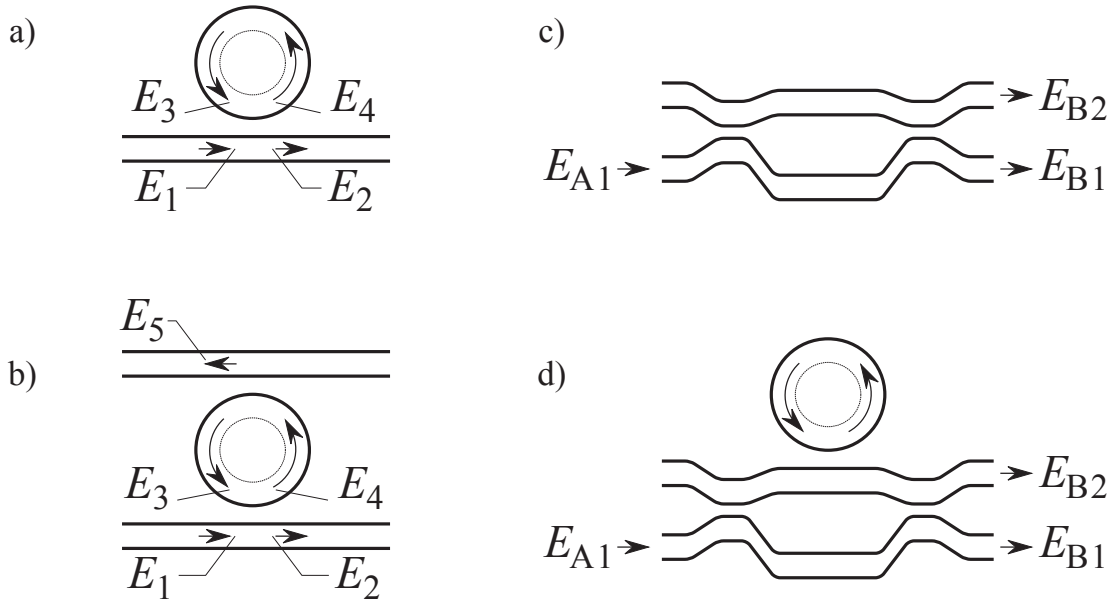
Figure 5.5: a) a singly-coupled microresonator, b) a doubly-coupled microresonator or Fabry-Perot, c) a Mach-Zehnder interferometer (MZI), d) a resonator enhanced Mach-Zehnder (REMZ) interferometer.

and finesse are each lower by a factor of four in comparison with an all-pass resonator with the same coupling strength. In a REMZ, however, only half of the power enters the arm containing the resonator and its phase contributes in a manner that another factor of two is lost. Still, this results in a net improvement in switching threshold by a factor of four which can be seen by comparing the curves in the figure. It might be argued that this is not a valid analysis since the finesse is not maintained equal in the comparison. When the finesse is maintained equal, the curves are in fact equivalent. More significant, however, is the improvement in the shape of the switching curve when the REMZ is properly biased. Proper biasing is achieved by tuning the peak of the nonlinear phase sensitivity to the 50% transmission operating point of the unloaded Mach-Zehnder.
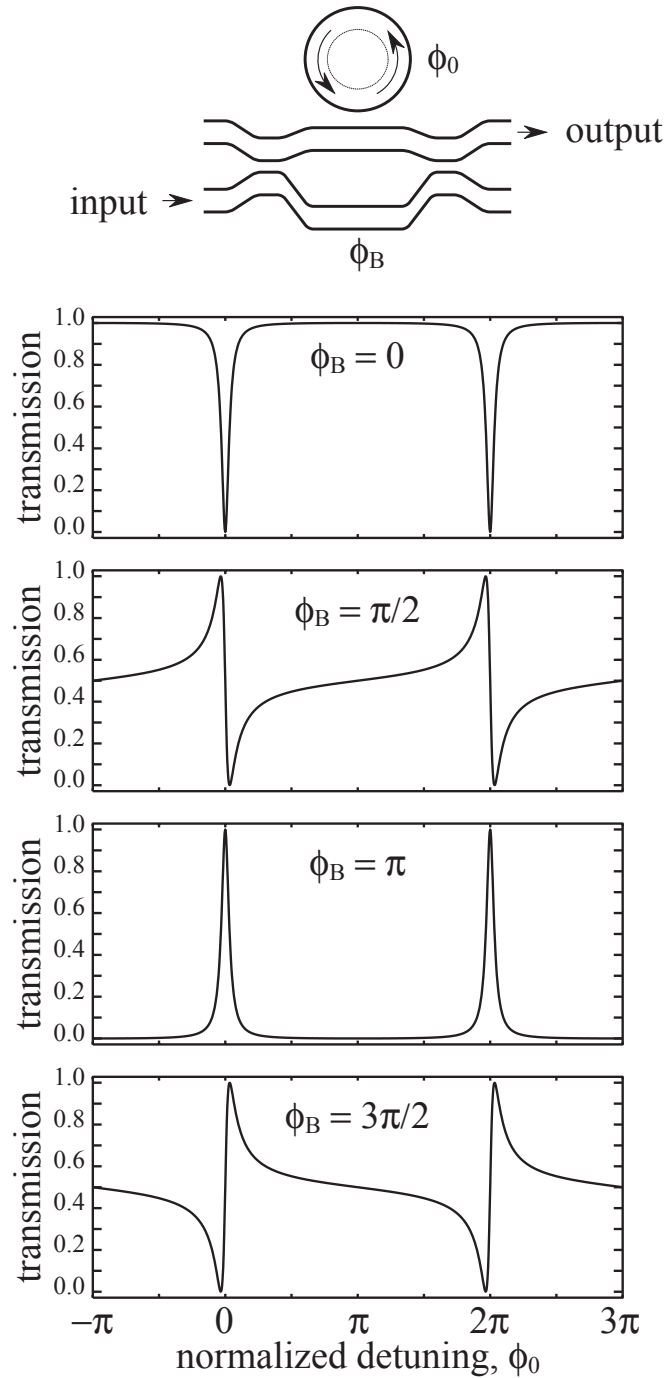
Figure 5.6: A comparison of the linear transmission spectra for a resonator-enhanced Mach-Zehnder (REMZ) interferometer with varying bias phase shift differences between arms.
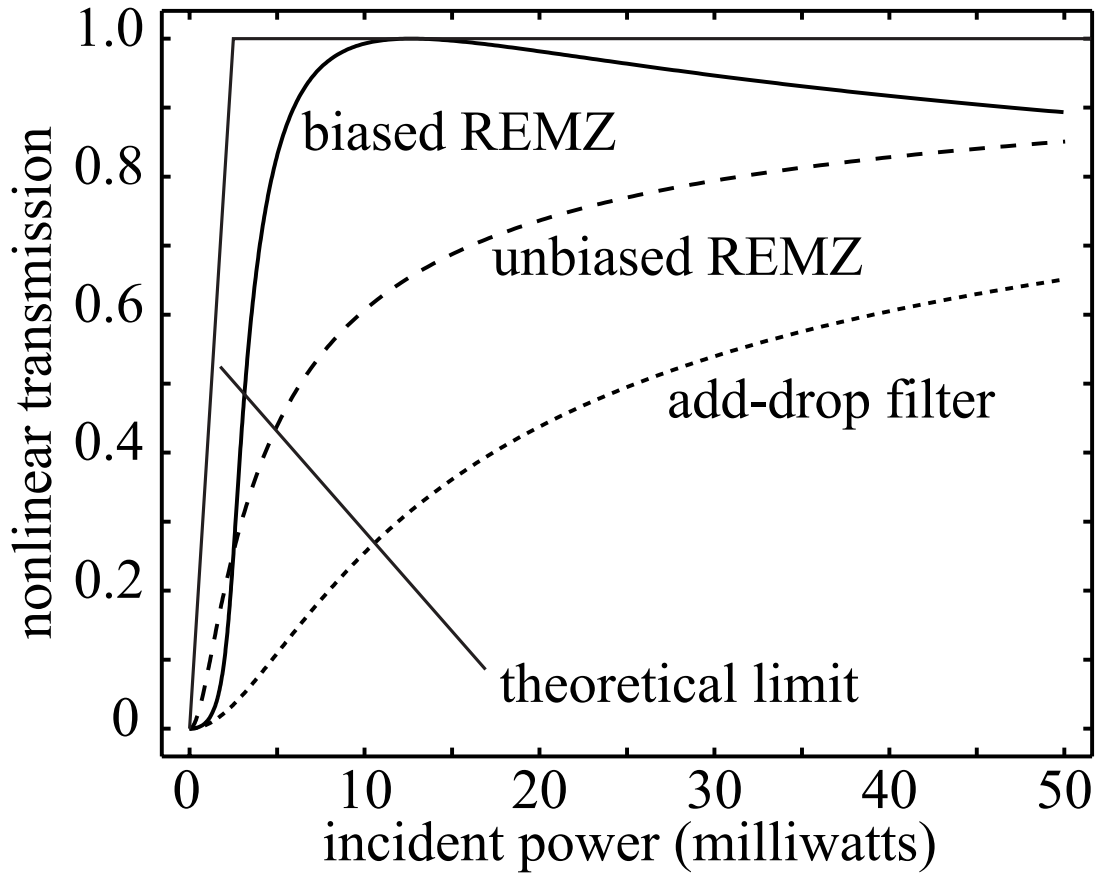
Figure 5.7: A comparison of the nonlinear switching characteristics of an add-drop filter (Fabry-Perot), an unbiased, and a properly-biased resonator-enhanced Mach-Zehnder (REMZ) interferometer.
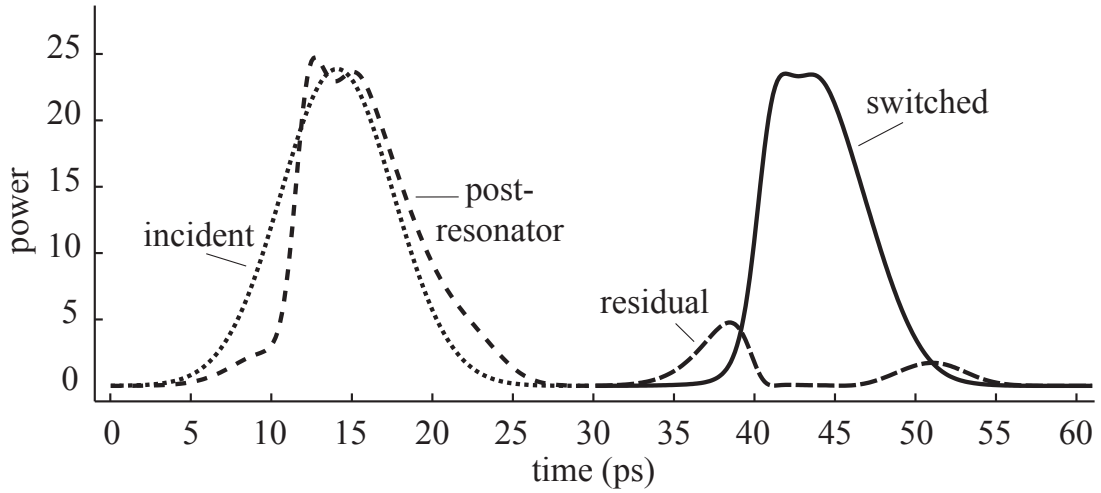
Figure 5.8: Pulse switching characteristics for a resonator-enhanced Mach-Zehnder (REMZ) interferometer. Here, an 8 picosecond, 25 Watt (peak power) optical pulse is switched out with high fidelity in a properly biased REMZ. Plotted are the incident pulse, the pulse after traversing the resonator (scaled by 2X), the switched out pulse, and the residual pulse energy in the originally transmitting arm. Here, the resonator bandwidth is only two times wider than the pulse bandwidth (FWHM). The base switching threshold is 3 kilowatts. The resonator consisted of a 5 micron diameter disk with a finesse of 30 and $n_2 = 1.5 10^{-17} \mathrm{m}^2/\mathrm{W}$.

## 5.6 Single Photon Switching

Microresonators have the potential for dramatically lowering thresholds required for all-optical switching. The question naturally arises as to whether it is possible to devise a microresonator-based switch that only requires a single photon. Expressing the energy threshold 5.2 in units of energy quanta, the photon number threshold is given by

$$N_\pi = \frac{\lambda}{hc} U_\pi = \frac{\lambda^4 \sqrt{\pi^3 ln(2)}}{64 \mathcal{F} n n_2 h c^2}. \tag{5.4}$$

For AlGaAs or chacogenide-based parameters, the finesse required to build such a sensitive device would be a (currently) prohibitively large value of greater than $10^8$.

## 5.7 Summary

In electronics, a revolution took place when vacuum-tube-based nonlinear electronic devices were replaced with integrated electronic circuits based on the transistor. For a similar revolution to occur in photonics, the integration of nonlinear optical components is required. This chapter examined the effectiveness of microresonators for use as all-optical switching components which are compact and can be integrated to form photonic circuits which are capable of performing complex tasks on a chip.

# Chapter 6

# SCISSORs

## 6.1 Introduction

In the previous chapters, the linear and nonlinear *transfer* characteristics of a single microresonator coupled to an ordinary optical waveguide were examined in detail. In this chapter, the linear and nonlinear *propagation* characteristics of a sequence of all-pass structures are examined. Parallel, [80] or indirectly coupled resonators are emphasized. These are rings coupled indirectly via a waveguide. By contrast, a serial coupled arrangement involves rings coupled to rings directly. The second case much like a coupled cavity and greatly restricts the operating bandwidth. For a detailed investigation of the use of such a configuration in the context of dispersion compensation see Madsen, et al. [28,46] and for filters see Little, Hryniewicz, and Orta. [81–83]
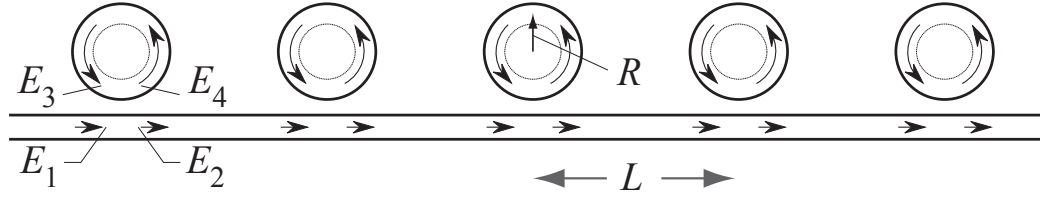
Figure 6.1: A structured, fully transmissive waveguide consisting of a side-coupled integrated spaced sequence of resonators (SCISSOR). $E_1$ is the incident field, $E_4$ is the field injected into the disk, $E_3$ is the field after one pass around the resonator, and $E_2$ is the transmitted field.

## 6.2   Linear Propagation

A pulse propagating though a single all-pass resonator acquires a frequency-dependent phase shift which serves to delay and/or distort the pulse shape. By arranging a sequence of resonators coupled to an ordinary waveguide the effective propagation constant of the guide can be modified. The modified effective propagation constant can be defined as the accumulated phase per unit length and is composed of the propagation constant of the waveguide itself plus a contribution from the transmitted phase of the resonators. For a resonator spacing of $L$, the effective propagation constant becomes

$$k_{\text{eff}}\left(\omega\right) = n_0\omega/c + \Phi\left(\omega\right)/L. \tag{6.1}$$

A plot of the dispersion relation (propagation constant vs. radian frequency) for various values of the coupling parameter $r$ is shown in figure 6.2. The deviation in the curve from the light line of the ordinary waveguide takes the form of periodic
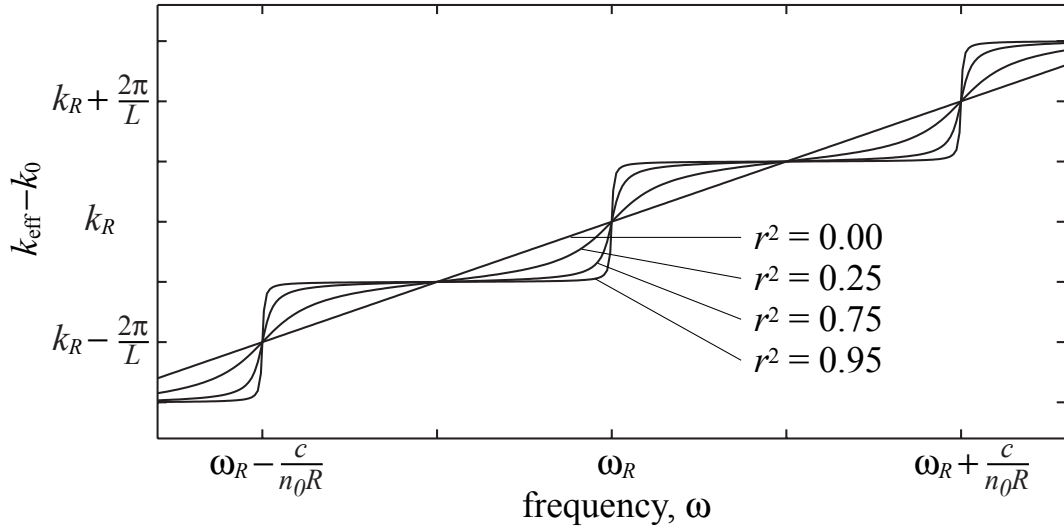
Figure 6.2: The dispersion relation (propagation constant vs. frequency) for light propagation in a SCISSOR with differing values of the self-coupling coefficient $r$. For generality, the waveguide contribution of constant slope $k_0$ has been subtracted from the effective propagation constant $k_{\mathrm{eff}}$.

changes in the group velocity and group velocity dispersion with a periodicity of $c/n_0 R$. Here, the material and waveguide dispersion are assumed to be negligible. In fact, it will later be shown that the dispersive nature of the resonators in general dominates the intrinsic dispersion by many orders of magnitude.[1].

A pulsed waveform can be decomposed into the product of a slowly-varying envelope $A(t)$ and a carrier wave with frequency $\omega_0$ as $E(t) \equiv \frac{1}{2}A(t)\exp(-i\omega_0 t)$ +c.c.. The relationship of the carrier frequency to some resonance frequency sets the central operating point on the dispersion relation curve and thus prompts the definition of a *normalized detuning* $\phi_0 = (\omega_0 - \omega_R)T_R$ where $T_R =$FSR$^{-1}$ is the resonator transit time and $\omega_R$ is the closest resonance

---

[1]The group velocity dispersion for $\mathrm{Al}_{0.2}\mathrm{Ga}_{0.8}\mathrm{As}$ is of the order of 1 ps$^2$/m. [84]

frequency. The transfer function of a single resonator can be expanded in two embedded Taylor's series: one for the transmitted phase shift (expanded about the normalized detuning $\phi_0$), and one for the exponential (expanded about the transmitted phase shift of the carrier $\Phi_0$):

$$H\left(\omega\right) = e^{i\Phi} = e^{i\Phi_0}\left\{1 + \sum_{n=1}^{\infty}\frac{i^n}{n!}\left[\sum_{m=1}^{\infty}\frac{1}{m!}\frac{d^m\Phi}{d\phi^m}\bigg|_{\phi_0}\left(\phi - \phi_0\right)^m\right]^n\right\}. \qquad (6.2)$$

Using this formal expansion, the transmitted field is related to the incident field with the assumption that the transmitted phase shift induced by each resonator is distributed over the spacing $L$ so that the effective propagation constant is independent of propagation distance at the macroscopic scale. The field at some point $z_{j+1}$ separated an infinitesimally small distance $\delta z$ from the field at another $z_j$ is given by a similar equation which distributes the resonator contribution and includes that of the waveguide:

$$E_{j+1}\left(\omega\right) = e^{i\left(\frac{n\omega_0}{c} + \frac{\Phi_0}{L}\right)\delta z}\times$$

$$\left\{1 + \sum_{n=1}^{\infty}\frac{i^n}{n!}\left[\frac{n_0}{c}\Delta\omega\delta z + \sum_{m=1}^{\infty}\frac{1}{m!}\frac{\delta z}{L}\frac{d^m\Phi}{d\phi^m}\bigg|_{\phi_0}\left(\phi - \phi_0\right)^m\right]^n\right\}E_j\left(\omega\right). \quad (6.3)$$

Taking the Fourier transform of this equation results in a difference equation relating the pulse envelopes at the two points:

$$A_{j+1}\left(t\right) = A_j\left(t\right) + \sum_{n=1}^{\infty}\frac{i^n}{n!}\left[i\frac{n_0}{c}\delta z\frac{\partial}{\partial t} + \sum_{m=1}^{\infty}\frac{1}{m!}\frac{\delta z}{L}\frac{d^m\Phi}{d\omega^m}\bigg|_{\phi_0}\left(i\frac{\partial}{\partial t}\right)^m\right]^n A_j\left(t\right). \quad (6.4)$$

Finally, the differential approximation $[A_{j+1}(t) - A_j(t)]/\delta z \to dA/dz$ is made $\delta z$ is allowed to go to zero.[2] This procedure yields a linear propagation equation for the pulse envelope:

$$\frac{dA}{dz} = \left[ -\frac{n_0}{c}\frac{\partial}{\partial t} + i\sum_{m=1}^{\infty} \frac{1}{m!}\frac{1}{L}\frac{d^m\Phi}{d\omega^m}\bigg|_{\phi_0}\left(i\frac{\partial}{\partial t}\right)^m \right] A. \tag{6.5}$$

The different terms in this equation are isolated and examined in what follows.

## 6.2.1 Group Velocity Reduction

The increased phase sensitivity on resonance is related to an increased group delay per resonator. This extra delay distributed amongst the resonators is responsible for a slower group velocity. The inverse of the group velocity is proportional to the frequency derivative of the propagation constant,

$$k'_{\text{eff}} = \frac{dk_{\text{eff}}}{d\omega} = \frac{n_0}{c} + \frac{1}{L}\frac{d\Phi}{d\omega} = \frac{n_0}{c}\left[ 1 + \frac{2\pi R}{L}\left(\frac{1-r^2}{1 - 2r\cos\phi_0 + r^2}\right) \right]$$

$$\xrightarrow[\phi_0=0, r\approx 1]{} \frac{n_0}{c}\left(1 + \frac{4R}{L}\mathcal{F}\right). \tag{6.6}$$

The group velocity $1/k'_{\text{eff}}$ is seen to be composed of contributions from propagation in the waveguide and discrete delays introduced by the resonators. The component of the group velocity reduction introduced by the resonators is proportional

---

[2]Implicit in this assumption is that each resonator is not strongly driven i.e. the transmitted phase shift $\Phi$ per resonator is small with respect to unity.

to the finesse and can dominate the waveguide component for moderate values of
the finesse.

## 6.2.2   Group Velocity Dispersion

While propagation in the waveguide itself is assumed to be dispersionless, strong
dispersive effects are induced by the resonator contribution. The group velocity
dispersion (GVD) is proportional to the second frequency derivative of the effective
propagation constant,

$$
k''_{\text{eff}} = \frac{dk^2_{\text{eff}}}{d\omega^2} = \frac{1}{L}\frac{d^2\Phi}{d\omega^2} = \frac{T_{\text{R}}^2}{L}\left[\frac{-2r\left(1-r^2\right)\sin\phi_0}{\left(1-2r\cos\phi_0+r^2\right)^2}\right]_{\phi_0=\pm\pi/\mathcal{F}\sqrt{3},r\approx1} \xrightarrow{\quad} \mp\frac{3\sqrt{3}\mathcal{F}^2 T_{\text{R}}^2}{4\pi^2 L}.
$$

(6.7)

While the GVD coefficient is zero on resonance, appreciably strong normal (posi-
tive) or anomalous (negative) values of the dispersion can be obtained on the red
(lower) or blue (higher) side of resonance respectively. The dispersion maxima
occur at detunings $\phi_0 = \pm\pi/\mathcal{F}\sqrt{3}$ where the magnitude of the group velocity
dispersion is proportional to the square of the finesse. This induced structural
dispersion can be many orders of magnitude greater than the material dispersion
of typical optical materials. [45] For example, a 10 picosecond optical pulse prop-
agating in a sequence of resonators with a finesse of $10\pi$, free-spectral range of 10
terahertz ($\sim$5 $\mu$m diameter), and a spacing of 10 $\mu$m experiences a group veloc-
ity dispersion coefficient $k''_{\text{eff}}$ of roughly 100 ps$^2$ per millimeter. In general, this
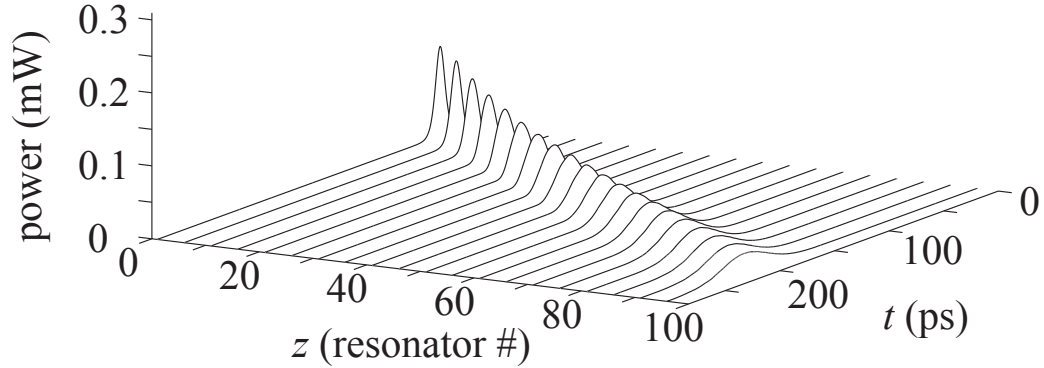
Figure 6.3: A weak pulse tuned to the dispersion maxima disperses while propagating in a SCISSOR. A 10 picosecond FWHM hyperbolic secant pulse tuned for maximum anomalous GVD ($B = 0.13$) enters the system consisting of 100 resonators each with a 5 $\mu$m diameter and finesse of $10\pi$, spaced by 10 $\mu$m. Note that the peak power is reduced by a factor of about 4 after propagating only 1 mm as a consequence of the strong induced dispersion.

structural dispersion can be as much as 7 orders of magnitude greater than material dispersion in conventional materials such as silica fiber (20 ps$^2$ per kilometer).

Figure 6.3 shows the pulse evolution for a 10 picosecond pulse propagating through 100 resonators, each tuned to the anomalous dispersion maxima.

## 6.2.3   Higher Order Dispersion

Higher orders of dispersion may be derived from eqn. 6.5, each subsequently possessing a maximum that is proportional to the cavity lifetime $\mathcal{F}T_{\mathrm{R}}$ to the n$^{\text{th}}$

power. Specifically, the third order dispersion coefficient is

$$k'''_{\text{eff}} \equiv \frac{1}{L}\frac{d^3\Phi}{d\omega^3} = \frac{T_{\text{R}}^3}{L}\left[\frac{-2r\left(1-r^2\right)\left[\left(1+r^2\right)\cos\phi_0 - 3r + r\cos 2\phi_0\right]}{\left(1 - 2r\cos\phi_0 + r^2\right)^3}\right]$$

$$\xrightarrow[\phi_0=0,r\approx 1]{} -\frac{4}{\pi^3}\frac{\mathcal{F}^3 T_{\text{R}}^3}{L}. \quad (6.8)$$

It is important to note that all orders of dispersion become significant when the pulse bandwidth is nearly as wide as the resonance bandwidth.

## 6.3  Nonlinear Propagation

In addition to inducing a strong group delay and dispersion, a resonator may enhance a weak nonlinearity. If the resonator possesses a nonlinear refractive index i.e. Kerr nonlinearity, then the internal phase shift will be intensity dependent. For simplicity the nonlinearity of the waveguide is neglected in what follows since it is expected to be small. The intensity-dependent contribution of the resonators to the internal phase shift is given by $\gamma 2\pi R|E_3|^2$, where $\gamma$ represents the strength of the intrinsic nonlinear propagation constant. This parameter is of course traditionally fixed for a given material system. The more useful parameter $\gamma/A_{\text{eff}}$ can be as low as $0.002$ m$^{-1}$W$^{-1}$ for standard single mode silica fiber or as high as $10^2$ m$^{-1}$W$^{-1}$ in an air-clad GaAs or chalcogenide glass based waveguide.[3] Near

---

[3]For the purpose of quoting the material nonlinearities, I have defaulted to the more useful parameter $\gamma$ whereby the nonlinear propagation constant is scaled by the effective mode area such that $\gamma PL$ is the nonlinear phase shift acquired for a power level of $P$ over a distance $L$.

resonance, the transmitted phase shift is *sensitively* dependent upon the internal phase shift, which is in turn dependent on an *enhanced* circulating intensity. The combined action of these effects gives rise to a dually-enhanced effective nonlinear propagation constant $\gamma_{\text{eff}}$, calculated from the derivative of the transmitted phase shift with respect to the input intensity:

$$\gamma_{\text{eff}} \equiv \frac{1}{L}\frac{d\Phi}{d|E_1|^2} = \frac{1}{L}\frac{d\Phi}{d\phi}\frac{d\phi}{d|E_3|^2}\frac{d|E_3|^2}{d|E_1|^2} = \frac{\gamma 2\pi R}{L}\left(\frac{1-r^2}{1-2r\cos\phi_0+r^2}\right)^2$$

$$\xrightarrow[\phi_0=0,r\approx1]{} \gamma\frac{8R}{\pi L}\mathcal{F}^2. \quad (6.9)$$

As can be seen from this equation, the increased phase sensitivity (or group velocity reduction) and the build-up of intensity contribute equally to quadratically enhance the nonlinear propagation constant with respect to the finesse. [65] In order to properly account for the all the third-order Kerr nonlinear contributions of the spectral components of three fields, a double convolution of the three interacting fields is performed in the spectral domain. In the time domain, the double convolution operation is equivalent to multiplication. This allows for the straightforward addition of a nonlinear contribution [85] to the internal phase shift term in the linear propagation equation (eqn. 6.5):

$$\frac{dA}{dz} = \left\{-\frac{n_0}{c}\frac{\partial}{\partial t} + i\sum_{m=1}^{\infty}\frac{1}{m!}\frac{1}{L}\frac{d^m\Phi}{d\phi^m}\bigg|_{\phi_0}\left[\gamma 2\pi R\mathcal{B}|A|^2 + iT_{\text{R}}\frac{\partial}{\partial t}\right]^m\right\}A. \quad (6.10)$$

For two nonlinearly interacting resonant pulses, the results here derived for the self-phase modulation (SPM) effect similarly apply to the effect of cross-phase modulation (XPM) though with an extra degeneracy factor of 2.

### 6.3.1 Solitons

Next, the nonlinear propagation equation that retains only the lowest order dispersive and nonlinear terms in eqn. 6.10 is examined. The time coordinate is shifted to the reference frame of the pulse ($t' = t - k'_{\mathrm{eff}}z$). It is found that, in this limit, the pulse evolution is governed by a nonlinear Schrödinger equation (NLSE) with effective GVD and SPM parameters:

$$\frac{\partial}{\partial z}A = -i\frac{1}{2}k''_{\mathrm{eff}}\frac{\partial^2}{\partial t'^2}A + i\gamma_{\mathrm{eff}}\left|A\right|^2 A. \tag{6.11}$$

Appendix F describes solutions to this equation. Soliton solutions exist provided that the enhanced nonlinearity and induced dispersion are of opposite sign. [86–88] While the sign of the enhanced nonlinearity is predetermined by the sign of the intrinsic nonlinearity, the sign of the induced dispersion is as previously shown in eqn. 6.7, determined by the sign of the normalized detuning from resonance. Figure 6.4 shows the frequency dependence of the lowest-order GVD $k''_{\mathrm{eff}}$ and enhanced nonlinearity $\gamma_{\mathrm{eff}}$ and also indicates the optimum detuning for soliton propagation.
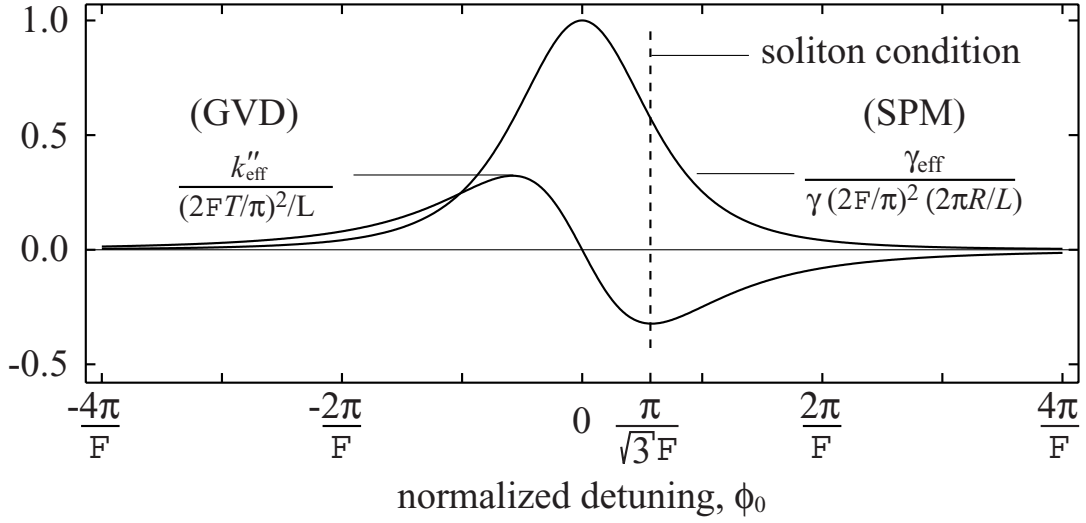
Figure 6.4: A SCISSOR soliton is created from a balance between resonator enhanced nonlinearity and resonator induced anomalous dispersion.

The fundamental soliton solution for this equation is [89]

$$A\left(z,t'\right) = A_0 \operatorname{sech}\left(t'/T_{\mathrm{P}}\right) e^{i\frac{1}{2}\gamma_{\mathrm{eff}}|A_0|^2 z}, \tag{6.12}$$

where the amplitude and pulsewidth are related according to $|A_0|^2 = |k''_{\mathrm{eff}}| \,/\, \gamma_{\mathrm{eff}}\, T_{\mathrm{P}}^2$, below which the pulse is severely distorted by all orders of dispersion. The finite response time of the resonator places a lower bound on the pulsewidth $T_{\mathrm{P}}$. A scaling factor $B$ is defined to be the ratio of the pulse bandwidth $\left(2\operatorname{arcsech}\left(1/\sqrt{2}\right)/\pi^2 T_{\mathrm{P}}\right)$ to the resonator bandwidth $(1/\mathcal{F}T_{\mathrm{R}})$, such that $B = \left(2\operatorname{arcsech}\left(1/\sqrt{2}\right)/\pi^2\right)\mathcal{F}T_{\mathrm{R}}/T_{\mathrm{P}}$. A nonlinear strength parameter, $\Gamma = (4/\pi^2)\,\mathcal{F}^2\gamma\,|A_0|^2 R$ is also defined. With these definitions, a simple relation

holds between $\Gamma$ and $B$ for the fundamental soliton operating at the anomalous dispersion peak:[4]

$$\Gamma = \frac{\pi}{2\sqrt{3}\operatorname{arcsech}^2\left(1/\sqrt{2}\right)}B^2 \approx B^2. \qquad (6.13)$$

Higher order dispersive and nonlinear terms become increasingly significant when either $B$ and/or $\Gamma$ approach unity.

To test the validity of this approximation I have conducted rigorous time domain simulations[5] in an attempt to propagate solitons. Figure 6.3 shows the pulse evolution of a low-power 10 picosecond FWHM hyperbolic secant pulse tuned for maximum anomalous GVD ($B = 0.13$) in an AlGaAs or chalcogenide glass-based system. The system consists of 100 resonators spaced by 10 $\mu$m each with a 5 $\mu$m diameter and finesse of $10\pi$. As can be seen, the temporal pulse profile is greatly dispersed. Figure 6.5 shows the pulse evolution for the same system, but with a peak power of 125 mW, corresponding to the fundamental SCISSOR soliton ($\Gamma = 0.0196$). As can be seen, the pulse shape is well preserved upon propagation. Many of the familiar characteristics of fundamental solitons such as robustness, reshaping, pulse compression, and pulse expansion have been

---

[4]The values of $k'_{\text{eff}}$ and $\gamma_{\text{eff}}$ are respectively lowered by factors of 3/4 and 9/16 from their given maximum values when operating at dispersion extremum points.

[5]The simulations used to study pulse evolution in a sequence of waveguide-coupled resonators were carried out using an iterative method in which each iteration consisted of linear & nonlinear phase accumulation during one round trip within the resonator followed by interference at the coupler. Traditional beam or pulse propagation split-step Fourier methods are unnecessary as *both* nonlinear phase accumulation *and* structural dispersion are more readily treated in the time domain. See appendix E for more a more detailed description of this method of simulation.
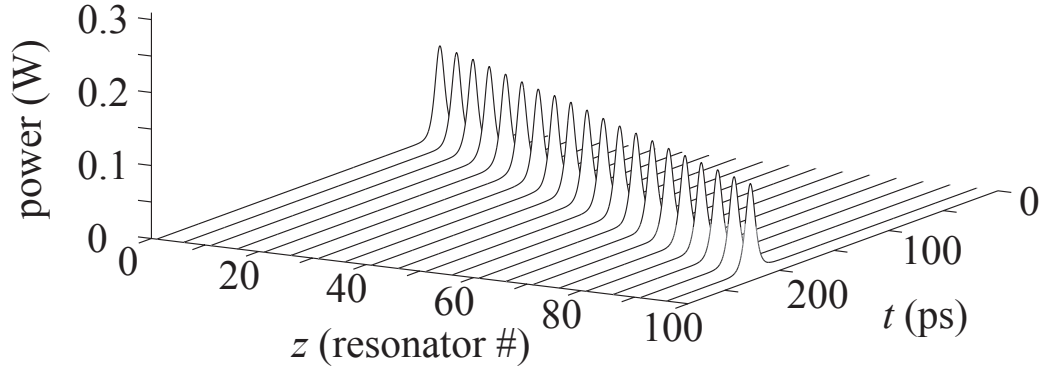
Figure 6.5: A pulse with amplitude corresponding to the fundamental soliton propagates in a SCISSOR without dispersing. The same parameters were used as in figure 4, but with a peak power of 125 mW ($\Gamma = 0.0196$) in a chalcogenide glass based system.

observed in simulations to carry over from the continuous-medium case. Higher-order solitons, satisfying $\Gamma \approx N_S^2 B^2$, where $N_S$ is an integer are readily observed in simulations, but are unstable because of higher-order dispersive nonlinear effects present in this system.[6]

Dark solitons which consist of an intensity dip in an otherwise uniform continuous-wave field can also be supported if the enhanced nonlinearity and induced dispersion are of the same sign (on the other side of resonance). The fundamental dark soliton possesses a hyperbolic tangent field distribution, [85]

$$A\left(z, t'\right) = A_0 \tanh\left(t'/T_P\right) e^{i\gamma_{\text{eff}}|A_0|^2 z}, \tag{6.14}$$

---

[6]Additionally, higher-order dispersive and/or nonlinear effects render the scattering of solitons to be inelastic. Under these conditions, the term *solitary wave* is more appropriate.
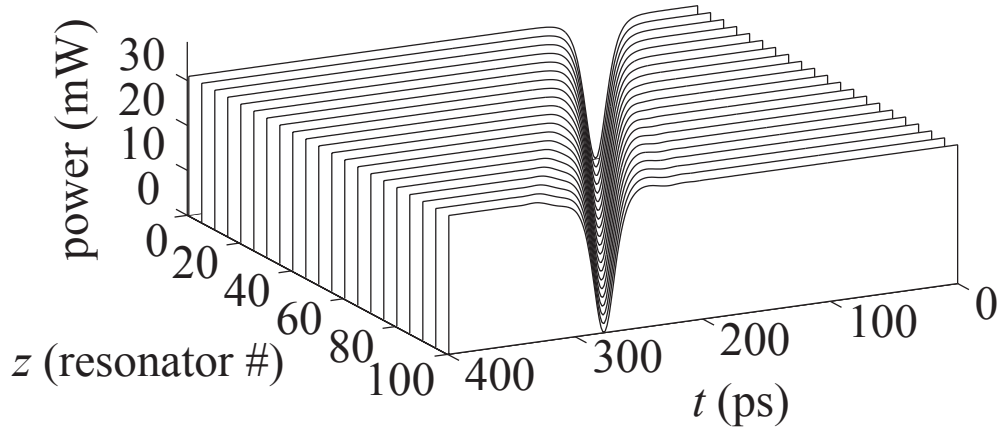
Figure 6.6: A negative pulse in a uniform intensity background with parameters corresponding to the fundamental dark soliton propagates in a SCISSOR without dispersing. The incident field distribution was a hyperbolic tangent with twice the pulse width of the bright soliton and a background power that was one fourth that of its peak power in figure 6.5.

Figure 6.6 shows the propagation of the fundamental dark SCISSOR soliton tuned to the normal dispersion peak.

## 6.3.2  Self-Steepening

In the previous section, frequency dependence of $\gamma_{\text{eff}}$ was neglected. One of the effects resulting from the frequency-dependent nature of $\gamma_{\text{eff}}$ is an intensity-dependent group velocity. This effect leads to the phenomenon of self-steepening (SS) of a pulse where the peak of a pulse travels slower than (+SS) or faster than (-SS) its wings. The self-steepening coefficient $s$ may be derived[7] from eqn. 6.10,

---

[7]So as to correctly expand eqn. 6.10, the $\mathcal{B}$ term must also be expanded which will generate more time derivative terms within the square brackets. Thus, the self-steepening contribution will not only consist of two $m = 2$ terms but also one $m = 1$ term. For terms such that $m > 1$,

but it is more readily obtained from the frequency derivative of the nonlinear coefficient:

$$s = \frac{\gamma'_{\text{eff}}}{\gamma_{\text{eff}}} = \frac{2}{\mathcal{B}}\frac{d\mathcal{B}}{d\omega} \underset{\phi_0=\pm\pi/\mathcal{F}\sqrt{3},r\approx1}{\longrightarrow} \mp\frac{\sqrt{3}\mathcal{F}T_{\text{R}}}{\pi}. \qquad (6.15)$$

While it is difficult to isolate this effect from induced GVD in a sequence of resonators to form a steepened pulse, it plays an important role in the breakup of higher-order solitons. The known phenomenon of soliton decay [85] involves the breakup of an $N_{\text{S}}$ order breathing soliton into $N_{\text{S}}$ fundamental solitons of differing pulse amplitudes and widths. Figure 6.7 shows a situation in which a second-order SCISSOR soliton with a launched peak power of 500 mW undergoes decay and splits into two stable fundamental SCISSOR solitons. The solitons are well isolated in time and uncorrupted by a background or pedestal. One of them possesses a higher peak power and narrower width than the original demonstrating the potential for pedestal-free optical pulse compression. The effects of induced self-steepening in a sequence of resonators can take place for picosecond and even nanosecond pulses because unlike in the case of intrinsic self-steepening, the relative strength of SS to SPM is not governed by how close the pulsewidth is to being a single optical cycle, $2\pi/\omega_0$ but rather how close the pulsewidth is to being a single cavity lifetime $\mathcal{F}T_{\text{R}}$. For the 10 picosecond pulse propagating in a SCISSOR with the above parameters, the non-dimensional self-

---

the time derivatives implicitly appear to the far left of each term when the square brackets are expanded.
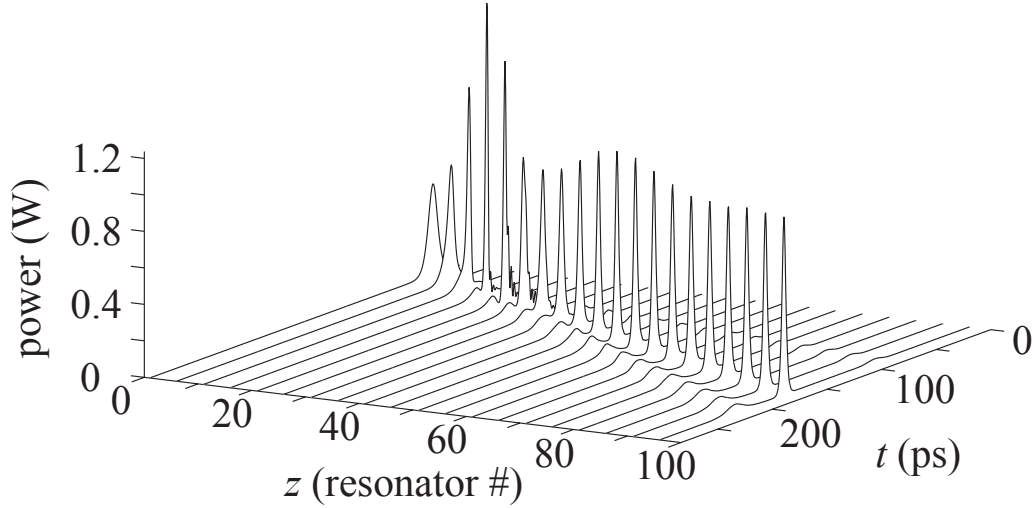
Figure 6.7: A higher-order breathing soliton is unstable under the influence the resonator-induced intensity-dependent group velocity (self-steepening). Here a second-order soliton splits into two stable fundamental solitons upon propagation in a SCISSOR. The incident field distribution was the same as in figure 6.5 but with four times the peak power.

steepening parameter $(s/T_{\mathrm{P}})$ is 0.173. In order to observe the same effect with traditional intrinsic self-steepening, a six cycle or 30 femtosecond pulse would be required.

## 6.3.3 Pulse Compression

More complicated interaction can exist between structural dispersion and enhanced self-phase modulation in a SCISSOR structure. The soliton order $N_S$, proportional to the injected amplitude, is a convenient measure of the relative strengths of the two processes. If the relative strengths of the processes are balanced $(N_S = 1)$, it was previously shown that soliton-like pulses may be prop-

agated. If however, the nonlinearity dominates the dispersion ($N_S > 1$), pulse compression can result. Because the enhanced nonlinearity and induced dispersion are each proportional to the finesse squared, [90] the soliton order for a SCISSOR can be set by simply choosing the ratio of the pulsewidth to the ring transit time ($T_R$),

$$N_S = \frac{8\pi}{3^{3/4}} \sqrt{\frac{n_2 I_0 R}{\lambda}} \frac{T_P}{T_R} \tag{6.16}$$

Figure 6.8 demonstrates the result of a simulation in which a 5 ps Fourier transform-limited pulse is injected into a 10 resonator SCISSOR tuned above resonance at the peak of anomalous dispersion. The injected $N_S = 5$ pulse fractures into multiple solitons of differing amplitudes along with some dispersing waves. The soliton with the largest amplitude emerges compressed by a factor of approximately five. It is worth noting that while this method can be used to compress a pulse on a very short distance scale, the amount of pulse compression is ultimately limited by the bandwidth of SCISSOR.

The process of temporal imaging is closely related to pulse compression. With temporal imaging, [91] intra-pulse structure can be preserved and magnified (or demagnified). An imaging condition must be satisfied in a setup which consists of an initial dispersive segment, an imposed quadratic phase and final dispersive segment of opposite sign to that of the initial. Owing to the large dispersive and nonlinear properties of microresonators, temporal imagers might be fabricated on an integrated photonic chip. Each of the three sections might be composed of

differently tuned SCISSOR elements. Sign selection of the dispersive segments is easily accomplished in SCISSORs tuned below (normally dispersive) or above (anomalously dispersive) resonances. The quadratic phase chirp providing the temporal lensing may be accomplished by cross-phase modulation imposed chirp enhanced in a resonant SCISSOR.

### 6.3.4 Saturation

Equation 6.9 was implicitly derived with the assumption of low intensity. Next, the intensity dependence of $\gamma_{\text{eff}}$ is examined. It is found that the circulating intensity and $\gamma_{\text{eff}}$ are in fact interdependent. The circulating intensity depends on the build-up factor, which in turn depends on the circulating intensity from the nonlinear detuning contribution. As a result nonlinear resonators can possess memory and multistable branches in the input-output relationships within certain operating regimes. [92,93] When operated near resonance, the onset of multistability occurs when the circulating power is high enough to generate a single-pass nonlinear phase shift of $2\pi$ radians. Saturation resulting from intensity-dependent detuning pulling the resonator off resonance generally takes place well before this effect. Working on the lower branch of the multistable relation for positive detunings, the saturation of the effective nonlinear propagation constant is well fitted
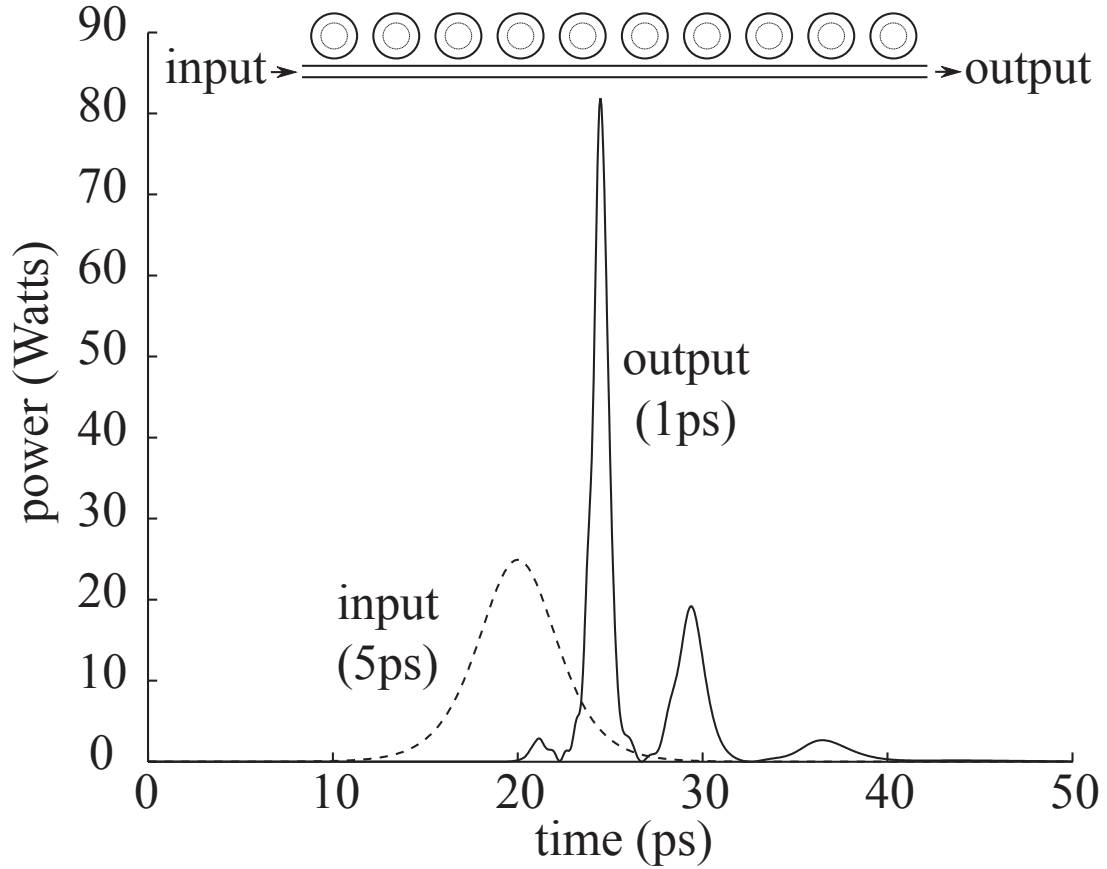
Figure 6.8: A highly compact microresonator-based 5X pulse compressor. A 25 Watt transform-limited input pulse ($N_S = 5$) of 5 ps width is compressed to 1 ps. In the process, some energy is shed in the form of other non-dispersing pulses which walk away from each other linearly in time owing to an intensity-dependent group velocity. These extra pulses might be eliminated through use of a saturable absorbing material which may even be microresonator-based. Here, 10 AlGaAs or chalcogenide-based microresonators of 10 $\mu$m diameter form a SCISSOR. The resonators possess a finesse of $5\pi$, coherent intensity build-up of 10, and nonlinear enhancement of 100.

by a $(1 + I/I_s)^{-1}$ type of saturation model which is given explicitly as

$$\gamma_{\text{eff}} \xrightarrow[r \approx 1]{} \frac{\gamma \frac{2\pi R}{L} \mathcal{B}_{\phi_0}^2}{1 + \frac{\gamma 2\pi R \mathcal{B}_{\phi_0}^2}{2\pi - \Phi_0} |A|^2} \tag{6.17}$$

where the saturating intensity near resonance is $|A_{\text{S}}|^2 = \pi / \gamma_{\text{eff}} L$. The saturating intensity is lower for higher detunings from resonance. A generalized nonlinear Schrödinger equation incorporating every effect discussed so far takes the following form:

$$\frac{\partial}{\partial z} A + k'_{\text{eff}} \frac{\partial}{\partial t} A = -i \frac{1}{2} k''_{\text{eff}} \frac{\partial^2}{\partial t^2} A + \frac{1}{6} k'''_{\text{eff}} \frac{\partial^3}{\partial t^3} A + i \left( 1 + i s \frac{\partial}{\partial t} \right) \frac{\gamma_{\text{eff}} |A|^2}{1 + \frac{|A|^2}{|A_{\text{S}}|^2}} A. \tag{6.18}$$

### 6.3.5 Nonlinear Frequency Mixing

The characteristics of frequency mixing processes such as harmonic generation and four-wave mixing can also be enhanced via waveguide-coupled resonators. As a general rule, the scaling of the enhancement of these processes can be inferred by including contributions from each intensity involved (lying within a resonance) and the interaction length. Each contributes a factor proportional to the finesse.

Four-wave mixing is a third-order nonlinear process that annihilates two photons at one frequency and generates two photons at a higher and lower frequency. Four-wave mixing can give rise to modulation instability whereby a low contrast amplitude ripple grows via the amplification of sidebands at the expense of the

central frequency.   Appendix F describes this coupling in detail.   In a disper-

sive medium, four-wave mixing is stifled due to phase mismatch.   However, in

an anomalous dispersive medium positive self-phase modulation generates new

frequency components that compensate for the mismatch. [64]   If the process

is allowed to continue, the modulation depth increases until a train of solitons

stabilizes.   Figure 6.9 shows the increase in modulation depth for a seeded 1%

amplitude ripple of 100 GHz with propagation distance for a sequence of 60 res-

onators. [90]   The peak of the effective instability gain, $g_{\mathrm{m}} = 2\gamma_{\mathrm{eff}} |A_0|^2$ occurs at

some modulation frequency

$$\Omega_{\mathrm{m}} = \pm\sqrt{2\gamma_{\mathrm{eff}} |A_0|^2 / |k''_{\mathrm{eff}}|} \tag{6.19}$$

provided that this value does not exceed the resonance bandwidth.   The gain is

enhanced by the square of the finesse.

Up until this point, attention has been restricted to pulses whose bandwidth

is of the order or less than that of a single resonance peak.   By co-propagating

pulses with carrier frequencies lying within differing resonance peaks, four-wave

mixing processes can be enhanced with frequency separations of pump and signal

equal to an integer number of free-spectral ranges.   Because the efficiency of idler

generation depends on the pump intensity, signal intensity, and grows quadrati-

cally with length, the efficiency scales as the fourth power of the finesse. [94]   I

expect such effects to be important in systems that have low intrinsic dispersion
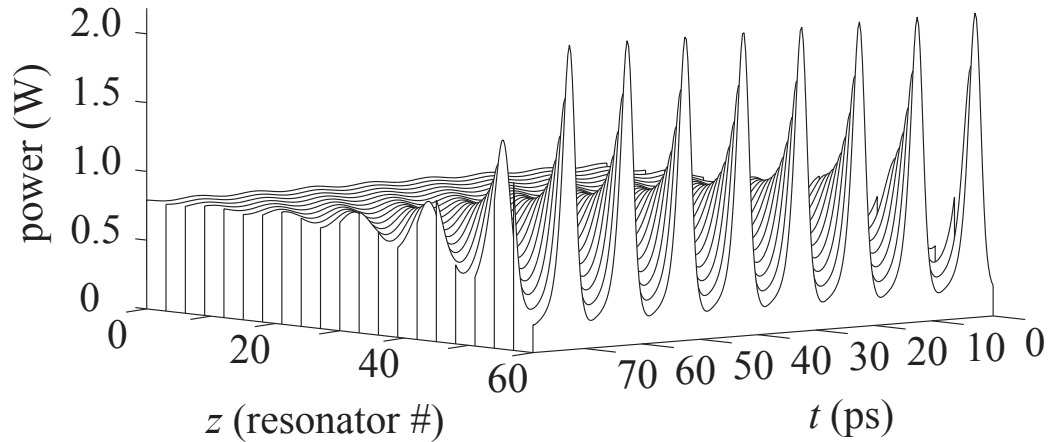
Figure 6.9: Demonstration of modulation instability in a SCISSOR. The input field consists of 800 mW of cw power with a 1% power ripple. The SCISSOR parameters have been chosen such that the peak of the instability gain is at the input modulation frequency of 100 GHz. Note that the modulation frequency given by eqn. 6.19 need not be a resonance frequency of the structure.

such that the FSR is independent of frequency so that the three enhancement linewidths coincide with signal, pump, and idler frequencies. Finally, the efficiency of harmonic generation processes may be increased. [95] The efficiency of second harmonic generation (SHG) for example would be enhanced cubically with the finesse.

## 6.4  Depth of Phase

Within a free spectral range, a *single* resonator can impart only a maximum phase depth of $2\pi$ radians. This limitation has important implications for the maximum delay, chirp, and a nonlinear phase that can be imposed on a pulse per resonator. As the imparted phase nears only $\pi/2$ radians, higher order effects

become increasingly significant such that the system can no longer be treated perturbatively. The extent of group velocity reduction that can be achieved in a SCISSOR is limited by how high the finesse can be made. A SCISSOR with an ultra-high value of finesse can be used to slow a pulse appreciably but that pulse must be long enough such that it is at least of the order of the finesse times the transit time of a single resonator. Thus, the maximum delay per resonator is fixed and equal to one pulse width at best. The same is true for the induced group velocity dispersion. A high GVD coefficient (proportional to $\mathcal{F}^2$) can be obtained by making the finesse very large. However, the increasing finesse places an increasing restriction on the pulse bandwidth $\Delta\omega$ (proportional to $1/\mathcal{F}$). As a result, the imposed spectral chirp per resonator, $1/2\ k''_{\mathrm{eff}}\Delta\omega^2 L$ is independent of finesse and only dependent on the scaling factor $B$. If the requirement is to broaden a pulse by $N$ pulse widths then the minimum number of resonators needed (occurring at $B \sim 1$) is roughly $N$. This is an important point: an ultra-high finesse is not required for designing dispersive devices based on resonators. However, while reducing the resonator size and increasing the finesse in inverse proportion maintains the same resonator bandwidth and thus the same linear properties, the nonlinear properties are enhanced. This is of fundamental importance since a low threshold power and small number of resonators is desirable practically. As a result of saturation, it is very difficult to achieve an effective nonlinear phase shift of $\pi$ radians from a single resonator when operating on

resonance. It is achieved only in the limit as the resonator's internal phase shift is power-detuned completely by $\pi$ radians resulting in an external phase shift of $\pi$ radians as well. As a result of this saturation, one completely loses the advantage of resonant enhancement. Achieving a phase shift of $\pi/2$ is however much easier to attain before the saturation takes place and requires a power-detuning of only $\phi = \pi/\mathcal{F}$. A nonlinear external phase shift of $\pi$ may be readily obtained from a single resonator taking advantage of enhancement by ensuring that the resonator is initially red-detuned by $\pi/\mathcal{F}$ and allowing the resonator to be power-detuned though resonance for a total value of $\pi$ radians.

## 6.5 Attenuation

Attenuation in microresonators is in general detrimental. Internal attenuation reduces the net transmission, build-up, and (in general) the nonlinear response. It also broadens the resonance limiting the achievable finesse. Attenuation in microresonators typically arises from three mechanisms: intrinsic absorption, radiation loss, [96,97] and scattering. Intrinsic absorption can typically be rendered insignificant over millimeter-sized propagation distances by choosing an appropriate material system at a given wavelength. Additionally, since the circulating intensity can greatly exceed the incident intensity, intensity-dependent absorption processes such as two-photon absorption may be significant in resonators. Two-photon absorption may be minimized by proper selection of a

material with a bandgap that is greater than twice the incident photon energy. [68,77] Whispering-gallery modes of a disk and modes of a ring waveguide suffer from bending or radiation loss which is increasingly important for small resonators with low refractive index contrast. Scattering can take place in the bulk or on the edges. Edge scattering is typically the dominant loss mechanism which results from roughness on the microresonator edges which in practice cannot be made perfectly smooth. [98] The surface perturbations phase-match the guided mode to radiating modes outside the disk structure [99] or into the contra-directional mode. [100] In the planar waveguide approximation, the attenuation constant associated with scattering loss is derived as: [101]

$$\alpha_{\text{scatt}} = \sigma^2 \left( n_{1,\text{eff}}^2 - n_{2,\text{eff}}^2 \right) k_0^2 \frac{k_x}{k_z} \left( E_{(x=-d/2)}^2 + E_{(x=+d/2)}^2 \right) \qquad (6.20)$$

Where $\sigma$ is the RMS edge roughness. Applying this result to a disk or ring results in the expression [102]

$$\alpha_{\text{scatt}} = \sigma^2 \left( n_{1,\text{eff}}^2 - n_{2,\text{eff}}^2 \right) k_0^2 \frac{k_{x,\text{eff}}}{k_{z,\text{eff}}} \left( E_{(r=R_1)}^2 + E_{(r=R_2)}^2 \right). \qquad (6.21)$$

Because the strength of the scattering loss coefficient increases with the square of the refractive index difference it can be expected that high-contrast ring and disk microresonators will possess high scattering losses. Figure 6.10(a) shows a finite-difference time domain (FDTD) [103] simulation of a 5 resonator SCISSOR
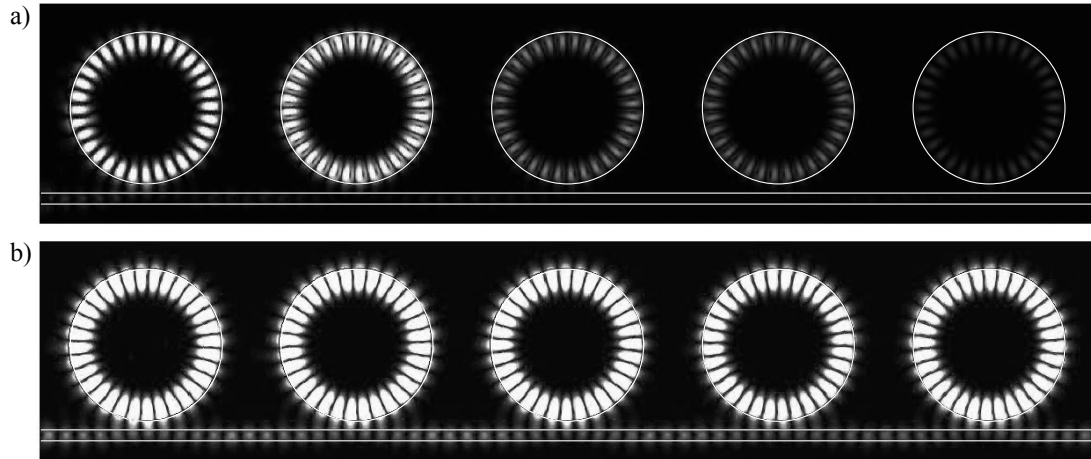
Figure 6.10:  Finite-difference time-domain (FDTD) method of solving Maxwell's equations for a SCISSOR structure composed of 5 microresonators. A TE field of wavelength 1.55 microns is launched into the 0.4 micron wide waveguide evanescently side-coupled to a disk with diameter of 5.1 microns. The refractive index of the air-clad disk and guide is 2. Exclusive coupling to the m=16 azimuthal whispering gallery mode (WGM) is achieved by careful selection of parameters.  In (a), strong scattering losses result due to roughness associated with a 50 nm grid.  In (b), scattering losses are made negligible by using a 30 nm grid.  Consequently, a build-up factor of 16 and finesse of 25 are achieved in this structure.

with 50 nm sidewall roughness displaying strong scattering losses and weak circulating intensity.  In figure 6.10(b), a lower sidewall roughness of 30 nm results in negligible scattering loss and strong intensity build-up.

Resonators have the ability to modify and in some cases enhance certain figures of merit (FOM).  A common FOM is the ratio of the nonlinear coefficient to the linear absorption.  While the nonlinear coefficient is quadratically dependent on the finesse, the linear absorption, much like the group velocity reduction exhibits only a linear proportionality.  As a result, the FOM is enhanced proportional to the finesse.  Gain may be implemented where possible to combat attenuation.

More interestingly, a dispersion decreasing system may be used to propagate a SCISSOR soliton in an attenuating structure. In this case, the pulsewidth is kept constant as the amplitude decreases via an exponential decrease in dispersion down the length of the structure. In general however, low-loss propagation through a SCISSOR constructed from $N$ resonators can be ensured if the single pass attenuation satisfies $\alpha 2\pi R << 1/N\mathcal{F}$.

## 6.6 Slow and Fast Light

In recent years there has been a flurry of activity aimed at the development of techniques that can lead to a significant modification of the group velocity of propagation of a light pulse through a material medium. [104] Proposed applications of these procedures include the development of optical delay lines [105] and the "storage" of light pulses [106,107] with possible applications in optical communications and quantum information. Most of this research has made use of the response of resonant media [108] and much of it has made use of the concept of electromagnetically induced transparency. [106,109]

### 6.6.1 Slow Light

Many properties of the SCISSOR system are in fact analogous to those found in atomic systems. In both cases, light is coupled into and out of discrete resonators without loss or dispersion, but with delay. It is known from studies of

slow light propagation in atomic systems displaying electromagnetically induced transparency (EIT) that the width of the induced transparency window in atomic systems with $N$ interacting atoms is reduced by a factor which scales as $1/\sqrt{N}$. [110] This fundamental limitation on bandwidth results from the fact that near the frequency of maximum transmission, the transmission decreases quadratically with detuning. Such a limitation is absent in a fully transmissive SCISSOR geometry used to propagate solitons, but a fundamental limitation is ultimately imposed by fourth-order dispersion. This point is next examined in detail.

The effective group index associated with a SCISSOR takes on its maximum value when the optical wave is tuned to a cavity resonance ($\phi = 0$), and can be expressed in any of the forms

$$n_g = n \left( 1 + \frac{2\pi R}{L} \frac{1+r}{1-r} \right) = n \left( 1 + \frac{2\pi R}{L} \mathcal{B}_0 \right) = n \left( 1 + \frac{4R}{L} \mathcal{F} \right) \qquad (6.22)$$

While the steep slope of the dispersion-relation curve near resonance is responsible for the reduced group velocity, the transition from the flat sections of the dispersion curve to the steep section is necessarily curved and introduces group velocity dispersion (GVD). On resonance, the lowest-order GVD parameter $k''_{\text{eff}}$ (and all other even orders) was previously shown to be zero. However, the distance over which pulses can propagate is limited ultimately by broadening induced by third-order dispersion. It is better to propagate off resonance and sacrifice some enhancement in order to gain much in terms of the maximum possible prop-

agation distance. Specifically, by tuning slightly above resonance ($\phi_0 = \pi/\mathcal{F}\sqrt{3}$) third-order dispersion can be eliminated. The lowest-order dispersion that is introduced by operating off resonance can be compensated for by the enhanced nonlinear response of the structure. The negative, lowest-order GVD occurring at this operating point can be precisely balanced by the nonlinearity to form a SCISSOR soliton. In the following paragraphs this conjecture will be proven.

An all-pass resonator is inherently a phase-only filter and possesses a field amplitude transmission function that is a pure phasor, which can be expanded at resonance about $\phi_0 = 0$:

$$e^{i\Phi} = e^{i\left[\Phi_0 + \frac{d\Phi}{d\phi}\phi + \frac{1}{2}\frac{d^2\Phi}{d\phi^2}\phi^2 + \frac{1}{6}\frac{d^3\Phi}{d\phi^3}\phi^3 + ...\right]} \qquad (6.23)$$

On resonance, the delay associated with the resonator is given by the value of the first normalized frequency derivative term ($T_{\mathrm{D}} = \frac{2}{\pi}\mathcal{F}T_{\mathrm{R}}$). Because there is no amplitude filtering function associated with the operation of this device, the normalized bandwidth is determined by the phase error induced by higher-order dispersive terms. On resonance, the even-order terms such as the group-delay dispersion vanish and the next non-zero higher-order limiting term is third-order dispersion. The dominant phase error on resonance is thus:

$$|\Phi_{\mathrm{error}}| = \left|\frac{1}{6}\frac{d^3\Phi}{d\phi^3}\phi^3 = \frac{1}{6}\frac{1}{2}\left(\frac{2}{\pi}\mathcal{F}\right)^3\phi^3\right|. \qquad (6.24)$$

Assuming that phase error of 1 radian is the maximum tolerable error, the usable bandwidth is restricted to $\Delta\nu = \left(\frac{3}{2}\right)^{1/3} \frac{1}{\mathcal{F}T_{\mathrm{R}}} \approx \frac{1}{\mathcal{F}T_{\mathrm{R}}}$. A SCISSOR, composed of a sequence of $N$ all-pass resonators possesses an effective phase shift equal to the single device phase shift multiplied by $N$. It follows that the net accumulated delay for such a system is simply equal to $N$ times the single-device delay. Fortunately, the net accumulated phase errors do not scale in the same fashion. That is, the phase-error limitation on usable bandwidth (governed on resonance by third-order dispersion) is not simply inversely proportional to $N$, but rather as $\Delta\nu/\sqrt[3]{N}$. As discussed previously, soliton propagation at the maximally dispersive frequency allows for the cancellation of group velocity dispersion and the elimination of third-order dispersion. This leaves fourth-order dispersion as the limiting phase error. The dominant phase error in this regime is thus

$$|\Phi_{\mathrm{error}}| = \left| \frac{1}{24} \left| \frac{d^4\Phi}{d\phi^4} \right|_{\phi_D} \phi^4 = \frac{1}{24} \left( \frac{27\sqrt{3}}{128} \right) \left( \frac{2}{\pi}\mathcal{F} \right)^4 \phi^4 \right| \qquad (6.25)$$

with a similar bandwidth restriction of $\Delta\nu = \left( \frac{2^4}{3^5} \right)^{1/8} \left( \frac{1}{\mathcal{F}T_{\mathrm{R}}} \right) \approx \frac{1}{\mathcal{F}T_{\mathrm{R}}}$ for a single resonator. It is easily shown that a less restricting scaling law of $\Delta\nu/\sqrt[4]{N}$ applies to propagation in the SCISSOR soliton regime.

Next, the analysis derived in the previous paragraph is tested via rigorous simulations. Figure 6.11 compares three approaches to attempting to propagate slow light in a SCISSOR with a group velocity of approximately c/(100 n). In

Fig. 6.11(a), a weak 100 ps pulse tuned to resonance is greatly delayed, but broadens and acquires ripples associated with negative third-order dispersion. In Fig. 6.11(b), the pulse frequency is tuned above resonance to the extremum of the lowest-order GVD. At this frequency, the third-order GVD necessarily vanishes, and pulse distortion of the sort shown in part (a) is noticeably decreased. However, the pulse broadens considerably as a result of non-vanishing second-order (lowest-order) dispersion. In Fig. 6.11(c), the same pulse but with a peak power corresponding to that of the fundamental SCISSOR soliton is seen to propagate with a preserved pulse shape. The group velocity reduction in this case is 75X as opposed to 100X in part (a), but the high fidelity of pulse propagation makes this strategy appear to be superior.

A sequence of resonators might someday be useful in studying the properties of slow light in the regime where acoustic and optical group velocities are of the same order of magnitude. [111,112] However, in order to slow the group propagation to this level in silica, a high finesse of about $10^5$ is required.

## 6.6.2 Tunable Optical Delay Lines

Because the group delay can in practice be controlled by detuning resonators thermally, [113] electro-optically, by carrier injection, [114] electroabsorption, [115] or other means, tunable optical delay lines may be constructed from microresonators. The net group delay, $T_D$ in a SCISSOR increases linearly with the number of res-
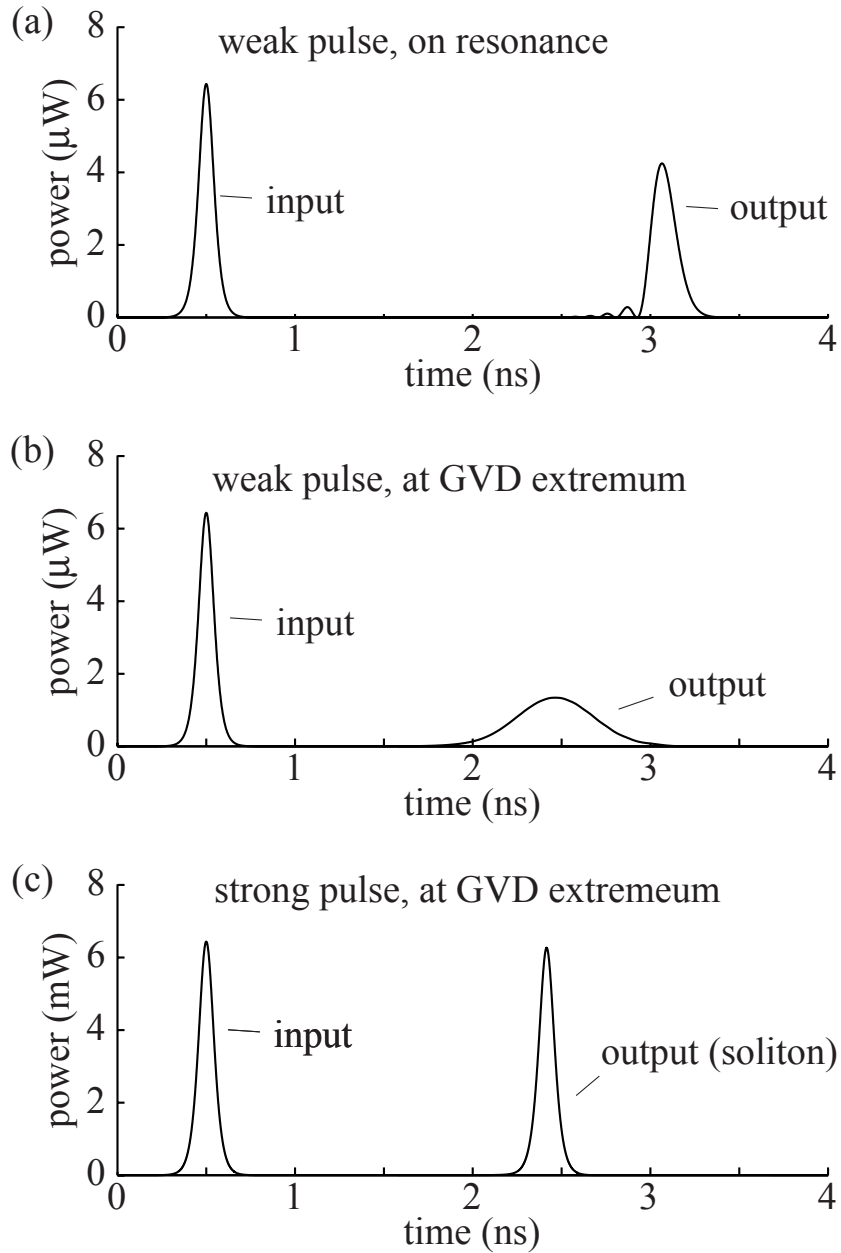
Figure 6.11: Numerical results showing the advantage of using optical nonlinearity on the propagation of slow light through a SCISSOR structure. The SCISSOR consists of 100 10$mum$ diameter resonators spaced by $10\pi\mu$m with $r = .98$ corresponding to a group velocity reduction of 100X. a) A weak 100 ps resonant pulse propagates at a group velocity of $(c/n)/100$ through the SCISSOR and is corrupted by resonator induced third-order dispersion. b) The same pulse, but with carrier frequency tuned to the anomalous GVD maximum propagates with a group velocity of $(c/n)/75$ but is greatly broadened. c) A 6.4 mW peak power, 100 ps pulse tuned to the anomalous GVD maximum propagates as the fundamental SCISSOR soliton with a group velocity of $(c/n)/75$ and is well preserved. Here, parameters typical of a GaAs or chalcogenide-glass based waveguiding structure, $(\gamma/A_{\text{eff}} = 60m^-1W^-1)$ were employed.

onators,

$$T_{\mathrm{D}} = N\frac{d\Phi}{d\omega}. \tag{6.26}$$

The net group delay is inversely proportional to the average group velocity which can be minimized by coupling the resonators in a manner that yields the maximum possible finesse. Under this condition, however, the bandwidth may be severely restricted. For example, reducing the group velocity in a SCISSOR by 6 orders of magnitude results in a bandwidth of less than 10 MHz for 10 $\mu$m diameter resonators. As a result, designing a SCISSOR for the minimum attainable group velocity (in practice limited by attenuation) is not desirable. The fractional group delay, defined as the group delay normalized to one pulsewidth $T_{\mathrm{P}}$ is a convenient figure of merit characterizing a resonator-based delay line. A fractional group delay near unity corresponds to a delay by one pulsewidth. This is the greatest delay that can be achieved in a single resonator without the introduction of higher-order dispersive effects. These higher-order dispersive effects result from frequency content in the spectral wings experiencing a lower delay. Fractional group delays greater than unity can be obtained by use of more resonators. However, dispersive effects accumulate and eventually severely distort pulses. For a desired net fractional delay, these phase errors might be reduced by relaxing the fractional delay per resonator and increasing the number of resonators. Alternatively, the phase errors might be corrected by some means of dispersion compensation, thereby increasing the system complexity. In princi-

ple, there is an advantage to using nonlinear soliton propagation in a SCISSOR.
Figure 6.12 displays the results of a simulation of a tunable delay line based on
a SCISSOR. Eight bits of a 160 Gb/s pulse train are delayed by 1 and 4 bit-
slots. For simplicity, the delay associated with propagation in the side-coupling
waveguide is removed. In (a) six resonators are sufficient to delay the pulse-train
by a single bit-slot while suffering minor third-order phase distortion. In (b) a
four bit-slot delay is achieved via the use of 26 resonators but the pulses emerge
greatly dispersed. By tuning the resonator and pulse energy to parameters near
the SCISSOR soliton for the structure, pulse fidelity can be improved as demon-
strated in (c). Note that a delay of 4 bit-slots corresponds to a fractional delay
of 12 for the duty cycle of 1/3 employed. For comparison, the same pulse train is
sent through the SCISSORs with the resonators tuned far away from resonance.
The delay accumulated either for weak or strong pulses in the off-resonance state
where pulses effectively bypass the resonators is negligible. This demonstrates
the possibility for tunable delay. Most importantly, this simulation demonstrates
that a unit fractional delay does not require an ultra-high finesse, but rather is
achieved when the pulse bandwidth is of the order of the resonator bandwidth.
In order that sequences of resonators forming the SCISSOR overlap in their delay
bandwidths, their effective optical circumferences must be made reproducibly to
within the wavelength divided by the finesse. If the reproducibility does not

conform to this standard, a Doppler-like broadening of the Lorentzian resonance linewidths will result in lowered group delay and broader bandwidth.

### 6.6.3  Fast Light

Lossy resonators forming a SCISSOR structure can be implemented to propagate light superluminally. [116]  If the coupling strength is chosen to be weaker than the round trip loss, the resonator is said to be undercoupled.  The dispersion relation for the SCISSOR in this regime is qualitatively different from that found in the overcoupled regime.  Figure 6.13 (a) displays the transmission for a single resonator in the three regimes.  In addition, figure 6.13 (b) displays the resonator contribution to the dispersion relation for all three regimes and displays the reversal of sign near resonance.  This negative slope implies that a pulse exiting from a resonator will emerge with its center advanced in time with respect to the incident pulse.  Causality is maintained because the discrete impulse response of the resonator does not possess any advanced impulses.  A pulse displays superluminal propagation but quickly attenuates in a multi-resonator undercoupled SCISSOR.  Gain (assumed flat across the pulse bandwidth) may be incorporated into the straight waveguide to offset the losses associated with the undercoupled configuration.  The group index near resonance in the undercoupled regime is given by [117]

$$n_g = n \left( 1 - \frac{2\pi R}{L} \frac{a(1 - r^2)}{(r - a)(1 - ra)} \right) \tag{6.27}$$
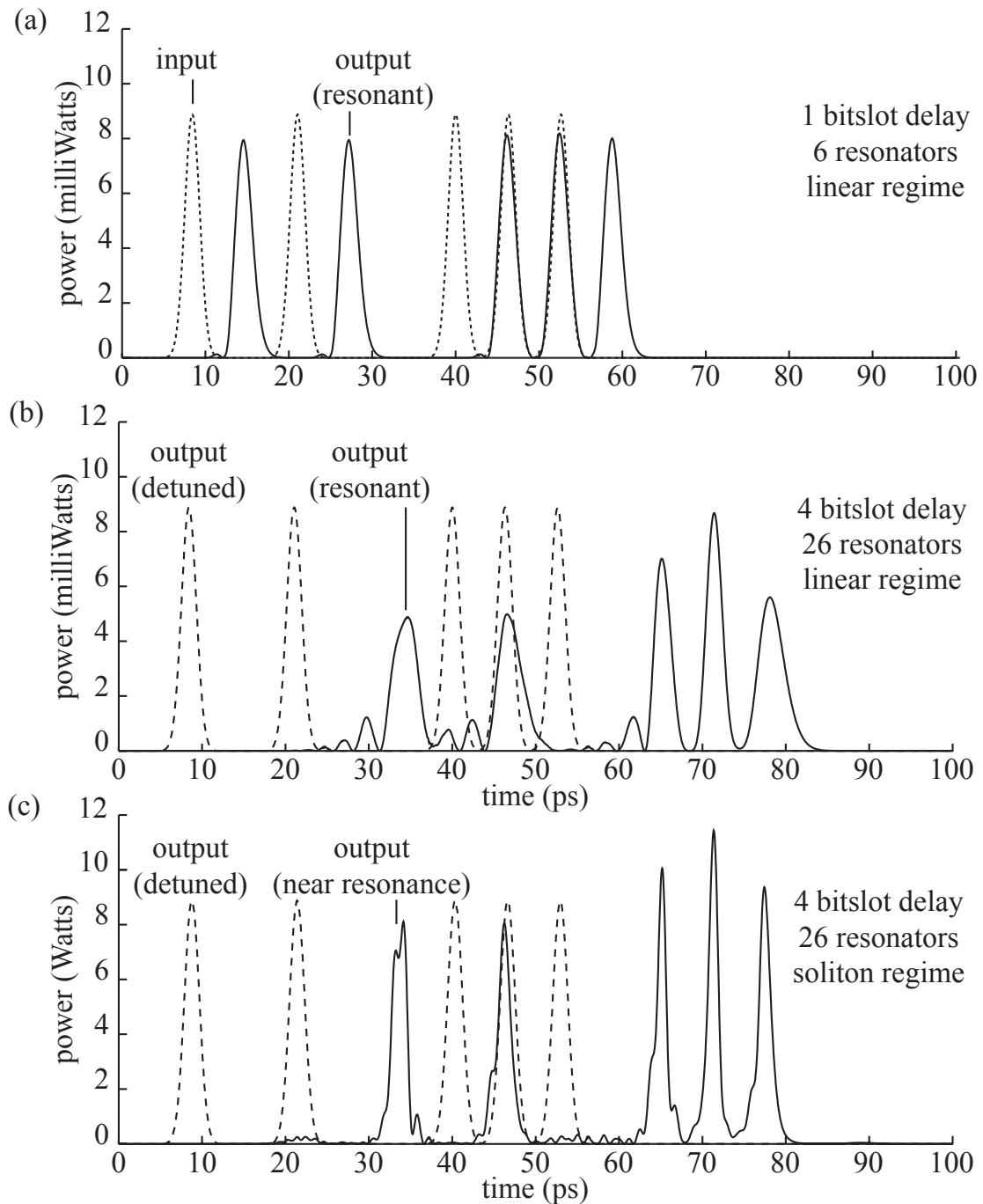
Figure 6.12: A microresonator-based tunable delay line.  Shown are 8 bits of a 160 Gb/s (duty cycle=1/3) pulse train.  In (a) 6 resonators achieve a delay of a single bit-slot with some minor distortion resulting from third-order dispersion.  In (b) 26 resonators achieve a delay of 4 bit-slots though with increased distortion.  In (c) propagation near parameters associated with a SCISSOR soliton results in noticeably less distortion.  Also shown in (b) and (c) are the same pulse trains when the resonator is detuned.  In all cases, a finesse of $10\pi$ and 4 $\mu$m diameters are used.  The bit sequence is 10100111.

where $a = e^{-\alpha\pi R}$. Figure 6.13 (c) demonstrates superluminal propagation of a linear, resonant pulse through undercoupled resonators situated near an amplifying waveguide. The exiting pulse experiences a negative time delay or, equivalently, a time advance. Moreover, the theory also predicts superluminal propagation for a SCISSOR in which each resonator is constructed of an amplifying medium in which the round trip gain is greater than the coupling strength[8]; however, our numerical simulations suggest that propagation is highly unstable in this regime.

## 6.7 Generalized Periodic Resonator Systems

Attention is now turned to comparing and contrasting the geometry and propagation characteristics of periodic SCISSORs with that of other well-known systems in optical physics which possess photonic band-gaps. In certain respects, the SCISSOR soliton is analogous to gap, [118] Bragg, [119] and discrete solitons [120] which result from nonlinear pulse propagation within or near the photonic band-gap [121] of a distributed feedback structure. The SCISSOR structure itself bears some similarity to a coupled resonator optical waveguide (CROW) [122] which consists of a multi-dimensional array of inter-coupled resonators and no side-coupled waveguide. Many other photonic crystal systems possess similar phase [123] and intensity enhancing properties [124–126] but in general possess band-gaps. Because each constituent resonator of a SCISSOR is an all-pass filter,

---

[8]this occurs in the equivalent undercoupled regime accompanying gain
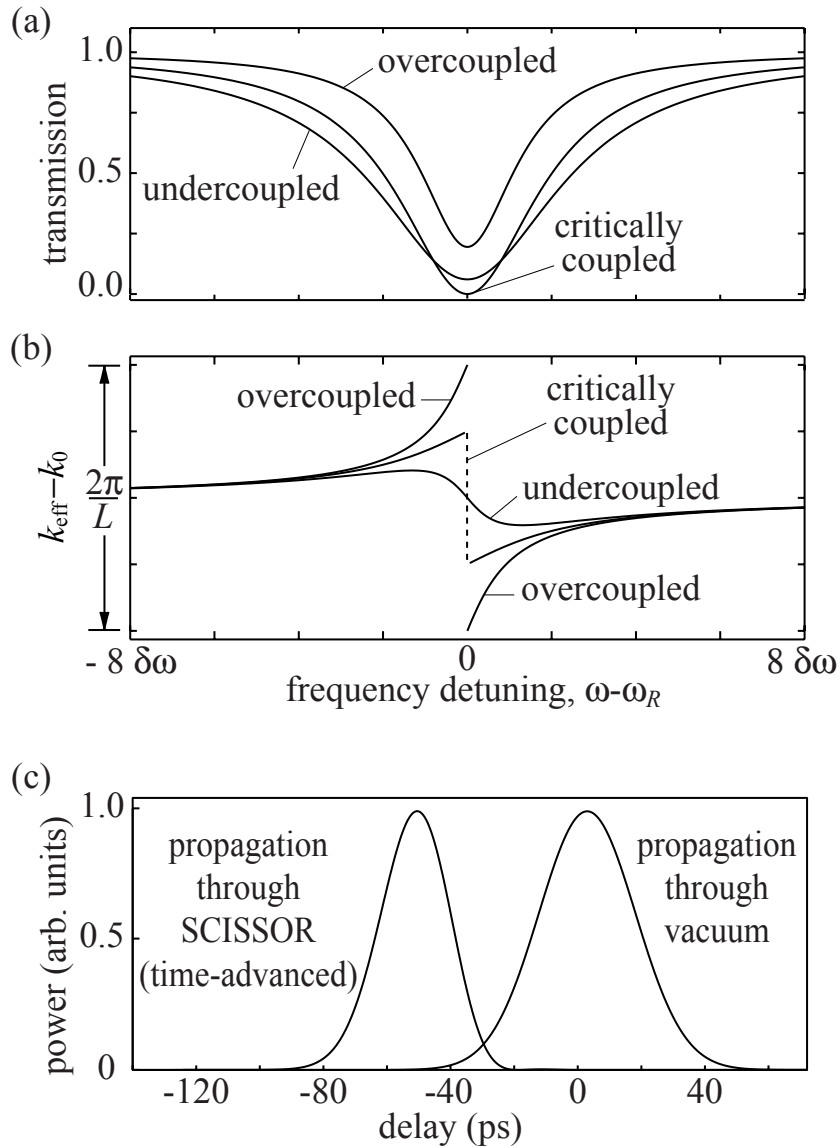
Figure 6.13: a) The transmission for a single resonator with $r = .9$ in the overcoupled ($a = .96$), critically coupled ($a = .9$), and undercoupled ($a = .84$) regimes. b) The dispersion relation for the same three cases. Note the change in the sign of the slope of the curve near resonance in the undercoupled case. In the critically coupled case, the curve undergoes a $\pi/L$ phase jump (where the transmission is zero) while in the overcoupled case, the second half of curve has been cut and displaced down by $2\pi/L$ for generality. The frequency units of $\delta\omega$ correspond to the nonattenuating resonance bandwidth. c) Numerical simulation demonstrating superluminal propagation of 36 ps pulses through a SCISSOR structure composed of 20 lossy undercoupled resonators with $10mum$ diameter, spaced by $10\pi$ $\mu$m. Gain has been added to the straight waveguide section to maintain pulse power.

feedback is present within each resonator but not amongst resonators. Alternatively, there is no intended mechanism for light to couple into the counterpropagating modes of the microresonator or guide[9]. As a result, there is no frequency at which light is restricted from propagating and thus the structure cannot possess a photonic band-gap (PBG). Nevertheless, the SCISSOR structure displays enhanced nonlinear optical response for much the same reason that a PBG structure can produce enhanced nonlinearity. Because of this, it is not necessary for the resonators to be periodically spaced: only the average density over a total interaction length (or net number) of resonators is important. The addition of a second guide on the other side of the resonator array; however, opens up the possibility for inter-resonator feedback and the existence of a photonic band-gap. This type of structure is interesting in its own right [128] and the propagation characteristics of this structure will be examined later in this section.

Microresonators can be connected to form sequences in a variety of ways. [129] The simplest way is simply to situated them close enough such that the evanescent fields circulating within them couple resonator to resonator directly. This structure is a one-dimensional coupled-resonator optical waveguide (CROW). [122,130] Another way to connect them is indirectly through a common waveguide as in a single-channel SCISSOR. Variants of the SCISSOR structure may include two

---

[9]Counterpropagating waves in a ring resonator can be coupled either via surface roughness or simply via a small perturbation such as a notch. When side coupled to a guide such a notched resonator can approximate a general second-order Chebyschev reflection response. This is because a single notched ring with one guide is equivalent to two coupled rings between two guides [79,127]

common coupling waveguides and/or more than one resonators connecting them.

This section will focus on these four archetypal geometries constructed from ring

or disk resonators. This set of four geometries may be considered to consist of

all the unique permutations by which a Fabry-Perot resonator may be connected

to form sequences of resonators. Figure 6.14 depicts these four configurations.

While in principle, actual Fabry-Perots could be combined to construct function-

ally equivalent devices, they can be quite clumsy to string together in sequences.

Ring or disk resonators have properties which are more naturally suited to some

sequencing geometries and are more readily integrated in practice.

Up to this point, the frequency analysis of sequenced all-pass resonators was

straightforward because of the serial non-feedback nature of the transmission.

That is, after the fields leave a resonator, they never return to it. Phase accu-

mulation is thus simply cumulative. In the case of a double-channel SCISSOR or

CROW which possess feedback amongst resonators, a different formalism must be

developed. The matrix formalism used to analyze photonic band-gap structures

based on Bloch's theorem is adopted with the assumption that the resonator se-

quences are infinite and periodic. Appendix G describes in detail the method used

to derive the dispersion relations for arbitrary one dimensional periodic structures

which include resonators. Using this formalism, the dispersion relations for the

four archetypal sequenced-resonator geometries are readily derived. Each will be

analyzed in the following subsections.
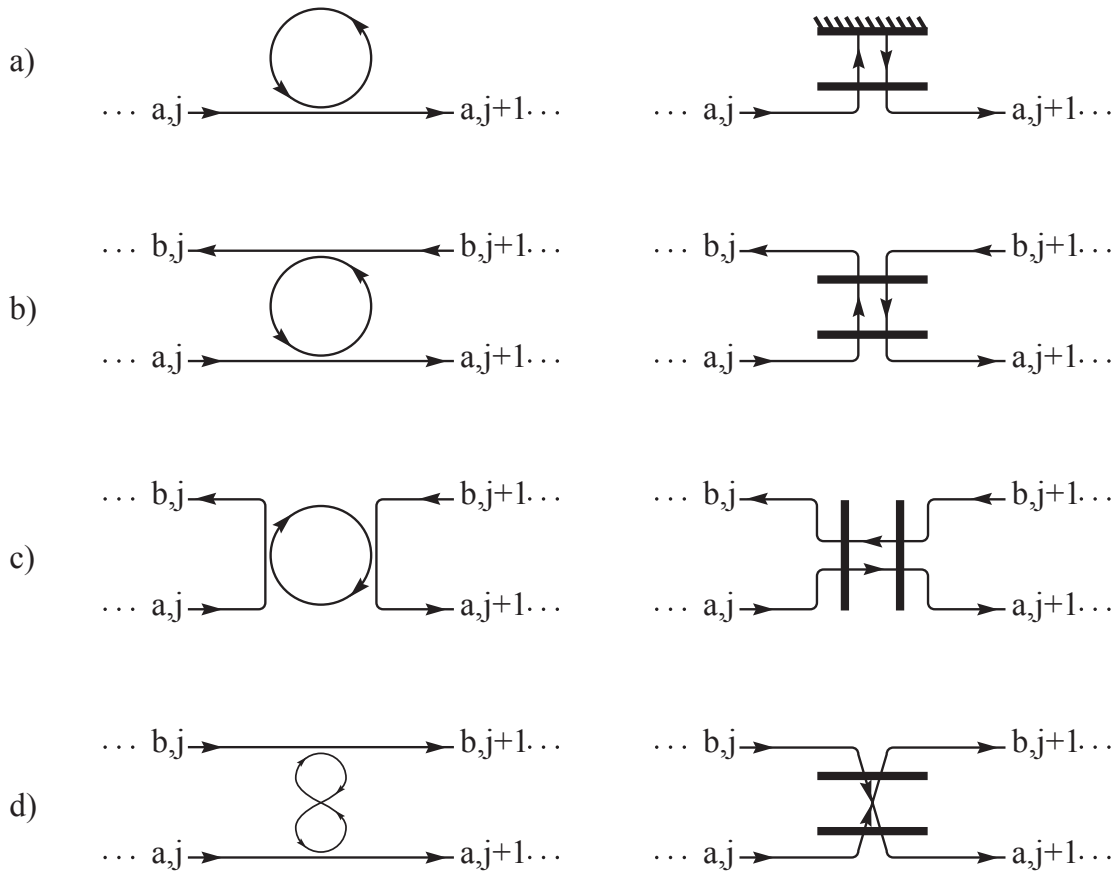
Figure 6.14: Illustrations of four archetypal ring resonator geometries and their free-space analogues which can be used as building blocks to construct sequences of resonators that serve as engineerable photonic media. The only way to connect singly-coupled ring resonators or Gires-Tournois resonators in series is depicted in (a). The three unique ways of connecting doubly-coupled ring resonators or Fabry-Perot resonators in series are illustrated in (b),(c) and (d).

## 6.7.1   Single-Channel SCISSORs

The dispersion relation for a (periodic) single-channel SCISSOR is a special case $(r_2 = 1)$ of the double-channel variety. Figure 6.15 displays the dispersion relation and build-up as derived from the formalism in appendix G. Nothing fundamentally new is introduced here. The dispersion relations are plotted in standard form as frequency vs. the Bloch vector with build-up and GVD alongside. The plots here are displayed for comparison with the other 3 structures. Notice that no photonic band-gaps are present in the dispersion relation. Near a resonance associated with the resonators, the build-up is strongly peaked and the group velocity (slope of dispersion relation) is greatly reduced. Both effects contribute to enhance nonlinear properties. In this structure, the maxima of each is coincident and centered on the resonance. As will be shown in the following sections, this is not always the case.

## 6.7.2   Double-Channel SCISSORs

A double-channel SCISSOR as depicted in figure 6.16 is composed of a sequence of resonators coupled to waveguides on both sides. In the single-channel case with all-pass resonators, feedback is solely intra-resonator; the double-channel case introduces inter-resonator feedback much like a concatenation of Fabry-Perot resonators or multi-layer stack. The mathematics here are nearly analogous to that of a multi-layer stack with the notable distinction that the forward- and
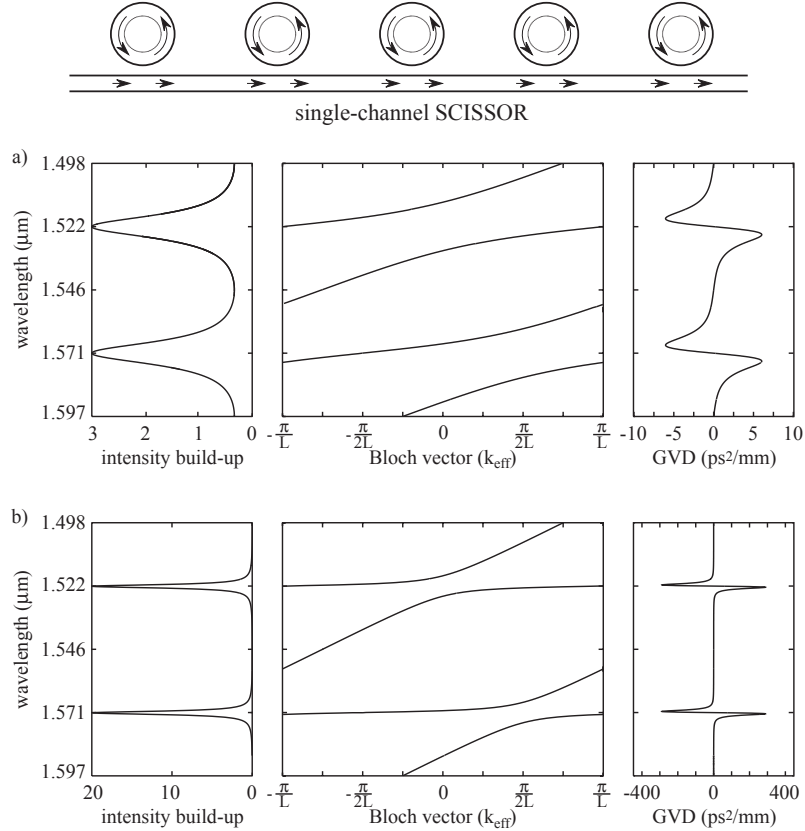
Figure 6.15: The build-up factor, dispersion relation, and group velocity dispersion for a) a low-finesse, and b) a high-finesse single-guide SCISSOR. Note that the dispersion relation for the single-guide SCISSOR does not display photonic band-gaps. Nevertheless, at the resonator resonances ($\lambda_{m_R} = n2\pi R/m_R$), both the intensity build-up in the resonators and the group velocity reduction, (inversely proportional to the slope of the dispersion curve), are coincidentally maximized. As a result, optical nonlinearities at the resonances are quadratically enhanced. Parameters include a refractive index of $n = 3.1$, and a radii of $R = 2.5$ $\mu$m. Resonances $m_R = 31$ and 32 at 1.571 $\mu$m and 1.522 $\mu$m are shown. In a), a high coupling strength, $t^2 = .75$ results in a wide bandwidth and a low build-up, $\mathcal{B}_0 = 3$. In b), a low coupling strength, $t^2 = .1814$ results in a narrow bandwidth and a high build-up, $\mathcal{B}_0 = 20$. To avoid redundancy, and because the forward and backward travelling waves do not couple, only the dispersion relation for the forward-travelling wave is shown.

backward-going coupled waves physically occupy different optical channels. There is a greater freedom of parameter choice in the realization of integrated double-channel SCISSORs with respect to multi-layer stacks or Bragg gratings since the effective reflectivities can be easily made stronger. While in the single-channel case, the transfer characteristics of a single resonator can be multiplied serially to obtain an overall transfer function, the same procedure fails for the double-channel case. This is of course because in the single-channel case, once light leaves a particular resonator, it never returns back to it. The double-channel case however, offers many routes for the light to recirculate back to earlier resonators previously visited; resonances can develop not only within but also amongst the resonators. As a result of this inter-resonator feedback, the periodicity of the resonator spacing becomes important and the possibility of photonic band-gaps exists. A comparison of the qualitative features of the band-gaps in figure 6.16 reveals that the band-gaps are wider for strongly-coupled resonators. The interpretation is simple. In the high-finesse case, the band over which the individual resonators are *reflecting* is narrow while in the low-finesse case it is wide. This directly carries over to the widths of the band-gaps in the infinitely periodic structure. This is in stark contrast to the situation of a multi-layer stack where high reflectivity results in a wider band-gap. This difference is due to the fact the double-guide SCISSOR is connected from individual resonators in a different manner than a multi-layer stack is connected from a sequence of individual Fabry-Perot cavities. Figure

6.17 qualitatively compares the transmission properties of unit structures and infinite periodic structures for a double-guide SCISSOR and a multi-layer stack. While a multi-layer stack (or CROW as will be later shown) allows propagation on resonance and taking advantage of maximum coherent build-up of intensity within the resonators, propagation is not allowed at resonances of the double-channel SCISSOR around which band-bands form. The fact that peak resonator build-up coincides with the center of the band-bands implies that this structure is potentially more useful for exciting gap solitons [118,131] and other nonlinear effects *within the band-gap.*

The dispersion relation for the double-channel case demonstrates the existence of two qualitatively different types of photonic band-gap. The first type of band-gap is a gap typical of a multi-layer stack or Bragg grating which opens centered at the Bragg wavelengths ($\lambda_j = 2nL/j$) associated with the periodicity of the structure. Within some range of wavelengths centered about this Bragg wavelength no real value of the propagation constant exists. This region is termed a Bragg gap. The dispersion relation at the low frequency side of the gap possesses a positive slope corresponding to a positive group velocity. The sign of the slope and group velocity changes sign just above the gap. Near the gap edges, the group velocity can go to zero and consequently, such a device might be useful as a delay line or optical buffer. A problem with this implementation is the existence of strong group velocity dispersion near the edge which imposes an

ultimate limit on the delay time. The second type of band-gap is a gap centered at the resonant wavelength ($\lambda_m = n2\pi R/m$) associated with the circumference of resonators. Just as in the first type, within some range of wavelengths centered about this resonant wavelength, no real value of the propagation constant exists. This region is termed a "resonator gap." [131] The dispersion relation at the low frequency side of the gap possesses a positive slope corresponding to a positive group velocity. In contrast to the Bragg gap, the sign of the slope and group velocity does not change across the gap. Near the gap edges, the group velocity can also go to zero but the group velocity dispersion is strikingly smaller near the edge. [132] Another, very striking difference between Bragg and resonator gaps is the position of minimum separation between bands. In the case of a Bragg gap, the gap is direct, while in the case of a resonator gap, the gap is indirect.

### 6.7.3 Inter-Coupled Resonators

A sequence of inter-coupled resonators with no waveguide as depicted in figure 6.18 may be considered to be a one dimensional version of a coupled resonator optical waveguide (CROW). Another interpretation is in considering every other resonator to be two waveguides which connect the resonators together in sequence. The output port connections here are reversed compared to that of the double-channel SCISSOR. As a result the optical properties are exactly analogous to a multi-layer stack. Forward propagation can occur only near resonances. Light

Figure 6.16: The build-up factor, dispersion relation, and group velocity dispersion for a) a low-finesse, and b) a high-finesse double-channel SCISSOR. Note that unlike the dispersion relation for the single-guide SCISSOR, the double-guide variety displays photonic band-gaps. Two qualitatively different band-gaps manifest themselves. At the structural Bragg resonances, $(\lambda_{m_B} = nL/2m_B)$ the band-gap is direct and results from distributed Bragg reflection. At the resonator resonances, $(\lambda_{m_R} = n2\pi R/m_R)$ the band-gap is indirect and results from strong resonator-mediated back-coupling. Parameters were chosen such that one Bragg gap was coincident with one resonator gap within the figure: refractive index $n = 3.1$, radii $R = 2.5$ $\mu$m, and spacing $L = 1.5\pi R$. Resonator resonances $m_R = 31$ and 32 and Bragg resonances $m_B = 64$, 65 and 66 are shown. The coincident resonator ($m_R = 32$) and Bragg ($m_B = 66$) resonance results in a wide direct gap. In a), a high coupling strength, $t^2 = .75$ results in wide band-gaps and a low build-up. In b), a low coupling strength, $t^2 = .1814$ results in narrow band-gaps and a high build-up. This structure is most suited to enhancement of nonlinearities near or a gaps due to the centering of intensity build-up peaks at mid-gap.
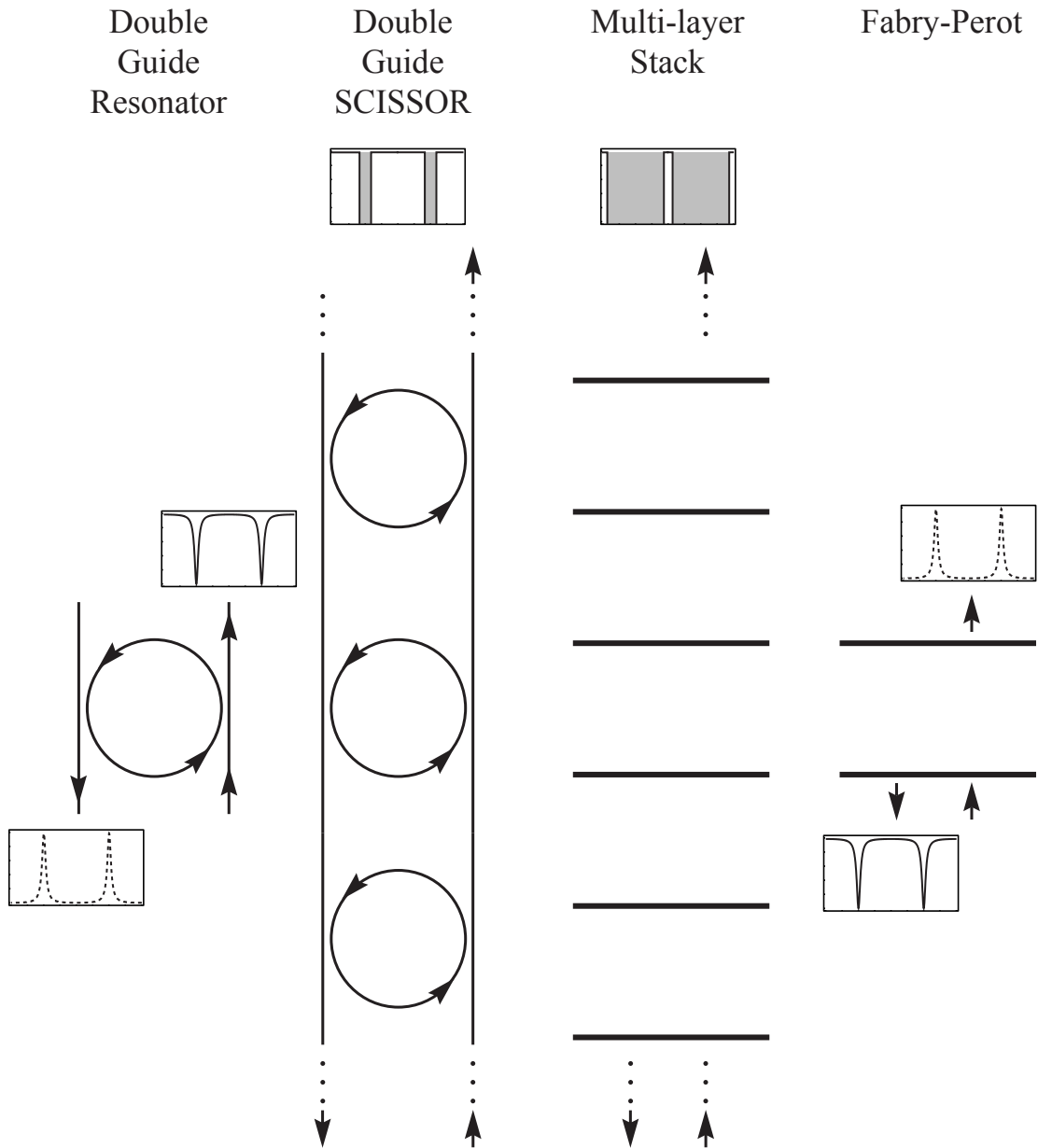
Figure 6.17: A comparison of the transmission properties of a) a double-channel resonator, b) a double-channel SCISSOR, c) a multi-layer stack, and d) a Fabry-Perot. Note that the qualitative features of the transmission peaks and valleys are equivalent but reversed for that of a a double-channel resonator and a Fabry-Perot. This results in very different band-gap widths when the individual units are connected to form a double-channel SCISSOR and a multi-layer stack.

within the band-gaps does not efficiently excite the resonators. Thus, the structure is not an ideal geometry for the excitation of gap solitons and other nonlinear effects *within the band-gap.* The structure is nevertheless useful for exciting the more general class of Bragg solitons [119] and for linear bandgap engineered devices.

## 6.7.4   Finite Stop-Gap Structures

Next, comparisons are drawn between the qualitative features of the transmission for a finite double-channel SCISSOR and 1-D CROW with the corresponding infinite periodic structures. Figure 6.19 displays the transmission for *low finesse* 1 and 5 unit-celled structures. Figure 6.20 displays the transmission spectra for equivalent *high finesse* structures. It is evident that both the double-channel SCISSOR structure and the 1-D multi-layer stack display complementary bandgaps in an infinite structure. However, for a finite double-channel SCISSOR, a deep ripple-free stop-gap can be achieved by use of merely 5 unit cells under high finesse operation. In contrast, the 1-D CROW (or multi-layer stack) requires a large number of unit cells to achieve a deep stop-gap. Also, in the high finesse case, apodization is essential to remove the deep ripples in the transmission spectrum of a CROW resulting from resonances developing from the abruptly terminated ends of the structure. This is somewhat unnecessary in the finite double-channel SCISSOR. However, strong intensity build-ups present in regions
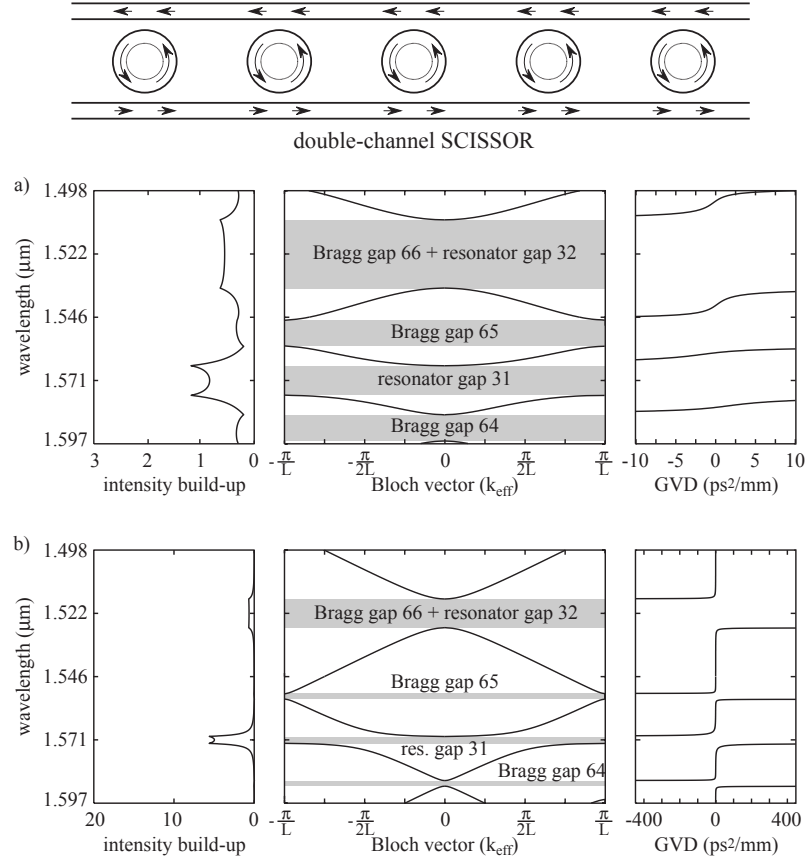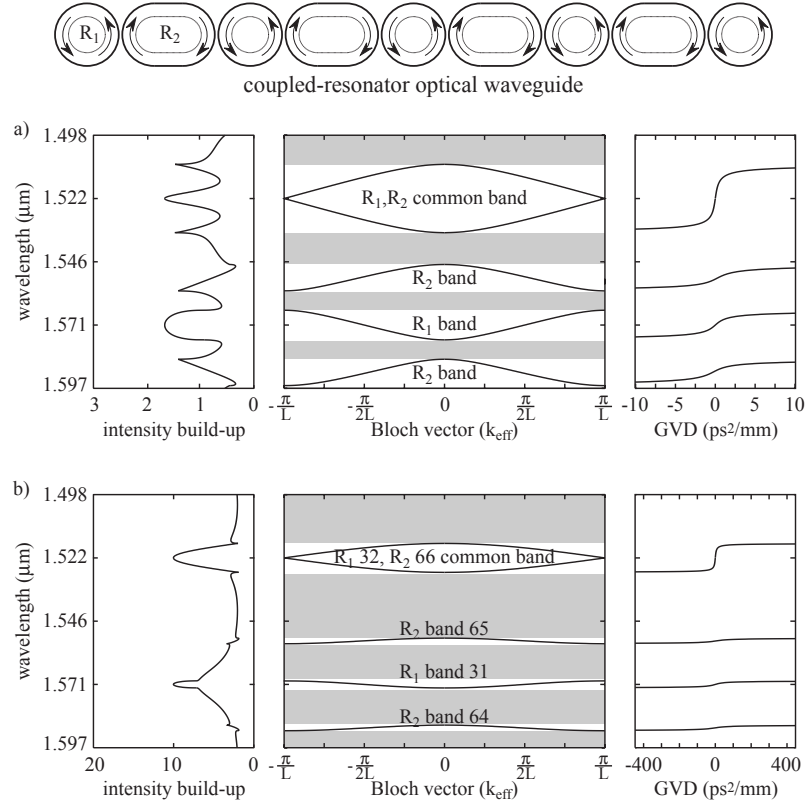
Figure 6.18: The build-up factor, dispersion relation, and group velocity dispersion a) a low-finesse, and b) a high-finesse coupled resonator optical waveguide. The dispersion relation is exactly analogous to that of a multi-layer stack. Band-gaps are always of the direct type and result from distributed Bragg reflection. Parameters include a refractive index of $n = 3.1$, alternating radii of $R_1 = 2.5$ $\mu$m and $R_2 = 1.5R_1$. Resonances $m_{R1} = 31$ and 32 and $m_{R2} = 64$, 65 and 66 are shown. In a), a high coupling strength, $t^2 = .75$ results in narrow band-gaps and a low build-up. In b), a low coupling strength, $t^2 = .1814$ results in wide band-gaps and a high build-up, $\mathcal{B}_0 = 20$. These qualitative features are directly opposite those found in the double-guide SCISSOR. This structure is most suited to enhancement of nonlinearities near the band-centers due to the centering of intensity build-up peaks at mid-band.

of high transmission for the CROW are shifted to regions of high reflection in a double-channel SCISSOR. A limited depth of penetration due to strong backward reflection will ultimately place restrictions on its use for nonlinear optical interactions.

High finesse multi-layer and CROW structures are optimum structures for simultaneously enhancing intensity build-up and phase sensitivity or group delays near transmission resonances. Operation near stop-gaps is however only optimized in the regime of lengthened distributed reflection resulting from low contra-directional coupling per unit cell (low finesse) over many unit cells. Such is often the case in Bragg gratings where the index contrast variations are very low. In contrast, high finesse double-channel SCISSORs are optimum structures for simultaneously enhancing intensity build-up and phase sensitivity or group delays near the stop-gaps. Operation near stop-gaps is optimized in the regime of strong contra-directional coupling per unit cell (high finesse) over a few unit cells. Thus, the engineering of nonlinear optical bands is best accomplished with a CROW while the engineering of nonlinear optical band-gaps is best accomplished with a double-channel SCISSOR. Finally, the displayed plots show that the dispersion relation can provide a heuristic guide to the width of the transmission dips in a finite structure.
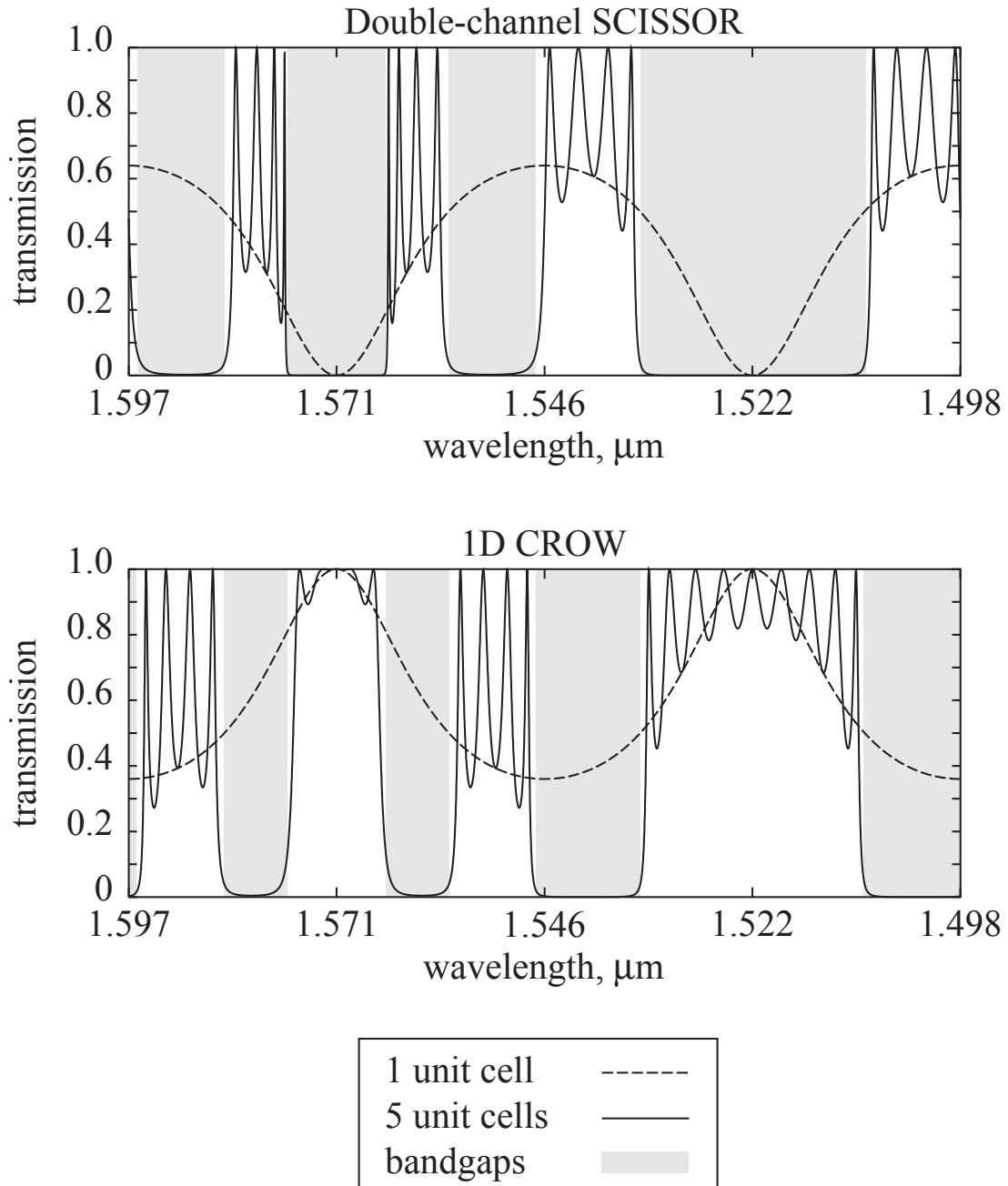
Figure 6.19: Transmission spectra for a *low finesse* ($t^2 = .75$) finite double-channel SCISSOR and finite 1D-CROW. Parameters are the same as in figures 6.16 and 6.18. Here, 5 unit cells are used to approximate the structures. For comparison, the transmission for a single resonator structure is shown in each case. Shaded regions correspond to 1D photonic bandgaps in the corresponding infinite structure.
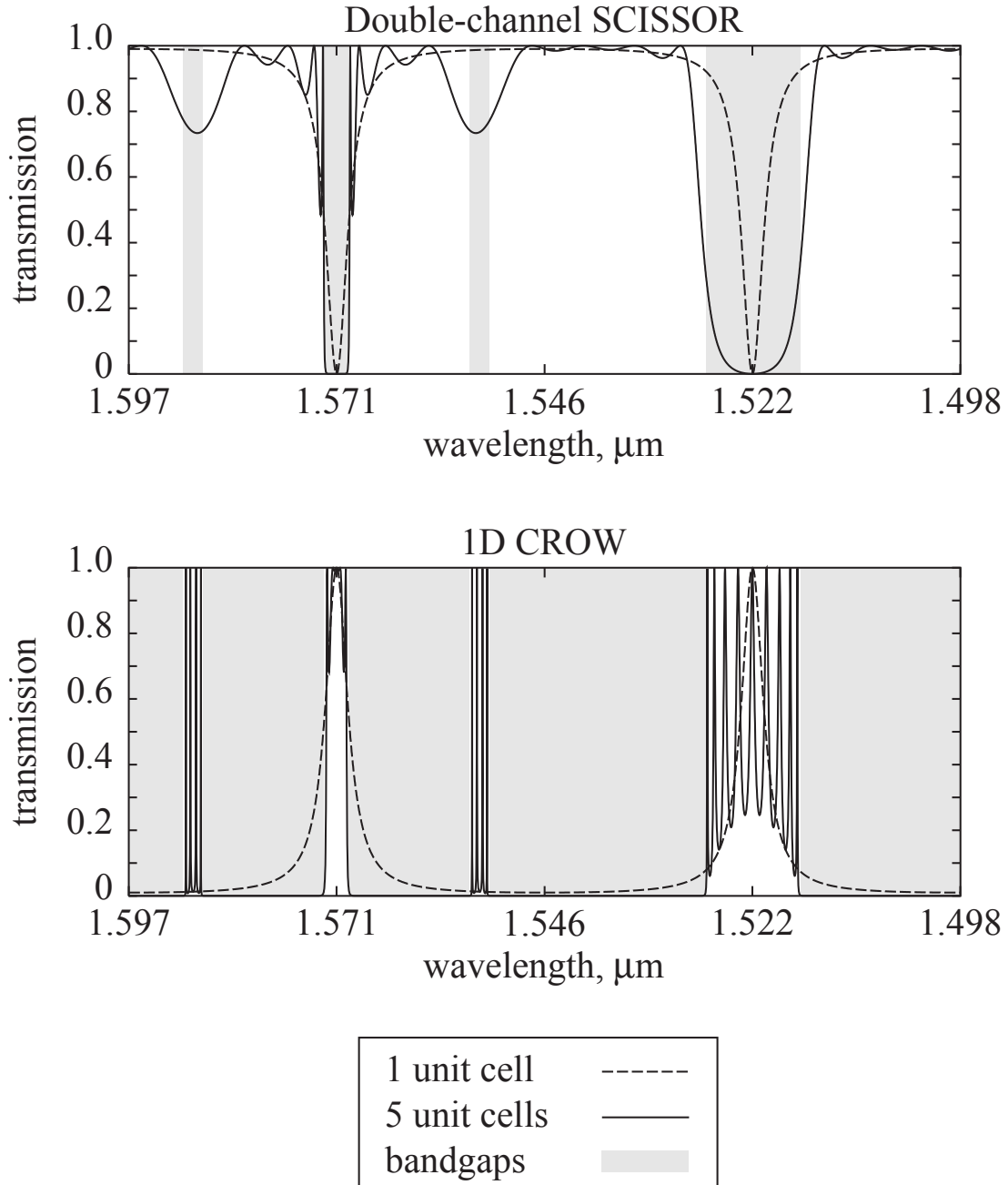
Figure 6.20: Transmission spectra for a *high finesse* ($t^2 = .1814$) finite double-channel SCISSOR and finite 1D-CROW. Parameters are the same as in figures 6.16 and 6.18. Here, 5 unit cells are used to approximate the structures. For comparison, the transmission for a single resonator structure is shown in each case. Shaded regions correspond to 1D photonic bandgaps in the corresponding infinite structure.

### 6.7.5 Twisted Double Channel SCISSORs

Another variety of the double channel SCISSOR which possesses qualitatively different optical properties is constructed using two inter-coupled resonators to connect the two channels. For completeness, it is analyzed here. This "twisted" double-channel SCISSOR is depicted in figure 6.21. Due to the extra resonator, the coupling direction relationships across the resonator are reversed compared with the ordinary double channel SCISSOR. As a result, in this configuration there is no mechanism for contra-directional coupling, but co-directional coupling across the channels is now mediated by the two resonators. Light injected into one of the ports thus only couples to either of the channels in the forward-going direction. This may be considered to be a resonator-enhanced directional coupler. Note the absence of band-gaps and similarity of the dispersion relation with that of the single-channel SCISSOR.

## 6.8 Summary

Passive, nonlinear resonators are still a relatively widely untapped area of research. At present, many single microresonator systems with excellent optical properties have been constructed. [133–136,38] In many of these cases, extending the fabrication techniques to construct long sequences of such devices to yield large-scale integration of photonic devices [137] is achievable. The aim of this chapter was to
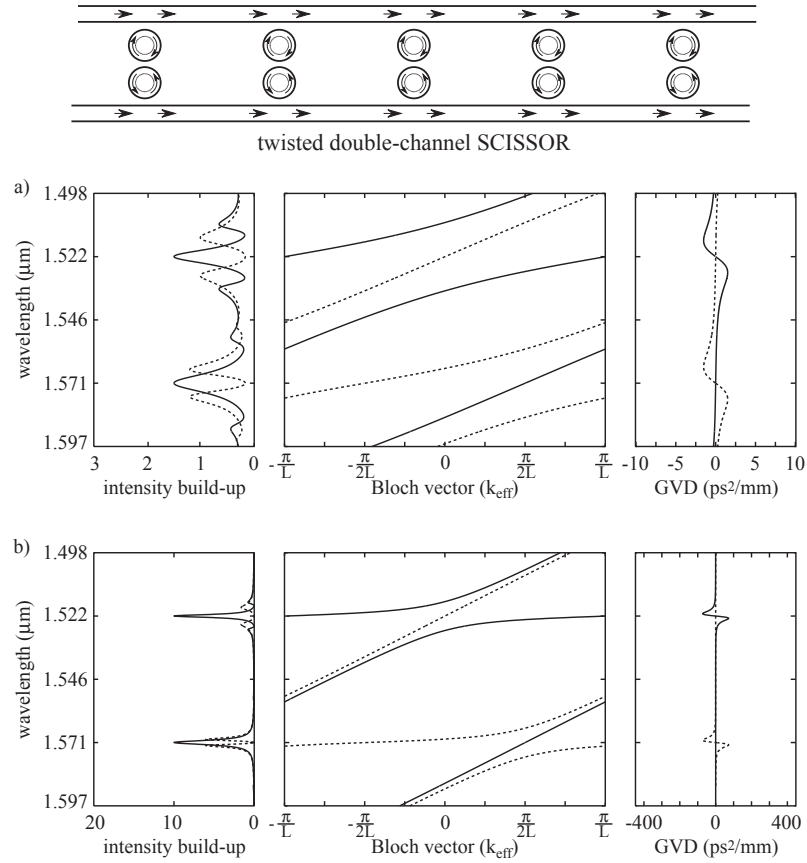
Figure 6.21: The build-up factor, dispersion relation, and group velocity dispersion for a) a low-finesse, and b) a high-finesse twisted double-channel SCISSOR. Band-gaps are absent in the dispersion relation which resembles that of the single-channel SCISSOR though a second branch is present. The two branches correspond to the two decoupled forward-travelling normal modes. Near the resonator resonances, $(\lambda_{m_R} = n2\pi R/m_R)$ the two branches are strongly coupled as in the case of a directional coupler. Parameters used are the same as in figure 6.16 except that there are two resonators each half in size and 100% coupled. Resonances $m_R = 31$ and 32 at 1.571 $\mu$m and 1.522 $\mu$m are shown. In a), a high coupling strength, $t^2 = .75$ results in wide-bandwidth channel-to-channel coupling and a low peak build-up. In b), a low coupling strength, $t^2 = .1814$ results in narrow-bandwidth channel-to-channel coupling and a high build-up. To avoid redundancy, and because the two forward and two backward travelling waves do not couple, only the two forward-travelling dispersion relation branches are shown.

describe some of the linear and nonlinear propagation characteristics of sequences of microresonators. Figure 6.22 summarizes the detuning dependence of the linear and nonlinear propagation parameters. The application of thermal or electrical fields to the resonators makes it possible to control the detuning and/or coupling coefficients. I envision that such structures could be used as artificial media to study and apply NLSE pulse propagation effects on an integrated chip where the propagation parameters may be chosen and/or modified in real-time. Other applications might include a testbed for studies of slow-light phenomena, variable optical delay lines, [105] clean pulse compression on a chip without pedestal formation via the soliton decay mechanism, and soliton-based optical switching and routing with low energy pulses. While all of these concepts have been implemented in various geometries and material systems, the SCISSOR system has the potential for providing a highly compact, integrated optical platform for such phenomena. Furthermore, it has the potential of creating familiar phenomena in regions of parameter space that typically do not manifest it such as the case of self-steepening for pulses greater than picoseconds. It is expected as manufacturing techniques continue to improve, microresonator-modified waveguides such as the SCISSOR will become important photonic devices.
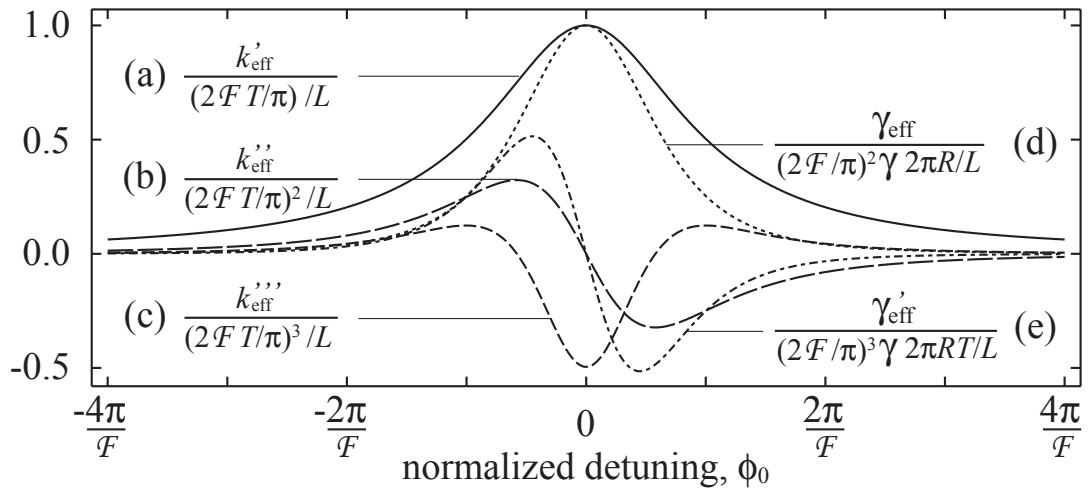
Figure 6.22: Functional dependence of a) the group velocity reduction, b) group velocity dispersion, c) third-order dispersion, d) self-phase modulation coefficient, and e) self-steepening coefficient on the normalized detuning $\phi$ for a SCISSOR. The parameters have been scaled such they the curves are universal and fit within the same plot limits.

# Chapter 7

# Microresonator Design

## 7.1  Introduction

There are several factors that must be taken into account when designing microresonator structures. The aim of this chapter is to describe the reasons for choosing a particular set of parameter choices. Some parameters are dictated by fundamental theoretical considerations; others are dictated by the practicality and availability of fabrication materials and tools.

## 7.2  Materials

The selection of a material system for fabrication of nonlinear microresonators must satisfy a number of requirements. First and foremost, it must be compatible with mature fabrication technology. Examples include optical fiber and fabrication on Silicon and GaAs substrates. Secondly, it should possess a high linear refractive index, a high nonlinear refractive index, low one-photon absorp-

tion loss, and low two-photon absorption loss. A careful analysis dictates that a semiconductor (or semiconductor-like) material with a band-gap slightly greater than twice the exciting photon energy satisfies the low (one and two photon) loss requirements and yet provides a reasonably high and ultrafast nonlinear Kerr coefficient 7.1. This is a result of applying the Kramers-Kronig relations to two-photon absorption and cross-phase modulation. Appendix C offers a closer look at this method.

There were a few material systems for which fabrication of ring resonators was feasible within the means of our research group: silica, AlGaAs, chalcogenide glass, and polymer. The relative merits of each will be discussed in turn.

## Silica

Despite a weak nonlinearity, ordinary silica drawn into fiber has the distinction of possessing the highest nonlinearity to attenuation ratio of any material system. It would be advantageous to design devices that make use of this property in an effective manner. Silica fiber based switching devices were analyzed where the introduction of a single-mode fiber ring resonator into one of the arms of a fiber Mach-Zehnder interferometer would effectively enhance the accumulated nonlinear phase shift and reduce the switching threshold-interaction length product by *four or more* orders of magnitude. [65] This analysis was presented in chapter 5. However the most significant problem associated with constructing ring res-
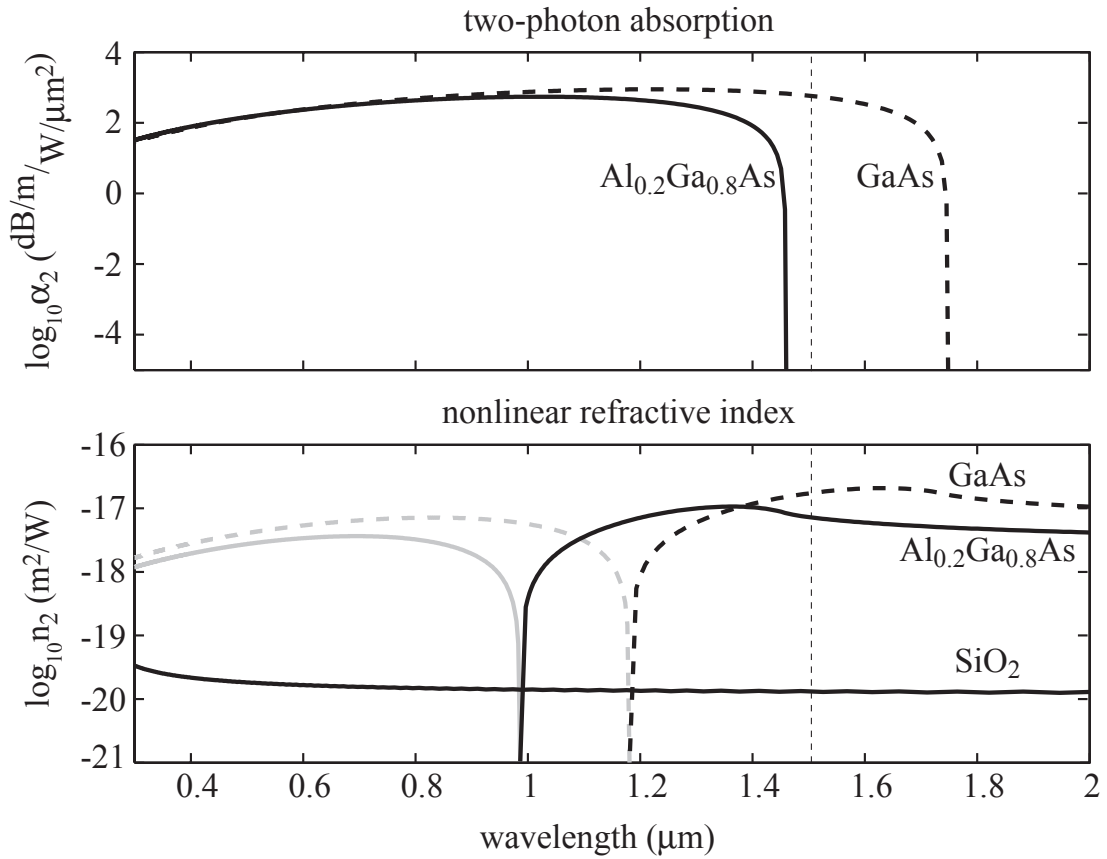
Figure 7.1: Plots of the two-photon absorption coefficient and nonlinear refractive index of $SiO_2$, GaAs, and $Al_{0.2}Ga_{0.8}As$ versus wavelength. The plot for two-photon absorption is derived from a two-band model. [138] The Kramers-Kronig relation applied to the third order susceptibility is subsequently used to generate the plot for the nonlinear refractive index in each case. The dip on the log plot of $n_2$ corresponds to a reversal of sign for the nonlinear refractive index and gray linestrokes correspond to negative nonlinear refractive indices.

onators from conventional optical fiber is low dielectric contrast. Conventional single-mode fibers (such as Corning SMF-28) posses index differences of the order of .0036 and as a result suffer large bending losses when made into rings of radii of the order of centimeters. This restricts the operating bandwidth of such devices to below 1 GHz. A 6 micron diameter *air-clad* silica microresonator could possess a 10 THz free-spectral range, but the weak nonlinearity requires such a high finesse to obtain a $\pi$ phase shift at reasonable powers, that the operating bandwidth would again fall well below in the GHz range. Thus for many practical reasons, all-optical switching devices with low latency[1] based on microresonators are not expected to be useful. Silica glass micro-spheres can be made with ultra-high quality (Q) factors, [96,54,52] but are difficult to fabricate reproducibly and not readily integrated. They have nevertheless found use as lasers [31] and have the potential for ultrafine filter or ultraprecise clock applications. Integrated microdisk or microring resonators can be fabricated more reproducibly although current fabrication techniques cannot achieve high quality factors. Integrated silica-based microresonators have and will continue find applications as dispersion compensators [46] and delay lines [105] with GHz bandwidths. Recently, a structure which combines the best features of spheres and disks was constructed

---

[1]Non-resonator based nonlinear interferometers such as the nonlinear optical loop mirror or nonlinear Mach Zehnder interferometer can compensate for low nonlinearity via long interaction lengths. While the long interaction lengths do not affect the bandwidth as in the case of a resonator, they introduce a long delay from input to output (latency). Furthermore, then cannot be fabricated at the integrated chip-level.

by a combination of microfabrication techniques and laser annealing to produce microdisks with smoothed sidewalls reformed by surface tension. [139]

## AlGaAs

Semiconductor nonlinearities result either from real (band-to-band) transitions or virtual transitions of charge carriers. The nonlinearities resulting from *real transitions* are typically strong, but their bandwidth is typically limited by the lifetime of generated excited state carriers which is of the order of 10-100 ps. This would dictate an operating bandwidth of 10-100 GHz for semiconductor-based all-optical switching[2] Furthermore, devices which rely on the saturation of gain to change the refractive index are active and thus ultimately require an electrical source of power to operate.

Nonlinearities resulting from *virtual transitions* are typically weak but nevertheless ultrafast. It was shown by Stegeman et al. that in a material possessing a band structure, the nonlinear refractive index is inextricably linked to two-photon absorption. [141] Sheik-Bahae et al. analyzed the theory of the dispersion of the nonlinear coefficient and found that, while two-photon absorption is a limiting factor, the nonlinear figure of merit (nonlinear refractive index to two-photon

---

[2]There exists a scheme that allows operation at terahertz bandwidths. Sokoloff, et al. demonstrated such a device in 1993 and called it a terahertz optical asymmetric demultiplexer (TOAD). [140] The device is essentially a nonlinear optical loop mirror (NOLM) with a semiconductor amplifier asymmetrically placed in the loop. The trick is that though the lifetimes are slow, the rise-times can indeed be fast enough to achieve a $\pi$ phase shift for picosecond pulses provided the device is continually operated far from steady-state.

absorption coefficient ratio) is maximized just below the half-gap of a material. [142,138] Shortly thereafter, Slusher, et al. demonstrated that phase shifts in excess of $\pi$ were obtainable with less than 100 pJ of energy in low-loss AlGaAs waveguides engineered to operate just below the half-gap. [143] The waveguide length required to achieve a nonlinear switch with reasonable pulse energies was still of the order of a few millimeters. Significant reduction of this length may be accomplished via use of an AlGaAs microresonator. $Al_x Ga_{1-x} As$ is a well-studied material system with well-developed processing procedures that can be engineered (via adjustment of composition, $x$) to satisfy the requirements dictated for nonlinear microresonators. Below the half-gap, AlGaAs has negligible two-photon absorption but just above it can reach values of 500 dB/mm for only 1 kW of peak pulse power. Figure 7.2 shows the half-gap wavelength dependence on the composition displaying compositions of x=20% for wavelengths in the near infrared around 1.55 $\mu$m. Just below the half-gap, though over a broad bandwidth of a few hundred nanometers, a nonlinearity which is about 100-1000 times greater than silica $n_2 \approx 10^{-17} m^2/W$ is typically found. The much larger nonlinear refractive index present in the lower bandgap AlGaAs is in accordance with a well-known scaling law ($E_g^{-4}$) for the third-order susceptibility. [144] This coupled with a refractive index above 3.0, make it an attractive choice for constructing nonlinear microresonator-based devices. Figure 7.3 displays the refractive index as a function of composition.
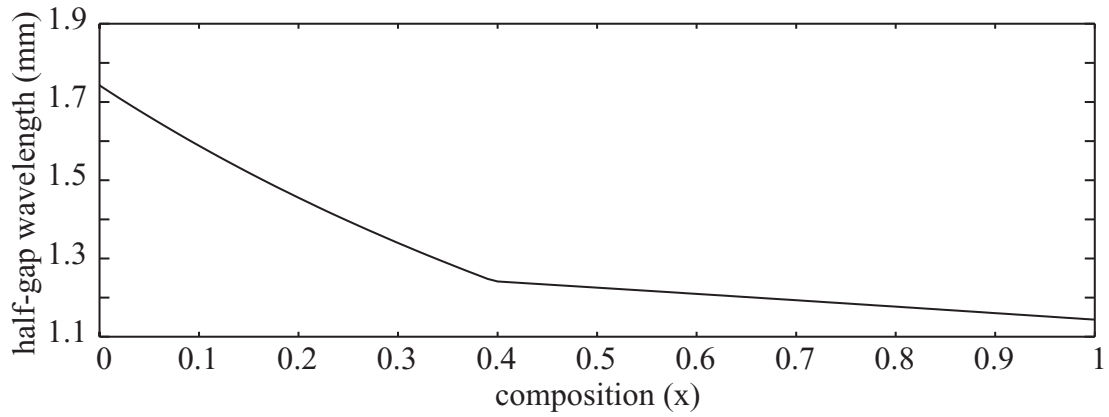
Figure 7.2: $Al_xGa_{1-x}As$ half-gap wavelength as a function of composition. [145]  The kink in the plot results from a crossover from direct ($GaAs$) to indirect ($AlAs$) band-gap.
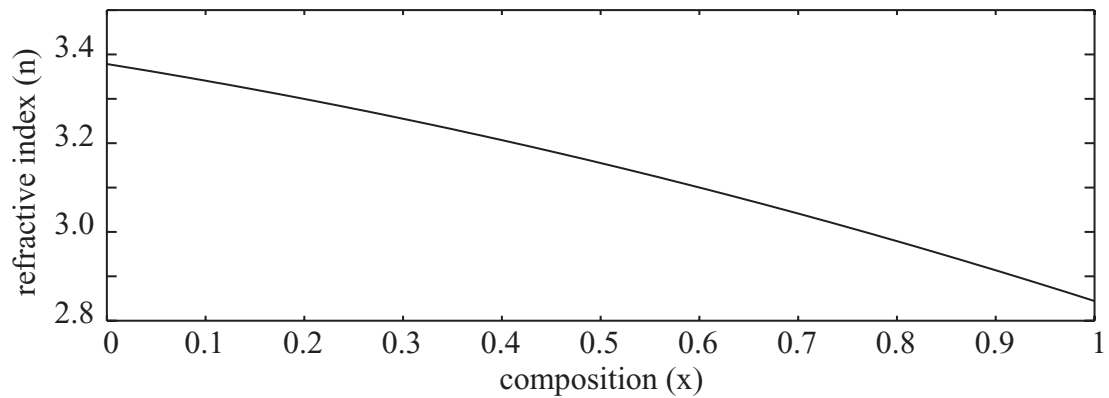


Figure 7.3: $Al_xGa_{1-x}As$ refractive index as a function of composition. [145]
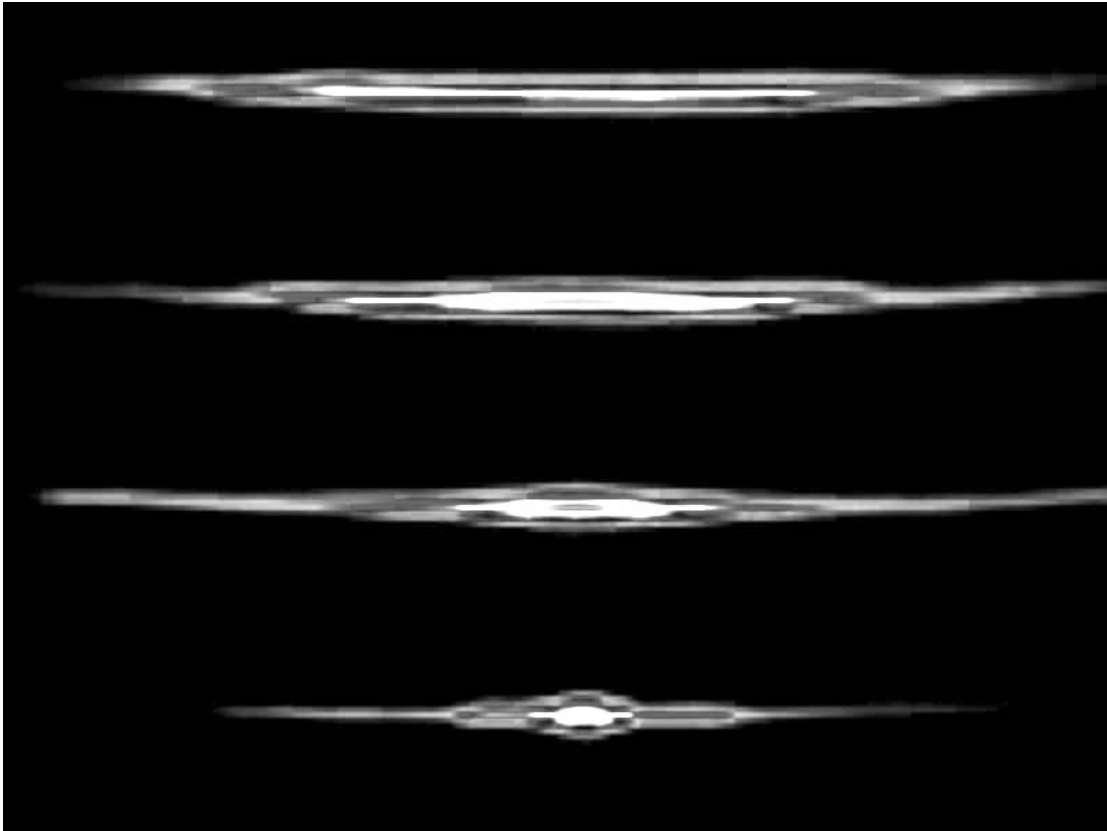
Figure 7.4: A demonstration of transverse, one dimensional self-focusing in
an AlGaAs planar waveguide. Shown are the output intensity profiles for
increasing pulse energies.

Evidence of the strong nonlinearity in AlGaAs was demonstrated via Kerr-lens

self-focusing experiments. [146] Figure 7.4 shows output intensity profiles for light

injected into one end of a planar AlGaAs waveguide.

## Chalcogenide

Certain classes of chalcogenide-based glasses ($As_2Se_3$) behave similarly to semi-

conductors with the benefit that they can be easily integrated with the better-

developed silica-on-silicon photonics infrastructure. Similarly, below the half-gap,

chalcogenide systems display negligible two-photon absorption. An attractive material for all-optical switching in the near infrared is arsenic selenide, $As_2Se_3$) which possesses a nonlinearity based upon virtual transitions that was measured to be 500 times greater than silica glass. [68,77] Arsenic selenide possesses a band-gap energy of 1.77 eV which is greater than twice the band-gap energy of a near infrared photon around 1.55 $\mu$m (0.8 eV) thus two-photon absorption processes are generally negligible. A refractive index of 2.5 allows for strong confinement and low whispering gallery losses. As a result of the high nonlinearity and strong confinement, the threshold for switching in chalcogenide is 5 mm. By use of a chalcogenide based ring resonator with a finesse of about 50, an overall enhancement of about 1000 can be achieved, thus reducing the physical length to a disk circumference of 5 $\mu$m, which could be accomplished in a 1 $\mu$m radius disk resonator. Chalcogenide glasses might be thought of as the glassy counterpart to crystal AlGaAs for constructing useful Kerr-based switching devices in the region of 1.55 microns. An effort was made in collaboration with Richart Slusher of Lucent technologies to fabricate such devices. Unfortunately, due to extrinsic factors, the project did not come to fruition.

## Polymer

Polymer-based photonics has attracted attention recently because of its potential for inexpensive mass production of integrated photonic systems. Processing poly-

mer materials is typically simpler, though often results in lossier and more thermally sensitive components than their glass or semiconductor based counterparts. There are many nonlinear optical polymers with high nonlinearities which maintain a high-speed response. Typically they are of the guest-host variety in which a workable polymer host is doped with a small concentration of dye molecules. A collaboration was established with Professor L. J. Guo (University of Michigan) to attempt to fabricate microresonators via an advanced nano-imprinting technology they developed. Nano-imprinting implements a hard mold with predefined nanoscale features to mechanically imprint into a polymer film cast on a substrate, while the polymer is heated to above its glass transition temperature (Tg). The pattern is subsequently fixed into the polymer during a cooling cycle. Resolutions of 10 nm are achievable.

## 7.3 Geometry

### 7.3.1 Resonator Size

The size of a microresonator is the primary factor dictating its operating bandwidth. The radius must be small enough to provide a large free-spectral range (FSR) which must be made greater (by a factor of the finesse) than the desired bandwidth. Another practical consideration is that a small resonator necessarily possess a small interaction length over which coupling to a waveguide is strong.

Careful attention must be made to ensure that ultra-small ($<5\mu$m) resonators are optimized for strongest possible coupling per unit length. Ultimately, small enough microresonators will possess a *minimum* coupling finesse.

## 7.3.2  Resonator Finesse or Q-factor

The other factor determining the operating bandwidth of a resonator is its finesse ($\mathcal{F}$) or quality-factor ($Q$). While they only differ by a factor corresponding to the number of optical cycles in a round trip ($Q = m\mathcal{F}$), for some applications, the finesse is the important parameter, while for others it is the Q. The Q is a normalized measure of the bandwidth of a resonator and corresponds to the number of optical cycles stored within the device at any given time near resonance. The Q dictates how well one can resolve small changes in the propagation constant. For sensing applications, analytes which induce refractive index changes can be measured when the change is one part in Q. The finesse is a normalized measure of how well the bandwidth can be resolved within the range between resonances and corresponds to the number of "round trips" stored within the device at any given time near resonance. Provided that the actual resonance number is unknown as it usually is in spectroscopic applications, this parameter characterizes a Fabry-Perot spectrometer. The finesse also characterizes the group index of SCISSOR-like structures and thus dictates the group velocity for slow light applications. However, neither the finesse, nor the Q is important for sin-

gle pulse synchronization (optical pulse delay lines) or dispersion compensation; these processes are solely dependent upon the resonator-to-pulse bandwidth ratio. Typically for nonlinear switches, a compromise between high bandwidth and high nonlinearity is desirable. While the bandwidth is reduced by the Q, the nonlinearity is increased by the factor $m\mathcal{F}^2 = Q\mathcal{F}$. The later section on coupling will explain how to engineer a given finesse or Q-factor.

### 7.3.3 Vertical and Lateral Confinement

Optical guidance in microresonators and guides used to couple them is accomplished via total internal reflection both vertically and laterally. Because the requirements for confinement in each dimension can be very different, the factors involved in choosing design parameters are treated separately. A common requirement is that confinement in each dimension be single-moded so as to greatly simplify many optical properties. A stringent requirement on the lateral index contrast is that it be high enough to support low loss whispering gallery modes at a desired radius. Such a requirement does not apply to the vertical confinement however. As a result, the vertical confinement can be accomplished via three layers (one core, two claddings) of slightly differing composition with a large dimension and still be single-moded. Particular attention must be made in the choice of refractive indices because it is well known that a symmetric planar guide

has no cutoff, while an asymmetric planar guide has a cutoff[3]. The horizontal guidance should, of course be single-moded if possible. However, a minimum lateral resolution will be dictated by imperfect patterning processes which will in turn govern minimum practical guide widths. These minimum practical guide widths may be multiply-moded an possibly unavoidable. Such a restriction is virtually absent in the vertical design because heights along this dimension can be controlled to near atomic precision. In the later section on coupling, it will be shown that the lateral guide width in the coupling region will also (along with that gap width) determine the coupling strength. Practically, the guides should be made as close to single-moded as possible though if they become too small, surface perturbations associated with fabrication processes may become proportionately large enough to cause extreme scattering losses. Finally, as an alternative to TIR based guidance, photonic-crystal-based resonators where the presence of defects in an otherwise periodic structure may be used to form equivalent resonators. [147] Such resonators may be employed to confine light to circulate within small distributed-feedback-guiding structures and would display qualitatively similar phenomena.

---

[3]If air is used as the top cladding, there is a good chance that a mode is not supportable
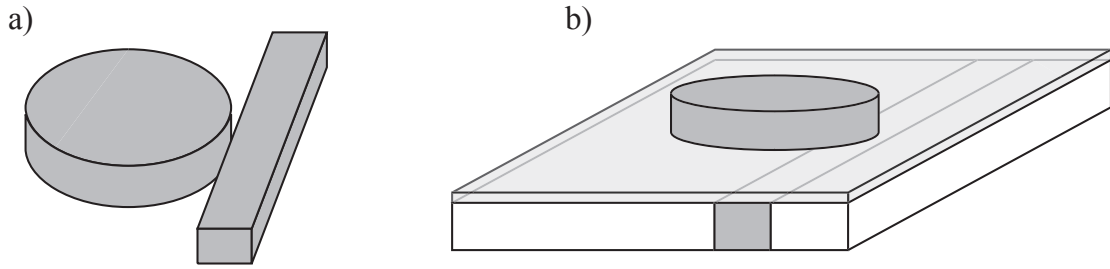
Figure 7.5: a) Laterally coupled resontor. b) Vertically coupled resonator.

## 7.3.4 Coupling

There are two practical geometries for situating a resonator and waveguide such that they can exchange optical power: lateral coupling or vertical coupling. Figure 7.5 depicts the two geometries. Vertical coupling has the advantages of easily met tolerances on guide-to-resonator gaps but requires advanced fabrication techniques (such as wafer bonding) to be realized. [148–150,30,151] Lateral coupling is the only geometry that was achievable within the resources of our group. The coupling strength should be optimized so as to be able to achieve the greatest possible coupling coefficient and thus a low enough finesse that is not loss-limited. In this respect, the chalcogenide system is better than the AlGaAs system because of lower index (2.5 vs 2.9-3.4) which allows for wider guide dimensions. This allows for better coupling, though increases the minimum resonator size dictated by bending loss slightly. An FDTD simulation should be performed as a final check, but there are fundamental limitations on the maximum achievable coupling per unit length. At best a distributed coupling of no more than $\kappa = 0.3k_1$ is achievable. The required distributed coupling is obtained from the desired cross-

coupling coefficient,$t$ from $t = sin(\kappa z_{\text{int}})$ where $z_{\text{int}}$ is the effective interaction length. An analytic expression for the TM distributed coupling in terms of normalized waveguide parameters is given by:

$$\kappa = k_0 \sqrt{n_1^2 - n_2^2} \frac{2b\left(1-b\right)e^{-V\sqrt{b}\frac{s}{d}}}{\left(2 + V\sqrt{b}\right)\sqrt{\frac{1}{n^2-1} + b}} \xrightarrow[n\to\infty]{} k_1 \frac{2\sqrt{b}\left(1-b\right)e^{-V\sqrt{b}\frac{s}{d}}}{2 + V\sqrt{b}}. \qquad (7.1)$$

There are two crucial implications resulting from the high index contrast limit. The first is that in the high contrast approximation, the coupling coefficient is independent of index contrast though it implicitly appears in the normalized frequency (V-parameter). The second is that for high contrast laterally coupled TM modes, the normalized frequency and normalized gap width completely dictate the coupling. Thus, practically, there are two parameters which are critical, though which can be adjusted to determine the coupling. Provided that the material parameters and wavelength are fixed, both the gap width and the guide width must be chosen appropriately. Even if the guides are touching, their coupling may *still* be too weak because they may be too wide. The TE distributed coupling is more complicated and cannot be written in such a compact form[4]. Moreover, the TE mode has a strong longitudinal component which peaks at the disk edge exactly where the index perturbations serve to severely scatter the mode energy. It also

---

[4]To avoid confusion, the convention for distinguishing between TE and TM modes is with reference to the substrate. A mode with a dominant electric field perpendicular to the substrate surface is denoted TM. Such a mode field is however, *parallel* with respect to the lateral interface and thus the TE Fresnel reflection and planar waveguide laws apply

extends farther outside the boundaries of the guide where it can easily couple to the substrate. Thus the TE modes are more sensitive to surface roughness induced scattering and substrate losses; a fact been confirmed by experiments. [135] Figure 7.6 shows the variation of coupling strength versus the normalized frequency and gap width in the high index contrast planar waveguide approximation for TM modes. Note that it predicts a maximum coupling strength between $V = 0$ and $V = \pi$, that is, in the region of single-moded behavior. The intuition for this peak is easily understood. For evanescent coupling, the evanescent tail of a mode extending beyond one guide excites the material polarization in a second guide which in turn reradiates into the second mode. For large enough guides, the portion of confined optical power present in the evanescent tail is negligibly small leading to low coupling. For small enough guides, the evanescent tail becomes the dominant portion of the confined optical power and is spread widely throughout space such that only a small fraction of it excites the other mode.

A racetrack geometry in which the coupling region is extended with a straight waveguide section can be used to greatly increase the coupling, at a modest lowering of the FSR and introduction of some junction loss. [152] This may be the only way to achieve a desired low finesse in small resonators where the effective interaction length is limited. Figure 7.9 displays the required interaction length to achieve a given finesse along with the necessary interaction length for a bal-
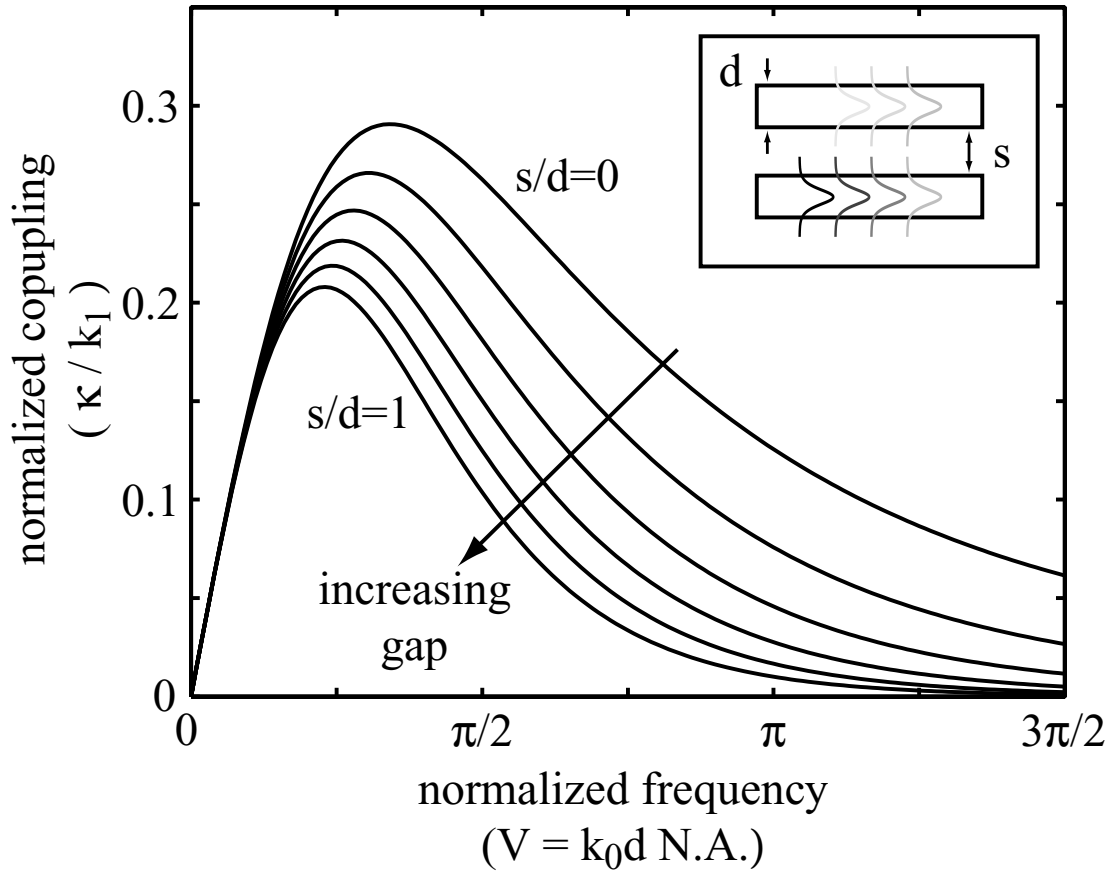
Figure 7.6: Normalized coupling strength ($\kappa/k_1$) Vs. normalized frequency ($V = k_0 d$N.A.), and normalized gap (s/d) in the limit of high index contrast for the planar waveguide approximation to TM guide-to-disk coupling.
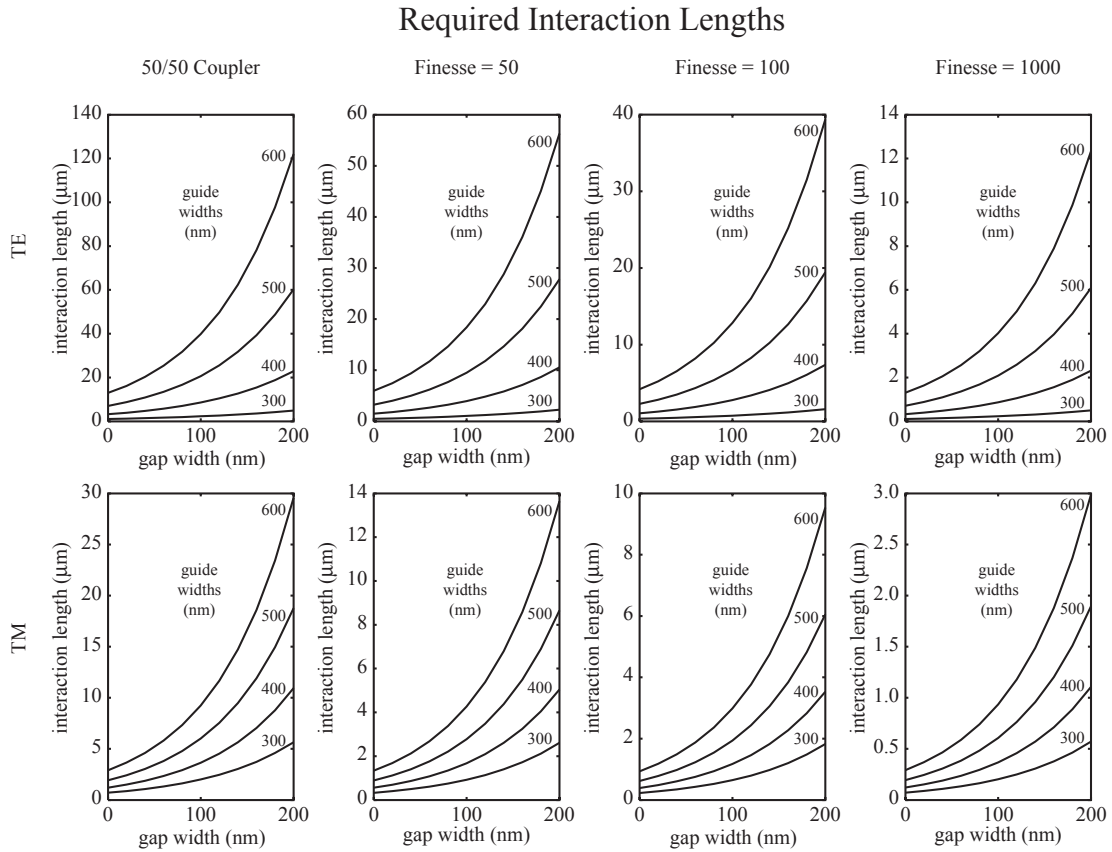
Figure 7.7: The required interaction lengths for TE and TM coupling to achieve a balanced coupler for a Mach Zehnder interferometer, a resonator finesse of 50, finesse of 100, and finesse of 1000. Note that in many cases, the required interaction length varies greatly with differing gap and guide widths indicating a need for extremely fine tolerances on design geometry.

anced coupler. Other considerations for tweaking the coupling strength lie in the choice of air-cladding, filled cladding, or rib waveguiding.

## 7.3.5   Phase Matching

Phase matching the waveguide mode to the mode of the ring or disk may be an important consideration when requiring a high lumped coupling or (low finesse). Specifically, ensuring that the modes are phase matched is important when the

difference in propagation constants, $\Delta k_z$ is greater than a critical value determined by the coupling per unit length, $\kappa$ and the desired lumped coupling coefficient $t^2$ such that $\Delta k_z < \kappa\sqrt{(1 - t^2)/t^2}$. Fortunately, for small enough resonators, phase matching is not a significant issue. The tolerance on maximum allowable beta-mismatch increases with inverse proportion to the interaction length of guide and resonator. The gap dimension and quality are, however critical.

## 7.3.6 Loss Minimization

A critically coupled resonator transmits nothing. Thus, it is important to stay well into the over-coupled regime. Bending loss at a fixed index contrast increases with decreasing resonator size. Scattering loss (at a fixed roughness of the resonator walls) and absorption loss (set by the choice of materials) in contrast decrease with decreasing resonator size. As a result there typically exists an optimum size at which net losses are minimized. Figure 7.8 displays the optimum diameter for a particular choice of parameters associated with AlGaAs microresonators. Coincidentally, the optimum diameter is very close to the desirable diameters for realizing many of the interesting devices proposed in this thesis.

## 7.3.7 Spheres vs. Cylinders, Rings Vs. Disks

The quality factors associated with silica microspheres have attracted much attention for their ultra-high measured quality factors. Their current method of
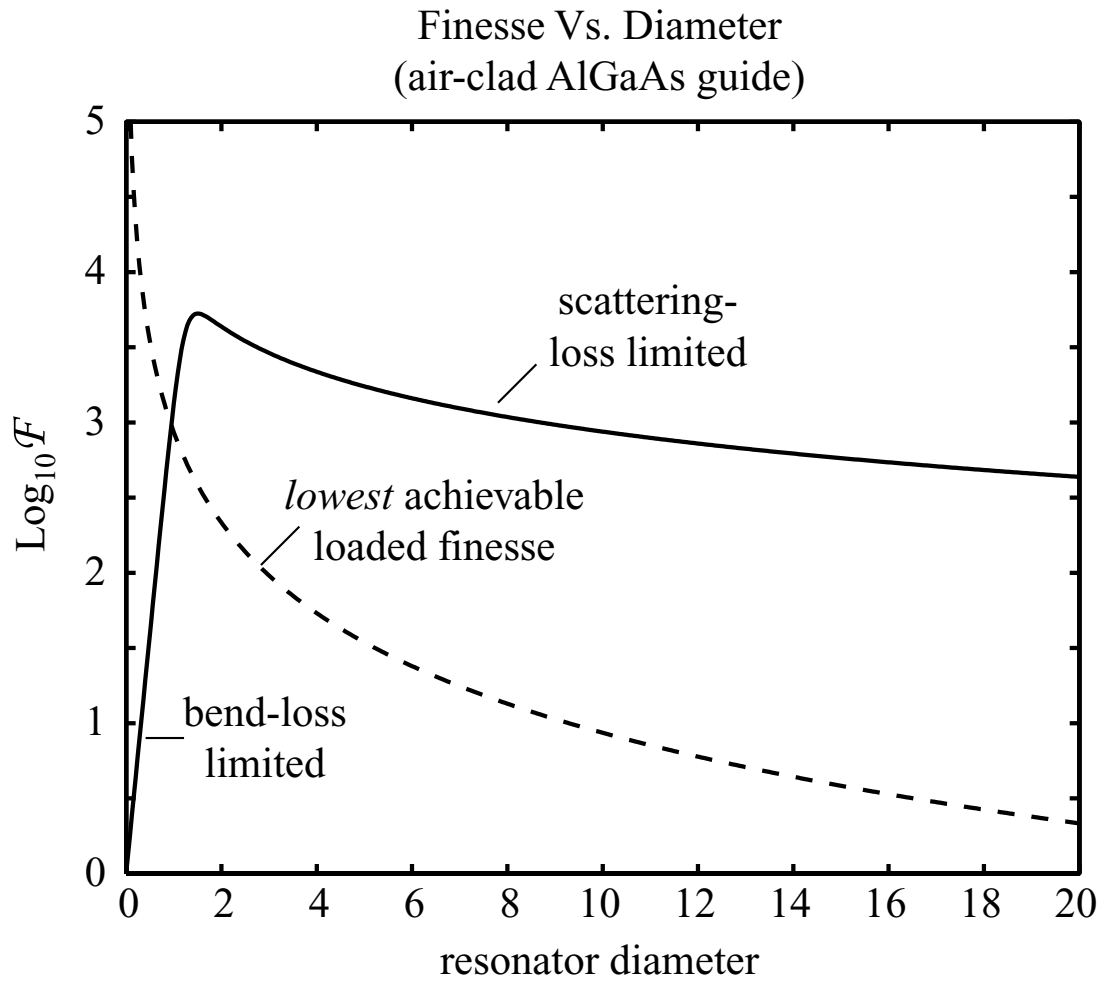
Figure 7.8: The loss-limited finesse (solid line) is dominated by bending loss for low diameters and scattering loss at high diameters. Because the finesse is dictated by coupling and a small resonator only has a limit interaction region for coupling, a small resonator is characterized by a minimum loaded finesse (dashed line). The desirable overcoupled regime can only be obtained for diameters greater than 1 micron. The greater the separation between the curves the better the prospects for obtaining a low-loss resonator.

production relies on melting silica (usually a fiber tip) and allowing surface tension forces to reshape the liquid glass into a sphere which is then allowed to cool. Unfortunately, this method does not allow for the fabrication of spheres of reproducible diameters, nor does it allow for spheres much smaller than 20 microns. Microdisks and rings constructed using the techniques of nanofabrication however, can be fabricated reproducibly to designed dimensions down to 1 micron. The main drawback of planar fabricated microresonators is the surface roughness left on the edges due to etching processes which result in resonators of much lower quality factors. Fortunately, the ideas presented for photonic devices in this thesis do not rely on the requirement of ultra-high Qs but rather modest values around 1000.

A ring has two bounding edges which can be used to properly design a single-moded guide. A disk only has one bounding edge - the other boundary is an effective one arising from an inner caustic. As a result, a disk possesses roughly half the scattering losses than that of a corresponding ring geometry but is multi-moded. If the FSR is high, and/or the side coupling guides preferentially couple to one of the radial modes of the disk, then disks are preferable. If not, then a ring geometry is better and the extra loss must be taken into account. [153]

## 7.4 Actual Design

Figures 7.10 and 7.11 illustrate both the designs for the vertically grown MBE structure and the lithographically patterned horizontal structure as designed for experimentation.

In early designs, a relatively high index contrast was used to guide light vertically. It was later realized that this is in fact unnecessary and only makes the guided modes possess small effective heights and high numerical apertures rendering coupling into them difficult. In order to confine light in a tightly bending resonator, it is only necessary that the lateral index contrast be high. Furthermore, in order to make the guides single moded laterally and maintain high lateral coupling by exposing a higher fraction of the evanescent tail of the modes, the guides would have to be very thin laterally. This still makes it difficult to couple a significant fraction of light from free space or low N.A. single mode fiber. However, while it is difficult to taper the guides out in the vertical dimension it is straightforward in the lateral dimension. Thus, in summary, the difficulty of input coupling was eased by making the guides possess a reasonably large yet singly-moded low N.A. in the vertical dimension and a tapered, initially highly multi-moded high N.A. in the lateral dimension.

Three methods were used to independently solve for the mode propagation constants and the coupling coefficients. Because a full three-dimensional simulation of the photonic structures is too numerically intensive to be practical, approximate

methods were used to reduce the dimensionality of the problem. One method employed consisted of using a finite-element solver (FEMLAB) to solve for the 2D modes and coupling coefficients associated with the cross-section of a pair of waveguides. This was found to be most useful for determining the coupling coefficient (per unit length) of a Mach-Zehnder interferometer which could then be integrated (along $z$) to find the requires coupling length for a desired coupling coefficient. This method was not feasible for the problem of determining the coupling associated with a waveguide and resonator because the coupling per unit length varies longitudinally, peaking in the vicinity of the gap. The method employed for determining the resonator coupling coefficients thus involved first reducing the problem to two dimensions by employing the effective index method. This method is implemented by first solving for the propagation constants of equivalent planar waveguides of regions that possess similar vertical guidance. Once the propagation constants for differing regions is known, an effective vertical refractive index is assigned to them and the problem eliminates any further need to calculate along the vertical dimension. These effective indices are then used to model the photonic structure in two dimensions from a top view perspective using a finite difference time domain (FDTD) solver. By measuring the power associated with fields coupled into a ring or disk resonator after a single round-trip, the FDTD method readily gives estimates of the coupling coefficient.
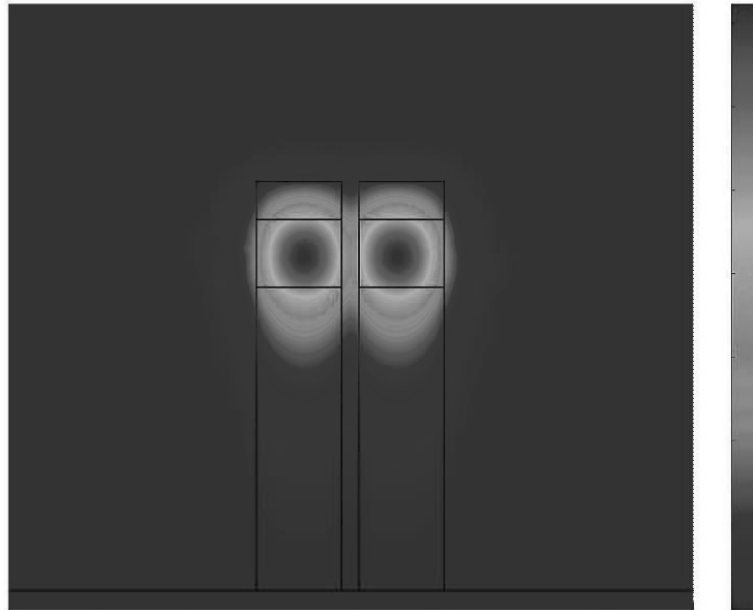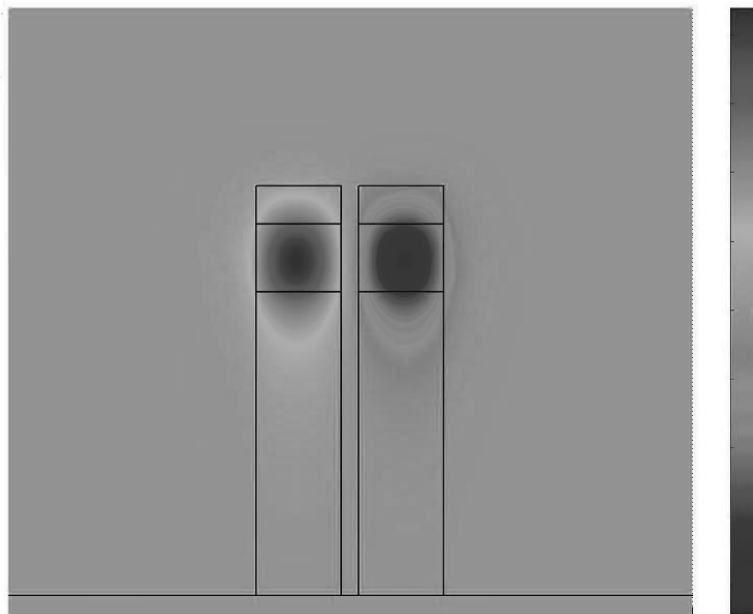
Figure 7.9: FEMLAB finite element simulation of the normal modes of the designed structure. The symmetric and antisymmetric modes propagate with different propagation constants such that their spatial beat length is directly related to the distributed coupling strength.

# Vertical Design

Not drawn to scale
All dimensions in microns

| refractive index | layer composition | structure |
|---|---|---|
| $n = 3.10$ | $Al_{0.62}Ga_{0.38}As$ | 0.5 |
| $n = 3.22$ | $Al_{0.36}Ga_{0.64}As$ | 1.0 |
| $n = 3.00$ | $Al_{0.80}Ga_{0.20}As$ | 2.0 |

GaAs
(substrate)
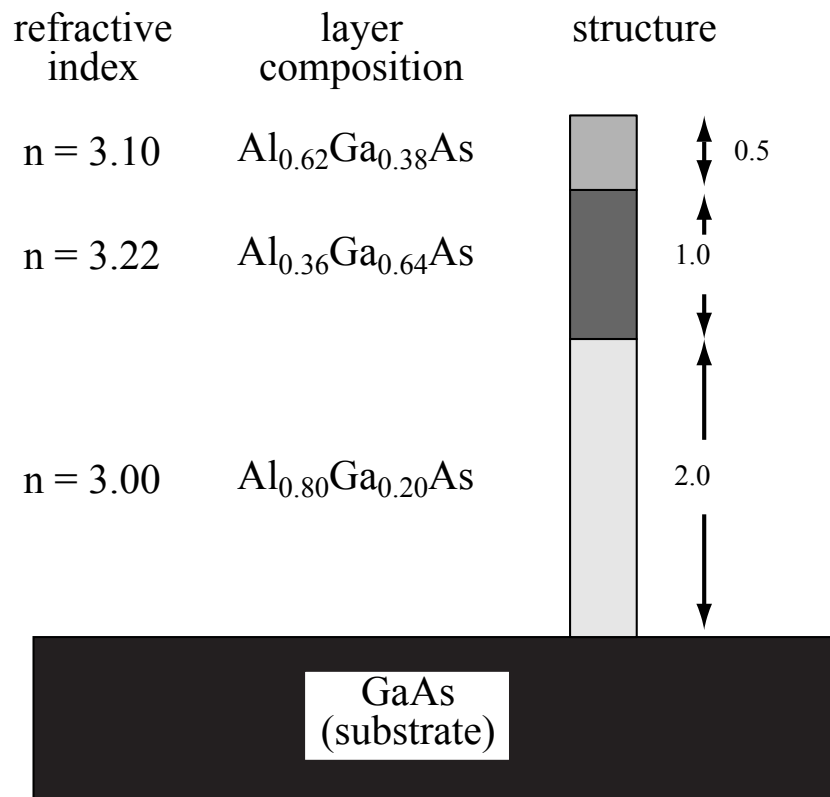
Figure 7.10: Vertical design of resonator structures constructed via molecular beam epitaxy for this work.
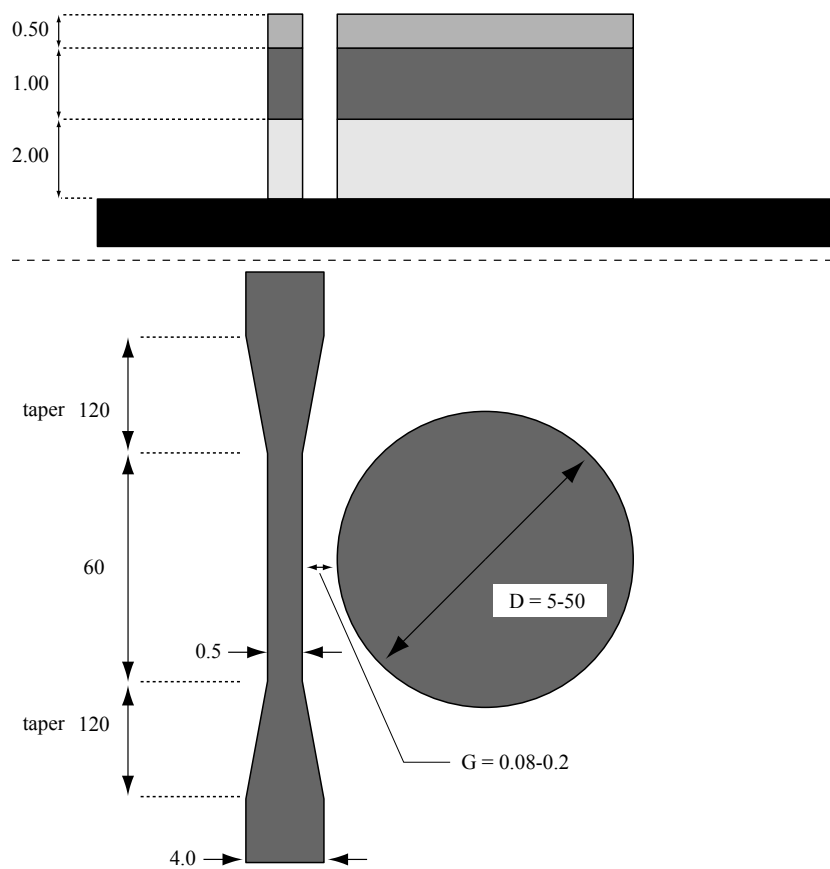
Figure 7.11: Lateral design of resonator structures constructed via nanofabrication tools.

## 7.5   Summary

This chapter examined the relevant material and structural parameters encountered when designing a high-bandwidth nonlinear microresonator-based photonic device.  Optimal design solutions exist in general but the number of considerations is high enough such that generalizations are difficult to make.  Reasons for the choices made in the design of microresonator-based devices for this thesis were examined and for some reduced parameter spaces, optimal solutions were found. The next chapter is devoted to the attempted realization of the design strategies set forth in this chapter.

# Chapter 8

# Microresonator Fabrication

## 8.1  Introduction

A variety of microresonator-based devices were fabricated in AlGaAs. This chapter summarizes the pitfalls and successes encountered while developing processes used to construct these devices within the means of the nonlinear optics research group. Strict requirements on the fabrication tolerances are imposed by the design parameters detailed in the last chapter. The most critical feature is the guide to resonator gap width which controls the coupling and resonator finesse. Because sub-100nm resolution is required for the laterally coupled devices I intended to fabricate, electron beam lithography was required to define the patterns. The fundamental requirements on subsequent etching methods for transferring the pattern into the guiding structure are that they preserve the fidelity of the lithographically patterned mask and result in smooth and steep sidewalls. Excessive sidewall roughness leads to severe scattering losses which reduce the transmission

and finesse to unusable levels. While deviation from verticality in sidewall angle slightly distorts the mode profile, a more significant problem is the introduction of polarization rotation. This results because the principal axes are no longer parallel and orthogonal to the substrate. [154]

## 8.2 Process Development

The first stage of the process involved growing a vertically layered structure which would support guided waves. Structures corresponding to the design presented in the previous chapter were grown by Mike Koch and Professor Wicks via Molecular Beam Epitaxy (MBE). The target compositions were grown with a precision of 1 percent and an accuracy of 2 percent as measured by x-ray diffraction.

Most of the subsequent transverse patterning was performed at Cornell Nanofabrication Facility (CNF). In overview, the patterning procedure consisted of using electron beam lithography to raster a pattern in resist, transferring the resist pattern onto an underlying intermediate masking layer via reactive ion etching (RIE) and finally transferring that intermediate pattern into the AlGaAs structure via one of three highly anisotropic etching techniques. This two step transfer was required since the resist itself was not sufficiently robust to serve as a high-quality mask that could withstand either of the final chlorine-based etches of the AlGaAs directly.

During the development of the process procedure and tooling parameters, rel-

atively inexpensive GaAs wafers were used to simulate a vertically structured AlGaAs-GaAs sample. The first step in transverse patterning consisted of depositing the intermediate etch mask layer of $SiO_2$. Initially, a wafer was cleaned with acetone and isopropyl alcohol. A layer of $SiO_2$ was deposited via plasma enhanced chemical vapor deposition (PECVD) for a thickness of 300-800 nm[1]. Initially, part of the substrate was covered with a broken piece so that an estimation of the deposited height could be made with a (Tencor) profilometer. In general this did not result in accurate measurements since the deposited film tapered slowly away from the masked edge. Better results were obtained using a spectrophotometer (Leitz MVSP)[2]. The process parameters used for the PECVD (IPE inc.) closely followed recipes developed at CNF. They consisted of a process temperature of 240 degrees Celsius, pressure of 450 mTorr, $N_2O$ gas flow of 50 sccm, $SiH_4$ gas flow of 20 sccm, and an RF power of 4.5%. The recipe quoted a deposition rate of approximately 37 nm/min but was actually measured to be less. For a deposition time of 17.5 minutes, a layer of 500 nm was measured indicating an average deposition rate of only 20-29 nm/min.

Next, the desired patterns were transferred from computer based drawings to a resist atop the sample using electron beam lithography. E-beam lithography was chosen because its sub-100nm resolution (5 nm beam step) was required to

---

[1]Oxide layers of 300 nm were used for direct masking and layers of 800 nm were used as a support for chrome masking

[2]The film thickness could be estimated by gauging its color noting that a quarter-wave oxide layer gives peak reflectivity

define the resonator-to-guide gap spacings. A variety of electron beam sensitive resists were attempted (both positive and negative). Satisfactory results were only obtained with PMMA (positive) resist; negative resists (NEB-31, UVN-30) exhibited poor adhesion to the $SiO_2$ layer. Because pattern transfer to the intermediate oxide layer would later be accomplished by one of two ways (inverting and noninverting), the pattern was initially drawn either inverted (with trenches defining the guides [135,155,82]) or noninverted (with the guides drawn directly). Patterns were drawn in AutoCAD (DXF, version 12) and converted to machine readable format via the ebeam pattern generator (CATS). The PMMA resist was deposited in solution (4.0% in anisole solvent) via spin coating at 2200 RPM to approximately 180 nm thick and baked for 15 mins at 170 degrees Celsius to remove the solvent. A metal (non-diamond) scribe was then used to scratch a small trench into the resist on an unusable part of the substrate. The (Tencor) profilometer was used to estimate the resist height. The measurements typically matched very well with empirical spin-curve predictions. An electron beam lithography tool (Leica VB6) was then used to expose the resist at a beam current of 2-5 nA with a raster scan rate around 25 MHz (depending on the actual dose) and a pixel step size of 5 nm (VRU=1). A dose matrix trial of varying exposures on simple test patterns was run prior to each run to determine the optimum electron beam dose needed to fully expose the resist. Underexposed patterns exhibited narrower trenches - especially near the trench bottoms. Overexposed

patterns shrunk the width and reduced the height of small nearby features such as resonator to guide gaps. Additionally, proximity effects due to backscattering of electrons off the substrate floor overexposed certain areas of resist in the neighborhood of widely exposed areas. Subsequent CAD drawings were modified to mitigate this effect by making trenches no wider than 1.25 microns and keeping critical dimensions away from wide trenches. A beam dose of 600-700 $\mu C/cm^2$ was typically found to be optimal though varied from run to run. Exposures typically lasted 30 mins to expose roughly 100 devices coupled to 3 mm long bus guides defined by 1.25 micron wide trenches on either side. Faster write times were found when exposing patterns directly since the guides were much smaller then the trenches. After exposure, the resist was developed in a 1:1 solution of methyl isobutyl ketone (MIBK) in isopropanol for 1 minute to remove the exposed areas defining the trenches.

After development, the wafer surface was cleaned with isopropanol and descummed with an oxygen plasma (Branson barrel etcher) for one minute to remove approximately 10 nm of resist and remaining residue in exposed regions. Patterns were inspected under optical microscope at up to 250X to ensure that the overall pattern had been exposed correctly. Scanning electron microscopy (SEM, Leo 982) and atomic force microscopy (AFM, Digital Instruments) were then used as primary diagnostics for the measurement of etched guide widths, trench widths, and most importantly, coupling gap widths.

The process procedure branched at this point into two alternate methods completing the transverse patterning of AlGaAs. In the first method, a reactive ion etch of the oxide using the resist as a masking layer resulted in a noninverting pattern transfer. In the second method, chrome deposition, liftoff, and reactive etching resulted in an inverting pattern transfer. The final etching of AlGaAs was performed by collaborators. Figures 8.1 and 8.9 visually depict these procedures.

## 8.3 Noninverting Pattern Transfer

The PMMA resist containing patterned trenches bordering guiding regions provided a suitable etch mask by which to transfer the trenches into the underlying oxide layer. A reactive ion etcher (Applied Materials) was used to etch the $SiO_2$ using $CHF_3$. The parameters used were 30 sccm gas flow, 30 mTorr pressure, and 65% RF power. An etch selectivity of 2:1 was measured and was sufficient to etch completely through oxide layers of about 300 nm. The etch rate was approximately 30 nm/min. Samples were slightly over-etched to ensure that the AlGaAs floor was in fact reached. Following the RIE etch, the resist was no longer needed and was thus stripped completely with an oxygen plasma (Branson/IPC P2000 barrel etcher) for 5-10 mins.

In order to properly nanofabricate any photonic device, it was imperative that each step of the process procedure be characterized thoroughly before attempting an actual process run on an MBE-grown sample which was in low supply and

# Photonic Microresonator Fabrication Procedure #1

(1) MBE growth



AlGaAs
structure

(2) Deposit oxide



Oxide (SiO$_2$)
AlGaAs
structure

(3) Spin-coat e-beam resist



PMMA
Oxide (SiO$_2$)
AlGaAs
structure
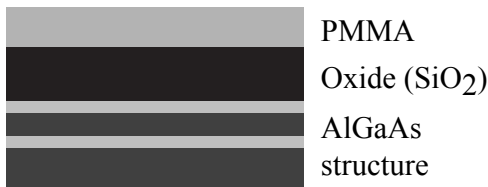
(4) Pattern inverse with
     e-beam & develop



PMMA
Oxide (SiO$_2$)
AlGaAs
structure

(5) RIE etch oxide



PMMA
Oxide (SiO$_2$)
AlGaAs
structure

(6) Remove PMMA



Oxide (SiO$_2$)
AlGaAs
structure

(7) CAIBE/ECR etch AlGaAs



Oxide (SiO$_2$)
AlGaAs
structure
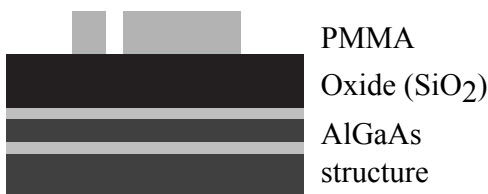
(8) Strip oxide



AlGaAs
structure

Figure 8.1: The first procedure developed to fabricate microresonators. Here, the lithographically defined patterns form voids in a mask which become trenches after etching.
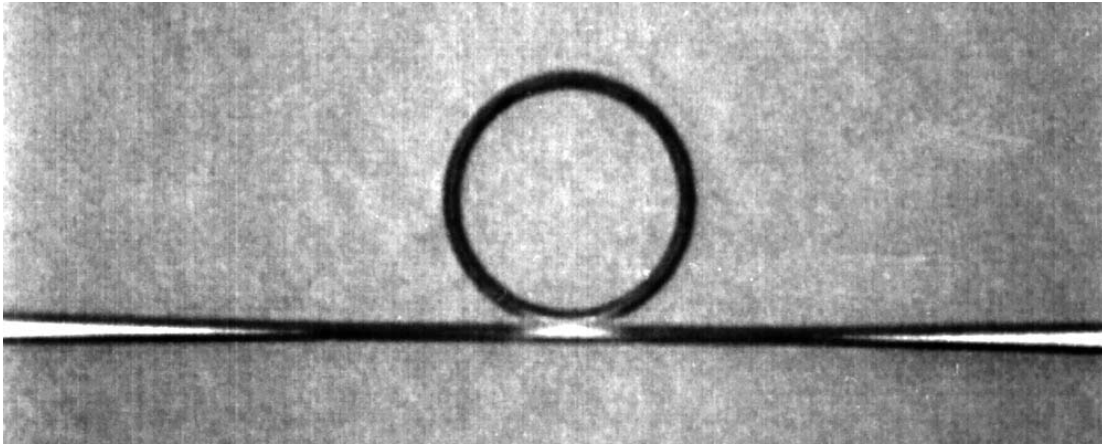
Figure 8.2: A micro-ring resonator pattern in PMMA resist.

costly. Characterization was largely accomplished on bare GaAs wafers and poor quality AlGaAs MBE growths.

The exposed patterns in PMMA resist typically looked good under optical microscopy; see for example figures 8.2, 8.3, and 8.4. The sidewalls of the developed resist, however possessed a slope of about 45 degrees. This limited the actual resolution in an amount proportional to the resist height. However, because the SiO2-to-PMMA etch selectivity was only 2:1, some thickness of resist was needed. A resist height of 180 nm proved to be a good compromise. Because the CHF$_3$ RIE etch provided a 2:1 etch selectivity, the sidewall slope was slightly magnified (compare figures 8.5 and 8.6).

The resulting patterned oxide layer was then used as a mask to etch trenches into the AlGaAs completely defining photonic devices. The final etch into the AlGaAs was performed via one of two anisotropic dry etch methods primarily involving chlorine plasma.
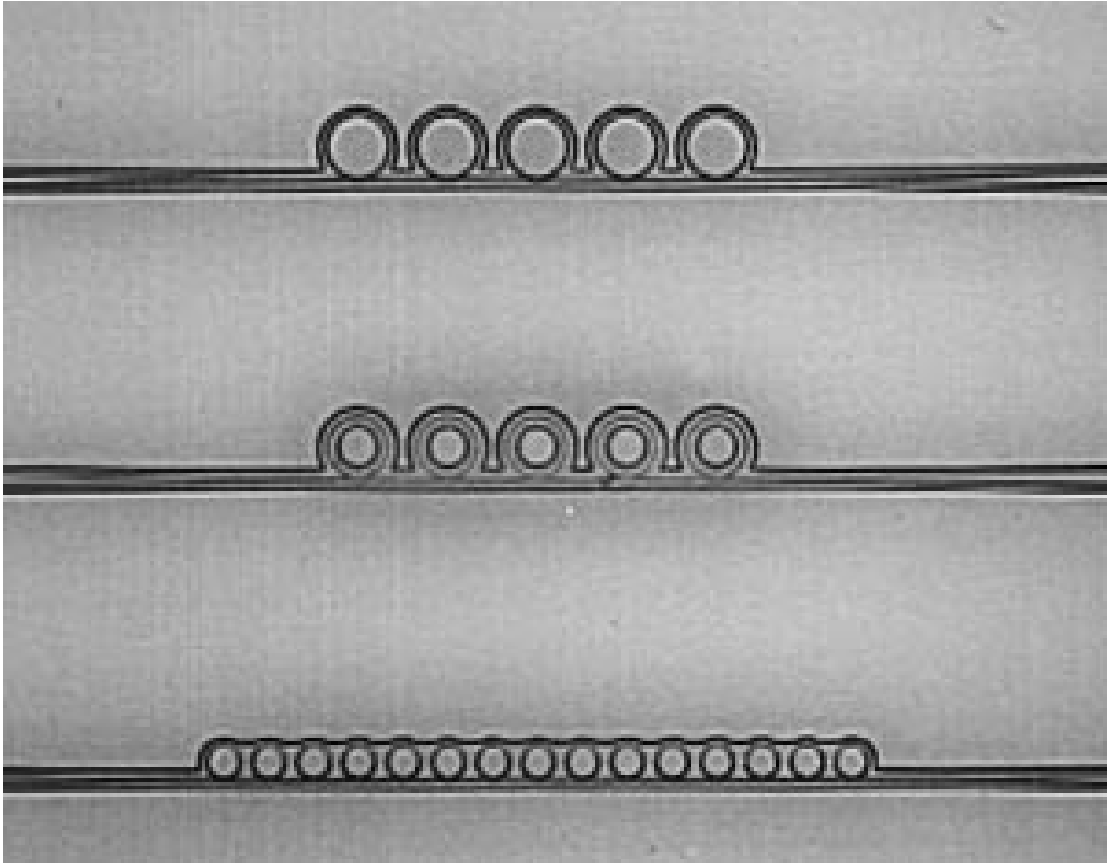
Figure 8.3: A few patterned SCISSORs in PMMA resist.
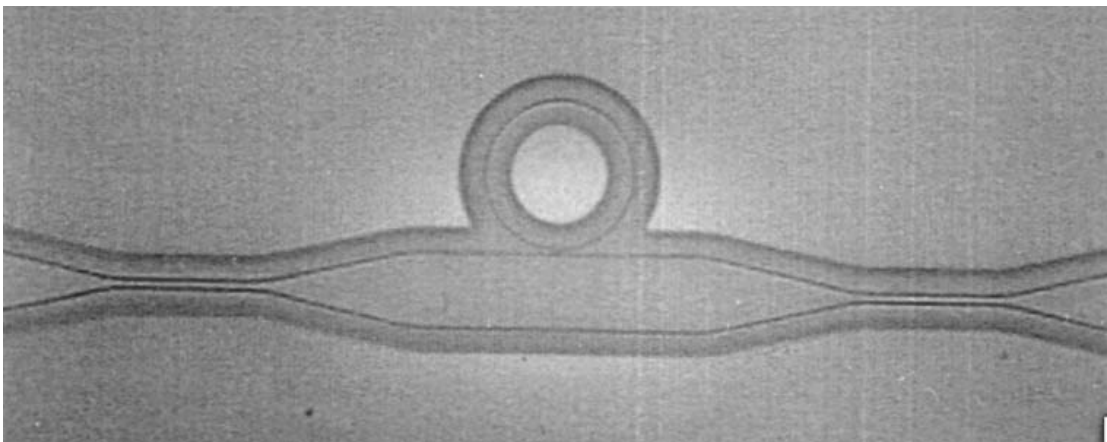


Figure 8.4: A resonator enhanced Mach-Zehnder interferometer in PMMA resist.
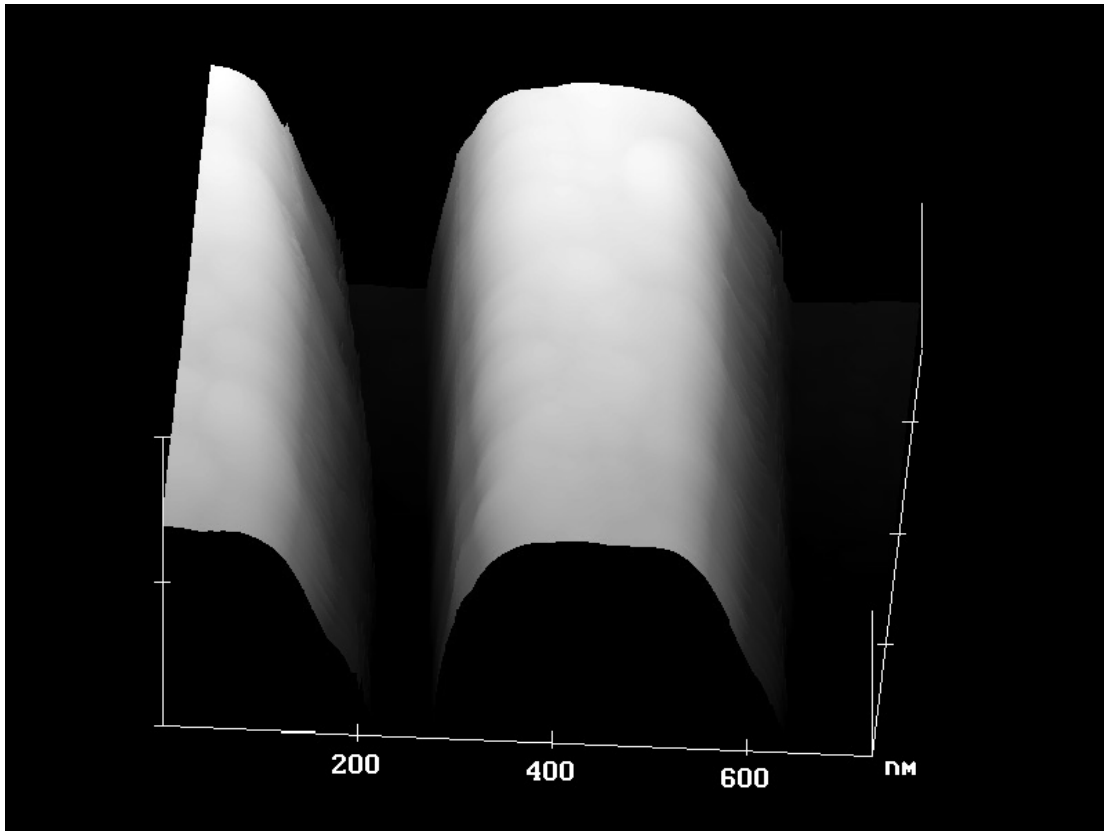
Figure 8.5: Atomic force microscopy (AFM) image of a resonator gap after electron beam exposure and development of PMMA resist.
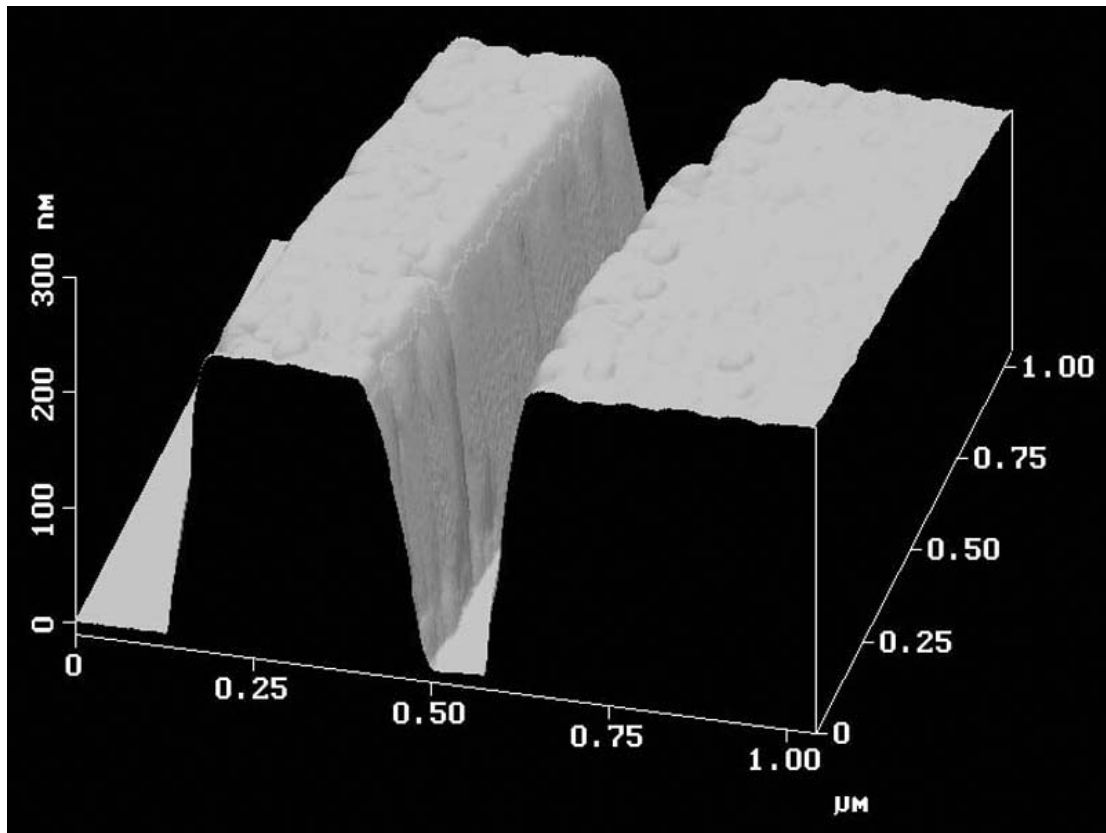
Figure 8.6: Atomic force microscopy (AFM) image of a resonator gap etched into $SiO_2$ via reactive ion etching using $CHF_3$.
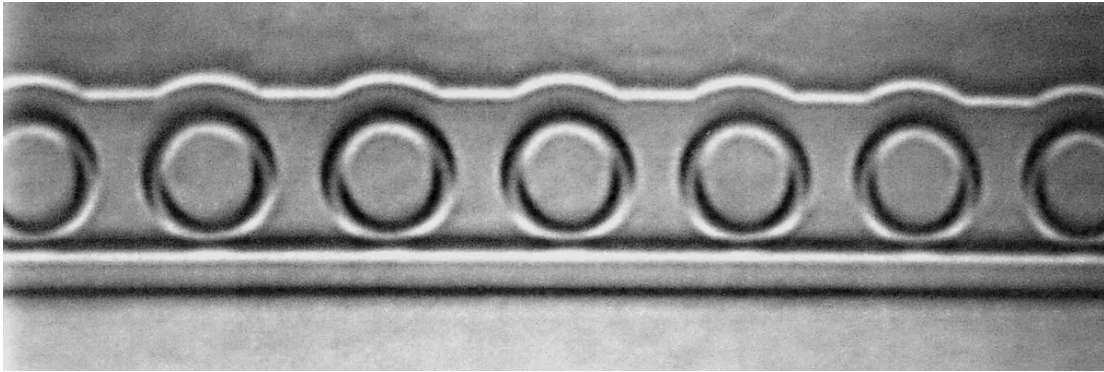
Figure 8.7: A fabricated SCISSOR.

The first method tried held more promise due from reports in the literature but ultimately failed for extrinsic reasons.   BinOptics housed and operated a CNF-owned Chemically Assisted Ion Beam Etching (CAIBE) machine on which CNF users could have their samples etched by their technician.   The parameters used were developed by BinOptics and consisted of a sample temperature at 120 degrees Celsius, pressure of 54 $\mu$Torr, Cl flow of 20.74 sccm, Ar flow of 5.4 sccm, beam current of 74 mA, beam voltage of 500 V, beam current density of 0.325 mA/cm$^2$, for a total time of 7 minutes (2 microns).   Only one out of five samples turned out to be guiding.   The inconsistency associated with results (and use of) this particular tool ultimately forced its abandonment.   Figure 8.7 shows an image of a SCISSOR which looks good under optical microscopy but does not show the roughened surfaces that resulted in high losses.

The second method tried was performed by Rebecca Welty at Lawrence Livermore National Laboratory.   An electron-cyclotron resonance (ECR) etch was performed with good results.   Process parameters included a sample temperature

of 25 degrees Celsius, chamber pressure of 1 mtorr, He backside pressure of 8 Torr,
Cl flow of 10 sccm, Ar flow of 40 sccm, microwave power at 850 W, RF power at
250 W, and an electromagnet current at 180 A for an etch rate of approximately
220 nm/min.  The etch profile could be tweaked to achieve vertical smooth side-
walls by varying the chamber pressure.  Figure 8.8 shows trenches etched around
a ring resonator in GaAs via the ECR etch.  The 10 $\mu$m diameter ring (guide
width=500nm) with a 100 nm gap width is etched here to 2 $\mu$m depth.   For
unknown reasons, however the same high quality etch could not be achieved on
guiding AlGaAs samples after multiple attempts.

## 8.4   Inverting Pattern Transfer

Patterns directly exposed and developed in the PMMA resist served as regions
onto which a chrome mask could be deposited.  The chrome was deposited on top
of the oxide layer which was accessible in the developed regions of resist (which
would later become the guiding regions).  Chrome was deposited via electron
gun evaporation (CVC SC4500) to about 40 nm.  When the PMMA resist was
lifted-off via acetone, the chrome was removed everywhere except for the desired
patterned regions.  Single layers of PMMA did not serve as good liftoff layers due
to a tendency of the chrome atop the resist to form a semi-continuous film with
the chrome sitting at the bottoms of developed regions.  A bilayer resist method
was used in which the lower resist layer developed isotropically faster leaving an
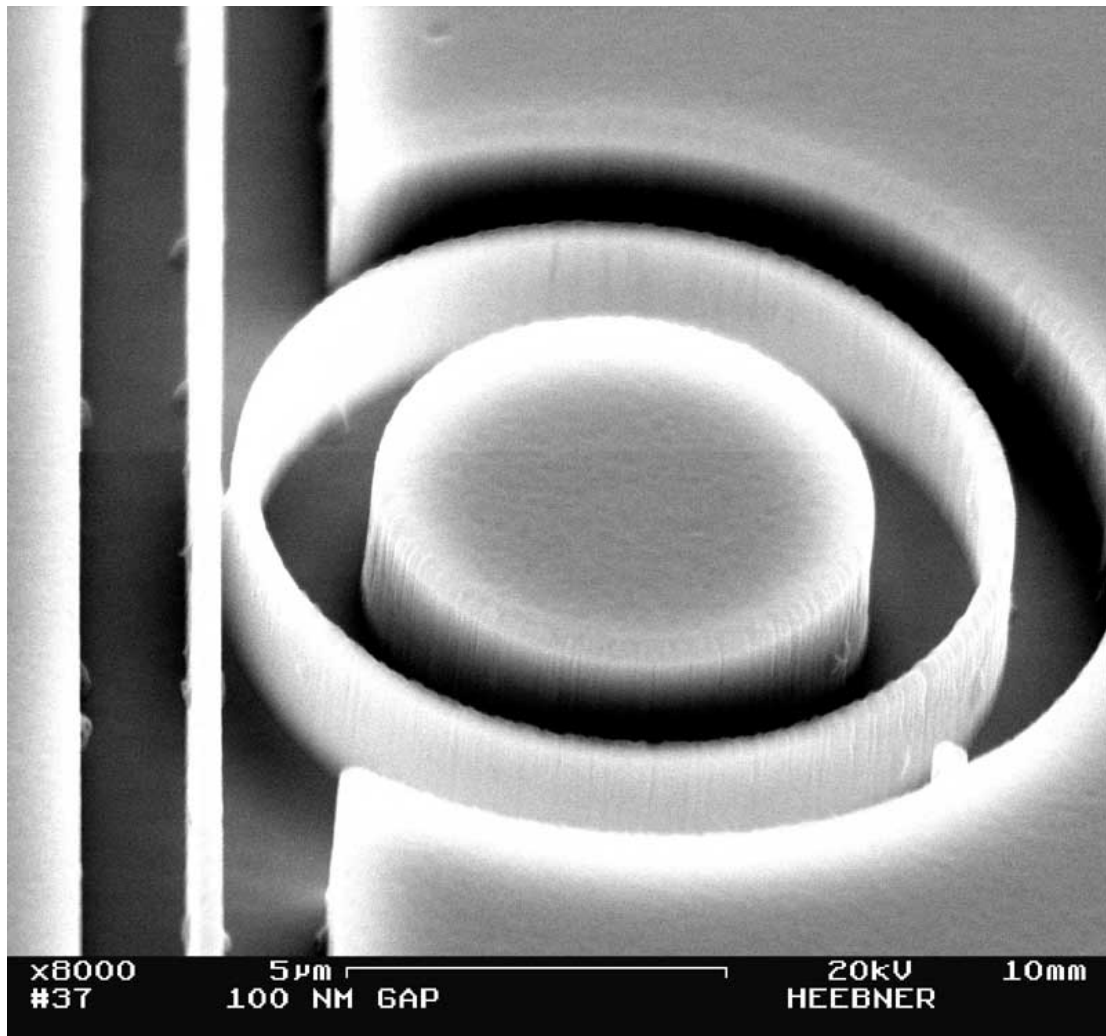
Figure 8.8: A 5 micron diameter all-pass ring resonator etched into GaAs with 500 nm wide guides and 100 nm coupling gap.

# Photonic Microresonator Fabrication Procedure #2

## (1) MBE growth

AlGaAs
structure

## (2) Deposit oxide

Oxide (SiO$_2$)
AlGaAs
structure

## (3) Spin-coat e-beam resist

PMMA
Oxide (SiO$_2$)
AlGaAs
structure
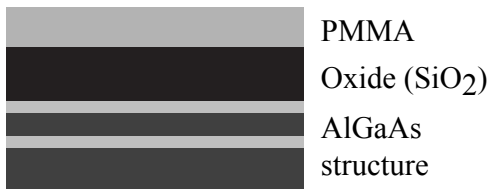
## (4) Pattern directly with e-beam & develop

PMMA
Oxide (SiO$_2$)
AlGaAs
structure

## (5) Deposit chrome

Chrome
PMMA
Oxide (SiO$_2$)
AlGaAs
structure

## (6) Liftoff PMMA

Chrome
Oxide (SiO$_2$)
AlGaAs
structure

## (7) RIE etch oxide

Oxide (SiO$_2$)
AlGaAs
structure

## (8) ICP etch AlGaAs

Oxide (SiO$_2$)
AlGaAs
structure
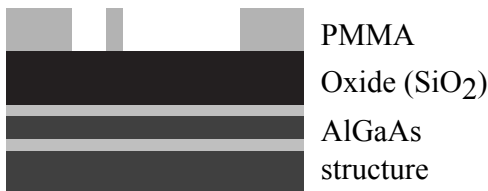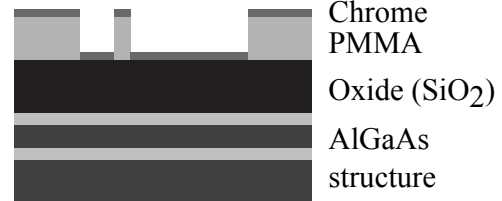
## (9) Strip oxide & chrome

AlGaAs
structure

Figure 8.9: The second procedure developed to fabricate microresonators. Here, the lithographically defined patterns form masking regions which become guiding structures after etching.

undercut which stifled this effect. The first (bottom) layer (100k MW 5%) was spin coated at 3000 RPM for a thickness of approximately 125 nm and baked. The second (top) high resolution layer (495k MW 4%) was then spin coated at 2600 RPM for a thickness of approximately 165 nm and baked. This bilayer method gave better liftoff results. Liftoff was subsequently improved via substituting a 60 degrees Celsius bath of 1-methyl-2-pyrrolidinone for the acetone. Care was taken to fully wash away all the chrome residue after liftoff. The patterned chrome served as a mask for reactive ion etching of the underlying 800 nm oxide layer. Finally, Cl based Inductively Coupled Plasma (ICP) etching was used to transfer the pattern into the AlGaAs. The etch was performed by Rohit Grover at Laboratory for Physical Sciences at the University of Maryland. Figures 8.10, 8.11, and 8.12 display SEM images of fabricated resonator based devices etched via ICP etching. Because these devices proved to be the best obtained, they were characterized optically. These experiments are described in the following chapter.

## 8.5 Summary

In this chapter, the process developed to nanofabricate microdisk and microring resonator based devices was described. Unfortunately, during the course of two years of nanofabrication, certain parameters drifted due to unknown causes. Specifically, the required electron beam dose and RIE selectivity drifted over time making it difficult to reliably fabricate devices with the extremely tight tolerances
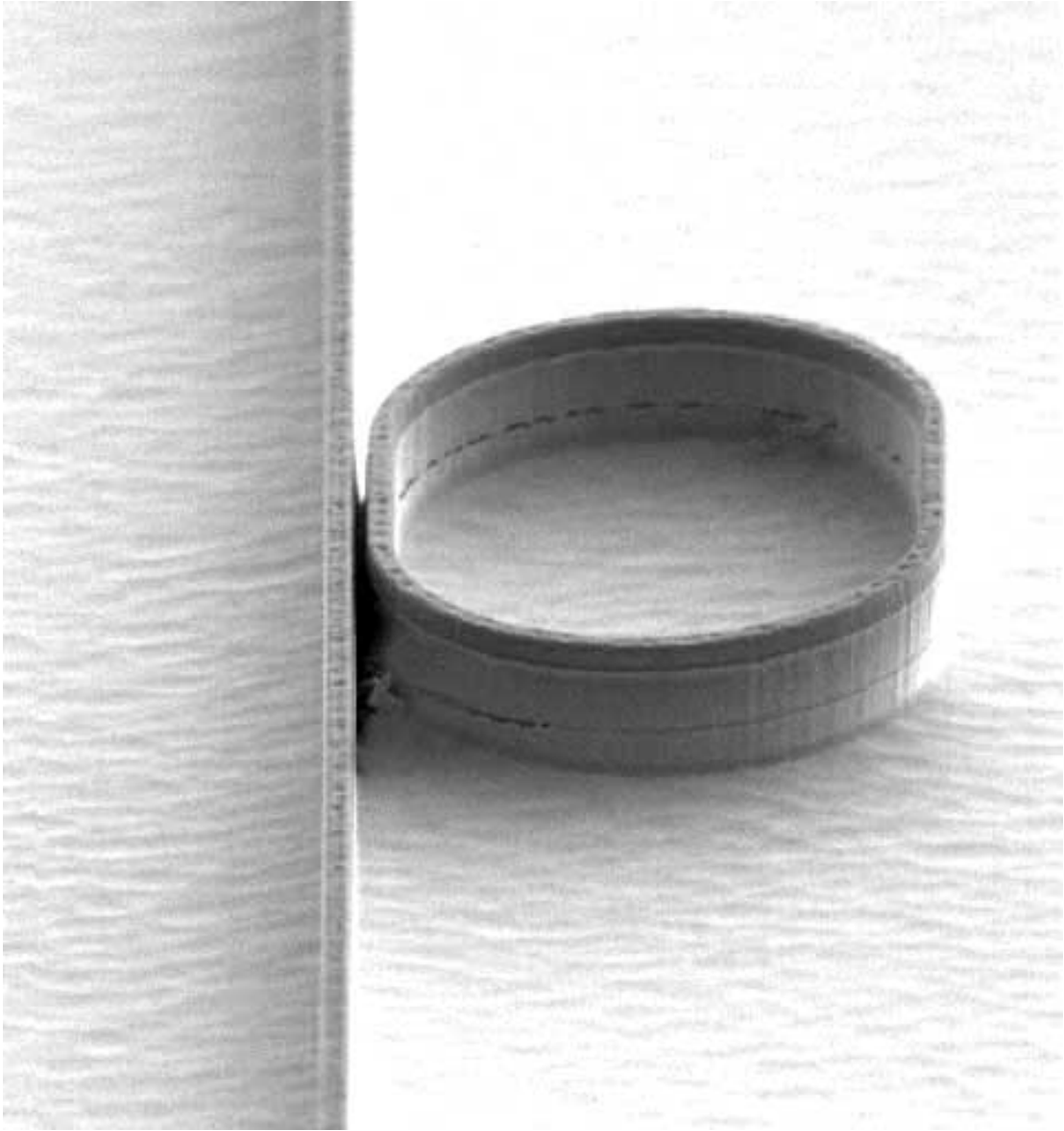
Figure 8.10: A 10 $\mu$m diameter all-pass racetrack ring resonator etched into guiding AlGaAs with 500 nm wide guides and a 100 nm coupling gap. The roughened top surface is from the leftover chrome mask.
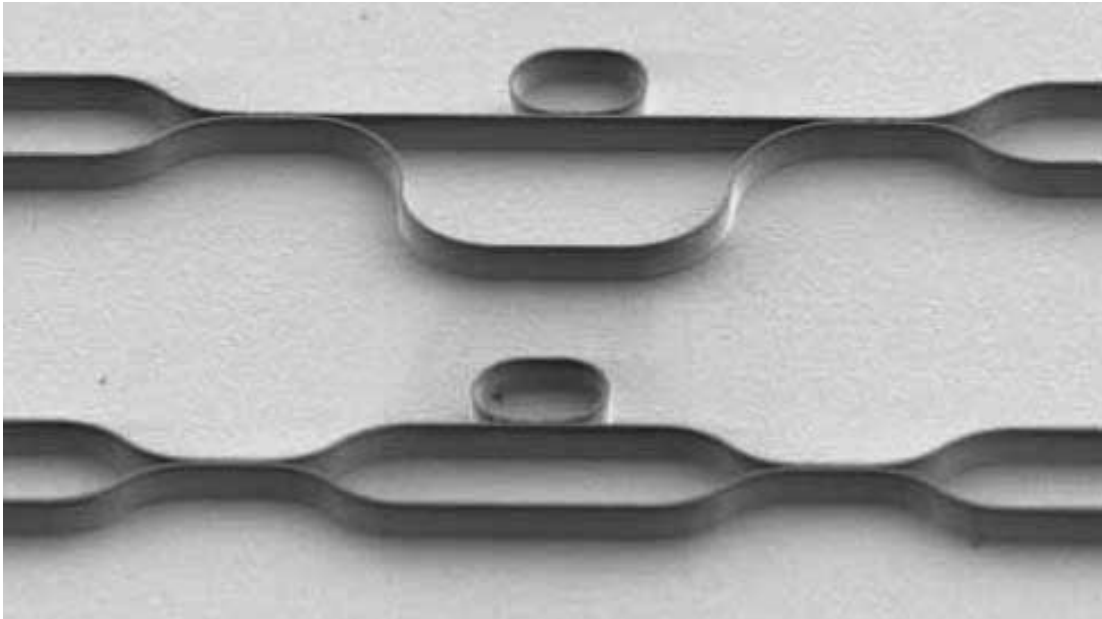
Figure 8.11:  A balanced REMZ and an imbalanced REMZ etched into Al-
GaAs.  The resonators are 10 $\mu$m diameter all-pass racetracks.

required to ensure the correct resonator coupling strengths.  Most importantly,
the critical final etch into the AlGaAs structure resulted in poor sidewalls after
most of the runs due to poor quality control.  Our turning to skilled technicians
for this final etch resulted in some decent etches and illuminated the difficulty
of fabricating these nanostructures.  Nevertheless, some devices were fabricated
close to design specifications.
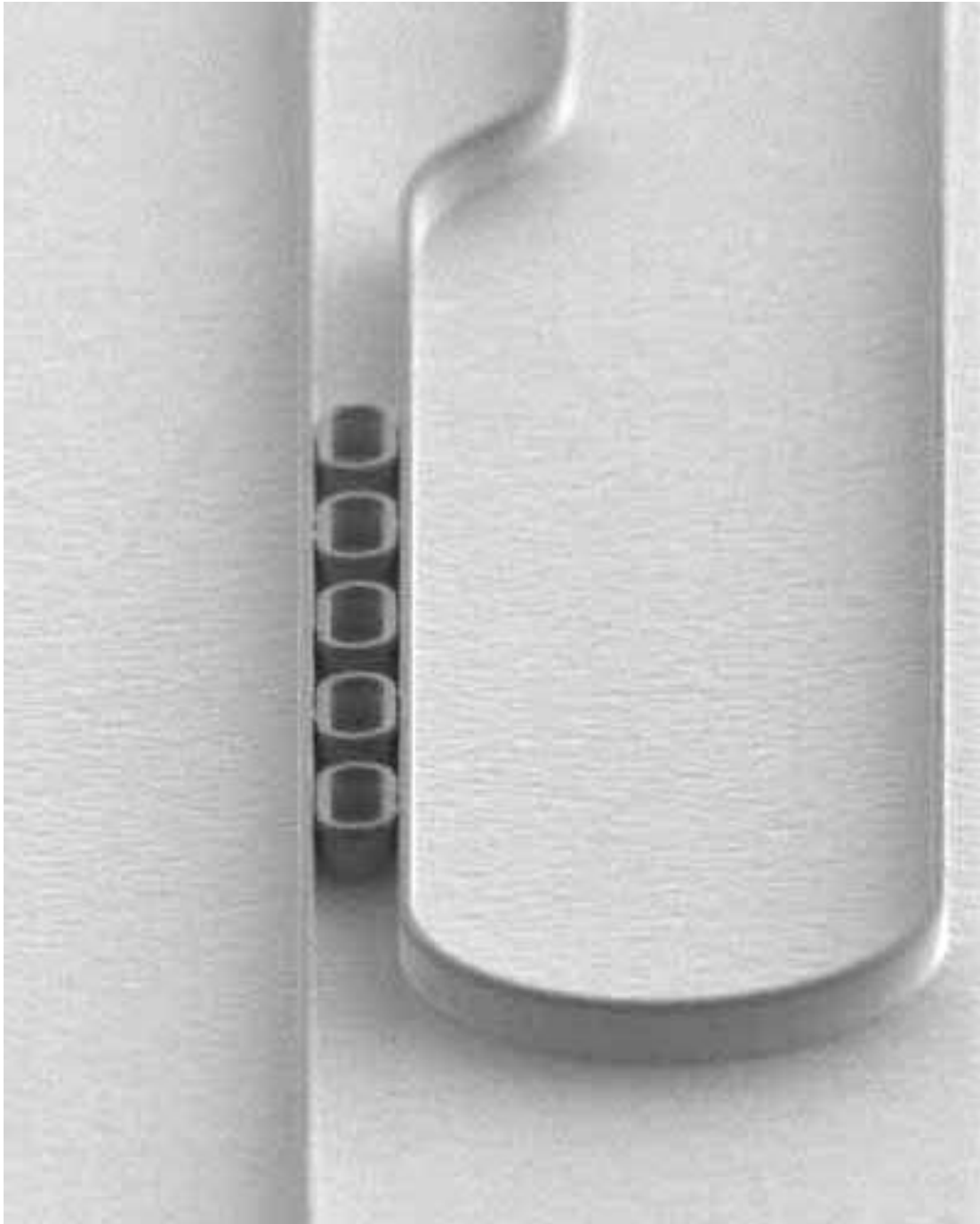
Figure 8.12: A double channel SCISSOR with 5X 5 $\mu$m diameter all-pass racetrack ring resonators etched into AlGaAs.

# Chapter 9

# Experiments

## 9.1    Introduction

This chapter describes the experimental effort to characterize the optical proper-
ties of fiber-ring-based and microresonator-based photonic devices.

## 9.2    Fiber Ring Resonator Experiments

A number of fiber ring resonators were constructed to demonstrate some of the
ideas presented in this thesis.

### 9.2.1    Fiber Ring Characterization with Tunable Coupler

An external cavity diode laser tunable from 1535-1575 nm was used to observe
spectral properties associated with resonances of a fiber ring resonator.    The
resonator was formed by fusion splicing one output of a tunable optical coupler
to one input port for a circumference of 31 cm.    The fused glass directional

coupler could be tuned by applying bending stress with a micrometer stub. A polarization controller was implemented prior to the resonator so as to excite with either in-plane or out-of-plane polarization but not both. The transmission of the resonator was measured versus wavelength for a variety of coupler settings. The laser wavelength was swept at 0.5 nm/s and the ring output was measured on an InGaAs detector and captured on a digital oscilloscope. Due to a finite single-pass loss in the ring resulting from losses in the coupler and fusion splice, the coupler could be tuned for under, critical, or overcoupled operation. Figure 9.1 displays the measured transmission spectra for a variety of coupler settings. Based on a measured finesse of 30 at critical coupling, it was estimated that the coupling and single-pass transmission parameters were $r \approx a \approx 0.95$. The single-pass loss resulting from the insertion loss of the coupler and splice loss was thus estimated to be $-10log_{10}(.95^2) = 0.45$ dB. A loss-limited finesse of 60 is predicted. In the first five traces, the finesse is low and primarily governed by strong coupling into the ring. In this overcoupled regime the resonator behaves qualitatively similar to a phase-only response. In the sixth trace, the coupler was set for critically-coupled transmission where the transmission is nearly extinguished at the resonances. In the remaining two traces, narrow dips appear at each resonance. In this undercoupled regime the finesse is primarily governed by the internal attenuation.

Next, the phase response of the ring resonator was measured by converting it into a measurable amplitude response. This was accomplished by inserting the

Fiber Ring Resonator
spectral transmission data vs. coupler setting
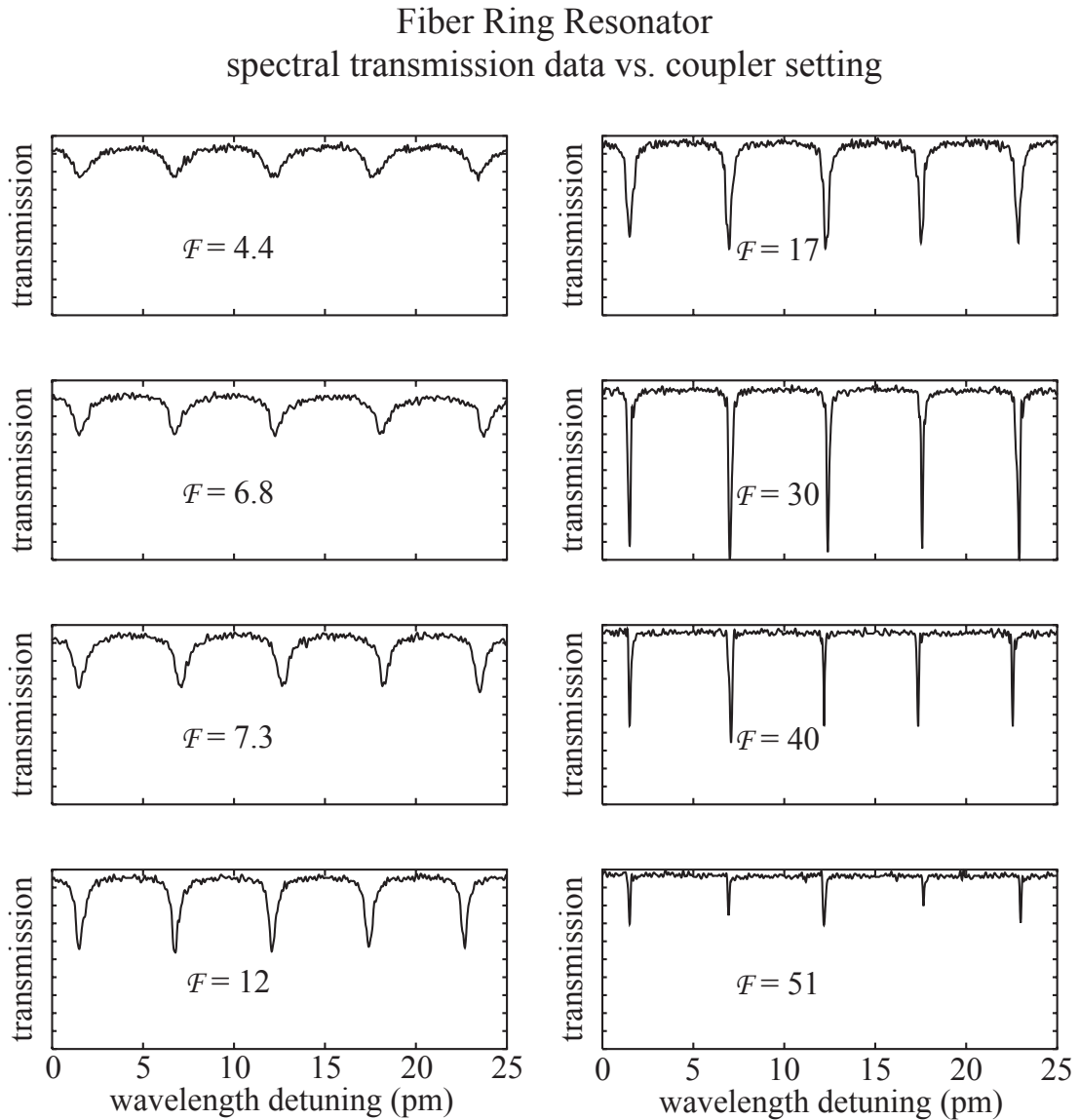


Figure 9.1: Measured spectral transmission for a 31 cm fiber ring resonator near 1.55$\mu$m for a variety of coupler settings. An FSR of 5.35 pm is in excellent agreement with the ring circumference measurement.

resonator into one arm of a nearly balanced Mach-Zehnder interferometer. The transmission of the resulting REMZ was then measured near 1.55 $\mu$m in a similar manner as described before. Figure 9.2 displays the measured transmission spectra for a variety of coupler settings. Due to a slight imbalance between the arm lengths of the Mach-Zehnder, the offset phase bias varies across the traces at a slower rate, $\phi_B \approx \phi_0/7.5$ than the detuning. Thus, in a single trace, different portions of the usual cosine-squared transmission response display increased phase sensitivity at the resonances. The ring resonances occur 7.5 times within the background Mach-Zehnder transmission periodicity. See figure 5.6 for comparison. Near over-coupled resonances (lower finesse values), the phase varies rapidly in a forward direction, advancing the phase by $\pi$ radians which has the effect of locally squeezing the cosine-squared curve. On the other hand, near under-coupled resonances (finesse values 40 and 51), the phase undergoes a wiggle which does not produce a net advance in phase. Figure 9.3 displays the phase responses that fit the data in figure 9.2.

Finally, the impulse response of the ring resonator for a variety of coupler settings was measured. A constructed figure-8 fiber laser H was used since the 1 ps pulses it generated were three orders of magnitude smaller than the ring transit time and thus approximated delta impulses. An InGaAs detector with a 20 ps rise time was used but the ultimate limitation on bandwidth was imposed by the 300MHz digital oscilloscope. The 1 ns resolution of the scope thus had

Fiber REMZ
spectral transmission data vs. coupler setting
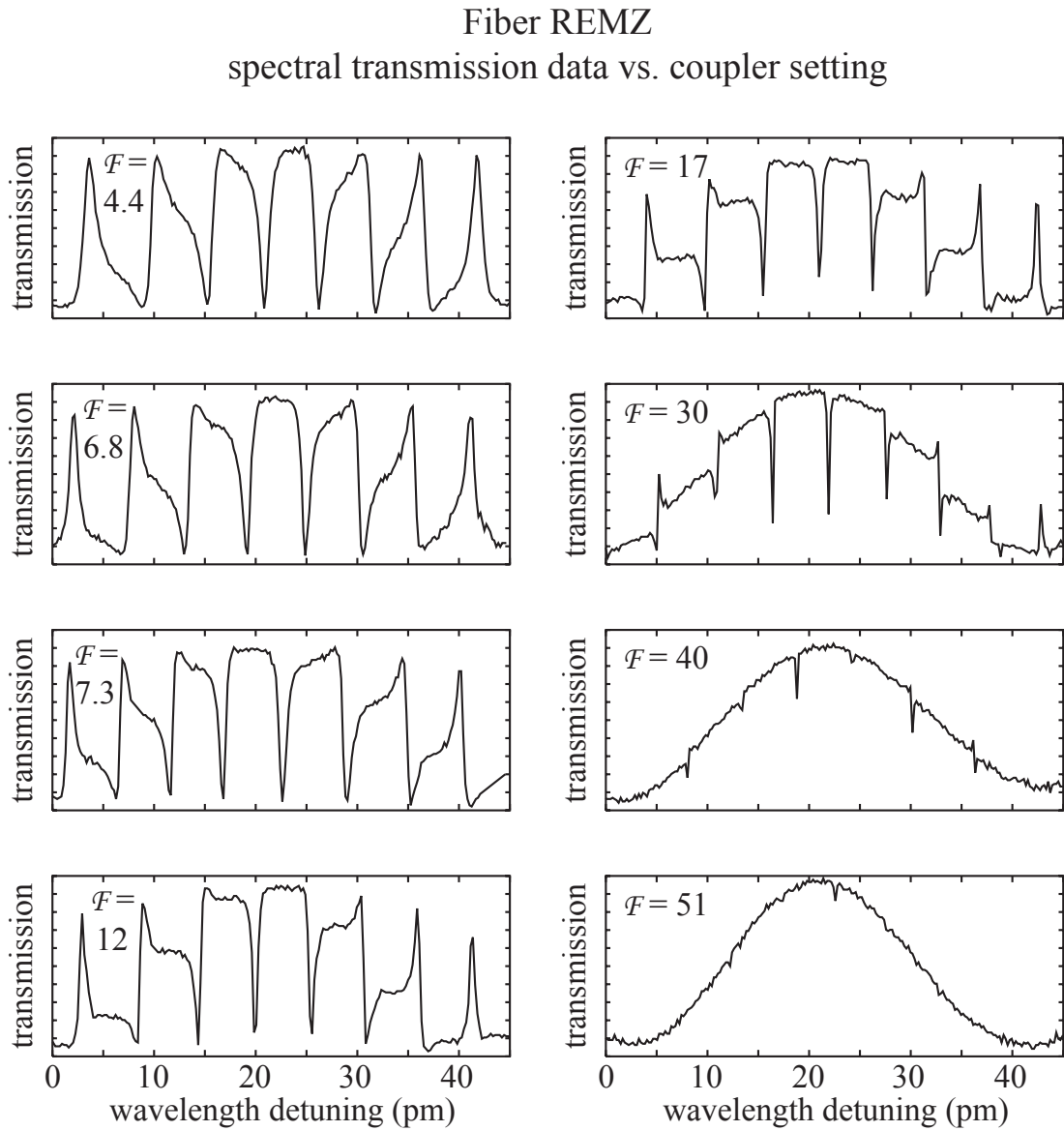


Figure 9.2: Measured spectral transmission for a 31 cm fiber ring resonator inserted into one arm of a nearly balanced Mach-Zehnder interferometer. Data was taken near $1.55\mu$m for the same coupler settings as in figure 9.1.

Fiber REMZ
fitted phase data vs. coupler setting
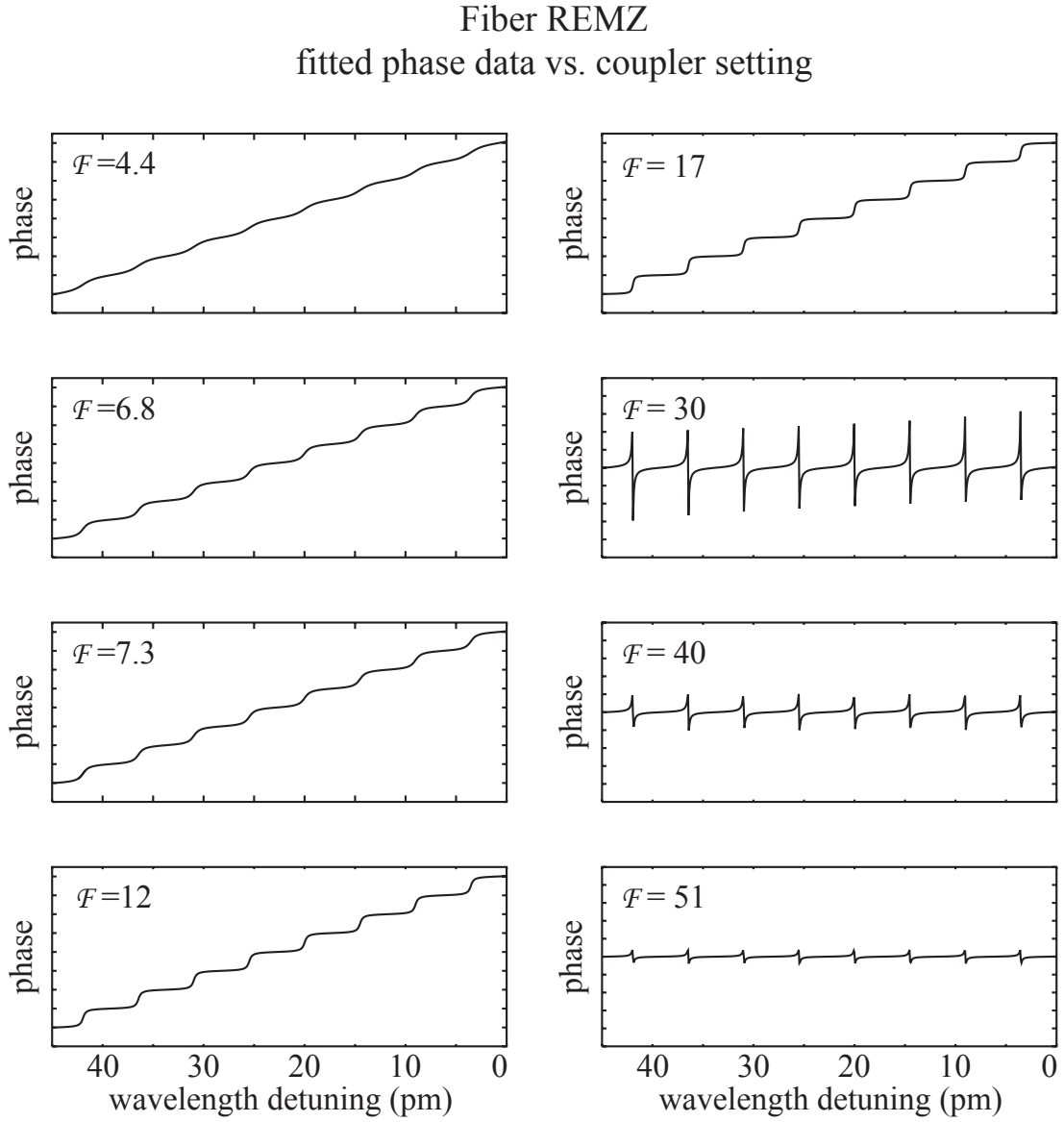


Figure 9.3: Phase responses which fit the data in figure 9.2.

the effect of blurring the data. Figure 9.4 displays the results of the experiment for various coupler settings. The ring circumference of 31 cm corresponds to a frequency FSR of 670 MHz or ring transit time of 1.5 ns and clearly corresponds to the distance between successive pulses emerging from the ring. For high finesse operation, most of the output power emerges in the first bypassed pulse. For very low finesse operation, most of the output power is instead contained in the second pulse which is delayed by a single round trip. It is only when the successively delayed emerging pulses are allowed to overlap in time and interfere constructively near resonance that coherent build-up and non-distorting delay can occur.

## 9.2.2 Fiber Ring for Optical True Time Delay

A second ring resonator (larger by a factor of 10) was constructed for the purpose of demonstrating tunable optical true-time delays. A dye laser tuned near 589 nm was coupled into one port of a 4 port directional coupler (single mode in the visible spectral region). One output port of the coupler was directly fusion spliced to the other input port forming a 3 m all-pass ring resonator. The coupling coefficient was 2/3 resulting in an ultra-low finesse resonator. A low finesse was employed so that it was easy to detect the resonances hiding within the thermal drift. Moreover, the fractional delay which was to be measured is independent of finesse. The optical power emerging from the output port was directed onto a silicon PIN detector and collected on a digital oscilloscope. Thermal drifts
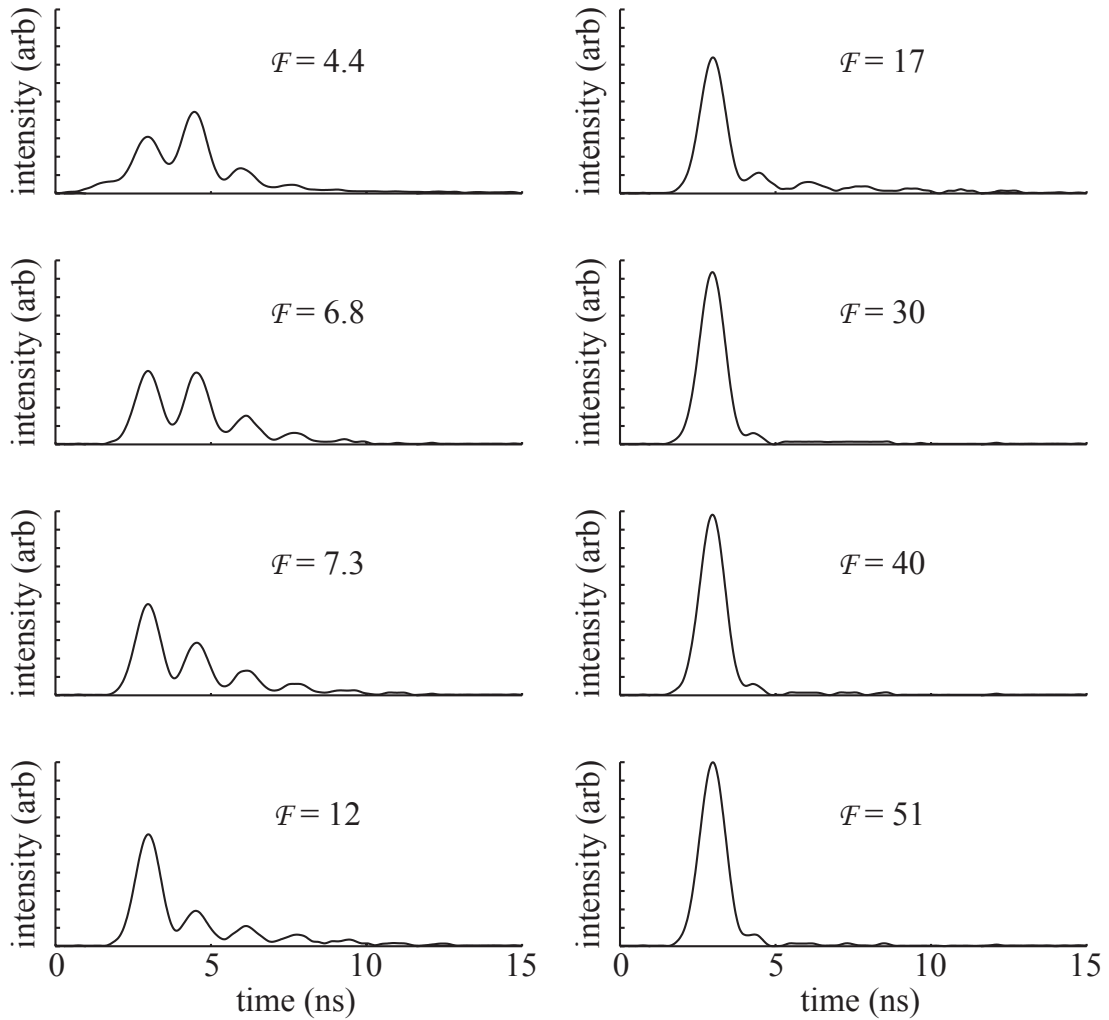
Figure 9.4: Measured squared modulus of the impulse response for a 31 cm fiber ring resonator. The finesse for each trace is based on the measurements on the transmission in figure 9.1. The pulse spacing of 1.5 ns corresponds to the calculated ring transit time.

in the ambient temperature caused the resonances to shift on a slow time scale (ms). These drifts were partially stabilized by immersing the fiber ring in a water bath at room temperature. The dye laser was then swept across a free-spectral range (70 MHz). An acousto-optic modulator was used to amplitude modulate the sweeping dye laser and generate 50 ns pulses. A beam-splitter picked off a fraction of the modulated beam for use as a trigger reference. As the laser frequency was swept through a resonance, the detected pulses emerging from the ring underwent a variable delay with respect to the reference pulses. Figure 9.5 compares the timing of an off-resonance pulse to that of an on-resonance pulse. In the experiment, a 51 ns pulse was delayed by 27 ns for a fractional delay of approximately 1/2.

## 9.3 Microresonator Experiments

A large number of microresonators fabricated as described in the previous chapter were characterized optically. Only a small number of them produced desirable results.

### 9.3.1 Sample Mounting and Optical Setup

In order to deliver light to the resonator-based devices, tapered bus waveguides were fabricated on the same substrate. The final preparation step needed before attempting to couple light into the guides was the cleaving of these guide end-
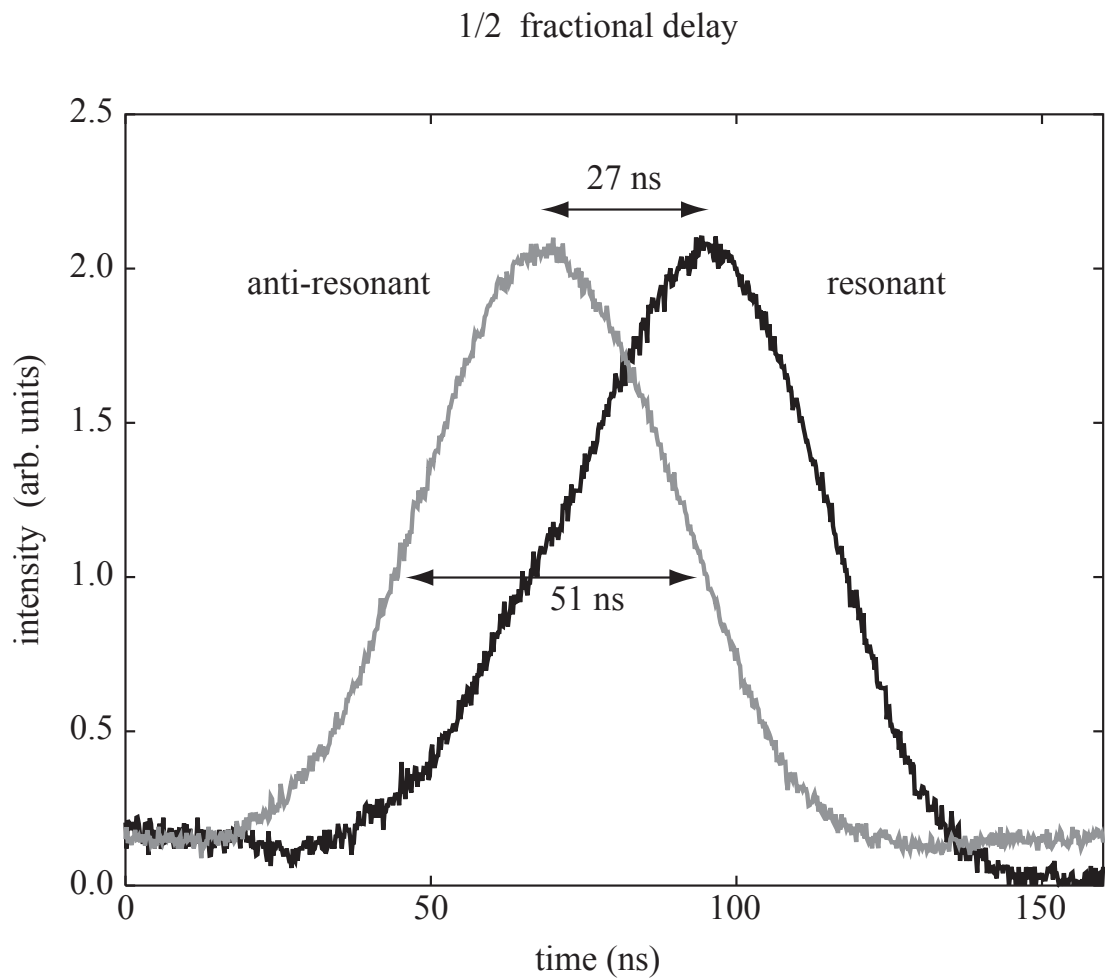
Figure 9.5: Demonstration of tunable optical delay in an all-pass fiber ring resonator. Here a 51 ns pulse is delayed by 27 ns for a fractional delay of 1/2.

facets. First, the guides were mounted in wax face down on a glass plate. The plate was then placed faced down onto an alumina-water slurry and ground until the substrate thickness was reduced from 500 to approximately 100 $\mu$m. This technique ensured that subsequent cleaves would result in high optical quality endfacets. The substrate was then scribed with a diamond tip and cleaved.

In order to successfully couple light into the chip-based fabricated devices, high N.A. microscope objectives and a rigid 3-axis translation stage, with sub-micron positioning accuracy were required. A coupling bench incorporating these components was constructed atop a 12"x12" breadboard for portability to many different laser systems available in different laboratories.

Light was accepted onto the stage as input from an (FC) connectorized fiber which was promptly collimated with a fiber to free-space coupling stage by a 10X (0.25 N.A.) microscope objective. The collimated light was guided by two mirrors into the input coupling objective (60X, 0.65 N.A.) which focused light down to a spot size diameter of approximately 1.5 microns. The 600 micron long samples were mounted on the edge of a glass slide or metal ribbon with wax (Crystalbond). Care was taken to prevent wax from accumulating on the endfacets. Due to the small size of the samples, sometimes this was not preventable. While the wax was easily dissolved in acetone, dipping the samples would often release them. Instead, an airbrush was loaded with acetone and used to thoroughly clean the endfacets without affecting the bonding. The mounted sample was then rigidly
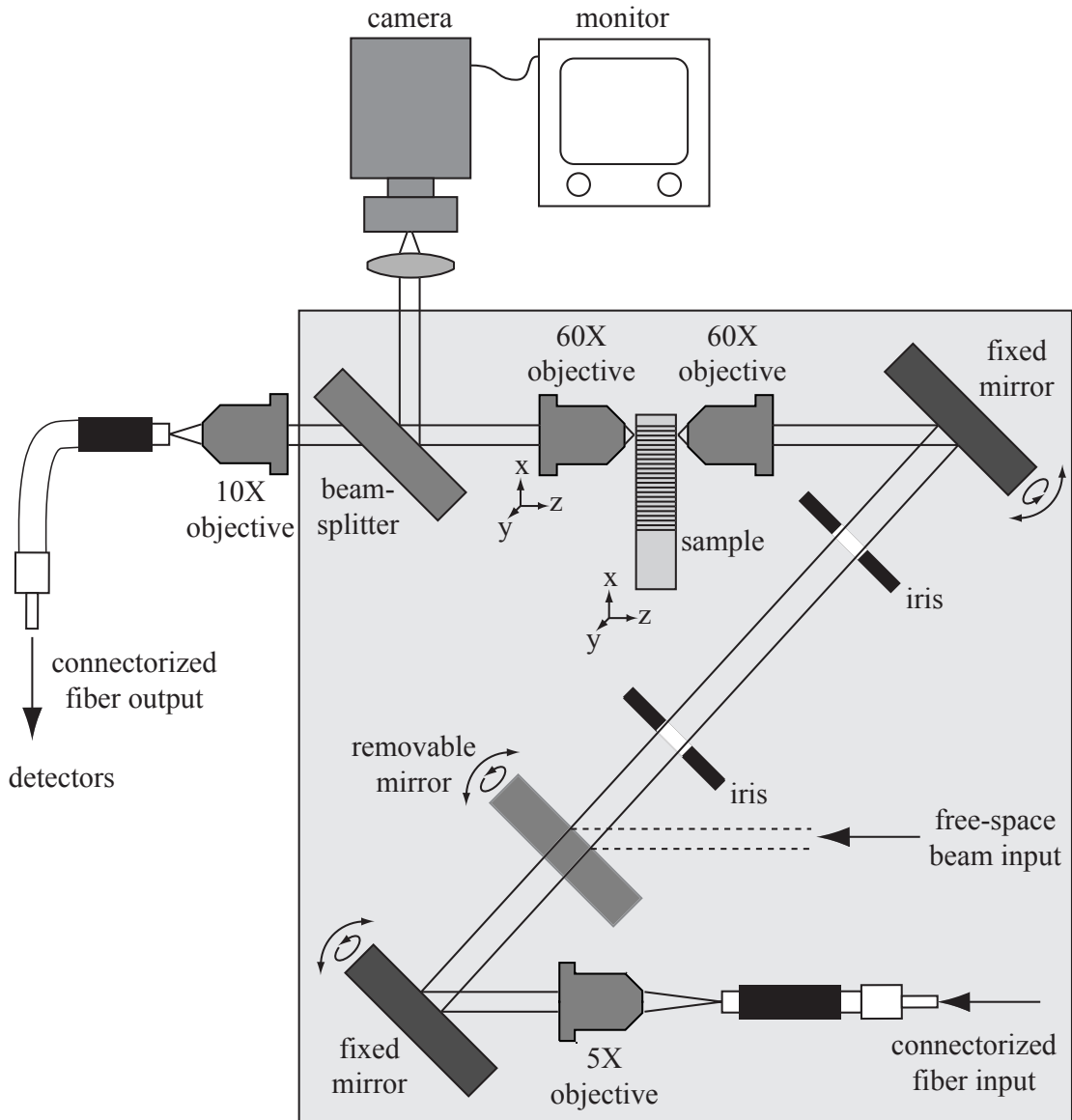
Figure 9.6: Optical setup built to couple light from either a fiber or free-space beam into the high-contrast waveguides leading to the microresonators. Different devices of roughly 100 per sample were accessed by translating the sample. Light exiting the guides was imaged onto a camera or collected and coupled back into a fiber and sent to diagnostic equipment.

mounted to a 3 axis translation stage operated by differential micrometers, each of which was scanned to find then tweaked to optimize the end-fire coupling of light into the individual bus waveguides. A milliwatt level cw diode laser was used for the purpose of finding the guides. Light was collected on the output side of the waveguides via another objective (60X, 0.65 N.A.) which imaged the cleaved sample endfacet onto an infrared camera (lead-sulfide vidicon). This would indicate whether light was actually propagating in a desired waveguide with optimal coupling.

Attempting to find the guides was initially analogous to looking for a needle in a haystack. In order to ease the process, certain degrees of freedom were consecutively eliminated in turn. First, the collecting (imaging) objective was focused on the output facet by imaging the edge surface under strong white light illumination. Next, the sample was translated laterally to a portion that did not contain any laterally patterned trenches and thus mimicked a planar waveguide (if present). The sample was then scanned vertically until light was seen to be spilling both above and into the sample substrate. The injection (illumination) objective was then translated longitudinally (with small vertical movements) until the splitting fraction of light was observed to be sensitively dependent upon the vertical translation. Typically near these conditions, an observable amount of light could be found to emerge from the vertically guiding structure or a patterned guide. Careful tweaking of the horizontal and vertical angles of entry could

then be employed to optimize the transmitted power. Finally, provided that the sample was mounted orthogonal to the stage axes, the sample was translated laterally until desired channel waveguide was found. Once a particular guide (of approximately 100 per sample) was found, the others could be excited by laterally translating the sample and subsequent re-tweaking.

Because it was not clear which waveguide was excited by simply looking at the position of the microscope objective and the 100+ array of waveguides with the naked eye[1], a top-down aimed inspection microscope was used to choose a particular guide for excitation. The fiber source was disconnected and replaced with another fiber source into which visible light from a red laser diode was coupled. While this light (within the band-gap) did not propagate in the guide, light scattered off of the input face was clearly discernible on the microscope and thus effectively marked the excitation guide.

## 9.3.2  Microresonator Characterization

Due to a strong dependence of all coupling coefficients with respect to incident polarization, a polarization controller was inserted before the coupling bench to select either TE or TM excitation. It was found that TM polarization had the best results due to lower losses as predicted. The transmission characteristics for a variety of devices were measured.

---

[1]To the naked eye, the array spaced at around 25 $\mu$m resembled a diffraction grating, to say nothing of the resonators which were for the most part indistinguishable from dust.

Spectral characterization of the microresonators was performed with the tunable diode laser near 1.55 $\mu$m. Minimum losses of the order of 10-20 dB throughput from facet to facet were measured. Losses due to Fresnel reflection at the interfaces were theoretically computed to be 3 dB. Losses due to imperfect mode-matching were determined to be of the order of another 3 dB. Looking from above with an infrared viewer, a large amount of unquantifiable scattered light was observed emerging near the input face. Perhaps higher losses were present due to imperfections on the cleaved facet. Losses due to propagation in the waveguides resulting from scattering off edge roughness made up the remainder. Despite the difficulty of fabricating low loss high index contrast guiding structures, spectral transmission traces of the devices displayed good agreement with theoretical fits. Figure 9.7 displays the spectral transmission data for the through port of an add-drop filter. Here, a racetrack resonator of 12.5 $\mu$m radius coupled to two waveguides on either side possesses a measured free-spectral range of 8.5 nm. A finesse of 10 is estimated from the data. The finesse turned out to be lower than designed due to excess scattering losses resulting from roughness imperfections in the mask and a slightly narrower fabricated coupling gap width than designed.

Figure 9.8 displays the spectral transmission data for an output port of a REMZ. Here, a racetrack resonator of 5 $\mu$m radius is coupled to one arm of a nearly balanced Mach-Zehnder interferometer. A free-spectral range of 18.3 nm and a finesse of 10 is estimated from the data. Just as in the case of the larger

## Microresonator-based Add-Drop Filter
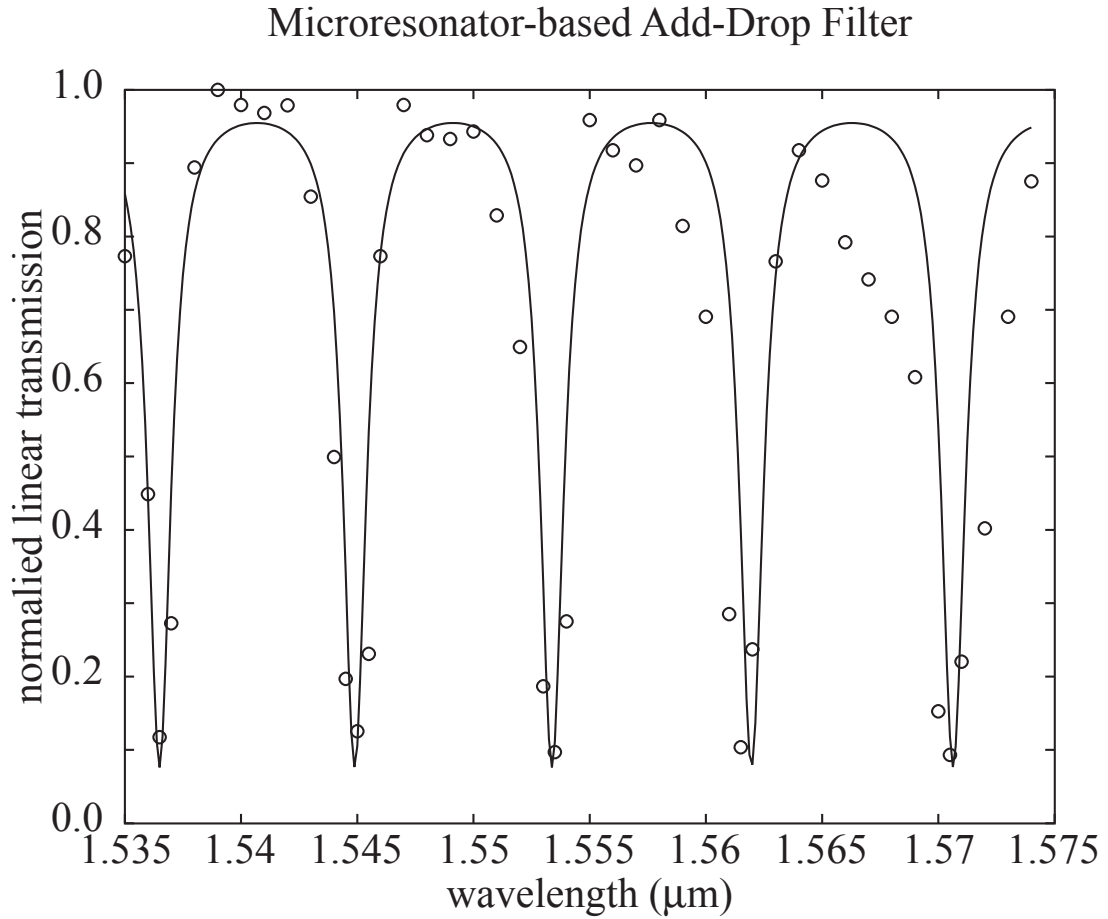


Figure 9.7: Transmission spectrum of a fabricated racetrack resonator with 12.5 $\mu$m bend radius coupled to two waveguides  An FSR of 8.5 nm and finesse of 10 results in an operating bandwidth of 110 GHz near 1.55 $\mu$m for this device.

## Microresonator-based REMZ
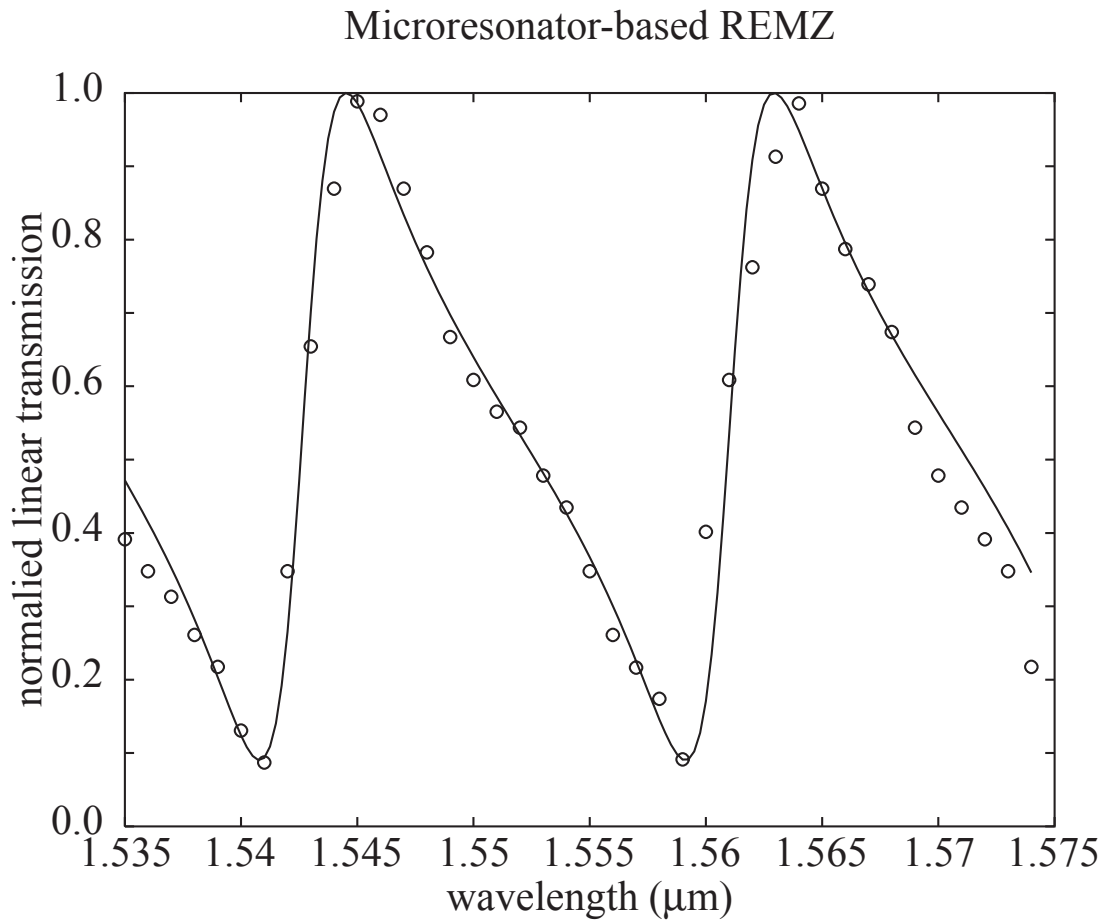


Figure 9.8: Transmission spectrum of a fabricated racetrack resonator with 5 $\mu$m bend radius coupled to one arm of a nearly balanced Mach-Zehnder interferometer. An FSR of 18.3 nm and finesse of 10 results in an operating bandwidth of 230 GHz near 1.55 $\mu$m for this device.

add-drop resonator, the finesse turned out to be lower than desired due to excess scattering losses resulting from roughness imperfections in the mask and a slightly narrower fabricated coupling gap width than designed. Figure 9.9 displays the phase responses that fit the data in figure 9.8.

A coherent pulsed light source was then employed in an attempt to obtain all-optical self-switching. A mode-locked third harmonic of a ND:YAG laser pumped
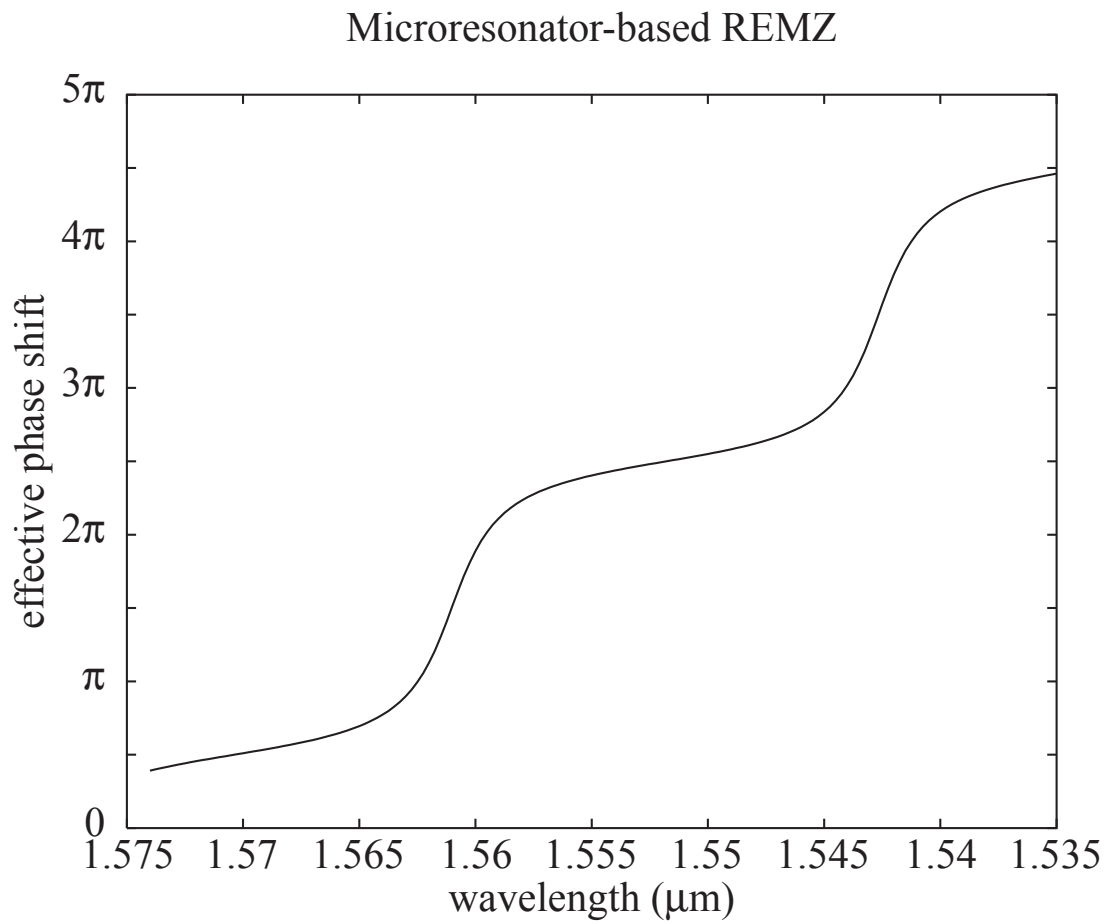
Figure 9.9: Phase response which fits the data in figure 9.8.

an optical parametric generator (OPG). Output from this (Eksma/Ekspla) OPG was first coupled into an optical fiber and subsequently coupled into the guides for experimentation. Sending the OPG output directly into the input fiber ensured auto-alignment with the guides. The spatially filtered OPG light delivered 1 $\mu$J energy, 30 ps pulses at 10 Hz tunable across the visible and infrared spectrum. The low repetition rate, short pulses were of such low average optical power that the attenuated output from the guide was difficult to image. The threshold for detection on the IR camera governed by the *average* power exiting the guides was of the order of nanoWatts ( 1 nJ x 10 Hz). It was found that this threshold for detection was of the same order as the threshold for nonlinearity and optical damage. Consequently, many devices were damaged in the process of attempting to characterize their nonlinear behavior. A laser source with higher repetition rate could have solved this problem but was unavailable within the means of the research group. Nevertheless, switching was clearly observed in some samples. Figure 9.10 displays the output traces of a REMZ with dimensions similar to that of figure 9.8. Three traces are shown each with increasing pulse energies. The actual pulse energies injected into the waveguides was unknown but estimated to be near 1 nanojoule. The relative distribution of output power is clearly seen to shift from one output guide to the other as the pulse energy is increased. Unfortunately, due to the extreme difficulty of the measurement and induced optical damage, more data samples could not be obtained.

## Microresonator-Based All-Optical Switching
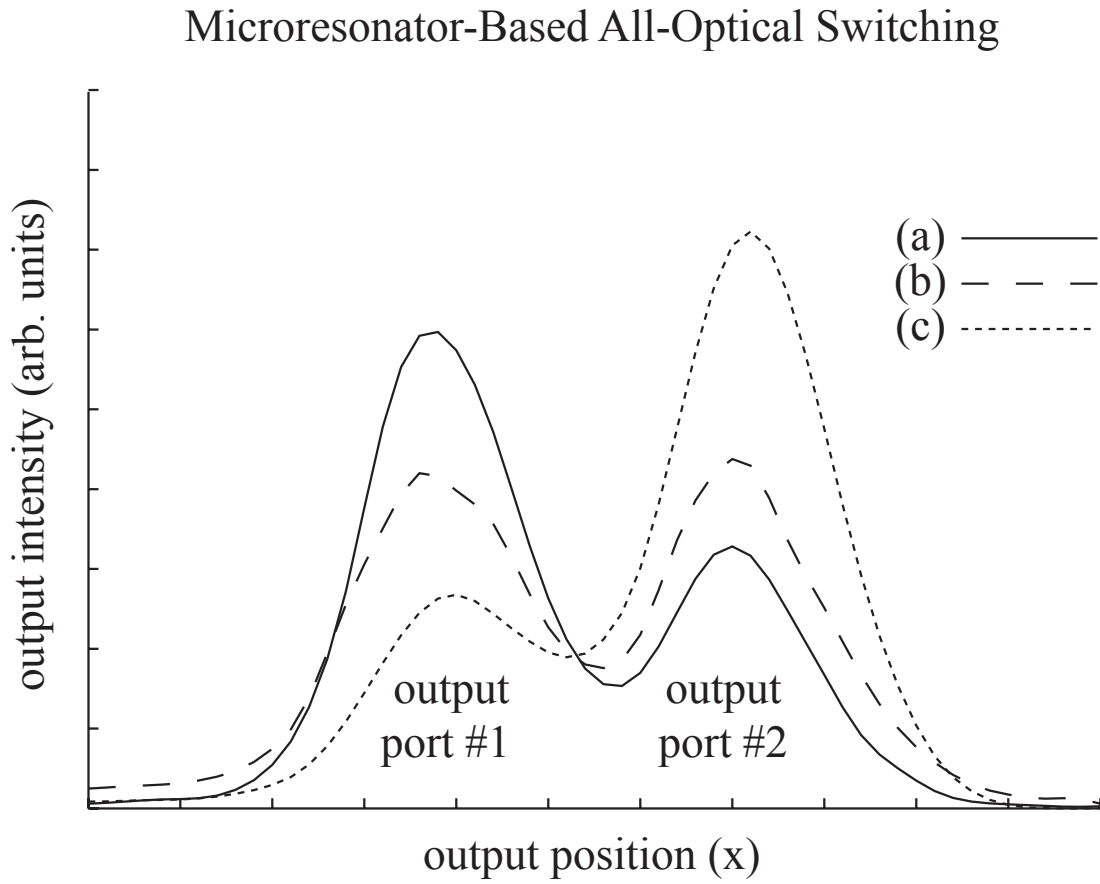


Figure 9.10: Transverse intensity profile trace across the two outputs of a REMZ. Traces a,b and c correspond to increasing pulse energy for pulse energies close to 1 nJ. A shift in transmission from one port to the other is clearly observed with increasing pulse energy.

## 9.4 Summary

In this chapter, the experiments conducted to verify some of the predictions of this thesis were described. Linear results obtained for fiber-based and microresonator-based devices were in excellent agreement with theoretical predictions. All-optical switching was difficult to measure due to lack of an ideal mode-locked source. Nevertheless, all-optical switching was clearly observed.

# Chapter 10

# Conclusions

In this thesis, I have presented a study of the nonlinear transfer properties of whispering gallery ring and disk resonators. Starting from a simplified linear harmonic analysis, the key expressions for coherent build-up of intensity and enhancement of phase sensitivity were presented. Tradeoffs between sensitivity and bandwidth were analyzed, resulting in predictions for the resonator size required to achieve bandwidths of the order of gigahertz to terahertz. The predictions indicated that very small resonators of the order of 5 microns would be required. In order to properly confine light to circulation around such tight bends, very high index contrasts are required. As a result, the majority of resonators considered in the thesis are of the whispering gallery variety - meaning that optical guidance is primarily governed by a single curved interface. Traditionally, the analysis of the quality factors associated with bending losses has been based upon approximate and perturbative methods. Such methods are generally unreliable for low

azimuthal numbers encountered when pushing the bandwidth envelope. A novel method for obtaining the quality factor based on direct solution of the complex dispersion relation via 2D optimization was developed. From this computation, quality factors crucial to defining limitations on resonator size and bandwidth, were reliably estimated.

An early prediction and primary motivator in this work was to recognize that nonlinear effects might be dually enhanced by a combination of the coherent build-up of intensity and enhancement of phase sensitivity. It was predicted that the intensity-dependent nonlinear phase shift for a resonator would be enhanced in quadratic proportion to its finesse. A natural application of this effect is in ultra-compact all-optical switching. An examination of the scaling laws and tradeoffs between switching energy and bandwidth revealed that the exact tradeoffs for linear phenomena might be circumvented for nonlinear phenomena.

A problem with the accumulation of nonlinear phase in a resonator or in most geometries is that for pulses, the phase accumulates in direct proportion to its intensity and thus varies with time across the pulse. It is well-known that solitons can accumulate nonlinear phase in a uniform manner across a pulse via a careful balance between this self-phase modulation and group velocity dispersion. It is also known that resonators exhibit strong dispersive effects near resonance. While the search for a magic pulse or resonator parameters that would accomplish

the same thing in a single resonator proved to be somewhat fruitless, it inspired the concept of distributed resonator systems as artificial materials.

Shortly thereafter, the existence of solitons based on a balance between resonator enhanced nonlinearities and resonator induced group-velocity dispersion was numerically verified. Further investigation of the phenomena, termed SCISSOR solitons, revealed the presence of more exotic nonlinear effects. While attempting to launch higher-order breathing solitons, it was discovered that self-steepening phenomena induced by the resonator would not allow the higher order solitons propagate. It was also discovered that the propagation of slow light had advantages if accomplished with SCISSOR solitons. Finally, the qualitative differences between various multi-resonator systems such as multi-layer stacks, CROWs, and single and double guide SCISSOR systems were analyzed in depth. Some systems exhibit photonic band-gap phenomena while others do not. The ones that do not, such as the ordinary SCISSOR, nevertheless retain high dispersive and nonlinear affects normally associated with propagation near the edge of a photonic band-gap.

Following the theoretical analysis of microresonators in this thesis, I describe the factors involved in the design of high contrast microresonators. The specific reasons for, and choices of parameters for an AlGaAs-based microresonator were presented. An attempt was made to nanofabricate several microresonator-based devices. The processes developed over the course of time spent learning

nanofabrication are presented in full such that the project may continue. Finally, the experimental apparatus and setup used to attempt to characterize fabricated microresonator-based structures is presented.

Experiments were conducted both on large scale fiber ring resonators and fabricated microresonators. The linear properties of each were measured to be in agreement with theoretical predictions. Many difficulties were encountered in attempting to observe nonlinear optical effects. All-optical switching was observed in a nearly balanced Mach-Zehnder interferometer with a nonlinear microresonator coupled to one arm.

In conclusion, I believe that microresonators have great untapped potential for the construction of ultra-compact photonic devices. To date, the primary applications of these devices has been for add-drop filters, dispersion compensators, and laser cavities. Potential applications which have not matured yet include biosensors, optical delay lines, all-optical switches and logic gates, pulse compressors, and pulse imagers. Artificial media composed of sequences of microresonators are an unrealized though promising candidate for the construction of engineerable photonic waveguides with designer photonic properties. Fabrication technology has advanced such that high bandwidth microresonators are readily constructed from high dielectric contrast micro-rings, disks or spheres. I expect microresonator-based structures to become essential components for integrated linear and nonlinear photonic applications.

# Bibliography

[1] F. Gires and P. Tournois, "Interfromtre utilisable pour la compression dimpulsions lumineuses modules en frquence," C. R. Acad. Sci. **258**, 6112 (1964).

[2] L. Fabry and A. Perot, "A multipass interferometer," Ann. Chim. Phys. **16**, 115 (1899).

[3] A. Szoke and V. Daneu, "Bistable optical element and its applications," Appl. Phys. Lett. **15**, 376 (1969).

[4] J. H. Marburger and F. S. Felber, "Theory of a lossless nonlinear Fabry-Perot interferometer," Phys. Rev. A **17**, 335 (1978).

[5] D. A. B. Miller, "Refractive Fabry-Perot bistability with linear absorption: Theory of operation and cavity optimization," IEEE J. Quant. Elect. **17**, 306 (1981).

[6] L. F. Stokes and M. Chodorow, "All-single-mode fiber resonator," Opt. Lett. **7**, 288 (1982).

[7] Y. Ohtsuka, "Optical coherence effects on a fiber-sensing Fabry-Perot interferometer," Appl. Opt. **21**, 4316 (1982).

[8] B. Crosignani and A. Yariv, "Time-dependent analysis of a fiber-optical passive-loop resonator," Opt. Lett. **11**, 251 (1986).

[9] B. Crosignani and B. Daino, "Optical multistability in a fiber-optic passive-loop resonator," Opt. Commun. **59**, 309 (1986).

[10] R. M. Shelby and M. D. Levenson, "Generation of squeezed states of light with a fiber-optic ring interferometer," Phys. Rev. A **33**, 4008 (1986).

[11] R. M. Shelby and M. D. Levenson, "Bistability and other effects in a nonlinear fiber-optic ring resonator," J. Opt. Soc. Am. B **5**, 347 (1988).

[12] H. A. Bachor and M. D. Levenson, "Quantum nondemolition measurements in an optical-fiber ring resonator," Phys. Rev. A **38**, 180 (1988).

[13] V. B. Braginskii and V. S. Il'chenko, "Properties of optical dielectric microresonators," Doklady Akademii Nauk SSSR **293**, 4 (1987).

[14] V. B. Braginsky, M. L. Gorodetsky, and V. S. Ilchenko, "Quality-factor and nonlinear properties of optical whispering-gallery modes," Phys. Lett. A **137**, 393 (1989).

[15] L. J. Cimini and L. J. Greenstein, "Optical equalization for high-bit-rate fiber-optic communications," IEEE Phot. Tech. Lett. **2**, 200 (1990).

[16] G. S. Pandian and F. E. Seraji, "Optical pulse response of a fibre ring resonator," IEE Proceedings J Optoelectronics **138**, 235 (1991).

[17] S. Dilwali and G. S. Pandian, "Pulse response of a fiber dispersion equalizing scheme based on an optical resonator," IEEE Phot. Tech. Lett. **4**, 942 (1992).

[18] S. L. McCall, A. F. J. Levi, R. E. Slusher, S. J. Pearton, and R. A. Logan, "Whispering-gallery mode microdisk lasers," Appl. Phys. Lett. **60**, 289 (1992).

[19] Y. Yamamoto and R. E. Slusher, "Optical processes in microcavities," Physics Today **46**, 66 (1993).

[20] J. Capmany and F. J. Fraile-Pelaez, "Optical bistability and differential amplification in nonlinear fiber resonators," IEEE J. Quant. Elect. **30**, 2578 (1994).

[21] K. Inoue and H. Takahashi, "Wavelength conversion using a light injected DFB-LD and a Mach-Zehnder filter with a ring resonator," IEEE Phot. Tech. Lett. **7**, 998 (1995).

[22] V. Lefevre-Seguin, "Whispering-gallery mode lasers with doped silica microspheres," Optical Materials **11**, 2 (1999).

[23] D. W. Vernooy, A. Furusawa, N. P. Georgiades, V. S. Ilchenko, and H. J. Kimble, "Cavity QED with high-Q whispering gallery modes," Phys. Rev. A **57**, R2293 (1998).

[24] J. Popp, M. H. Fields, and R. K. Chang, "Q switching by saturable absorption in microdroplets: elastic scattering and laser emission," Opt. Lett. **22**, 1296 (1997).

[25] F. C. Blom, D. R. van Dijk, H. J. Hoekstra, A. Driessen, and T. J. A. Popma, "Experimental study of integrated-optics microcavity resonators: toward an all-optical switching device," Appl. Phys. Lett. **71**, 747 (1997).

[26] F. C. Blom and H. Kelderman, "A single channel dropping filter based on a cylindrical microresonator," Opt. Commun. **167**, 1 (1999).

[27] B. E. Little, J. S. Foresi, G. Steinmeyer, E. R. Thoen, S. T. Chu, H. A. Haus, E. P. Ippen, L. C. Kimerling, and W. Greene, "Ultra-compact Si-SiO2 microring resonator optical channel dropping filters," IEEE Phot. Tech. Lett. **10**, 549 (1998).

[28] C. K. Madsen and G. Lenz, "Optical all-pass filters for phase response design with applications for dispersion compensation," IEEE Phot. Tech. Lett. **10**, 994 (1998).

[29] C. K. Madsen, "Efficient architectures for exactly realizing optical filters with optimum bandpass designs," IEEE Phot. Tech. Lett. **10**, 1136 (1998).

[30] K. Djordjev, S. Choi, S. Choi, and P. D. Dapkus, "High-Q vertically coupled InP microdisk resonators," IEEE Phot. Tech. Lett. **14**, 331 (2002).

[31] S. M. Spillane, T. J. Kippenberg, and K. J. Vahala, "Ultralow-threshold Raman laser using a spherical dielectric microcavity," Nature **415**, 621 (2002).

[32] P. Michler, A. Kiraz, C. Becher, W. V. Schoenfeld, P. M. Petroff, L. Zhang, E. Hu, and A. Imamoglu, "A quantum dot single-photon turnstile device," Science **290**, 2282 (2000).

[33] A. Kiraz, P. Michler, C. Becher, B. Gayral, A. Imamoglu, L. Zhang, E. Hu, W. V. Schoenfeld, and P. M. Petroff, "Cavity quantum electrodynamics using a single InAs quantum dot in a microdisk structure," Appl. Phys. Lett. **78**, 3932 (2001).

[34] V. Van, T. A. Ibrahim, K. Ritter, P. P. Absil, F. G. Johnson, R. Grover, J. Goldhar, and P.-T. Ho, "All-optical nonlinear switching in GaAs-AlGaAs microring resonators," IEEE Phot. Tech. Lett. **14**, 74 (2002).

[35] T. A. Ibrahim, V. Van, and P.-T. Ho, "All-optical time-division demultiplexing and spatial pulse routing with a gaas/algaas microring resonator," Opt. Lett. **27**, 803 (2002).

[36] T. A. Ibrahim, W. Cao, J. Li, J. Goldhar, P.-T. Ho, and C. H. Lee, "All-

optical switching in a laterally coupled microring resonator by carrier injection," IEEE Phot. Tech. Lett. **15**, 36 (2003).

[37] D. R. Rowland and J. D. Love, "Evanescent wave coupling of whispering gallery modes of a dielectric cylinder," IEE Proceedings J Optoelectronics **140**, 177 (1993).

[38] M. Cai, O. Painter, and K. Vahala, "Observation of critical coupling in a fiber taper to a silica-microsphere whispering-galley mode system," Phys. Rev. Lett. **85**, 74 (2000).

[39] K. P. Koo and A. D. Kersey, "An optical phase amplification technique for interrogating fiber resonator sensors," IEEE Phot. Tech. Lett. **7**, 209 (1995).

[40] H. A. Kramers, "La difusion de la lumiere pa les atoines," Estratto dagli Atti del Congresso Internazionale de Fisici Como **2**, 545 (1927).

[41] R. Kronig, "On the theory of the dispersion of x-rays," J. Opt. Soc. Am. **12**, 547 (1926).

[42] M. Beck, I. A. Walmsley, and J. D. Kafka, "Group delay measurements of optical components near 800 nm," IEEE J. Quant. Elect. **27**, 2074 (1991).

[43] R. H. J. Kop, P. deVries, R. Sprik, and A. Lagendijk, "Kramers-Kronig relations for an interferometer," Opt. Commun. **138**, 118 (1997).

[44] L. J. Wang, "Causal 'all-pass' filters and Kramers-Kronig relations," Opt. Commun. **213**, 27 (2002).

[45] G. Lenz, B. J. Eggleton, C. R. Giles, C. K. Madsen, and R. E. Slusher, "Dispersive properties of optical filters for WDM systems," IEEE J. Quant. Elect. **34**, 1390 (1998).

[46] C. K. Madsen and J. H. Zhao, *Optical Filter Design and Analysis: A Signal Processing Approach* (Wiley Inc., New York, 1999).

[47] J. M. Choi, R. K. Lee, and A. Yariv, "Control of critical coupling in a ring resonator-fiber configuration: Application to wavelength selective switching, modulation, amplification, and oscillation," Opt. Lett. **26**, 1236 (2001).

[48] L. Mandel and E. Wolf, *Optical Coherence and Quantum Optics* (Cambridge University Press, Cambridge, 1995).

[49] L. Rayleigh, "The problem of the whispering gallery," Scientific Papers **5**, 617 (1912).

[50] J. Sarma and K. A. Shore, "Electromagnetic theory for optical disc resonators," IEE Proceedings J Optoelectronics **132**, 325 (1985).

[51] A. W. Snyder and J. D. Love, "Tunnelling leaky modes on optical waveguides," Opt. Commun. **12**, 326 (1974).

[52] L. Collot and V. Lefevre-Seguin, "Very high-Q whispering-gallery mode resonances observed on fused silica microspheres," Europhys. Lett. **23**, 327 (1993).

[53] C. K. Madsen and J. H. Zhau, "Increasing the free spectral range of silica waveguide rings for filter applications," Opt. Lett. **23**, 186 (1998).

[54] S. Schiller and R. L. Byer, "High-resolution spectroscopy of whispering gallery modes in large dielectric spheres," Opt. Lett. **16**, 1138 (1991).

[55] V. V. Vassiliev, V. L. Velichansky, V. S. Ilchenko, M. L. Gorodetsky, L. Hollberg, and A. V. Yarovitsky, "Narrow-line-width diode laser with a high-Q microsphere resonator," Opt. Commun. **158**, 305 (1998).

[56] B. E. Little, S. T. Chu, H. A. Haus, J. Foresi, and J.-P. Laine, "Microring resonator channel dropping filters," J. Light. Technol. **15**, 998 (1997).

[57] A. Serpengzel, S. Arnold, and G. Griffel, "Excitation of resonances of microspheres on an optical fiber," Opt. Lett. **20**, 654 (1995).

[58] S. Blair and Y. Chen, "Resonant-enhanced evanescent-wave fluorescence biosensing with cylindrical optical cavities," Appl. Opt. **40**, 570 (2001).

[59] J. E. Heebner and R. W. Boyd, "Sensitive disk resonator photonic biosensor," Appl. Opt. **40**, 5742 (2001).

[60] J. C. Knight and N. Dubreuil, "Mapping whispering-gallery modes in microspheres with a near-field probe," Opt. Lett. **20**, 1515 (1995).

[61] J. C. Knight and N. Dubreuil, "Characterizing whispering-gallery modes in microspheres by direct observation of the optical standing-wave pattern in the near field," Opt. Lett. **21**, 698 (1996).

[62] M. L. M. Balisteri, D. J. W. Klunder, and F. C. Blom, "Visualizing the

whispering gallery modes in a cylindrical optical microcavity," Opt. Lett. **24**, 1829 (1999).

[63] B. E. Little, J. P. Laine, and H. A. Haus, "Analytic theory of coupling from tapered fibers and half-blocks into microsphere resonators," J. Light. Technol. **17**, 704 (1999).

[64] R. W. Boyd, *Nonlinear Optics, Second Edition* (Academic Press Inc., San Diego, 2003).

[65] J. E. Heebner and R. W. Boyd, "Enhanced all-optical switching by use of a nonlinear fiber ring resonator," Opt. Lett. **24**, 847 (1999).

[66] D. Sarid, "Analysis of bistability in a ring-channel waveguide," Opt. Lett. **6**, 552 (1981).

[67] T. Fukishima and T. Sakamoto, "Kerr-effect-induced S-R flip-flop operation in an optical fiber loop resonator with double couplers," Opt. Lett. **20**, 1119 (1995).

[68] G. Lenz, J. Zimmermann, T. Katsufuji, M. E. Lines, H. Y. Wang, S. Spalter, R. E. Slusher, S.-W. Cheong, J. S. Sanghera, and I. D. Aggarwal, "Large Kerr effect in bulk Se-based chalcogenide glasses," Opt. Lett. **25**, 254 (2000).

[69] S. Blair, J. E. Heebner, and R. W. Boyd, "Beyond the absorption-limited nonlinear phase shift with microring resonators," Opt. Lett. **27**, 357 (2002).

[70] I. R. Gabitov and P. M. Lushnikov, "Nonlinearity management in a dispersion-managed system," Opt. Lett. **27**, 113 (2002).

[71] G. P. Agrawal, *Fiber-Optic Communication Systems* (Wiley Inc., New York, 1997).

[72] W. H. Knox, "Ultrafast technology in telecommunications," IEEE J. Sel. Top. Quant. Elect. **6**, 1273 (2000).

[73] G. I. Stegeman, A. Villeneuve, J. Kang, J. S. Aitchison, C. N. Ironside, K. Al-Hemyari, C. C. Yang, C. H. Lin, H. H. Lin, G. T. Kennedy, R. S. Grant, and W. Sibbett, "AlGaAs below the half-gap: The silicon of nonlinear optical materials," Int. J. of Nonlin. Opt. Phys. **3**, 347 (1994).

[74] M. N. Islam, *Ultrafast Fiber Switching Devices And Systems* (Cambridge University Press, Cambridge, 1992).

[75] G. I. Stegeman and C. Seaton, "Nonlinear integrated optics," J. Appl. Phys. **58**, 57 (1985).

[76] N. D. Sankey, D. F. Prelewitz, and T. G. Brown, "All-optical switching in a nonlinear periodic waveguide structure," Appl. Phys. Lett. **60**, 1427 (1992).

[77] S. Spalter, H. Y. Wang, J. Zimmermann, G. Lenz, T. Katsufuji, S.-W. Cheong, and R. E. Slusher, "Strong self-phase modulation in planar chalcogenide glass waveguides," Opt. Lett. **27**, 363 (2002).

[78] J. M. Harbold, F. O. Ilday, F. W. Wise, J. S. Sanghera, V. Q. Nguyen, L. B. Shaw, and I. D. Aggarwal, "Highly nonlinear As-S-Se glasses for all- optical switching," Opt. Lett. **27**, 119 (2002).

[79] B. E. Little, S. T. Chu, and H. A. Haus, "Track changing by use of the phase response of microspheres and resonators," Opt. Lett. **23**, 894 (1998).

[80] R. Grover, V. Van, T. A. Ibrahim, P. P. Absil, L. C. Calhoun, F. G. Johnson, J. V. Hryniewicz, and P.-T. Ho, "Parallel-cascaded semiconductor microring resonators for high-order and wide-FSR filters," J. Light. Technol. **20**, 900 (2002).

[81] S. T. Chu, B. E. Little, W. Pan, T. Kaneko, and Y. Kokubun, "Second-order filter response from parallel coupled glass microring resonators," IEEE Phot. Tech. Lett. **11**, 1426 (1999).

[82] J. V. Hryniewicz, P. P. Absil, B. E. Little, R. A. Wilson, and P.-T. Ho, "Higher order filter response in coupled microring resonators," IEEE Phot. Tech. Lett. **12**, 320 (2000).

[83] R. Orta, P. Savi, R. Tascone, and D. Trinchero, "Synthesis of multiple ring resonator filters for optical systems," IEEE Phot. Tech. Lett. **7**, 1447 (1995).

[84] M. Asobe, K. Naganuma, T. Kaino, T. Kanamori, S. Tomaru, and T. Kurihara, "Switching energy limitation in all optical switching due to group velocity dispersion of highly nonlinear optical waveguides," Appl. Phys. Lett. **64**, 2922 (1994).

[85] G. P. Agrawal, *Nonlinear Fiber-Optics* (Academic Press Inc., San Diego, 1995).

[86] V. E. Zakharov and A. B. Shabat, "Interaction between solutions in a stable medium," Sov. Phys. JETP **37**, 923 (1973).

[87] A. Hasegawa and F. Tappert, "Transmission of stationary nonlinear optical pulses in dispersive dielectric fibers," Appl. Phys. Lett. **23**, 142 (1973).

[88] L. F. Mollenauer, R. H. Stolen, and J. P. Gordon, "Experimental observation of picosecond pulse narrowing and solitons in optical fibers," Phys. Rev. Lett. **45**, 1095 (1980).

[89] J. E. Heebner, R. W. Boyd, and Q. Park, "Slow light, induced dispersion, enhanced nonlinearity, and optical solitons in a resonator-array waveguide," Phys. Rev. E **65**, 036619 (2002).

[90] J. E. Heebner, R. W. Boyd, and Q. Park, "SCISSOR solitons and other propagation effects in microresonator modified waveguides," J. Opt. Soc. Am. B **19**, 722 (2002).

[91] C. V. Bennett and B. H. Kolner, "Upconversion time microscope demonstrating 103x magnification of femtosecond waveforms," Opt. Lett. **24**, 783 (1999).

[92] H. M. Gibbs, *Optical Bistability: Controlling Light with Light* (Academic Press Inc., New York, 1985).

[93] H. M. Gibbs, S. L. McCall, and T. N. C. Venkatesan, "Differential gain and bistability using a sodium filled Fabry-Perot-interferometer," Phys. Rev. Lett. **36**, 1135 (1976).

[94] P. Absil, J. V. Hryniewicz, B. E. Little, P. S. Cho, R. A. Wilson, L. G. Jonekis, and P.-T. Ho, "Wavelength conversion in GaAs micro-ring resonators," Opt. Lett. **25**, 554 (2000).

[95] Y. Xu, R. K. Lee, and A. Yariv, "Propagation and second-harmonic generation of electromagnetic waves in a coupled-resonator optical waveguide," J. Opt. Soc. Am. B **17**, 387 (2000).

[96] M. L. Gorodetsky, A. A. Savchenkov, and V. S. Ilchenko, "Ultimate Q of optical microsphere resonators," Opt. Lett. **21**, 453 (1996).

[97] M. L. Gorodetsky and V. S. Ilchenko, "Optical microsphere resonators: optimal coupling to high-Q whispering-gallery modes," J. Opt. Soc. Am. B **16**, 147 (1999).

[98] D. Rafizadeh, J. P. Zhang, R. C. Tiberio, and S. T. Ho, "Propagation loss measurements in semiconductor microcavity ring and disk resonators," J. Light. Technol. **16**, 1308 (1998).

[99] B. E. Little and S. T. Chu, "Estimating surface-roughness loss and output coupling in microdisk resonators," Opt. Lett. **21**, 1390 (1996).

[100] B. E. Little and J. P. Laine, "Surface-roughness-induced contradirectional coupling in ring and disk resonators," Opt. Lett. **22**, 4 (1997).

[101] P. K. Tien, "Light waves in thin films and integrated optics," Appl. Opt. **10**, 2395 (1971).

[102] V. Van, P. P. Absil, J. V. Hryniewicz, and P.-T. Ho, "Propagation loss in single-mode GaAs-AlGaAs microring resonators," J. Light. Technol. **19**, 1734 (2001).

[103] A. Taflove and S. C. Hagness, *Computational Electrodynamics, The Finite-Difference Time-Domain Method* (Artech House, Boston, 2000).

[104] R. W. Boyd and D. J. Gauthier, *Slow and Fast Light, Progress in Optics*, E. Wolf Ed. (Elsevier Science, Amsterdam, 2002).

[105] G. Lenz, B. J. Eggleton, C. K. Madsen, and R. E. Slusher, "Optical delay lines based on optical filters," IEEE J. Quant. Elect. **37**, 525 (2001).

[106] C. Liu, Z. Dutton, C. H. Behroozi, and L. V. Hau, "Observation of coherent optical information storage in an atomic medium using halted light pulses," Nature **409**, 490 (2001).

[107] D. F. Phillips, M. Fleischhauer, A. Mair, R. L. Walsworth, and M. D. Lukin, "Storage of light in atomic vapor," Phys. Rev. Lett. **86**, 783 (2001).

[108] S. Chu and S. Wong, "Linear pulse-propagation in an absorbing medium," Phys. Rev. Lett. **48**, 738 (1982).

[109] S. E. Harris, "Electromagnetically induced transparency," Physics Today **50**, 36 (1997).

[110] M. D. Lukin, M. Fleischhauer, A. S. Zibrov, H. G. Robinson, V. L. Velichansky, L. Hollberg, and M. O. Scully, "Spectroscopy in dense coherent media: Line narrowing and interference effects," Phys. Rev. Lett. **79**, 2959 (1997).

[111] A. B. Matsko, Y. V. Rostovtsev, H. Z. Cummins, and M. O. Scully, "Using slow light to enhance acousto-optical effects: Application to squeezed light," Phys. Rev. Lett. **84**, 5752 (2000).

[112] A. B. Matsko, Y. V. Rostovtsev, M. Fleischhauer, and M. O. Scully, "Anoma-

lous stimulated Brillouin scattering via ultraslow light," Phys. Rev. Lett. **86**, 2006 (2001).

[113] C. K. Madsen, G. Lenz, A. J. Bruce, M. A. Cappuzzo, L. T. Gomez, and R. E. Scotti, "Integrated all-pass filters for tunable dispersion and dispersion slope compensation," IEEE Phot. Tech. Lett. **11**, 1623 (1999).

[114] K. Djordjev, S. Choi, S. Choi, and P. D. Dapkus, "Microdisk tunable resonant filters and switches," IEEE Phot. Tech. Lett. **14**, 828 (2002).

[115] K. Djordjev, S. Choi, S. Choi, and P. D. Dapkus, "Vertically coupled InP microdisk switching devices with electroabsorptive active regions," IEEE Phot. Tech. Lett. **14**, 1115 (2002).

[116] R. Y. Chiao and A. M. Steinberg, in *Progress in Optics XXXVII* E. Wolf Ed. (Elsevier Science, Amsterdam, 1997).

[117] J. E. Heebner, R. W. Boyd, and Q. Park, "'slow and 'fast light in resonator-coupled waveguides," J. Mod. Opt. **49**, 2629 (2002).

[118] W. Chen and D. L. Mills, "Gap solitons and the nonlinear optical response of superlattices," Phys. Rev. Lett. **58**, 160 (1987).

[119] B. J. Eggleton, R. E. Slusher, C. M. de Sterke, P. A. Krug, and J. E. Sipe, "Bragg grating solitons," Phys. Rev. Lett. **76**, 1627 (1996).

[120] D. N. Christodoulides and N. K. Efremidis, "Discrete temporal solitons along a chain of nonlinear coupled microcavities embedded in photonic crystals," Opt. Lett. **27**, 568 (2002).

[121] J. D. Joannopoulos, R. D. Meade, and J. N. Winn, *Photonic Crystals* (Princeton University Press, Singapore, 1995).

[122] A. Yariv, Y. Xu, R. K. Lee, and A. Scherer, "Coupled resonator optical waveguide: a proposal and analysis," Opt. Lett. **24**, 711 (1999).

[123] M. Notomi, K. Yamada, A. Shinya, J. Takahashi, C. Takahashi, and I. Yokohama, "Extremely large group-velocity dispersion of line-defect waveguides in photonic crystal slabs," Phys. Rev. Lett. **87**, 253902 (2001).

[124] M. Soljacic, S. G. Johnson, S. Fan, M. Ibanescu, E. Ippen, and J. D. Joannopoulos, "Photonic-crystal slow-light enhancement of nonlinear phase sensitivity," J. Opt. Soc. Am. B **19**, 2052 (2002).

[125] M. D. Rahn, A. M. Fox, M. S. Skolnick, and T. F. Krauss, "Propagation of ultrashort nonlinear pulses through two-dimensional AlGaAs high-contrast photonic crystal waveguides," J. Opt. Soc. Am. B **19**, 716 (2002).

[126] S. Mingaleev and Y. Kivshar, "Nonlinear transmission and light localization in photonic-crystal waveguides," J. Opt. Soc. Am. B **19**, 2241 (2002).

[127] B. E. Little, S. T. Chu, and H. A. Haus, "Second-order filtering and sensing with partially coupled travelling waves in a single resonator," Opt. Lett. **23**, 1570 (1998).

[128] B. E. Little, S. T. Chu, J. V. Hryniewicz, and P. P. Absil, "Filter synthesis for periodically coupled microring resonators," Opt. Lett. **25**, 344 (2000).

[129] Y. Xu, R. K. Lee, and A. Yariv, "Scattering theory analysis of waveguide-resonator coupling," Phys. Rev. E **62**, 7389 (2000).

[130] S. Mookherjea, D. S. Cohen, and A. Yariv, "Nonlinear dispersion in a coupled-resonator optical waveguide," Opt. Lett. **27**, 933 (2002).

[131] S. Pereira, J. E. Sipe, J. E. Heebner, and R. W. Boyd, "Gap solitons in a two-channel SCISSOR structure," Opt. Lett. **27**, 536 (2002).

[132] S. Pereira, P. Chak, and J. E. Sipe, "Gap-soliton switching in short microresonator structures," J. Opt. Soc. Am. B **19**, 2191 (2002).

[133] S. Arnold, C. T. Liu, W. B. Whitten, and J. M. Ramsey, "Room-temperature microparticle-based persistent spectral hole burning memory," Opt. Lett. **16**, 420 (1991).

[134] N. Dubreuil, J. C. Knight, D. K. Leventhal, V. Sandoghdar, J. Hare, and V. Lefevre, "Eroded monomode optical fiber for whispering-gallery mode excitation in fused-silica microspheres," Opt. Lett. **20**, 813 (1995).

[135] D. Rafizadeh, J. P. Zhang, S. C. Hagness, A. Taflove, K. A. Stair, S. T. Ho, and R. C. Tiberio, "Waveguide-coupled AlGaAs/GaAs microcavity ring and disk resonators with high finesse and 21.6 nm free-spectral range," Opt. Lett. **22**, 1244 (1997).

[136] J. P. Laine, B. E. Little, and H. A. Haus, "Etch-eroded fiber coupler for whispering-gallery-mode excitation in high-Q silica microspheres," IEEE Phot. Tech. Lett. **11**, 1429 (1999).

[137] B. E. Little and S. T. Chu, "Toward very large-scale integrated photonics," Opt. and Phot. News **11**, 24 (2000).

[138] M. Sheik-Bahae, D. C. Hutchings, D. J. Hagan, and E. W. van Stryland, "Dispersion of bound electronic nonlinear refraction in solids," IEEE J. Quant. Elect. **27**, 1296 (1991).

[139] D. K. Armani, T. J. Kippenberg, S. M. Spillane, and K. J. Vahala, "Ultra-high-Q toroid microcavity on a chip," Nature **421**, 925 (2003).

[140] J. P. Sokoloff and P. R. Prucnal, "A terahertz optical asymmetric demultiplexer (toad)," IEEE Phot. Tech. Lett. **5**, 787 (1993).

[141] V. Mizrahi, K. W. DeLong, G. I. Stegeman, M. A. Saifi, and M. J. Andrejco, "Two photon absorption as a limitation to all-optical switching," Opt. Lett. **14**, 1140 (1989).

[142] M. Sheik-Bahae, D. J. Hagan, and E. W. van Stryland, "Dispersion and band-gap scaling of the electronic kerr effect in solids associated with two-photon absorption," Phys. Rev. Lett. **65**, 96 (1990).

[143] S. T. Ho, C. E. Soccolich, M. N. Islam, W. S. Hobson, A. F. J. Levi, and R. E. Slusher, "Large nonlinear phase shifts in low-loss AlGaAs waveguides near half-gap," Appl. Phys. Lett. **59**, 2558 (1991).

[144] B. S. Wherrett, "Scaling rules for multiphoton interband absorption in semiconductors," J. Opt. Soc. Am. B **1**, 67 (1984).

[145] G. Wicks and M. C. Gupta, *Handbook of Photonics* (CRC Press, New York, 1997).

[146] G. I. Stegeman, D. N. Christodoulides, and M. Segev, "Optical spatial solitons: Historical perspectives," IEEE J. Sel. Top. Quant. Elect. **6**, 1419 (2000).

[147] S. Fan, P. R. Villeneuve, J. D. Joannopoulos, and H. A. Haus, "Channel drop filters in photonic crystals," Opt. Exp. **3**, 4 (1998).

[148] B. E. Little, S. T. Chu, W. Pan, D. Ripin, T. Kaneko, Y. Kokubun, and E. Ippen, "Vertically coupled glass microring resonator channel dropping filters," IEEE Phot. Tech. Lett. **11**, 215 (1999).

[149] P. P. Absil, J. V. Hryniewicz, B. E. Little, F. G. Johnson, K. J. Ritter,

and P.-T. Ho, "Vertically coupled microring resonators using polymer wafer bonding," IEEE Phot. Tech. Lett. **13**, 49 (2001).

[150] R. Grover, P. P. Absil, V. Van, J. V. Hryniewicz, B. E. Little, O. King, L. C. Calhoun, F. G. Johnson, and P.-T. Ho, "Vertically coupled GaInAsP-InP microring resonators," Opt. Lett. **26**, 506 (2001).

[151] K. Djordjev, S. Choi, S. Choi, and P. D. Dapkus, "Study of the effects of the geometry on the performance of vertically coupled inp microdisk resonators," IEEE Phot. Tech. Lett. **14**, 1485 (2002).

[152] M. K. Chin, C. Youtsey, W. Zhao, T. Pierson, Z. Ren, S. L. Wu, L. Wang, Y. G. Zhao, and S. T. Ho, "GaAs microcavity channel-dropping filter based on a race-track resonator," IEEE Phot. Tech. Lett. **11**, 1620 (1999).

[153] S. C. Hagness and D. Rafizadeh, "FDTD microcavity simulations: design and experimental realization of waveguide-coupled single-mode ring and whispering-gallery-mode disk resonators," J. Light. Technol. **15**, 2154 (1997).

[154] B. E. Little and S. T. Chu, "Theory of polarization rotation and conversion in vertically coupled microresonators," IEEE Phot. Tech. Lett. **12**, 401 (2000).

[155] P. P. Absil, J. V. Hryniewicz, B. E. Little, R. A. Wilson, L. G. Jonekis, and P.-T. Ho, "Compact microring notch filters," IEEE Phot. Tech. Lett. **12**, 398 (2000).

[156] M. Heiblum and J. H. Harris, "Analysis of curved optical waveguides by conformal transformation," IEEE J. Quant. Elect. **11**, 75 (1975).

[157] M. K. Chin and S. T. Ho, "Design and modelling of waveguide-coupled single-mode microring resonators," J. Light. Technol. **16**, 1433 (1998).

[158] W. Berglund and A. Gopinath, "WKB analysis of bend losses in optical waveguides," J. Light. Technol. **18**, 1161 (2000).

[159] M. Kuznetsov and H. A. Haus, "Radiation loss in dielectric wavguide structures by the volume current method," IEEE J. Quant. Elect. **19**, 1505 (1983).

[160] A. Kastler, "Transmission of light pulse through a Fabry-Perot interferometer," Nouvelle Revue D'Optique **5**, 133 (1974).

[161] I. N. Duling, "All-fiber ring soliton laser mode-locked with a nonlinear loop mirror," Opt. Lett. **16**, 539 (1991).

[162] N. J. Doran and D. Wood, "Nonlinear-optical loop mirror," Opt. Lett. **13**, 56 (1988).

[163] M. E. Fermann, F. Haberl, M. Hofer, and H. Hochreiter, "Nonlinear amplifying loop mirror," Opt. Lett. **15**, 752 (1990).

# Appendix A

# Lorentz Approximation for Resonator Build-Up

While the resonator build-up is a periodic function of frequency with periodicity equal to the free-spectral range, near resonance, the frequency dependence of the build-up is to good approximation a Lorentzian function. The Lorentzian expression can be derived by first making the small angle approximation: $\cos\phi \approx 1 - \frac{1}{2}\phi^2$.

$$\mathcal{B} = \frac{I_3}{I_1} \approx \frac{\frac{\left(1-r^2\right)a^2}{(1-ra)^2}}{1 + \frac{ra}{(1-ra)^2}\phi^2} \tag{A.1}$$

In order to further simplify this equation into a form that offers insight the constant numerator is redefined as $\mathcal{B}_a \equiv \frac{\left(1-r^2\right)a^2}{(1-ra)^2}$ and the finesse is approximated as: $\frac{\sqrt{ra}}{1-ra} \approx \mathcal{F}/\pi$. This results in a simple expression for the build-up as a function of

frequency near resonance.

$$\mathcal{B} \approx \frac{\mathcal{B}_a}{1 + \left(\mathcal{F}\frac{\phi}{\pi}\right)^2} = \frac{\mathcal{B}_a}{1 + \left(2Q\frac{\omega - \omega_{\mathrm{R}}}{\omega_{\mathrm{R}}}\right)^2} \tag{A.2}$$

As a final check it should be noted that the full width of this Lorentzian is $2\pi/\mathcal{F}$ which preserves the correct bandwidth of the original periodic function. This approximation is valid for pulsed waveforms with a bandwidth less than a free-spectral range. Accordingly because the Fourier transform of a Lorentzian is an exponential function, it follows that the transient "charging" and "discharging" of the resonator will follow an exponential rise and fall. Figure 2.8a demonstrates the exponential charging and discharging at the leading and trailing edges of the rect response curve for the build-up. Finally, it is worth comparing this Lorentz approximation to two other well known Lorentz models in physics. Notice the similarity with the susceptibility of the Lorentz atom model:

$$|\chi| \approx \frac{Q\frac{\omega_p^2}{\omega_{\mathrm{R}}^2}}{\sqrt{1 + \left[2Q\frac{\omega - \omega_{\mathrm{R}}}{\omega_{\mathrm{R}}}\right]^2}} \tag{A.3}$$

and the impedance of an RLC circuit:

$$|Z| \approx \frac{R}{\sqrt{1 + \left[2Q\frac{\omega - \omega_{\mathrm{R}}}{\omega_{\mathrm{R}}}\right]^2}} \tag{A.4}$$

# Appendix B

# Transforms and All-Pass Filters

## B.1    Hilbert Transform For a Causal Function

If the response of system is causal (i.e. causes preceed effects), then the impulse response function is zero for all time values prior to zero.   This allows one to separate any function into even and odd components which, are exact though of opposite sign for all $t < 0$ and are identical for $t > 0$.   Thus, for all $t < 0$ they add destructively to yield zero, and for all $t > 0$ they add constructively in equal proportions to form the impulse response function.

$$h(t) = h_{\text{even}}(t) + h_{\text{odd}}(t) \tag{B.1}$$

The even and odd components are simply related in the time domain by the

signum function

$$h_{\text{even}}(t) = sgn(t)h_{\text{odd}}(t) \tag{B.2}$$

$$h_{\text{odd}}(t) = sgn(t)h_{\text{even}}(t) \tag{B.3}$$

If, furthermore, the system is linear, and time-translation invariant, then a frequency dependent transfer function can be assigned to spectral components traversing the system. The Fourier transform of the impulse response equations may be employed to generate the Hilbert transform relations:

$$H_{\text{real}}(\omega) = +\frac{2}{\omega} \star H_{\text{imag}}(\omega) = +2 \int_{-\infty}^{+\infty} d\omega' \frac{H_{\text{imag}}(\omega')}{\omega - \omega'} \tag{B.4}$$

$$H_{\text{imag}}(\omega) = -\frac{2}{\omega} \star H_{\text{real}}(\omega) = -2 \int_{-\infty}^{+\infty} d\omega' \frac{H_{\text{real}}(\omega')}{\omega - \omega'} \tag{B.5}$$

These relations apply to the real and imaginary parts of the transfer functions of any causal signal. These are also known as one form of the Kramers-Kronig relations. [40,41]

## B.2 Z-Transform for a Weighted Sum of Delta Impulses

The impulse response function of a ring resonator with no internal dispersion (ie delta pulses propagate within the ring without dispersing) is a weighted sum of equally spaced delta functions.

$$h(t) = r\delta(t) - \left(1 - r^2\right) e^{+i\phi_0} \sum_{m=1}^{\infty} \left(re^{+i\phi_0}\right)^{m-1} \delta(t - mT_{\mathrm{R}}) \qquad \text{(B.6)}$$

An impulse response function consisting of a weighted sum of delta impulses spaced by the transit time, $T_{\mathrm{R}} = n2\pi R/c$ in the time domain can be interpreted as the Fourier series for some periodic function in the frequency domain. The periodic function is of course the transfer function whose fundamental period or free-spectral range (FSR) is equal to the inverse of the transit time. The functions form a Z-transform pair which is simply a time domain version of a Fourier series equation pair for discrete time signals.

The transfer function is given by the following expression which may be simplified by taking the limiting value of the infinite series (provided it is convergent, that is $r < 1$)

$$H(\omega) = r - \left(1 - r^2\right) e^{+i\omega T_{\mathrm{R}}} \sum_{m=1}^{\infty} \left(re^{+i\omega T_{\mathrm{R}}}\right)^{m-1} = \frac{r - e^{+i\omega T_{\mathrm{R}}}}{1 - re^{+i\omega T_{\mathrm{R}}}} \qquad \text{(B.7)}$$

Because the system is linear, time-translation invariant, and causal, the real and imaginary parts form a Hilbert transform pair

$$H_{\text{real}(\omega)} = \frac{-\cos \omega T_{\text{R}} + 2r - r^2 \cos \omega T_{\text{R}}}{1 - 2r \cos \omega T_{\text{R}} + r^2} \tag{B.8}$$

$$H_{\text{imag}(\omega)} = \frac{-\left(1 - r^2\right) \sin \omega T_{\text{R}}}{1 - 2r \cos \omega T_{\text{R}} + r^2} \tag{B.9}$$

## B.3 Kramers-Kronig Relations for All-Pass Resonators

In certain systems, if the natural logarithm of the transfer function is analytic in the upper half complex frequency plane, the amplitude and phase of a transfer function form a Hilbert transform pair as well.

$$|H(\omega)| = 1 \tag{B.10}$$

$$\arg\left[H(\omega)\right] = \pi + \omega T_{\text{R}} + 2 \arctan\left(\frac{r \sin \omega T_{\text{R}}}{1 - r \cos \omega T_{\text{R}}}\right) \tag{B.11}$$

The amplitude and phase can be mapped onto the real and imaginary axis by taking the natural logarithm of the transfer function. For all values of gain and some values of attenuation, with the exception of the under-coupled regime, the transfer function possesses zeros in the upper half complex frequency plane. At each of these zeros, the natural logarithm is undefined and thus, the amplitude

and phase do not satisfy the Kramers-Kronig relations. [44] In the under-coupled

regime, Kramers-Kronig relations for amplitude and phase do in fact exist.
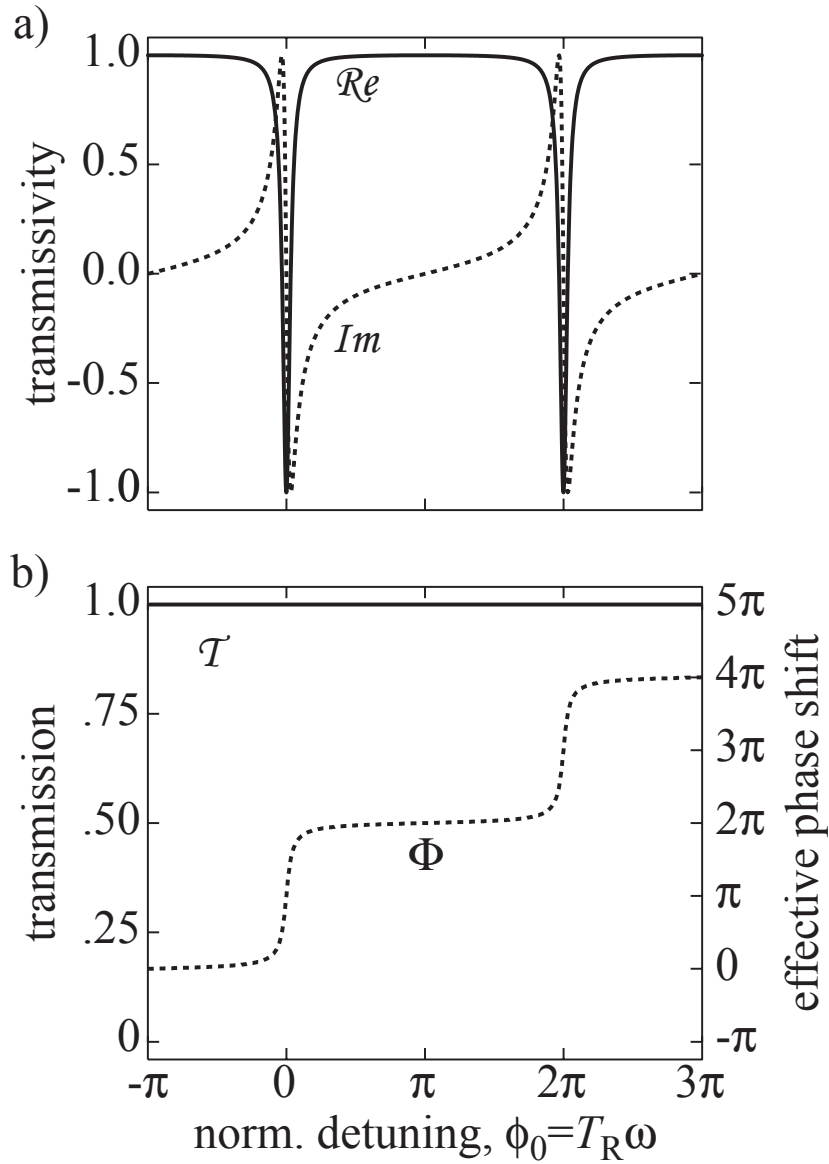
Figure B.1: a) Plots of the real and imaginary components of the field transmissivity for an all-pass resonator with $r = 0.9$. b) Plots of the amplitude square modulus (transmission) and phase.

# Appendix C

# Kramers-Kronig Relations for the Third-Order Susceptibility

The Kramers-Kronig relation connects the refractive and absorptive spectra of a linear optical material with a causal response,

$$n\left(\omega\right) - 1 = \frac{c}{\pi} \int_0^\infty d\omega' \frac{\alpha\left(\omega'\right)}{\omega'^2 - \omega^2}. \tag{C.1}$$

Changes to each of these quantities due to an *external perturbation* are causal and similarly related. However, in a strict mathematical sense, the Kramers-Kronig relations are invalid for degenerate third-order processes such as self-induced changes in refractive index because of the existence of a pole in the upper half complex frequency plane. [64] Nevertheless, it has been demonstrated that application of the Kramers-Kronig relation to the two-photon absorption spectrum of a material correctly predicts the magnitude and dispersion of the Kerr effect in solids. [142,138] The spectra of nonlinear refraction and two-photon absorption

are thus related as,

$$n_2\left(\omega\right) = \frac{c}{\pi} \int_0^\infty d\omega' \frac{\alpha_2\left(\omega'\right)}{\omega'^2 - \omega^2}. \tag{C.2}$$

A two-band model is generally sufficient for accurately predicting the third-order nonlinear absorptive and refractive properties of semiconductors. Under this model, the two-photon absorption coefficient is given as:

$$\alpha_2\left(\omega\right) = \frac{2^9 \pi e^4}{5\sqrt{m_0}c^2} \frac{\sqrt{\frac{2|p_{vc}|^2}{m_0}}}{n_0^2 E_g^3} \frac{\left(2\frac{\hbar\omega}{E_g} - 1\right)^{3/2}}{\left(2\frac{\hbar\omega}{E_g}\right)^5} \tag{C.3}$$

For most direct gap semiconductors, many of the parameters are constant such that to good approximation, the two-photon absorption spectrum can be simplified to be only dependent on the band-gap energy and the linear refractive index as

$$\alpha_2\left(\omega\right) \approx \frac{1.42 \cdot 10^{-7}}{n_0^2 E_g^3} \frac{\left(2\frac{\hbar\omega}{E_g} - 1\right)^{3/2}}{\left(2\frac{\hbar\omega}{E_g}\right)^5} \text{ m/W} \tag{C.4}$$

where $E_g$ is assumed to be given in electron volts. Equations C.2 and C.4 can then be used to calculate the nonlinear refractive index spectrum. This procedure will result in the bandgap scaling law of $E_g^{-4}$ for the magnitude of $n_2$. This scaling explains why chalcogenide and AlGaAs materials possessing bandgaps much smaller than silica, possess much higher nonlinear refractive indices.

# Appendix D

# Dispersion Relation for Whispering Gallery Modes

The dispersion relation for whispering gallery modes is similar to the relation for fiber modes with the exception that the axial propagation constant, $k_z$ is much smaller. The dominant propagation constant is of course directed in the azimuthal direction. For an infinite cylinder and a longitudinal propagation constant of zero, the dispersion relation has eigensolutions with imaginary propagation constants. This implies that either the refractive index and/or the frequency must be complex. This is due to the radiation losses present in the system. Should the disk possess a negative imaginary component of the refractive index (representing gain) solutions exist that maintain a constant field energy in the resonator while power is steadily radiated. In the case of a lossless/gainless dielectric resonator however, solutions of the equation necessarily involve a complex frequency, implying a decay rate of energy confined within the resonator. Obtaining solutions to

the WGM dispersion relation is not trivial because they exist as complex roots of a complex equation. There are many approximations which have been employed to simplify this equation, for example conformal transformation, [156,157] WKB, [158] and volume current methods. [159,99] Because the validity of these methods are in doubt when the resonator circumference approaches a small number of optical cycles, I chose to solve the equation numerically. In order to solve for roots of this equation, I applied a global optimization scheme to minimize the the absolute value of equation over two variables - the real and imaginary parts of the propagation constant. Equation 3.10 can be rewritten in terms of the normalized radius ($X = n_1 2\pi R/\lambda$) and the radiation-limited finesse.

$$n\frac{J'_m\left[X\left(1 - i\frac{1}{2m\mathcal{F}}\right)\right]}{J_m\left[X\left(1 - i\frac{1}{2m\mathcal{F}}\right)\right]} = \frac{H'^{(1)}_m\left[X/n\left(1 - i\frac{1}{2m\mathcal{F}}\right)\right]}{H^{(1)}_m\left[X/n\left(1 - i\frac{1}{2m\mathcal{F}}\right)\right]} \tag{D.1}$$

Using this method, I was able to generate universal plots of limiting finesse vs. size parameter for the fundamental whispering gallery mode of a system of low azimuthal numbers.

# Appendix E

# Numerical Simulation Methods

## E.1  Finite Difference Time Domain (FDTD) Method

The Finite Difference Time Domain (FDTD) Method solves Maxwell's equations directly, by numerically approximating the first order derivatives of the electric and magnetic fields with difference equations on a grid. The real and imaginary parts of permittivity and permeability may vary across the grid to define different material regions. The difference equations are then used to march in time and update the electric and magnetic field components on the grid. Grid resolution must be a small fraction of the material wavelength of the radiation modelled to obtain accuracy. Grid resolution is typically limited by computation time and/or memory. A microresonator with a given Q-factor must be simulated with no greater uncertainty in its dimensions than $1/Q$. This translates into the simple requirement that a grid resolution of lambda/$\mathcal{F}$ is necessary to preserve

the quality of the resonator. A resolution of $\lambda/20 - \lambda/100$ is reasonable for most applications. Computation time scales with the cubic power of the grid resolution in a 2D FDTD since the time step is forced to scale with the grid to keep the equations stable. Because of the demanding computational effort required by the FDTD method, it should be reserved for the modelling of devices with scale sizes close to a small number of wavelengths or for cases where devices cannot be modelled with other faster methods such as the Beam Propagation Method. Resonances of a microresonator may be easily obtained by injecting a wide bandwidth impulse, letting the resonator "ring," collecting the output and Fourier analyzing the spectrum. [103]

## E.2 Splitstep Beam Propagation Method (BPM)

The Splitstep Beam Propagation Method (BPM) solves the reduced wave equation for slowly varying envelopes by numerically stepping in one direction. At each step, the field is perturbed first in the time (or space) domain, then fourier transformed numerically using an fast fourier transform (fft) routine, where it is perturbed in the spectral (or spatial spectral) domain, and finally inverse transformed. [85] At first glance, this method appears to be very complicated and time consuming. In fact the method is very fast because it avoids the need for field con-

volutions and relies on FFT algorithms whose computation time generally scales as $N \log_2(N)$. The method is useful for solving the paraxial diffraction equation with waveguiding terms, the nonlinear Schrödinger equation, and other variants of these. However, it has the limitation of being inherently unidirectional and thus cannot handle abrupt changes in refractive index, reflections, and feedback such as is encountered in a ring resonator geometry.

## E.3 Finite Element Method (FEM)

The Finite Element Method (FEM) is a method of variational calculus that solves for solutions of the Helmholtz equation[1] by globally finding field configurations satisfying the principle of least action. Instead of directly solving the Helmholtz equation, FEMs solve the equivalent variational expression by discretizing the simulation area with faceted elements (usually triangles in 2D) and minimizing an integral expression (in matrix form) which is a function of the values of the field at the element vertices and the value of the derivative of the field at the element edges. This method can very fast and unlike the finite difference method, is not restricted to implementation on a uniform grid. It is very useful for finding eigenvalues (propagation constants) and eigenvectors (field profiles) of a 2D arbitrarily shaped waveguide cross-section. Additionally, it was discovered that the FEM can be implemented to determine the coupling coefficient between

---

[1] as well as the Heat equation, Poisson equation, and others

two 2D waveguides.   This is possible because solution of the composite system yields symmetric and antisymmetric normal modes whose propagation constants differ by twice the constant of coupling.   A commercial FEM package (Femlab) was used to refine the determination of the mode profiles, propagation constants, and coupling constants of the waveguides designed in this thesis.

## E.4   DISCRETE

The Delayed Impulse Simulation of Cavity Resonances for Exact Time Evolution or DISCRETE method may be applied to model nonlinear propagation of arbitrary shaped pulses though multiple ring cavities or layered media.   It requires that the impulse response of the system be composed of a discrete, finite number (truncated if necessary) of spaced delta functions.   Such is the impulse response of a cavity or other feedback structure as demonstrated by Kastler in 1974 [160] for the Fabry-Perot interferometer.   The response associated with material dispersion is continuous however, and thus cannot be accurately modelled with this method.   Fortunately, material dispersion is in general insignificant when compared with the dispersion arising from structural resonances.   For equally spaced delta functions of varying amplitudes in the time domain, as in the case of the reverberating impulses associated with a cavity, the amplitudes correspond to Fourier coefficients of a periodic dispersion relation in the frequency domain.

For a ring resonator, the impulse response is given by

$$h\left(t\right) = r\delta\left(t\right) - t^2 e^{+i\phi} \sum_{m=1}^{\infty} \left(re^{+i\phi}\right)^{m-1} \delta\left(t - mT_{\mathrm{R}}\right). \qquad \text{(E.1)}$$

If the resonator is linear, then the accumulated phase per round trip, $\phi$ is simply a constant and the impulse response can be Fourier transformed to obtain the linear transfer function which contains complete information regarding the amplitude and phase of transmission at all frequencies. The linear transmission is thus trivially obtained by multiplying the incident spectrum by the transfer function and Fourier transforming to the temporal domain. In the case of a nonlinear resonator however, this linear systems technique fails because the phase parameter $\phi$ contained in the impulse response is dependent upon the internal field strength which is in turn time dependent. The exiting field in the time domain must be constructed by summing all the contributions from multiple passes as in the case of the impulse response but with a phase term that is continuously updated by the current field circulating in the resonator. The DISCRETE method of simulation accomplishes this and is iterated in the following manner. First, the input field is specified for the entire time axis. At first iteration, the field is split at the coupler. The component of the field exiting (bypassing) the resonator is set aside. The component of the field entering the resonator is then simply delayed, attenuated (if loss is included) and linear and nonlinear phase shifts are applied. The delayed circulating field is fed back into the coupler where it is

split and interfered with the original field.   The process then continues to the next iteration.   The output fields collected at each iteration are then summed to obtain the output field.   Typically the number of iterations required to obtain sufficient numerical accuracy is of the order of a 3-4 times the resonator finesse. Figure E.1 compares the results of a DISCRETE and BPM simulations of second order soliton splitting.   The DISCRETE method has the advantage of being correct to all orders while the BPM used here only includes dispersion through third order, self-phase modulation, self-steepening, and saturation for modelling the nonlinearity.   Nevertheless, the results are qualitatively very similar.   Because the nature of the dispersion is structural, it is treated more naturally in the time domain as opposed to material dispersion which is more naturally treated in the frequency domain.   Because the impulses need not actually be propagated in the guiding segments, DISCRETE simulations are much faster than the BPM method.
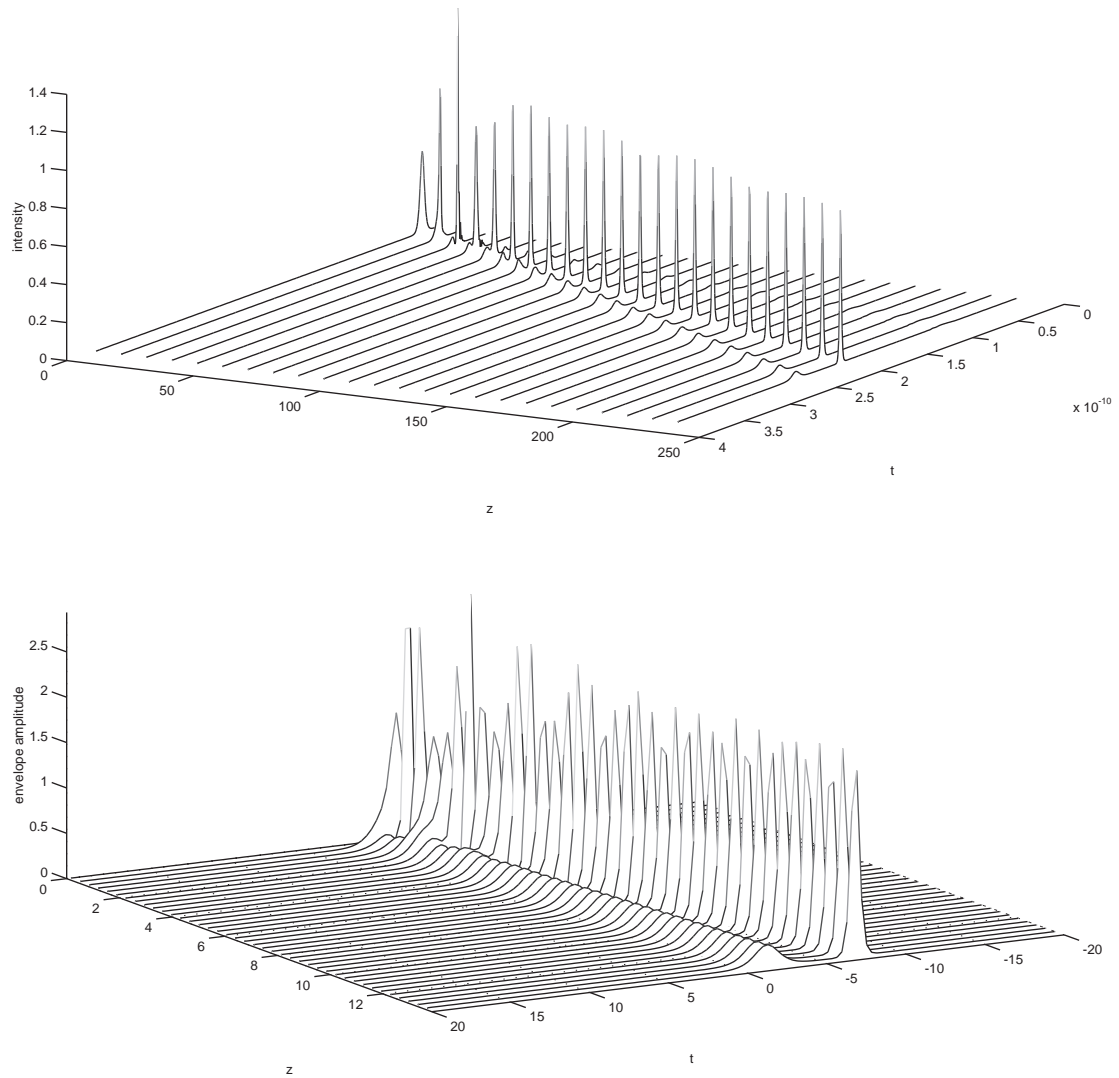
Figure E.1: a) DISCRETE and b) BPM simulations of soliton splitting in a SCISSOR structure.

# Appendix F

# Nonlinear Schrödinger Equation

The nonlinear Schrödinger equation (NLSE) is the governing equation for soliton propagation and modulation instability in nonlinear optics, [64,85]

$$\frac{\partial}{\partial z}A = -i\frac{1}{2}k''\frac{\partial^2}{\partial t^2}A + i\gamma \left|A\right|^2 A. \tag{F.1}$$

Here, the time $t$ is the temporal coordinate in the frame of the pulse moving with group velocity $v_g = 1/k'$. The collection of parameters, $\gamma \left|A\right|^2$ is equivalent to the nonlinear propagation constant, $k_{\mathrm{NL}} = \frac{2\pi}{\lambda}n_2 I$.

## F.1   Solitons

Solitons are analytic solutions to the NLSE whereby the dispersive and nonlinear terms balance each other to form pulses that are stationary with propagation

variable $z$. The fundamental soliton solution is,

$$A\left(z, t - k'z\right) = A_0 \operatorname{sech}\left(\frac{t - k'z}{T_{\mathrm{P}}}\right) e^{i\frac{1}{2}\gamma|A_0|^2 z}. \tag{F.2}$$

Higher order solutions exist which "breath" with a periodicity of $\frac{\pi}{2}T_{\mathrm{P}}^2/k''$. Each of these is characterized by the soliton integer,

$$N = \sqrt{\frac{\gamma A_0^2 T_{\mathrm{P}}^2}{k''}}. \tag{F.3}$$

## F.2 Modulation Instability

Modulation instability in the context of optical nonlinearities refers to the generation of sidebands in the vicinity of a strong cw pump. Closely related to four-wave mixing, it arises in a dispersive system when the self-phase modulation associated with perturbations is strong enough to phase match four ordinarily mismatched wavevectors. A constant (cw) background solution ($A_0$) to the NLSE is accompanied by a weak perturbation ($a$),

$$A = \left(A_0 + a\right) e^{i\gamma|A_0|^2 z}. \tag{F.4}$$

Inserting this assumed solution into the NLSE yields an evolution equation for the perturbing field in terms of itself and the (non-depleting) cw pump:

$$\frac{\partial}{\partial z}a = -i\frac{1}{2}k''\frac{\partial^2}{\partial t^2}a + i\gamma\left(A_0^2 a^* + |A_0|^2\,a + A_0\,|a|^2 + A_0\,|a|^2 + a^2 A_0^* + |a|^2\,a\right).$$

$$(F.5)$$

Without loss of generality, the cw pump is assumed to be real. Retaining only those terms linear in $a$ (or $a^*$) results in two equations for the perturbing field:

$$\frac{\partial}{\partial z}a = -i\frac{1}{2}k''\frac{\partial^2}{\partial t^2}a + i\gamma\,|A_0|^2\,(a + a^*), \qquad (F.6)$$

$$\frac{\partial}{\partial z}a^* = i\frac{1}{2}k''\frac{\partial^2}{\partial t^2}a^* - i\gamma\,|A_0|^2\,(a + a^*). \qquad (F.7)$$

The Fourier transform of these equations (in both $z$ and $t$) relates the perturbing propagation constant, $K$ to the perturbing frequency, $\Omega$:

$$\left[K - \frac{1}{2}k''\Omega^2 - \gamma\,|A_0|^2\right]a = \gamma\,|A_0|^2\,a^*, \qquad (F.8)$$

$$\left[K + \frac{1}{2}k''\Omega^2 + \gamma\,|A_0|^2\right]a^* = -\gamma\,|A_0|^2\,a. \qquad (F.9)$$

Multiplying the equations results in two solutions for the dispersion relation:

$$\left[K - \left(\frac{1}{2}k''\Omega^2 + \gamma\,|A_0|^2\right)\right]\left[K + \left(\frac{1}{2}k''\Omega^2 + \gamma\,|A_0|^2\right)\right] = -\left(\gamma\,|A_0|^2\right)^2, \quad (F.10)$$

$$K = \pm\frac{\Omega k''}{2}\sqrt{\Omega^2 + \text{sgn}\,(k'')\left(\frac{4\gamma\,|A_0|^2}{|k''|}\right)}. \quad (F.11)$$

If the sign of $k''$ is negative, the propagation constant can be imaginary, leading to exponential growth or decay for the perturbing field. The modulation gain is

$$g\left(\Omega\right) = \pm\Omega k''\sqrt{\left(\frac{4\gamma\left|A_0\right|^2}{\left|k''\right|}\right) - \Omega^2}. \tag{F.12}$$

Where the gain occurs up to a cutoff modulation frequency,

$$\Omega_c = \sqrt{\frac{4\gamma\left|A_0\right|^2}{\left|k''\right|}}, \tag{F.13}$$

peaking at

$$\Omega_{\mathrm{m}} = \pm\Omega_c/\sqrt{2} = \pm\sqrt{\frac{2\gamma\left|A_0\right|^2}{\left|k''\right|}}, \tag{F.14}$$

where the peak gain is given by

$$g_{(\Omega_{\mathrm{m}})} = 2\gamma\left|A_0\right|^2. \tag{F.15}$$

# Appendix G

# Dispersion Relations for Periodic Photonic Structures

## G.1   Finite Periodic Structures

In the case of finite periodic structure consisting of N unit cells, the transfer matrix is constructed from individual 2×2 transfer matrices by simple multiplication:

$$
\begin{pmatrix} E_{a,N} \\ E_{b,N} \end{pmatrix} = \begin{pmatrix} M_{11} & M_{12} \\ M_{21} & M_{22} \end{pmatrix}^N \begin{pmatrix} E_{a,0} \\ E_{b,0} \end{pmatrix} = \begin{pmatrix} T_{11} & T_{12} \\ T_{21} & T_{22} \end{pmatrix} \begin{pmatrix} E_{a,0} \\ E_{b,0} \end{pmatrix}
\tag{G.1}
$$

If excitation is restricted to the lower left channel only $(a, j)$, with outputs $(a, N)$ and $(b, 0)$, the condition dictates that $E_{b,N} = 0$. The transfer matrix coefficients can then be used to uniquely obtain the fields at $E_{a,N}$ and $E_{b,0}$. The complex transmission and reflection coefficients are extracted from the elements of the

transfer matrix as follows:

$$\frac{E_{a,N}}{E_{a,0}} = \frac{1}{T_{22}} \tag{G.2}$$

$$\frac{E_{b,0}}{E_{a,0}} = -\frac{T_{21}}{T_{22}} \tag{G.3}$$

However, if excitation is restricted to the lower left channel only $(a, j)$, with outputs $(a, N)$ and $(b, N)$, the condition dictates that $E_{b,0} = 0$. The transfer matrix coefficients can then be used to uniquely obtain the fields at $E_{a,N}$ and $E_{b,N}$. The complex transmission and reflection coefficients are extracted from the elements of the transfer matrix as follows:

$$\frac{E_{a,N}}{E_{a,0}} = T_{11} \tag{G.4}$$

$$\frac{E_{b,N}}{E_{a,0}} = T_{21} \tag{G.5}$$

## G.2 Infinite Periodic Structures (Bloch's Theorem)

For an infinite periodic coupled structure with four ports, Bloch's theorem states:

$$E_{a,j+1} = e^{ik_{\text{eff}}L} E_{a,j} \tag{G.6}$$

$$E_{b,j+1} = e^{ik_{\text{eff}}L} E_{b,j} \tag{G.7}$$

Applying this to a structure composed of unit cells described by the unitary $M$

matrix results in an equation which can be used to derive the dispersion relation,

$$
\det \begin{pmatrix} e^{ik_{\mathrm{eff}}L} - M_{11} & -M_{12} \\ -M_{21} & e^{ik_{\mathrm{eff}}L} - M_{22} \end{pmatrix} = 0 \tag{G.8}
$$

The quadratic formula is then used to explicitly generate the dispersion relation:

$$
e^{i2k_{\mathrm{eff}}L} - (M_{11} + M_{22}) e^{ik_{\mathrm{eff}}L} + (M_{11}M_2 - M_{12}M_{21}) = 0 \tag{G.9}
$$

$$
k_{\mathrm{eff}} = \frac{1}{L} \arg \left[ \frac{(M_{11} + M_{22})}{2} \pm \left( \frac{(M_{11} - M_{22})^2}{4} + M_{12}M_{21} \right)^{1/2} \right] \tag{G.10}
$$

The eigenvector relations are

$$
E_{b,j} = \frac{e^{ik_{\mathrm{eff}}L} - M_{11}}{M_{12}} E_{a,j} \tag{G.11}
$$

$$
E_{b,j} = \frac{M_{21}}{e^{ik_{\mathrm{eff}}L} - M_{22}} E_{a,j} \tag{G.12}
$$

which, when combined with the eigensolutions gives two unique relations based

only on the coupling coefficients:

$$
E_{b,j} = -\frac{\frac{(M_{11}-M_{22})}{2} \mp \left( \frac{(M_{11}-M_{22})^2}{4} + M_{12}M_{21} \right)^{1/2}}{M_{12}} E_{a,j} \tag{G.13}
$$

$$
E_{b,j} = +\frac{M_{21}}{\frac{(M_{11}-M_{22})}{2} \pm \left( \frac{(M_{11}-M_{22})^2}{4} + M_{12}M_{21} \right)^{1/2}} E_{a,j} \tag{G.14}
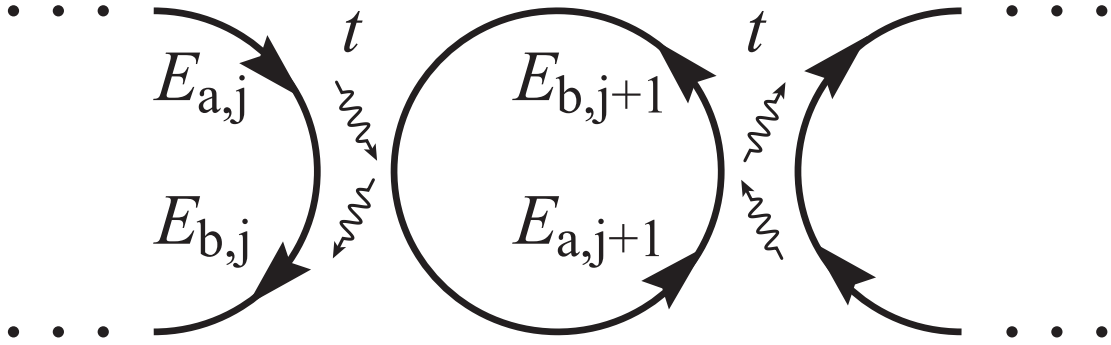$$

Figure G.1: Fields in a Coupled Resonator Optical Waveguide.

This procedure will be applied to derive dispersion relations for a variety of resonator-based, 4-port infinite periodic structures.

## G.3   CROW

A coupled-resonator optical waveguide (CROW) is mathematically equivalent to a multi-layer stack.   The direction of circulation of optical power flow however alternates from resonator to resonator.   So long as the convention of alternating the designation of $a$ and $b$ fields is applied, the mathematical derivation for a multi-layer stack directly carries over to that of a CROW.   The path length between couplers becomes $\pi R$ and the periodicity of the structure, $L = 2R$.

Relating the fields at the coupling interfaces results in two equations:

$$E_{a,j+1} = it e^{i\frac{n\pi R}{c}\omega} E_{a,j} + r e^{i2\frac{n\pi R}{c}\omega} E_{b,j+1} \tag{G.15}$$

$$E_{b,j} = r E_{a,j} + it E_{b,j+1} e^{i\frac{n\pi R}{c}\omega} \tag{G.16}$$

The fields at $j + 1$ are related to the fields at $j$, according to:

$$E_{a,j+1} = -\frac{1}{it}e^{i\frac{n\pi R}{c}\omega}E_{a,j} + \frac{r}{it}e^{i\frac{n\pi R}{c}\omega}E_{b,j} \tag{G.17}$$

$$E_{b,j+1} = -\frac{r}{it}e^{-i\frac{n\pi R}{c}\omega}E_{a,j} + \frac{1}{it}e^{-i\frac{n\pi R}{c}\omega}E_{b,j} \tag{G.18}$$

Equations G.17 and G.18 are combined in a matrix formulation:

$$\begin{pmatrix} E_{a,j+1} \\ E_{b,j+1} \end{pmatrix} = \begin{pmatrix} M_{11} & M_{12} \\ M_{21} & M_{22} \end{pmatrix} \begin{pmatrix} E_{a,j} \\ E_{b,j} \end{pmatrix} \tag{G.19}$$

Where the matrix coefficients are explicitly given by:

$$M_{11} = -\frac{1}{it}e^{i\frac{n\pi R}{c}\omega} \tag{G.20}$$

$$M_{12} = \frac{r}{it}e^{i\frac{n\pi R}{c}\omega} \tag{G.21}$$

$$M_{21} = -\frac{r}{it}e^{-i\frac{n\pi R}{c}\omega} \tag{G.22}$$

$$M_{22} = \frac{1}{it}e^{-i\frac{n\pi R}{c}\omega} \tag{G.23}$$

For an infinite CROW, applying the procedure based on Bloch's theorem, the dispersion relation is thus:

$$k_{\text{eff}} = \frac{1}{2R}\arg\left[i\frac{\left(e^{i\frac{n\pi R}{c}\omega} - e^{-i\frac{n\pi R}{c}\omega}\right)}{2t} \pm i\left(\frac{\left(e^{i\frac{n\pi R}{c}\omega} + e^{-i\frac{n\pi R}{c}\omega}\right)^2}{4t^2} - \frac{r^2}{t^2}\right)^{1/2}\right] \tag{G.24}$$
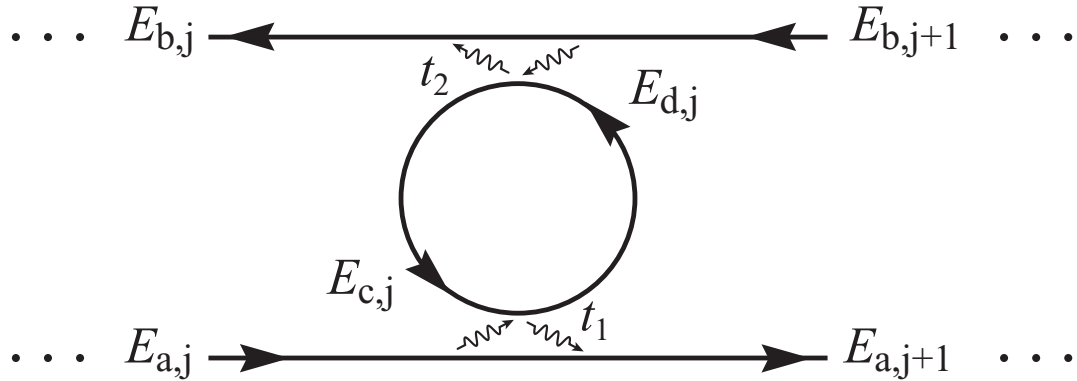
Figure G.2: Fields in a double-channel SCISSOR.

The two solutions represent the forward- and backward-going waves in the multi-layer structure.  The matrix for an alternating CROW structure in which subsequent resonators possess different circumferences is easily derived by simple matrix multiplication.

## G.4   SCISSOR

A side-coupled, integrated spaced sequence of resonators can be constructed with a few variations.  The dispersion relation for a double-channel SCISSOR is first derived and later a limiting case will provide the dispersion relation for a single-channel SCISSOR.

## G.4.1 Double-Channel SCISSOR

The lower coupler provides two relations for the fields:

$$E_{a,j+1} = r_1 e^{i\frac{nL}{c}\omega} E_{a,j} + it_1 e^{i\frac{1}{2}\frac{nL}{c}\omega} E_{c,j} \tag{G.25}$$

$$E_{d,j} = it_1 e^{i\frac{1}{2}\frac{n2\pi R}{c}\omega} e^{i\frac{1}{2}\frac{nL}{c}\omega} E_{a,j} + r_1 e^{i\frac{1}{2}\frac{n2\pi R}{c}\omega} E_{c,j} \tag{G.26}$$

The upper coupler provides two more relations for the fields:

$$E_{b,j} = r_2 e^{i\frac{nL}{c}\omega} E_{b,j+1} + it_2 e^{i\frac{1}{2}\frac{nL}{c}\omega} E_{d,j} \tag{G.27}$$

$$E_{c,j} = it_2 e^{i\frac{1}{2}\frac{n2\pi R}{c}\omega} e^{i\frac{1}{2}\frac{nL}{c}\omega} E_{b,j+1} + r_2 e^{i\frac{1}{2}\frac{n2\pi R}{c}\omega} E_{d,j} \tag{G.28}$$

The circulating field equations G.26 and G.28, are manipulated algebraically such that the circulating fields, $E_{d,j}$ and $E_{c,j}$ are only dependent on the two input fields, $E_{a,j}$ and $E_{b,j+1}$:

$$E_{d,j} = \frac{it_1 e^{i\frac{1}{2}\frac{n2\pi R}{c}\omega} e^{i\frac{1}{2}\frac{nL}{c}\omega}}{1 - r_1 r_2 e^{i\frac{n2\pi R}{c}\omega}} E_{a,j} + \frac{it_2 r_1 e^{i\frac{n2\pi R}{c}\omega} e^{i\frac{1}{2}\frac{nL}{c}\omega}}{1 - r_1 r_2 e^{i\frac{n2\pi R}{c}\omega}} E_{b,j+1} \tag{G.29}$$

$$E_{c,j} = \frac{it_2 e^{i\frac{1}{2}\frac{n2\pi R}{c}\omega} e^{i\frac{1}{2}\frac{nL}{c}\omega}}{1 - r_1 r_2 e^{i\frac{n2\pi R}{c}\omega}} E_{b,j+1} + \frac{it_1 r_2 e^{i\frac{n2\pi R}{c}\omega} e^{i\frac{1}{2}\frac{nL}{c}\omega}}{1 - r_1 r_2 e^{i\frac{n2\pi R}{c}\omega}} E_{a,j} \tag{G.30}$$

These expressions are then used in conjunction with equations G.25 and G.27, to describe the output fields, $E_{a,j+1}$ and $E_{b,j}$ solely dependent on the input fields,

$E_{a,j}$ and $E_{b,j+1}$:

$$E_{a,j+1}e^{-i\frac{nL}{c}\omega} = \frac{r_1 - r_2 e^{i\frac{n2\pi R}{c}\omega}}{1 - r_1 r_2 e^{i\frac{n2\pi R}{c}\omega}}E_{a,j} - \frac{t_1 t_2 e^{i\frac{1}{2}\frac{n2\pi R}{c}\omega}}{1 - r_1 r_2 e^{i\frac{n2\pi R}{c}\omega}}E_{b,j+1} \tag{G.31}$$

$$E_{b,j}e^{-i\frac{nL}{c}\omega} = -\frac{t_1 t_2 e^{i\frac{1}{2}\frac{n2\pi R}{c}\omega}}{1 - r_1 r_2 e^{i\frac{n2\pi R}{c}\omega}}E_{a,j} + \frac{r_2 - r_1 e^{i\frac{n2\pi R}{c}\omega}}{1 - r_1 r_2 e^{i\frac{n2\pi R}{c}\omega}}E_{b,j+1} \tag{G.32}$$

The fields at $j+1$ are related to the fields at $j$, according to:

$$E_{a,j+1} = \frac{1 - r_1 r_2 e^{-i\frac{n2\pi R}{c}\omega}}{r_1 - r_2 e^{-i\frac{n2\pi R}{c}\omega}}e^{i\frac{nL}{c}\omega}E_{a,j} - \frac{t_1 t_2 e^{i\frac{1}{2}\frac{n2\pi R}{c}\omega}}{r_2 - r_1 e^{i\frac{n2\pi R}{c}\omega}}E_{b,j} \tag{G.33}$$

$$E_{b,j+1} = -\frac{t_1 t_2 e^{-i\frac{1}{2}\frac{n2\pi R}{c}\omega}}{r_1 - r_2 e^{-i\frac{n2\pi R}{c}\omega}}E_{a,j} + \frac{1 - r_1 r_2 e^{i\frac{n2\pi R}{c}\omega}}{r_2 - r_1 e^{i\frac{n2\pi R}{c}\omega}}e^{-i\frac{nL}{c}\omega}E_{b,j} \tag{G.34}$$

Equations G.33 and G.34 are combined in a matrix formulation:

$$\begin{pmatrix} E_{a,j+1} \\ E_{b,j+1} \end{pmatrix} = \begin{pmatrix} M_{11} & M_{12} \\ M_{21} & M_{22} \end{pmatrix}\begin{pmatrix} E_{a,j} \\ E_{b,j} \end{pmatrix} \tag{G.35}$$

Where the matrix coefficients are explicitly given by:

$$M_{11} = \frac{1 - r_1 r_2 e^{-i\frac{n2\pi R}{c}\omega}}{r_1 - r_2 e^{-i\frac{n2\pi R}{c}\omega}}e^{i\frac{nL}{c}\omega} \tag{G.36}$$

$$M_{12} = -\frac{t_1 t_2 e^{i\frac{1}{2}\frac{n2\pi R}{c}\omega}}{r_2 - r_1 e^{i\frac{n2\pi R}{c}\omega}} \tag{G.37}$$

$$M_{21} = -\frac{t_1 t_2 e^{-i\frac{1}{2}\frac{n2\pi R}{c}\omega}}{r_1 - r_2 e^{-i\frac{n2\pi R}{c}\omega}} \tag{G.38}$$

$$M_{22} = \frac{1 - r_1 r_2 e^{i\frac{n2\pi R}{c}\omega}}{r_2 - r_1 e^{i\frac{n2\pi R}{c}\omega}}e^{-i\frac{nL}{c}\omega} \tag{G.39}$$

For an infinite SCISSOR, applying the procedure based on Bloch's theorem, the
dispersion relation is thus:

$$
k_{\text{eff}} = \frac{1}{L} \arg \left[ \frac{\left( \frac{1-r_1 r_2 e^{-i\frac{n2\pi R}{c}\omega}}{r_1 - r_2 e^{-i\frac{n2\pi R}{c}\omega}} e^{i\frac{nL}{c}\omega} + \frac{1-r_1 r_2 e^{i\frac{n2\pi R}{c}\omega}}{r_2 - r_1 e^{i\frac{n2\pi R}{c}\omega}} e^{-i\frac{nL}{c}\omega} \right)}{2} \right.
$$

$$
\left. \pm \left( \frac{\left( \frac{1-r_1 r_2 e^{-i\frac{n2\pi R}{c}\omega}}{r_1 - r_2 e^{-i\frac{n2\pi R}{c}\omega}} e^{i\frac{nL}{c}\omega} - \frac{1-r_1 r_2 e^{i\frac{n2\pi R}{c}\omega}}{r_2 - r_1 e^{i\frac{n2\pi R}{c}\omega}} e^{-i\frac{nL}{c}\omega} \right)^2}{4} + \frac{\left(1-r_1^2\right)\left(1-r_2^2\right)}{\left( r_2 - r_1 e^{i\frac{n2\pi R}{c}\omega} \right) \left( r_1 - r_2 e^{-i\frac{n2\pi R}{c}\omega} \right)} \right)^{1/2} \right]
$$

(G.40)

The two solutions represent the forward- and backward-going waves in the pho-
tonic structure. The coherent build-up of intensity in the resonators with respect
to the guides can be derived from equations G.29, G.30, the eigenvector relations
G.11 and G.12, and the Bloch relation:

$$
\left| \frac{E_{d,j}}{E_{a,j}} \right|^2 = \left| \frac{it_1}{1 - r_1 r_2 e^{i\frac{n2\pi R}{c}\omega}} + \frac{it_2 r_1 e^{i\frac{1}{2}\frac{n2\pi R}{c}\omega} e^{ik_{\text{eff}}L}}{1 - r_1 r_2 e^{i\frac{n2\pi R}{c}\omega}} \left( \frac{e^{ik_{\text{eff}}L} - M_{11}}{M_{12}} \right) \right|^2 \qquad (G.41)
$$

$$
\left| \frac{E_{c,j}}{E_{a,j}} \right|^2 = \left| \frac{it_2 e^{ik_{\text{eff}}L}}{1 - r_1 r_2 e^{i\frac{n2\pi R}{c}\omega}} \left( \frac{e^{ik_{\text{eff}}L} - M_{11}}{M_{12}} \right) + \frac{it_1 r_2 e^{i\frac{1}{2}\frac{n2\pi R}{c}\omega}}{1 - r_1 r_2 e^{i\frac{n2\pi R}{c}\omega}} \right|^2 \qquad (G.42)
$$

## G.4.2 Single-Channel SCISSOR

Testing the particular case $(r_2 = 1)$ should return the dispersion relation for an infinite periodic single-channel SCISSOR:

$$k_{\text{eff}} = \frac{1}{L} \arg \left[ \left( \frac{1}{2} \frac{r_1 - e^{i\frac{n2\pi R}{c}\omega}}{1 - r_1 e^{i\frac{n2\pi R}{c}\omega}} e^{i\frac{nL}{c}\omega} + \frac{1}{2} e^{-i\frac{nL}{c}\omega} \right) \pm \left( \frac{1}{2} \frac{r_1 - e^{i\frac{n2\pi R}{c}\omega}}{1 - r_1 e^{i\frac{n2\pi R}{c}\omega}} e^{i\frac{nL}{c}\omega} - \frac{1}{2} e^{-i\frac{nL}{c}\omega} \right) \right]$$

(G.43)

$$= -\frac{n}{c}\omega \ , \ \frac{n}{c}\omega + \frac{1}{L} \arg \left[ \frac{r_1 - e^{i\frac{n2\pi R}{c}\omega}}{1 - r_1 e^{i\frac{n2\pi R}{c}\omega}} \right] = -\frac{n}{c}\omega \ , \ \frac{n}{c}\omega + \frac{\Phi(\omega)}{L} \tag{G.44}$$

The first solution simply describes light propagating backwards in the upper (isolated) waveguide. The second solution is that of the single-channel SCISSOR.

## G.4.3 Twisted Double-Channel SCISSOR

This configuration may be considered to be a double-channel SCISSOR with the top ports of each unit cell reversed. This would have the effect of twisting the resonator into a figure-8. Alternatively, the structure may be considered to be composed of two channels coupled via two resonators which are 100% coupled to each other.

Equations G.31 and G.32 derived for the ordinary double-channel SCISSOR are used as a starting point in the derivation of the dispersion relation for the twisted variety. The distinction is made if the fields, $E_{b,j}$ and $E_{b,j+1}$ are reversed. Furthermore, the total path length around the resonator remains $2\pi R$ for direct
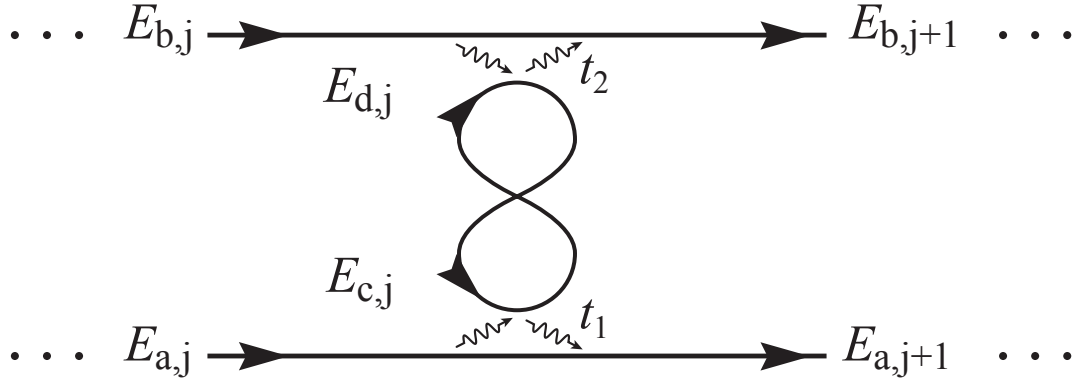
Figure G.3: Fields in a twisted double-channel SCISSOR.

comparisons.  The fields at $j + 1$ are thus related to the fields at $j$, according to:

$$E_{a,j+1}e^{-i\frac{nL}{c}\omega} = +\frac{r_1 - r_2e^{i\frac{n2\pi R}{c}\omega}}{1 - r_1r_2e^{i\frac{n2\pi R}{c}\omega}}E_{a,j} - \frac{t_1t_2e^{i\frac{1}{2}\frac{n2\pi R}{c}\omega}}{1 - r_1r_2e^{i\frac{n2\pi R}{c}\omega}}E_{b,j} \tag{G.45}$$

$$E_{b,j+1}e^{-i\frac{nL}{c}\omega} = -\frac{t_1t_2e^{i\frac{1}{2}\frac{n2\pi R}{c}\omega}}{1 - r_1r_2e^{i\frac{n2\pi R}{c}\omega}}E_{a,j} + \frac{r_2 - r_1e^{i\frac{n2\pi R}{c}\omega}}{1 - r_1r_2e^{i\frac{n2\pi R}{c}\omega}}E_{b,j} \tag{G.46}$$

Equations G.45 and G.46 are combined in a matrix formulation:

$$\begin{pmatrix} E_{a,j+1} \\ E_{b,j+1} \end{pmatrix} = \begin{pmatrix} M_{11} & M_{12} \\ M_{21} & M_{22} \end{pmatrix} \begin{pmatrix} E_{a,j} \\ E_{b,j} \end{pmatrix} \tag{G.47}$$

Where the matrix coefficients are explicitly given by:

$$M_{11} = \frac{r_1 - r_2 e^{i\frac{n2\pi R}{c}\omega}}{1 - r_1 r_2 e^{i\frac{n2\pi R}{c}\omega}} e^{i\frac{nL}{c}\omega} \tag{G.48}$$

$$M_{12} = -\frac{t_1 t_2 e^{i\frac{1}{2}\frac{n2\pi R}{c}\omega}}{1 - r_1 r_2 e^{i\frac{n2\pi R}{c}\omega}} e^{i\frac{nL}{c}\omega} \tag{G.49}$$

$$M_{21} = -\frac{t_1 t_2 e^{i\frac{1}{2}\frac{n2\pi R}{c}\omega}}{1 - r_1 r_2 e^{i\frac{n2\pi R}{c}\omega}} e^{i\frac{nL}{c}\omega} \tag{G.50}$$

$$M_{22} = \frac{r_2 - r_1 e^{i\frac{n2\pi R}{c}\omega}}{1 - r_1 r_2 e^{i\frac{n2\pi R}{c}\omega}} e^{i\frac{nL}{c}\omega} \tag{G.51}$$

For an infinite SCISSOR, applying the procedure based on Bloch's theorem, the dispersion relation is thus:

$$k_{\text{eff}} = \frac{1}{L} \arg \left[ e^{i\frac{nL}{c}\omega} + \frac{\left( \frac{r_1 - r_2 e^{i\frac{n2\pi R}{c}\omega}}{1 - r_1 r_2 e^{i\frac{n2\pi R}{c}\omega}} + \frac{r_2 - r_1 e^{i\frac{n2\pi R}{c}\omega}}{1 - r_1 r_2 e^{i\frac{n2\pi R}{c}\omega}} \right)}{2} \right.$$

$$\left. \pm \left( \frac{\left[ \left( r_1 - r_2 e^{i\frac{n2\pi R}{c}\omega} \right) - \left( r_2 - r_1 e^{i\frac{n2\pi R}{c}\omega} \right) \right]^2 + 4\left(1 - r_1^2\right)\left(1 - r_2^2\right) e^{i\frac{n2\pi R}{c}\omega}}{4 \left( 1 - r_1 r_2 e^{i\frac{n2\pi R}{c}\omega} \right)^2} \right)^{1/2} \right]$$

$$\tag{G.52}$$

The solutions represent the two coupled forward-going waves in the photonic structure. The coherent build-up of intensity in the resonators with respect to the guides can be derived from equations G.29, G.30, and the eigenvector relations G.11 and G.12.

Testing the particular case $(r_2 = 1)$ should return the dispersion relation for

an infinite periodic single-channel SCISSOR:

$$k_{\text{eff}} = \frac{n}{c}\omega + \frac{1}{L}\arg\left[\frac{\frac{r_1 - e^{i\frac{n2\pi R}{c}\omega}}{1 - r_1 e^{i\frac{n2\pi R}{c}\omega}} + 1}{2} \pm \frac{\frac{r_1 - e^{i\frac{n2\pi R}{c}\omega}}{1 - r_1 e^{i\frac{n2\pi R}{c}\omega}} - 1}{2}\right] \tag{G.53}$$

$$= \frac{n}{c}\omega \ , \ \frac{n}{c}\omega + \frac{1}{L}\arg\left[\frac{r_1 - e^{i\frac{n2\pi R}{c}\omega}}{1 - r_1 e^{i\frac{n2\pi R}{c}\omega}}\right] = \frac{n}{c}\omega \ , \ \frac{n}{c}\omega + \frac{\Phi(\omega)}{L} \tag{G.54}$$

The first solution simply describes light propagating fowards in the upper (isolated) waveguide. The second solution is that of the single-channel SCISSOR.

# Appendix H

# Figure-8 Laser

In order to test the fabricated samples containing microresonator-based devices, a pulsed laser source capable of providing picosecond, high peak power pulses was required. A passively mode-locked fiber figure-eight laser (F8L) [161] was constructed for this purpose. The laser consists of two loops of fiber connected by a central 50/50 directional coupler, see figure H.1. One loop functions as a nonlinear amplifying loop mirror (NALM) [162,163] while the other serves to complete the ring cavity. A nonlinear amplifying loop mirror behaves much like a fiber Sagnac interferometer but with the inclusion of an amplifying element (here, a pumped erbium-doped fiber) and a fiber with nonzero intensity-dependent refractive index. An ordinary Sagnac interferometer consists of a loop of fiber connecting two outputs of a 50/50 directional coupler. Light entering one of the input ports of the coupler is split into counter-propagating fields within the loop which constrains them to recombine after one round trip. There are four possible paths that the light can take in reemerging from the coupler input ports,

two for each. Because both fields pass through the same optical channel, albeit in opposite directions, they will acquire exactly the same phase shift due to the optical reciprocity of the fiber. The resulting interference of the two paths at each port is thus completely dictated by the phase shifts acquired in self- and cross-couplings within the directional coupler. It is easy to show that the interference is such that the two paths interfere in a completely constructive manner at the original input port and in a completely destructive manner at the other port - hence the term "loop mirror." This is, of course provided that the fiber loop behaves symmetrically for counterpropagating fields. The symmetry is broken if the fiber loop is rotating about its axis whereby counterpropagating fields are doppler shifted in opposite directions and acquire a differential phase shift (fiber gyroscope principle). The symmetry may also be broken if an amplifying element is asymmetrically positioned within the loop. In this configuration, one of the counterpropagating fields is amplified earlier in its round trip journey around the loop and thus acquires a larger nonlinear phase shift relative to the other. Both pulses are, however, equally amplified. If the differential nonlinear phase shift is equal to $\pi$ radians, then light can be "switched" out of the loop and the device becomes transmissive rather than reflective. Now, if the two coupler inputs are connected with another fiber loop which includes an inline Faraday isolator, a laser oscillator with a "passive" mode-locking mechanism may be obtained. The complete configuration suppresses continuous-wave laser oscil-

lation and favors high intensity pulsed operation because the isolator only allows a continuous cycling of light when the NALM is transmitting. The NALM and isolator combination effectively operate as a saturable absorber and gain medium (or simply an intensity-induced gain medium) - a configuration commonly used to produce mode-locked laser output. An output coupler (10%) is included in the second loop to extract a fraction of the pulse cycling within the cavity. An angle-tuned 2.5 nm bandpass Fabry-Perot filter was placed in the cavity narrowed the free-running bandwidth (of about 10 nm) and provided wavelength tunability. It was initially found that the laser would not mode-lock after placement of the filter inside the cavity. It was postulated that the reason was that rejected wavelengths outside the pass-band set up spurious oscillations which robbed the desired transmitted pass-band of gain. To test this theory, an additional isolator was added such that the filter was situated between two isolators. Following this adjustment, it was found that indeed the laser would again mode-lock.

The constructed figure-eight laser provided 100 $\mu$W of average power at 1530 nm. An erbium doped fiber amplifier (EDFA) was assembled to boost this by 20dB. The repetition rate of the laser, dictated by the longitudinal mode spacing, was measured to be 1.5 MHZ. The pulse-width, inferred from the 2.5 nm FWHM spectrum H.2 was approximately 1 ps. From these measurements, it was estimated that the amplified pulses possessed 10 kW of peak power or approximately 10 nJ energies.
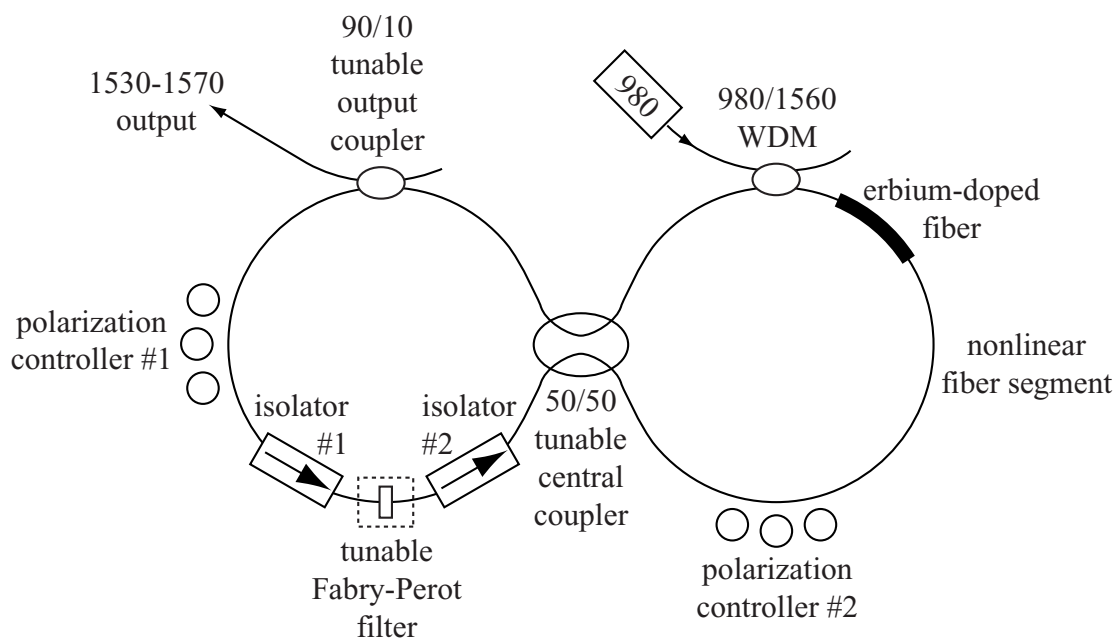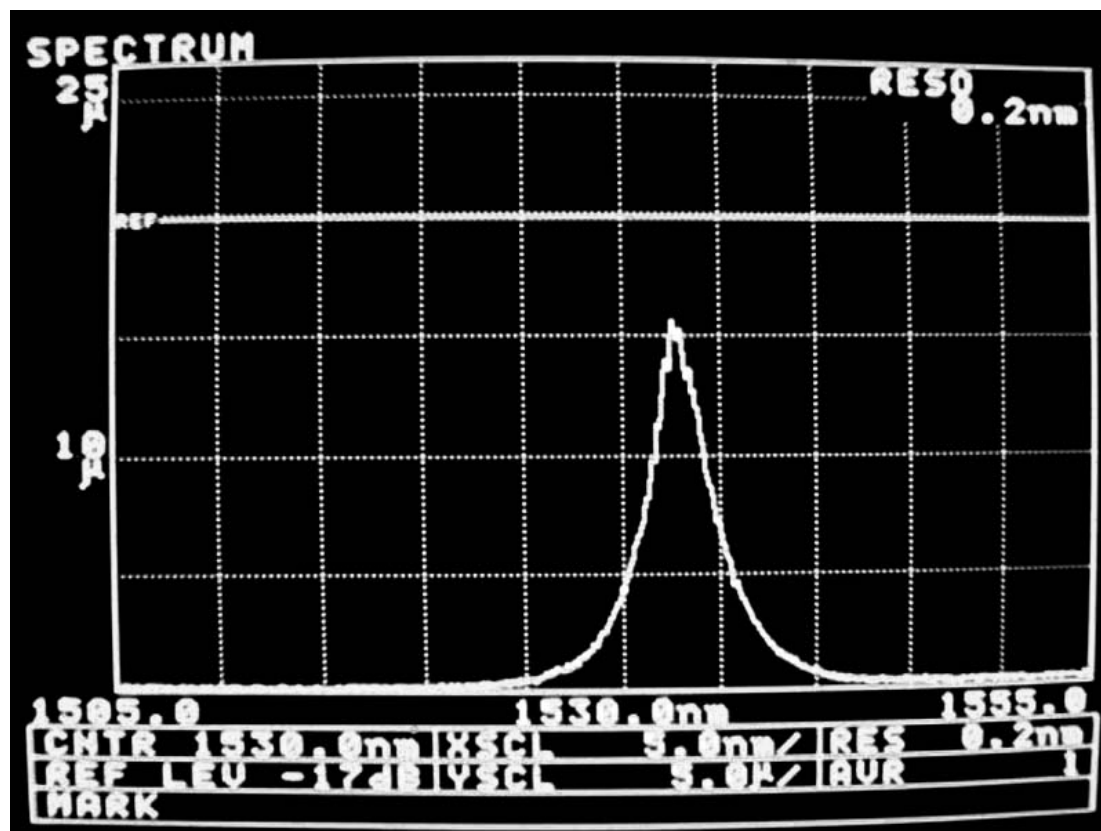
Figure H.1: A mode-locked fiber figure-eight laser.



Figure H.2: Spectrum of the mode-locked fiber figure-eight laser.